

# Superresolution Reconstruction for Magnetic Resonance Spectroscopic Imaging Exploiting Low-Rank Spatio-Spectral Structure

THÈSE N° 6546 (2015)

PRÉSENTÉE LE 20 MARS 2015

À LA FACULTÉ DES SCIENCES ET TECHNIQUES DE L'INGÉNIEUR  
GROUPE VAN DE VILLE

PROGRAMME DOCTORAL EN BIOTECHNOLOGIE ET GÉNIE BIOLOGIQUE

ÉCOLE POLYTECHNIQUE FÉDÉRALE DE LAUSANNE

POUR L'OBTENTION DU GRADE DE DOCTEUR ÈS SCIENCES

PAR

Jeffrey Adam KASTEN

acceptée sur proposition du jury:

Prof. N. Stergiopoulos, président du jury  
Prof. D. Van De Ville, Prof. F. Lazeyras, directeurs de thèse  
Prof. A. Comment, rapporteur  
Dr L. Florack, rapporteur  
Dr A. Henning, rapporteur



ÉCOLE POLYTECHNIQUE  
FÉDÉRALE DE LAUSANNE

Suisse  
2015

**Thèse N° 6546 (February 2015)**

*Thèse présentée à la faculté des sciences et techniques de l'ingénieur  
pour l'obtention du grade de docteur ès sciences  
et acceptée sur proposition du jury*

**Prof. Nikolaos Stergiopoulos**, *président*  
**Prof. Dimitri Van De Ville**, *directeur de thèse*  
**Prof. François Lazeyras**, *co-directeur*  
**Prof. Arnaud Comment**, *rapporteur*  
**Prof. Anke Henning**, *rapporteur*  
**Prof. Luc Florack**, *rapporteur*

**École polytechnique fédérale de Lausanne—2015**

*Cover design by Dimitri Van De Ville and Jeffrey Kasten  
Printing and binding by Repro-EPFL  
Copyright © 2015 by Jeffrey Adam Kasten  
Available at <http://miplab.epfl.ch/>*

# Abstract

Magnetic resonance spectroscopic imaging (MRSI) is a rapidly developing medical imaging modality, capable of furnishing both spatial and spectral information content, and has become a powerful clinical tool. The ability to non-invasively observe spatial maps of metabolite concentrations, for instance, in the human brain, can offer functional, as well as pathological insights, perhaps even before structural aberrations or behavioral symptoms are evinced. Despite its lofty clinical prospects, MRSI has traditionally remained encumbered by a number of practical limitations. Of primary concern are the vastly reduced concentrations of tissue metabolites when compared to that of water, which forms the basis for conventional MR imaging. Moreover, the protracted exam durations required by MRSI routinely approach the limits of patient compliance.

Taken in conjunction, the above considerations effectively circumscribe the data collection process, ultimately translating to coarse image resolutions that are of diminished clinical utility. Such shortcomings are compounded by spectral contamination artifacts due to the system pointspread function, which arise as a natural consequence when reconstructing non-band-limited data by the inverse Fourier transform. These artifacts are especially pronounced near regions characterized by substantial discrepancies in signal intensity, for example, the interface between normal brain and adipose tissue, whereby the metabolite signals are inundated by the dominant lipid resonances.

In recent years, concerted efforts have been made to develop alternative, non-Fourier MRSI reconstruction strategies that aim to surmount the aforementioned limitations. In this dissertation, we build upon the burgeoning medley of innovative and promising techniques, proffering a novel superresolution reconstruction framework predicated on the recent interest in low-rank signal modeling, along with state-of-the-art regularization methods. The proposed framework is founded upon a number of key tenets. Firstly, we proclaim that the underlying spatio-spectral distribution of the investigated object admits a bilinear representation, whereby spatial and spectral signal components can be effectively segregated. We further maintain that the dimensionality of the subspace spanned by the components is, in princi-

ple, bounded by a modest number of observable metabolites. Secondly, we assume that local susceptibility effects represent the primary sources of signal corruption that tend to disallow such representations. Finally, we assert that the spatial components belong to a class of real-valued, non-negative, and piecewise linear functions, compelled in part through the use of a total variation regularization penalty. After demonstrating superior spatial and spectral localization properties in both numerical and physical phantom data when compared against standard Fourier methods, we proceed to evaluate reconstruction performance in typical *in vivo* settings, whereby the method is extended in order to promote the recovery of signal variations throughout the MRSI slice thickness.

Aside from the various technical obstacles, one of the cardinal prospective challenges for high-resolution MRSI reconstruction is the shortfall of reliable ground truth data prudent for validation, thereby prompting reservations surrounding the resulting experimental outcomes. Though phantom studies may serve to provide reassurances, current designs lack the necessary geometrical sophistication and spectral heterogeneity necessary for emulating complex biological systems. We therefore develop a custom haptic Shepp-Logan phantom as part of a novel design and testing platform, motivated by current trends in additive manufacturing, which accords an important link between the analytically-predicted ideal signal and the acquired real-world MRSI measurements. We conclude the dissertation through a renewed assessment of the proposed reconstruction method using the newly-contrived phantom, tendering a number of auspicious results, and thereby presaging further advances in MRSI reconstruction and analysis.

**Keywords:** magnetic resonance spectroscopic imaging, chemical shift imaging, constrained reconstruction, low-rank approximation, non-convex optimization, total variation, MR phantoms, 3D printing, spatio-spectral modeling

# Résumé

L'imagerie spectroscopique par résonance magnétique (ISRM) est une modalité d'imagerie médicale qui est en train de se développer très rapidement, qui est capable de conférer à la fois des contenus d'informations spatiales et spectrales, et est devenue un outil clinique très utile. La capacité d'observer de manière non-invasive des cartes spatiales de concentration des métabolites, par exemple, dans le cerveau humain, peut fournir des perspectives fonctionnelles, ainsi que pathologiques, parfois avant même que des altérations structurelles ou de symptômes comportementaux se manifestent. Malgré ses perspectives cliniques uniques, l'utilisation de l'ISRM reste restreinte par un certain nombre de limitations pratiques. La principale préoccupation est la faible concentration des métabolites de tissu par rapport à celle de l'eau, sachant que celle-ci constitue la base de l'imagerie par résonance magnétique classique. En outre, la durée importante de l'examen d'ISRM approche régulièrement les limites de confort du patient.

Pris conjointement, les considérations ci-dessus circonscrivent efficacement le processus de collecte de données, qui se traduit par une résolution grossière de l'image métabolique qui par conséquent diminue son utilité clinique. Ces lacunes sont aggravées par des artefacts de contamination spectrales dues à la fonction de dispersion engendrée par l'échantillonnage limité de la transformée de Fourier inverse. Ces artefacts sont particulièrement prononcées à proximité des régions caractérisées par des écarts importants dans l'intensité du signal, par exemple, l'interface entre le cerveau normal et le tissu adipeux, dans lequel les signaux de métabolites sont altérés par les résonances de lipides.

Au cours des dernières années, d'importants efforts ont été déployés pour développer des stratégies alternatives à la transformée de Fourier, et qui visent à surmonter les limitations mentionnées ci-dessus. Dans cette thèse, nous construisons, sur la base de techniques novatrices et prometteuses, un nouveau cadre de reconstruction super-résolution fondé sur la modélisation à faible rang du signal, ainsi que sur des méthodes de régularisation connues dans la littérature. Le cadre proposé est fondé sur un certain nombre de principes clés. Tout d'abord, nous stipulons que la distribution spatio-spectrale

sous-jacente de l'objet étudié admet une représentation bilinéaire, dans laquelle les composantes spatiales et spectrales du signal peuvent être séparés. Nous admettons en outre que la dimension du sous-espace engendré par les composantes est, en principe, bornée par un nombre restreint de métabolites observables. Deuxièmement, nous supposons que les effets locaux de sensibilité représentent les principales sources de corruption du signal qui ont tendance à refuser ces représentations. Enfin, nous affirmons que les composantes spatiales appartiennent à une classe de fonctions réelles, non-négatifs, et linéaires par morceaux, contrainte en partie grâce à l'utilisation d'une pénalité de régularisation de la variation totale. Après avoir démontré des propriétés de localisation spatiales et spectrales supérieures aux méthodes de Fourier standards, à la fois sur des test-objets numérique et physique, nous avons procédé à l'évaluation des performances de reconstruction dans des conditions *in vivo* typiques, dans laquelle le procédé a été étendu afin de prendre en compte les variations du signal tout au long de l'épaisseur de l'IMRS.

Mis à part divers obstacles techniques, l'un des principaux défis futurs dans la reconstruction de l'IRMS de haute résolution, est l'insuffisance des données réelle qui permettent une validation pertinente, validant ainsi les résultats expérimentaux obtenus. Bien que les études sur les données fantômes puissent soutenir les résultats, les modèles actuels n'ont pas la complexité géométrique et l'hétérogénéité spectrale nécessaires pour simuler les systèmes biologiques complexes. Nous avons donc développé un fantôme Shepp-Logan physique et personnalisé utilisant la technologie de l'impression 3D. La nouveauté de cette approche tient dans le fait qu'elle apporte un lien unique entre le signal idéal prédit analytiquement et les mesures de l'IRMS réellement acquises. Nous concluons la dissertation par une nouvelle évaluation de la méthode de reconstruction proposée en utilisant le fantôme artificiel nouvellement conçu, apportant un certain nombre de résultats de bon augure, et présageant ainsi de nouveaux progrès dans la reconstruction et l'analyse dans le domaine de l'ISRM.

**Mots clés :** imagerie spectroscopique par résonance magnétique, l'imagerie du déplacement chimique, reconstruction sous contrainte, superrésolution, approximation à faible rang, l'optimisation non convexe, variation totale, fantômes RM, l'impression 3D, la modélisation spatio-spectrale

# Acknowledgements

Although a dissertation is often acclaimed as a hallmark of individual achievement, it is impossible for me to imagine the completion of this work without the contributions of numerous individuals whose insights and encouragement have guided me over the last several years.

I would first like to express my sincere gratitude to my thesis advisors, Professor Dimitri Van De Ville and Professor François Lazeyras, for granting me the opportunity to pursue my doctorate in Switzerland, and for their unremitting confidence and support. I cannot imagine a more stimulating yet nurturing research environment, and I remain in continual awe of their expansive scientific acumen and unrelenting enthusiasm. I would also like to thank the remaining members of my thesis committee: Dr. Anke Henning, Dr. Luc Florack, and Dr. Arnaud Comment, as well as the jury president, Dr. Nikolaos Stergiopoulos, for their commentaries and suggestions for improving the dissertation.

I would also like to extend my thanks to all members of the MIPLab and the CIBM in Geneva, especially to Zafer, Nora, Elena, Giulia, Jonas, Djano, Yury, Djalel, Frank, Naghmeh, Kirsten, Rotem, and Ruth, for the many stimulating discussions, advice, fond memories, and companionship over the years. I would like to offer my special thanks to Işık Karahanoğlu, for her generosity and patience in advancing my edification of advanced signal processing methodologies during the initial stages of the thesis.

In addition to all my family and friends back in the United States, who have been a continuing source of support, despite my being so far from home, I would like to thank all my wonderful friends here in Lausanne with whom I have continued to grow since the initial PhD hiring days.

Most of all, however, I reserve my deepest gratitudes to my wife Ksenya, who has steadfastly supported me throughout all the trials and tribulations typically encountered throughout one's doctoral years, and who has served as both my greatest advocate, as well as my harshest critic. I greatly value her encouragement, fortitude, and profound expertise, and it is to her and our growing family that I dedicate this thesis.



# Contents

<b>Abstract</b>	<b>i</b>
<b>Résumé</b>	<b>iii</b>
<b>Acknowledgements</b>	<b>v</b>
<b>List of Notations</b>	<b>xi</b>
<b>1 Introduction</b>	<b>1</b>
1.1 Contributions . . . . .	3
1.1.1 MRSI Reconstruction by Low-Rank Component Analysis . . . . .	3
1.1.2 Haptic Phantoms for MRSI Testing and Validation . . . . .	4
1.2 Thesis Outline . . . . .	4
<b>2 Magnetic Resonance Spectroscopic Imaging: Background</b>	<b>7</b>
2.1 Introduction . . . . .	7
2.2 Spin of Elementary Particles . . . . .	7
2.3 Protons in a Magnetic Field . . . . .	9
2.3.1 Precession . . . . .	10
2.3.2 Magnetization . . . . .	11
2.3.3 RF Spin Tipping and Relaxation . . . . .	13
2.4 The NMR Signal . . . . .	15
2.4.1 The Free Induction Decay . . . . .	15
2.4.2 Chemical Shift . . . . .	18
2.4.3 Spin-Spin Coupling . . . . .	19
2.4.4 The Spin Echo . . . . .	21
2.5 Magnetic Resonance Imaging . . . . .	21
2.5.1 Spatial Encoding . . . . .	22
2.5.2 Frequency Encoding and The Gradient Echo . . . . .	23
2.5.3 Phase and Slice Encoding . . . . .	25
2.5.4 Discretization and Sampling . . . . .	25
2.6 Localization Methods in Spectroscopy . . . . .	28
2.6.1 Single Voxel Spectroscopy . . . . .	29

2.6.2	Chemical Shift Imaging . . . . .	29
2.6.3	Accelerated Acquisition Techniques . . . . .	31
<b>3</b>	<b>MRSI Processing and Reconstruction</b>	<b>33</b>
3.1	Limitations in MRSI . . . . .	33
3.1.1	Sensitivity . . . . .	33
3.1.2	Resolution and Pointspread Function . . . . .	34
3.1.3	Field Inhomogeneity . . . . .	35
3.2	Standard Acquisition and Pre-processing Pipeline . . . . .	36
3.2.1	Water Suppression . . . . .	36
3.2.2	Volume Selection . . . . .	37
3.2.3	Pre-processing . . . . .	38
3.3	Non-Fourier Reconstruction . . . . .	44
3.3.1	Model-Based Reconstruction . . . . .	44
3.3.2	Use of Explicit Prior Knowledge . . . . .	47
3.3.3	Regularization . . . . .	51
3.3.4	General Decomposition Models . . . . .	59
<b>4</b>	<b>MRSI Reconstruction by Low-Rank Component Analysis</b>	<b>63</b>
4.1	Introduction . . . . .	63
4.2	Bilinear Models for MRSI . . . . .	63
4.3	Proposed Method: Preliminaries . . . . .	65
4.3.1	Inhomogeneity Compensation . . . . .	66
4.3.2	Total Variation-Based Spatial Regularization . . . . .	67
4.4	Proposed Method: Reconstruction Framework . . . . .	69
4.4.1	Algorithm Description . . . . .	70
4.4.2	Model Order Determination . . . . .	72
4.4.3	Selection of the Regularization Penalty . . . . .	74
4.5	Validation in Phantom Data . . . . .	74
4.5.1	Simulated Data . . . . .	75
4.5.2	MRSI Phantom Data . . . . .	79
4.6	Adapting the Framework for <i>In Vivo</i> Settings . . . . .	83
4.6.1	Incorporation of 3D Information . . . . .	83
4.6.2	<i>In Vivo</i> Experiments . . . . .	85
4.7	Summary . . . . .	88
<b>5</b>	<b>Haptic Phantoms for MRSI Testing and Validation</b>	<b>91</b>
5.1	Introduction . . . . .	91
5.2	Limitations in Current Phantom-Based Testing . . . . .	92
5.2.1	Haptic Phantoms . . . . .	92
5.2.2	Numerical Phantoms . . . . .	92
5.3	3D Printing: A Flexible Framework for MR Phantom Generation . . . . .	93
5.3.1	The 3D Printing Platform . . . . .	94

---

5.3.2	Analytical Fourier Computations . . . . .	94
5.4	A 3D Printed Shepp-Logan Phantom for MRSI . . . . .	98
5.4.1	Conception and Design . . . . .	98
5.4.2	Fabrication Process . . . . .	98
5.5	Phantom Validation . . . . .	102
5.5.1	Structural Imaging . . . . .	102
5.5.2	Spectroscopic Imaging . . . . .	104
5.6	Component-Based Reconstructions . . . . .	106
5.7	Summary and Discussion . . . . .	108
<b>6</b>	<b>Discussion and Outlook</b>	<b>113</b>
6.1	Summary . . . . .	113
6.2	Outlook . . . . .	116
	<b>Appendix A</b>	<b>121</b>
	<b>Bibliography</b>	<b>127</b>
	<b>Curriculum Vitæ</b>	<b>152</b>



# List of Notations

## Acronyms

AL	Augmented Lagrangian
AWGN	Additive White Gaussian Noise
BW	Bandwidth
Cho	Choline
cm	Centimeter
Cr	Creatine
CSI	Chemical Shift Imaging
DFT	Discrete Fourier Transform
EPSI	Echo Planar Spectroscopic Imaging
FA	Flip Angle
FDM	Fused Deposition Modeling
FFT	Fast Fourier Transform
FID	Free Induction Decay
FOV	Field of View
FWHM	Full Width at Half Maximum
GRE	Gradient Refocused Echo
HSVD	Hankel Singular Value Decomposition
Hz	Hertz
kHz	Kilohertz
Lac	Lactate
LASER	Localized Adiabatic Spin-Echo Refocusing
Lip	Lipid
LS	Least Squares
MHz	Megahertz
mm	Millimeter
mmol	Millimole
mmol/L	Millimoles/liter
mol	Mole
MRI	Magnetic Resonance Imaging
MRSI	Magnetic Resonance Spectroscopic Imaging
ms	Millisecond
NAA	N-Acetyl-L-Aspartic Acid

NMR	Nuclear Magnetic Resonance
OVS	Outer Volume Suppression
PCA	Principal Component Analysis
ppm	Parts-per-million
PRESS	Point-resolved Spectroscopy
PSF	Pointspread Function
rad	Radian
rf	Radiofrequency
s	Second
SNR	Signal-to-Noise Ratio
SRF	Spatial Response Function
STEAM	Stimulated Acquisition Mode
SVD	Singular Value Decomposition
SVS	Single Voxel Spectroscopy
$T_1$	Longitudinal Relaxation Time
$T_2$	Transverse Relaxation Time
TE	Echo Time
TGV	Total Generalized Variation
TI	Inversion Time
TR	Repetition Time
TV	Total Variation
VOI	Volume of Interest

---

**Physical Constants and Mathematical Notations**

$h$	Planck's constant: $6.6206 \times 10^{-34}$ [Joule · s]
$\hbar$	$h/2\pi$ [Joule · s]
$k$	Boltzmann constant: $1.3806 \times 10^{-23}$ [Joule/Kelvin]
$\gamma$	Gyromagnetic ratio [rad/s/Tesla]
$\gamma$	$\gamma/2\pi$ [MHz/Tesla]
$j$	Imaginary unit such that $j^2 = -1$
$\mathbf{r}$	Spatial domain coordinates
$\mathbf{k}$	$k$ -space coordinates
$\mathbf{X}^T$	Transpose of the matrix $\mathbf{X}$
$\mathbf{X}^H$	Hermitian transpose of the matrix $\mathbf{X}$
$z^*$	Complex conjugate of a complex number $z$
$\mathcal{P}_C$	Euclidean projector onto the set $C$
$\mathbb{1}_C$	Characteristic function of the set $C$
$\otimes$	Kronecker product
$\text{vec}(\mathbf{A})$	Vectorization of a multidimensional signal, for $\mathbf{A} \in \mathbb{C}^{N_1 \times N_2 \times \dots \times N_d}$ , $\text{vec}(\mathbf{A}) \in \mathbb{C}^{N_1 N_2 \dots N_d}$
$\langle \mathbf{x}, \mathbf{y} \rangle$	Inner product between vectors $\mathbf{x}$ and $\mathbf{y}$ , $\langle \mathbf{x}, \mathbf{y} \rangle = \sum_{i=1}^N x_i y_i^*$
$ \cdot $	If the argument is a set, cardinality of the set, otherwise, the absolute value of the argument
$\ f\ _{L^p}$	$L^p$ -norm of a continuous-domain function, $\ f\ _{L^p} = \begin{cases} \left( \int_{\Omega}  f ^p dm \right)^{1/p} & 1 \leq p < \infty \\ \sup_{\mathbf{x} \in \Omega}  f(\mathbf{x})  & p = \infty \end{cases}$
$\ \mathbf{x}\ _{\ell_p}$	$\ell_p$ -norm of a vector, $\ \mathbf{x}\ _{\ell_p} = \begin{cases} \left( \sum_{i=1}^N  x_i ^p \right)^{1/p} & 1 \leq p < \infty \\ \max( x_1 , \dots,  x_N ) & p = \infty \end{cases}$
$\ \mathbf{X}\ _F$	Frobenius norm of a matrix, $\ \mathbf{X}\ _F = \left( \sum_{i,j}  X_{i,j} ^2 \right)^{1/2}$
$\ \mathbf{X}\ _S$	Absolute sum norm of a matrix, $\ \mathbf{X}\ _S = \left( \sum_{i,j}  X_{i,j}  \right)$



# Chapter 1

## Introduction

Since its inception over forty years ago, magnetic resonance imaging (MRI) has revolutionized the medical field as a versatile clinical tool, providing a non-invasive platform for both diagnostic and prognostic evaluations *in vivo*, without prompting additional concerns over the effects of ionizing radiation exposure. While traditional structural MRI has been extolled for its ability to generate a profusion of complementary tissue contrasts, thereby accentuating specific anatomical features or aberrations, it represents but one of the multifarious modi operandi achievable with modern MR systems. Another such technique is magnetic resonance spectroscopic imaging (MRSI), which coalesces the basic principles underlying MRI, and the spectral discrimination capabilities of nuclear magnetic resonance (NMR) spectroscopy in order to produce spatially localized distributions of metabolic content.

MRSI has been increasingly acknowledged as a powerful source of supplemental information in the study of diseases such as cancer, most notably in the evaluation and treatment of brain tumors [1,2]. For example, while contrast-enhanced structural MRI is a powerful and non-invasive diagnostic aid, its specificity for differentiating between tumor types, neoplastic and non-neoplastic lesions, and identifying regions of active tumor is minimal [3–7]. A number of studies have highlighted the discriminating capability of MRSI in differential diagnostics, emphasizing its capacity for elucidating tumor heterogeneity [8–12]. Additionally, some studies on high-grade gliomas reported that the extent of the spatial maps of metabolic abnormalities derived from MRSI measurements often exceeded the pathological volume defined on the accompanying structural MR images [13–16], and that correlations with tumor recurrence following radiosurgery could be observed [17–19]. Such findings consequently impugn the preeminence of structural MRI in resection planning, and highlight the potential discordance between tissue and spectral content. The expediency of MRSI has similarly been demonstrated in the study of breast [20] and prostate cancer [21–25],

psychiatric conditions [26, 27], neurodegenerative disorders [28–30], and in the localization of epileptogenic networks and foci [31–34].

Despite the extensive list of propitious clinical applications, MRSI has thus far remained stymied by a number of practical limitations. The foremost impediment is the paltriness of the metabolite signal, due to both the inherent insensitivity of the MR experiment itself, and the low *in vivo* concentrations of the metabolites compared to that of water or lipids. Furthermore, the need to acquire data along a separate spectral dimension leads to protracted measurement times when compared against those required for structural imaging. These considerations, along with additional pragmatic constraints dictated by expected patient compliance, therefore mandate substantial compromises between the comprehensiveness of the measurement process and the overall exam duration. Accordingly, the attendant concessions engender a number of consequences for conventional MRSI protocols, whereby the resultant spatio-spectral data is reconstructed by means of the inverse discrete Fourier transform (DFT). The first of these pertains to the resulting coarse reconstruction resolutions necessary to ensure an adequate signal-to-noise ratio (SNR) within each voxel (the three dimensional analog of an image pixel), thereby precluding the perusal of fine spatio-spectral features. A second ramification is a broad system pointspread function, giving rise to spectral contamination artifacts between spatially remote locations. Such artifacts are particularly egregious near regions defined by sharp transitions in signal intensity, and arise from the implicit assumption underlying the Fourier transform that the imaged object is band-limited to the extent of the acquired measurements, which is exceedingly violated as the acquisition process is further curtailed.

Throughout the years, various efforts have been made in order to overcome the aforementioned limitations, and typically fall into one of two categories. The first describes methods that focus on the measurement process itself, devising accelerated or adapted acquisition schemes that further explore the associated tradeoffs between measurement duration, achievable spatial resolution, and sensitivity. The second is characterized by endeavors to develop alternative reconstruction strategies that aim to circumvent the various shortcomings following from the direct use of the DFT. Most of these techniques are predicated on varying degrees of additional prior knowledge, often furnished through ancillary high-resolution structural reference scans, thereby promoting the notion of superresolution reconstruction. In this dissertation, we continue further along this latter avenue, proffering both a novel reconstruction method that identifies and exploits key signal properties, as well as a flexible platform whereby the attendant reconstructions can be suitably validated under typical experimental conditions. Our primary contributions are discussed in the following section.

---

All research endeavors presented in this dissertation were conducted in collaboration between the Medical Image Processing Laboratory (MIPLab) at the École Polytechnique Fédérale de Lausanne, and the Center for Biomedical Imaging (CIBM) at the University Hospital of Geneva.

## 1.1 Contributions

### 1.1.1 MRSI Reconstruction by Low-Rank Component Analysis

By and large, reconstruction methods for MRSI can be classified according to whether or not parametric models are specified for the underlying spatio-spectral distribution. Those that do adopt this route typically appeal to structural MR modalities in order to partially specify the model parameters in advance, the remainder of which are estimated during the reconstruction procedure. The often high-resolution nature of this supplemental information facilitates translation to high-resolution reconstruction frameworks, but may render the method particularly susceptible to additional artifacts when discrepancies exist between the reference data and the MRSI signal content. Alternatively, methods that refrain from such parametrizations permit more data-centric investigations, but generally lack the necessary problem conditioning for high-resolution settings.

We aim to exploit the advantages of both approaches in a single reconstruction framework, which prescribes an intrinsic bilinear model for the spatio-spectral distribution, thereby enabling spatial and spectral behavior to be effectively dissociated. Using this paradigm, only the model order (i.e., the dimensionality of the subspace spanned by the constituent components) is pre-determined, which is assumed to be bounded by a modest number of observable metabolites. We further assert that the primary sources of signal distortion are due to static inhomogeneity effects, the spatial contributions of which are estimated from high-resolution reference scans, and explicitly accounted for by the employed measurement model. Lastly, we posit that the comprising spatial components belong to a class of piecewise-linear, real-valued, and non-negative functions, encouraged through the use of state-of-the-art total variation regularization. We demonstrate in various experimental scenarios that the proposed framework affords the necessary problem conditioning for high-resolution MRSI reconstruction, and even enables the restoration of through-plane spatio-spectral variations that are otherwise irrecoverable when considering single-slice MRSI acquisitions.

### 1.1.2 Haptic Phantoms for MRSI Testing and Validation

While a number of innovative and propitious reconstruction methods have been proposed in recent years, both for MRSI and other MR modalities, efforts to inspire the necessary alacrity for widespread adoption within the clinical community have been characterized by limited success. These perceived shortfalls may be attributable to the fact that unlike established Fourier methods, the various artifacts and biases accompanying these new methodologies are not fully characterized or understood. Though such misgivings may be palliated by contrasting reconstruction performance with ground truth or gold standard measurements, results obtained in the absence of any such reference data may remain contentious, as is certainly the case when considering high-resolution MRSI undertakings.

One of the prevailing means for validating pioneering methodologies is through the use of phantoms, i.e., objects of known structure that serve as proxies for *in vivo* scenarios. While a plurality of phantoms have been developed for structural MRI evaluations, these typically lack the degree of spectral heterogeneity or sophistication necessary for emulating biological samples. To address this apparent deficiency, we develop a custom MRSI phantom as part of a novel design and fabrication platform, motivated by current trends in additive manufacturing (3D printing). We demonstrate the expedience of the proposed framework for producing a class of versatile, low cost, and easily transferrable phantom designs, which additionally admit closed-form continuous-domain Fourier transforms. Using our completed prototype, we further illustrate that this latter advantage enables a direct connection between the theoretically-predicted signal and the observed MR measurements, and that such phantoms serve as an effective channel for identifying the primary potencies or shortcomings of a given reconstruction strategy.

## 1.2 Thesis Outline

This dissertation is organized as follows: In chapter 2 we introduce the various theoretical underpinnings surrounding basic MRSI signal formation and data acquisition. We begin by chronicling a number of key principles and discoveries that motivated the development of modern nuclear magnetic resonance spectroscopy (NMR). After enumerating the salient aspects governing a basic NMR experiment, we introduce the concept of MRI as a means of spatially localizing the MR signal, as well as address a few of the practical considerations underlying real-world acquisitions. We conclude by portraying MRSI as a unification of NMR and MRI, furnishing both spatial and spectral content, and describe a number of proposed acquisition techniques.

---

In chapter 3, we detail the assorted limitations afflicting MRSI, such as the strong spectral contamination due to nuisance signals, and review some of the standard compensatory mechanisms and pre-processing routines. We then delve into the vast arena of MRSI reconstruction methodology, surveying and contrasting some of the key developments over the last thirty years. With this background, we proceed to chapter 4, where we introduce a novel superresolution reconstruction framework that parallels the current interest in low-dimensional signal representations. Following a comprehensive exposition of the principal tenets, we demonstrate the efficacy of this method in both numerical simulations, and in typical clinical settings. In chapter 5, we aim to compensate for the dearth of suitable validation platforms for high-resolution MRSI reconstruction by developing a custom phantom with the aid of 3D printing. We begin by illustrating that the 3D printing platform is compatible with a class of analytical Fourier transforms, thereby bearing an important link between the theoretical MR signal and the collected measurements. We then utilize the successfully fabricated phantom to further validate the proposed reconstruction technique, providing a number of promising results. Finally, in chapter 6, we offer a brief summary of the presented work, and discuss a number of additional considerations as well as potential avenues for future research.



## Chapter 2

# Magnetic Resonance Spectroscopic Imaging: Background

### 2.1 Introduction

On a basic level, magnetic resonance spectroscopic imaging (MRSI) represents the convergence between two pivotal and rapidly-evolving techniques in the biomedical sciences. The first, nuclear magnetic resonance (NMR) spectroscopy, utilizes powerful magnetic fields and radiofrequency pulses in order to investigate the structure and chemical composition of a given sample. The second, magnetic resonance imaging (MRI), extends these ideas to furnish spatially-localized images, and has become an indispensable diagnostic tool within the medical field. Although these modalities have arisen out of elegant theoretical foundations, reflecting a rich and captivating history, this chapter solely aims to present an overview of the fundamental principles and breakthroughs that have motivated this propitious yet intricate field.

### 2.2 Spin of Elementary Particles

In 1925 two physicists, George Uhlenbeck and Samuel Goudsmit, working at the University of Leiden under Paul Ehrenfest introduced the concept of the electron spin [35] as a means for explaining the anomalous splitting patterns previously observed in atomic spectra. Their discovery came just a few months after Wolfgang Pauli's publication of the now famed exclusion principle [36], roughly stating that no two electrons may share the same values of the four quantum numbers. This concept of spin was later incorporated

by Paul Dirac into a relativistic description of quantum mechanics [37], and was eventually formalized as a property of all elementary particles by Pauli in 1940 [38].

Though similar in certain aspects, the electron spin should not be confused with its classical counterpart as the sum of the orbital angular momentum of its constituent elements. Rather, spin is a fundamental intrinsic property of elementary and composite particles, proscribing for each a particular set of rules and behaviors. Protons, neutrons, and electrons, for example, are instances of fermions, and all have spin  $1/2$ . Photons and mesons, on the other hand, are examples of bosons, which possess integer spin.

Because the spin is fixed for any given particle, so are the number of possible states, dictated by the “spin quantum number”,  $m_s$ , where for  $s = 0, 1/2, 1, 3/2, 2, \dots$ ,  $m_s = -s, -s + 1, \dots, s - 1, s$ . In the case of spin  $1/2$  (by far the most common for MRI applications), there are only two eigenstates, referred to as “spin up” for  $m_s = +1/2$ , and “spin down” for  $m_s = -1/2$ , which according to convention are represented vectorially as:

$$\alpha = \begin{pmatrix} 1 \\ 0 \end{pmatrix} \quad (\text{spin up}), \quad \beta = \begin{pmatrix} 0 \\ 1 \end{pmatrix} \quad (\text{spin down}). \quad (2.1)$$

Observable quantities such as the components of the spin in any of the Cartesian directions (represented by linear operators in the statistical interpretation of quantum mechanics) can then be expressed as:

$$\hat{S}_x = \frac{\hbar}{2}\sigma_x, \quad \hat{S}_y = \frac{\hbar}{2}\sigma_y, \quad \text{and} \quad \hat{S}_z = \frac{\hbar}{2}\sigma_z, \quad (2.2)$$

where

$$\sigma_x = \begin{pmatrix} 0 & 1 \\ 1 & 0 \end{pmatrix}, \quad \sigma_y = \begin{pmatrix} 0 & -j \\ j & 0 \end{pmatrix}, \quad \sigma_z = \begin{pmatrix} 1 & 0 \\ 0 & -1 \end{pmatrix} \quad (2.3)$$

are the Pauli spin matrices.

The discovery and formulation of the nuclear spin paved the way for further studies by Isidor Rabi, who postulated that the Stern-Gerlach experiment [39] could be extended so as to measure the properties of the atomic nucleus, successfully measuring the magnetic moments of lithium using a molecular beam device [40]. The utilization of an oscillating magnetic field for these experiments effectively laid the foundation for nuclear magnetic resonance (NMR), and would later motivate the works of Felix Bloch [41] and Edward Purcell [42], who successfully measured NMR signals from water and paraffin, respectively. For his molecular beam experiments, Rabi received the Nobel prize in physics in 1944. The same prize was shared by Bloch and Purcell eight years later.

## 2.3 Protons in a Magnetic Field

For charged particles, the intrinsic spin accords the properties of a magnetic dipole – similar to that produced by a closed electric current loop in macroscopic settings. Regarding the latter, considering a charge  $q$ , its position  $\mathbf{r}$ , and velocity  $\mathbf{v}$ , the expression for the dipole is:

$$\boldsymbol{\mu} = \frac{q(\mathbf{r} \times \mathbf{v})}{2}. \quad (2.4)$$

Given the classical angular momentum  $\mathbf{L} = \mathbf{r} \times \mathbf{p}$ , with  $\mathbf{p} = m\mathbf{v}$ , (2.4) can also be expressed as:

$$\boldsymbol{\mu} = \frac{q}{2m}\mathbf{L}. \quad (2.5)$$

Assuming a single proton, and replacing  $\mathbf{L}$  with its spin equivalent,  $\mathbf{S}$ ,

$$\boldsymbol{\mu} = g_N \frac{q}{2m_N} \mathbf{S} = g_N \beta_N \mathbf{S} = \gamma \mathbf{S}, \quad (2.6)$$

where  $g_N$  is the “nuclear g factor,” and  $\beta_N = \frac{q}{2m_N}$  the nuclear magneton. The constant  $\gamma = g_N \beta_N$  is called the “gyromagnetic ratio,” which is characteristic for each particular nucleus.

When immersed in an external magnetic field,  $\mathbf{B}$ , a magnetic dipole will experience a torque that acts to align it, with an associated potential energy given by:

$$V = -\boldsymbol{\mu} \cdot \mathbf{B}. \quad (2.7)$$

Adopting the convention that  $\mathbf{B} = \mathbf{B}_0 = 0\hat{\mathbf{i}} + 0\hat{\mathbf{j}} + B_0\hat{\mathbf{k}}$ , where  $\hat{\mathbf{i}}$ ,  $\hat{\mathbf{j}}$ , and  $\hat{\mathbf{k}}$  are unit vectors pointing along the  $x$ ,  $y$ , and  $z$  Cartesian dimensions, respectively, (2.6) can be substituted for  $\boldsymbol{\mu}$  in (2.7) to obtain:

$$V = -\gamma B_0 S_z. \quad (2.8)$$

If  $S_z$  is supplanted by its corresponding quantum mechanical operator,  $\hat{S}_z$ , we obtain the Hamiltonian operator (the quantum mechanical analogue of the classical Hamiltonian, i.e., the sum of the potential and kinetic energies) for the isolated proton as:

$$\hat{H} = -\gamma B_0 \hat{S}_z. \quad (2.9)$$

The eigenfunctions of the time-independent Schrödinger equation,

$$\hat{H}\psi = -\gamma B_0 \hat{S}_z \psi = E\psi \quad (2.10)$$

are simply the eigenfunctions of  $\hat{S}_z$ , with energies given by:

$$E_\alpha = -\frac{\hbar\gamma B_0}{2} \quad (\text{spin up, parallel}) \quad (2.11)$$

$$E_\beta = \frac{\hbar\gamma B_0}{2} \quad (\text{spin down, anti-parallel}), \quad (2.12)$$

such that  $\Delta E = E_\beta - E_\alpha = \hbar\gamma B_0$ . Transitions from the lower energy state (2.11) to the high energy state (2.12) can then be effectuated by irradiating the proton with photons carrying an energy  $\Delta E = \hbar\gamma B_0 = \hbar\omega$ , corresponding to a radial frequency of

$$\omega_0 = \gamma B_0, \quad (2.13)$$

referred to as the ‘‘Larmor frequency.’’

It is important to note throughout the preceding that the conferral of a magnetic moment occurs only in the case of non-zero spin. For example, in nuclides containing even numbers of both protons and neutrons, the Pauli exclusion principle mandates that the total spin vanishes, leading to zero magnetic moment. Consequently, only certain nuclei may be observed by NMR; some common choices are listed in Table 2.1 along with their associated gyromagnetic ratios.

Nucleus	Gyromagnetic Ratio $\gamma/2\pi$ (MHz/Tesla)
$^1\text{H}$	42.576
$^7\text{Li}$	16.546
$^{13}\text{C}$	10.705
$^{14}\text{N}$	3.0766
$^{15}\text{N}$	-4.3156
$^{17}\text{O}$	-5.7716
$^{23}\text{Na}$	11.262
$^{31}\text{P}$	17.235
$^{19}\text{F}$	40.052
$^{129}\text{Xe}$	11.777
$^3\text{He}$	32.434

Table 2.1: Gyromagnetic ratios for commonly investigated NMR nuclei [43, 44].

### 2.3.1 Precession

The time-independence of the Hamiltonian operator allows us to construct the general solution to the time-dependent Schrödinger equation as a linear combination of the stationary states:

$$\Psi(t) = c_\alpha e^{-jE_\alpha t/\hbar} \begin{pmatrix} 1 \\ 0 \end{pmatrix} + c_\beta e^{-jE_\beta t/\hbar} \begin{pmatrix} 0 \\ 1 \end{pmatrix} = \begin{pmatrix} c_\alpha e^{j\gamma B_0 t/2} \\ c_\beta e^{-j\gamma B_0 t/2} \end{pmatrix}, \quad (2.14)$$

where  $\|\Psi(t)\|^2 = 1$ . The physical behavior of this system is revealed by

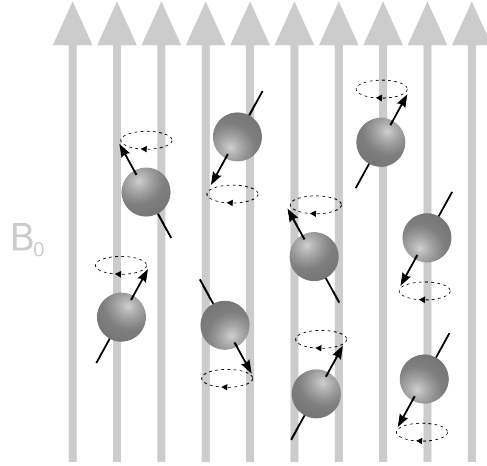


Figure 2.1: Spin precession in an external magnetic field.

calculating the expectation value of the  $x$ ,  $y$ , and  $z$  components of the spin:

$$\begin{aligned}
 \langle S_x \rangle &= \Psi(t)^H S_x \Psi(t) \\
 &= \begin{pmatrix} c_\alpha^* e^{-j\gamma B_0 t/2} & c_\beta^* e^{j\gamma B_0 t/2} \end{pmatrix} \frac{\hbar}{2} \begin{pmatrix} 0 & 1 \\ 1 & 0 \end{pmatrix} \begin{pmatrix} c_\alpha e^{j\gamma B_0 t/2} \\ c_\beta e^{-j\gamma B_0 t/2} \end{pmatrix} \\
 &= \frac{\hbar}{2} |c_\alpha| |c_\beta| \cos(\gamma B_0 t - (\varphi_\beta - \varphi_\alpha)). \tag{2.15}
 \end{aligned}$$

Allowing  $c_{\alpha,\beta} = |c_{\alpha,\beta}| e^{j\phi_{\alpha,\beta}}$ , such that  $|c_\alpha| = \cos(\theta/2)$ ,  $|c_\beta| = \sin(\theta/2)$ , and defining  $\varphi_0 = \varphi_\beta - \varphi_\alpha$ , (2.15) can be written as:

$$\langle S_x \rangle = \frac{\hbar}{2} \sin(\theta) \cos(\gamma B_0 t - \varphi_0). \tag{2.16}$$

Similarly,

$$\langle S_y \rangle = -\frac{\hbar}{2} \sin(\theta) \sin(\gamma B_0 t - \varphi_0) \tag{2.17}$$

$$\langle S_z \rangle = \frac{\hbar}{2} \cos(\theta), \tag{2.18}$$

implying that  $\langle \mathbf{S} \rangle$  precesses clockwise around  $\mathbf{B}_0$  at the Larmor frequency with a constant azimuthal angle  $\theta$ .

### 2.3.2 Magnetization

Though up to this point only single spins have been considered, typical NMR samples contain Avogadro's number of protons, representing many

spins. Given the energy discrepancy between the two possible spin states, the parallel state will be slightly overrepresented, in accordance with Maxwell-Boltzmann statistics:

$$\left(\frac{N_\alpha}{N_\beta}\right) = e^{\frac{\hbar\omega}{kT}}, \quad (2.19)$$

in which  $(N_\alpha/N_\beta)$  represents the population difference between state  $\alpha$  and  $\beta$ ,  $k$  is the Boltzmann constant and  $T$  the sample temperature. Note that even for a large number of spins, this population difference remains small. For example, the population difference for a sample at room temperature placed in a 3 Tesla field would amount to approximately 0.001% of the available spins, illustrating the relative insensitivity of NMR.

The net magnetization produced by a given sample consisting of  $N$  spins is simply the vector sum of the individual magnetic moments:

$$\mathbf{M} = \sum_{n=1}^N \boldsymbol{\mu}_n. \quad (2.20)$$

At equilibrium, however, there is no phase coherence among the spins, thereby producing no net magnetization in the transverse ( $xy$ ) plane. Nonetheless, the population difference does give rise to a net magnetization along the field direction (commonly referred to as the “longitudinal axis” in NMR nomenclature), with magnitude:

$$M_0 = \sum_{n=1}^N (\boldsymbol{\mu}_n \cdot \hat{\mathbf{k}}) = \frac{\gamma\hbar}{2} (N_\alpha - N_\beta). \quad (2.21)$$

Assuming that  $\hbar\omega \ll kT$ ,  $N_\alpha - N_\beta$  can be approximated as  $(N\hbar\omega/2kT)$ , leading to

$$M_0 = (\gamma\hbar)^2 \left(\frac{NB_0}{4kT}\right). \quad (2.22)$$

It is this magnetization that ultimately determines the NMR signal. Expression (2.22) illustrates that in addition to the external magnetic field strength and the sample size,  $\gamma$  plays a central role in determining the sensitivity of an NMR experiment – one of the reasons that proton ( $^1\text{H}$ ) NMR has remained the most popular choice. Furthermore, the relatively small values of  $\gamma$  for nuclei (when compared to that of the isolated electron) along with clinical static magnetic field strengths of around 1.0-3.0 Tesla place the Larmor frequency within the radiofrequency (rf) range, rendering *in vivo* NMR as a clinically safe and non-invasive modality.

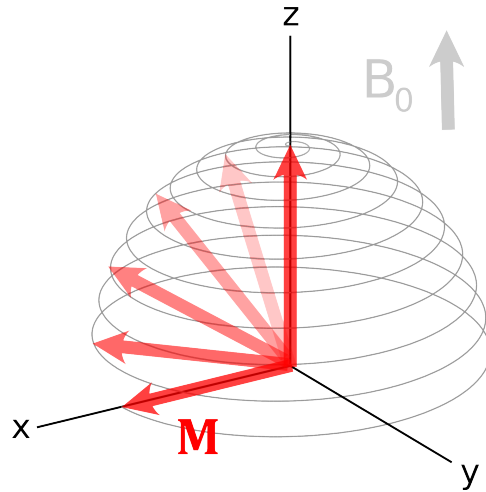


Figure 2.2: Precessing magnetization tipped onto the transverse plane following irradiation with a radiofrequency pulse.

### 2.3.3 RF Spin Tipping and Relaxation

Prior to 1966, NMR spectra were collected by continuously varying the rf frequency while holding the magnetic field strength fixed, or vice versa. This method of data collection was largely supplanted by the techniques proposed by Richard Ernst [45], in which wide-band rf pulses were used in conjunction with the Fourier transform, greatly improving sensitivity and reducing acquisition times. In order to produce the NMR signal, the net magnetization must first be rotated onto the transverse plane. This can be accomplished most efficiently through the application of an additional circularly-polarized rf pulse,  $\mathbf{B}_1$ , at the Larmor frequency:

$$\mathbf{B}_1(t) = B_1 \left( \cos(\omega_0 t) \hat{\mathbf{i}} - \sin(\omega_0 t) \hat{\mathbf{j}} \right). \quad (2.23)$$

During the pulse, transitions between the high and low-energy states are effectuated, reducing the population difference maintained at equilibrium. Furthermore, the spins gain greater phase coherence as they precess around both the static field ( $\mathbf{B}_0$ ), and the applied field ( $\mathbf{B}_1$ ), ensuring a net magnetization. Once the magnetization has been transferred to the transverse plane, it can then be detected using specialized receiver coils via Faraday's law of electromagnetic induction.

As the total magnetization represents a sum of the individual spin magnetic moments, the equation of motion can be generalized as:

$$\frac{d\mathbf{M}(t)}{dt} = \mathbf{M}(t) \times \gamma \mathbf{B}_{\text{tot}}(t), \quad (2.24)$$

where  $\mathbf{B}_{\text{tot}}$  represents the combined contributions of both the static and radiofrequency fields. Expression (2.24) simply reinforces the fact that when only the static field is present,  $d\mathbf{M}(t)/dt = 0$ .

Once the application of the radiofrequency pulse has ended, the system will tend towards its equilibrium state. This process is known as “relaxation,” and is governed by two sample-specific time constants known as  $T_1$  and  $T_2$ , described below.

### Longitudinal Relaxation - $T_1$

Also known as “spin-lattice” relaxation, longitudinal relaxation describes the process whereby energy from the spins is transferred to the surrounding lattice, with which the spins are assumed to be in thermal contact. As such, the system will tend towards its lowest energy configuration, leading to a regrowth of the magnetization along the longitudinal axis. The rate at which this process occurs is determined by the time constant  $T_1$ , such that:

$$\frac{dM_z(t)}{dt} = -\frac{M_z(t) - M_0}{T_1}. \quad (2.25)$$

### Transverse Relaxation - $T_2$ and $T_2^*$

Also known as “spin-spin” decay, transverse relaxation is a consequence of the spins’ interaction with their local environments. Energy exchange between spins and their neighbors leads to a loss of phase coherence, reducing the available transverse magnetization. The time scale for this process is reflected by the value  $T_2$  as:

$$\frac{dM_{xy}(t)}{dt} = -\frac{M_{xy}(t)}{T_2}, \quad (2.26)$$

where  $M_{xy}$  represents the magnetization in the transverse plane.

Although up until this point the static field has been considered to be purely homogeneous, small variations may exist, leading to a distribution of precessional frequencies across the sample. This causes an additional loss of coherence among the spins, hastening the decay of the transverse magnetization. The combined effects are reflected by the parameter  $T_2^*$ :

$$\frac{1}{T_2^*} \triangleq \frac{1}{T_2} + \frac{1}{T_2'}, \quad (2.27)$$

where  $T_2'$  encompasses the additional dephasing due to local field inhomogeneities. Although the processes governing  $T_2$  represent an inherent loss in magnetization, as will be shown later, the signal loss due to  $T_2'$  is recoverable.

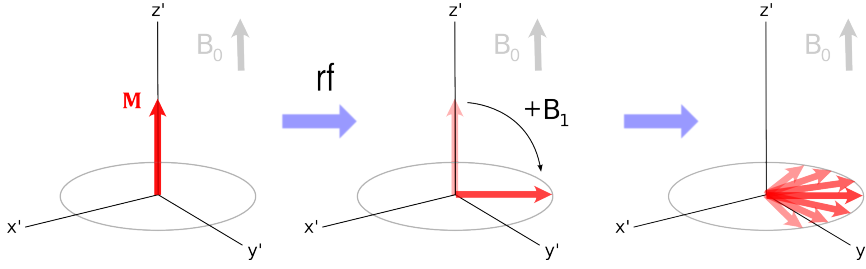


Figure 2.3: Phase decoherence due to  $T_2^*$  processes leads to a decaying transverse magnetization. Here, the magnetization is displayed in a rotating reference frame, which precesses around  $\mathbf{B}_0$  at the Larmor frequency.

## 2.4 The NMR Signal

### 2.4.1 The Free Induction Decay

The equation of motion for the precessing magnetization and the relaxation effects mentioned above can be combined into the well-known Bloch equations [46]:

$$\frac{dM_x(t)}{dt} = \gamma (M_y(t)B_0(t) - M_z(t)B_{1,y}(t)) - \frac{M_x(t)}{T_2} \quad (2.28)$$

$$\frac{dM_y(t)}{dt} = \gamma (M_z(t)B_{1,x}(t) - M_x(t)B_0(t)) - \frac{M_y(t)}{T_2} \quad (2.29)$$

$$\frac{dM_z(t)}{dt} = \gamma (M_x(t)B_{1,y}(t) - M_y(t)B_{1,x}(t)) - \frac{M_z(t) - M_0}{T_1}. \quad (2.30)$$

Assuming only a static field component, the Bloch equations can be solved to yield:

$$M_x(t) = e^{-t/T_2} (M_x(0) \cos(\omega_0 t) + M_y(0) \sin(\omega_0 t)) \quad (2.31)$$

$$M_y(t) = e^{-t/T_2} (M_y(0) \cos(\omega_0 t) - M_x(0) \sin(\omega_0 t)) \quad (2.32)$$

$$M_z(t) = M_z(0)e^{-t/T_1} + M_0 \left(1 - e^{-t/T_1}\right), \quad (2.33)$$

where  $M_x(0)$ ,  $M_y(0)$ , and  $M_z(0)$  represent initial values of the magnetization in each of the  $x$ ,  $y$ , and  $z$ -directions, respectively. The expression for the transverse components of the magnetization may be further simplified by adopting the polar form:

$$M_{xy}(t) = |M_{xy}(0)|e^{-t/T_2}e^{-j(\omega_0 t - \varphi_0)}, \quad (2.34)$$

where  $\varphi_0$  is the initial phase at  $t = 0$ .

Following an initial rf pulse, the produced transverse magnetization generates a magnetic flux,  $\Phi(t)$  in the receive coil. The measured signal is then

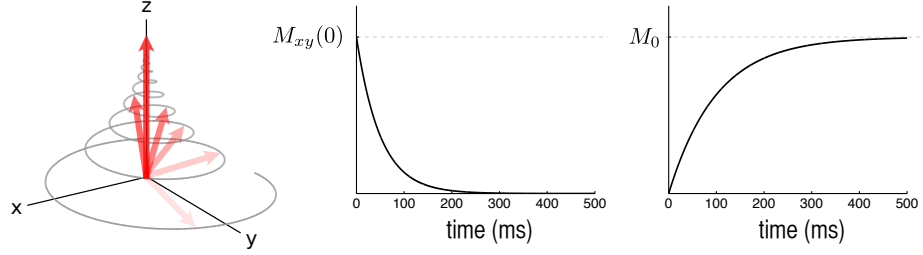


Figure 2.4: Regrowth of the longitudinal magnetization ( $M_0$ ) and the accompanying decay in transverse magnetization ( $M_{xy}$ ) following a  $90^\circ$  radiofrequency pulse.

proportional to the time-derivative of this flux, i.e., the induced electromotive force:

$$-\frac{d\Phi(t)}{dt} = -\frac{d}{dt} \int_{\Omega \subset \mathbb{R}^3} \mathbf{M}(\mathbf{r}, t) \cdot \mathbf{B}^{\text{rec}}(\mathbf{r}) d\mathbf{r}, \quad (2.35)$$

where  $\Omega$  represents the sample domain, and  $\mathbf{B}^{\text{rec}}$  the receive field of the coil. The most basic NMR experiment, where all the available longitudinal magnetization is transferred to the transverse plane following a  $90^\circ$  pulse applied on resonance, is referred to as a “free induction decay” (FID). Assuming  $\omega \gg (1/T_1, 1/T_2)$  such that the time-derivatives of the corresponding exponential terms can be disregarded, the measured signal is given by:

$$s(t) \propto \omega_0 \int_{\Omega \subset \mathbb{R}^3} e^{-t/T_2^*} M_{xy}(\mathbf{r}, 0) B_{xy}^{\text{rec}}(\mathbf{r}) e^{j((\omega_{\text{ref}} - \omega(\mathbf{r}))t + \varphi_0(\mathbf{r}) - \phi_B^{\text{rec}}(\mathbf{r}))} d\mathbf{r}. \quad (2.36)$$

Here,  $\omega_{\text{ref}}$  is a reference frequency used for signal demodulation, effectively removing the rapid oscillations at the Larmor frequency, and  $\phi_B^{\text{rec}}$  is the field angle of  $\mathbf{B}^{\text{rec}}$ .

For most NMR applications, the FID itself is seldom investigated directly. Of primary interest is the spectral content of the measured signal, which can be assessed with the aid of the Fourier transform. Neglecting  $T_2^*$  effects, and assuming a small homogeneous sample such that the spatial dependencies arising in the exponential term of (2.36) can be disregarded:

$$s(t) = C e^{-t/T_2} e^{j\omega' t}, \quad (2.37)$$

where the time-independent terms and hardware-dependent factors have been absorbed into the constant  $C$ , and  $\omega'$  is the demodulated frequency.

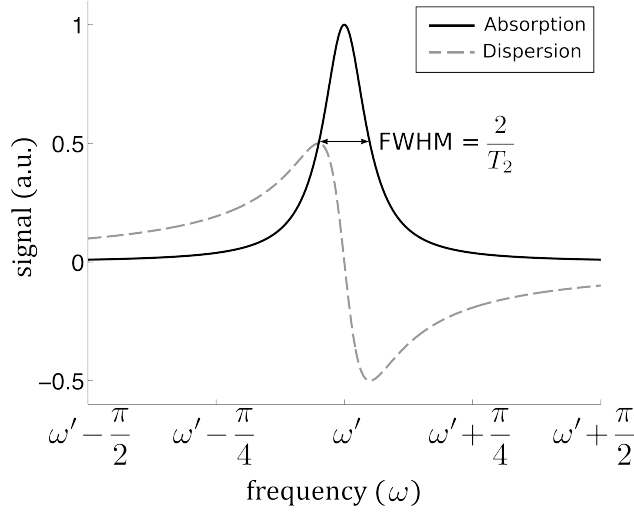


Figure 2.5: The absorption and dispersion components of a Lorentzian lineshape centered at  $\omega'$ .

The Fourier transform of this signal is:

$$\begin{aligned}
 \mathcal{F}\{s\}(\omega) &= \int_{-\infty}^{\infty} \left( C e^{j\omega' t} e^{-t/T_2} \right) e^{-j\omega t} dt \\
 &= \int_0^{\infty} C e^{-(j(\omega - \omega') + (1/T_2))t} dt \\
 &= \frac{C}{-j(\omega - \omega') + (1/T_2)} \\
 &= \underbrace{\frac{C(1/T_2)}{(\omega - \omega')^2 + (1/T_2)^2}}_{\text{absorption spectrum}} - j \underbrace{\frac{C(\omega - \omega')}{(\omega - \omega')^2 + (1/T_2)^2}}_{\text{dispersion spectrum}}. \quad (2.38)
 \end{aligned}$$

Expression (2.38) is referred to as a “Lorentzian” lineshape function, centered at frequency  $\omega'$ . The real-valued component is known as the “absorption” spectrum, and the imaginary part as the “dispersion” spectrum. One common metric for classifying Lorentzian lineshapes is the full width at half maximum (FWHM), which has the value  $2/T_2$  rad/s ( $1/\pi T_2$  Hz). In practice,  $T_2^*$  effects lead to amalgamated lineshapes that can no longer be described by pure Lorentzians, however, the standard FWHM criterion is often adopted for simplicity.

### 2.4.2 Chemical Shift

Though the formation of a measurable magnetization is an interesting phenomenon, the use of NMR would be rather limited if all spins simply resonated at the Larmor frequency. Indeed, if such were the case, NMR would be unable to provide any further insights into the molecular composition or local environments of a particular sample, and would simply function as a means of testing for the presence of the investigated nucleus. Fortunately, the precessional frequency of a particular nucleus depends not only upon the associated gyromagnetic ratio and the external field, but also upon its local magnetic environment. The latter is determined by the magnetic field produced by the local electron configuration, effectively “shielding” the nucleus from the effects of the external field. These environments are reflected through a dimensionless constant known as the “chemical shift,”  $\sigma$ , and were first noted by Proctor and Yu [47], and by Dickinson [48] in 1950. The effective field for a given chemical compound,  $l$ , can therefore be expressed as:

$$\mathbf{B}_{\text{eff}}(l) = (1 - \sigma_l)\mathbf{B}_0. \quad (2.39)$$

Nuclei in different chemical environments will therefore resonate at slightly different frequencies given by:

$$\omega_l = \gamma B_0(1 - \sigma_l), \quad (2.40)$$

permitting a robust investigation of the various physical and chemical properties of the sample. Allowing  $C(\sigma)$  to represent the density of spins with chemical shift  $\sigma$ , the (simplified) signal model in (2.37) becomes:

$$s(t) \propto e^{-t/T_2^*} \int_{-\infty}^{\infty} C(\sigma) e^{j\gamma\sigma B_0 t} d\sigma, \quad (2.41)$$

or,

$$s(t) \propto e^{-t/T_2^*} \sum_l C_l e^{j\gamma\sigma_l B_0 t} \quad (2.42)$$

if only a finite number of discrete nuclear species are considered.

Equation (2.40) implies that spectrometers employing different field strengths will lead to different resonance frequencies for the same compound. Thus, in order to enable comparisons between spectra recorded by different spectrometers, a standardized metric is needed, giving rise to the so-called “ppm scale,” in which the measured resonance is normalized to a pre-determined reference frequency:

$$\delta_{\text{ppm}} \triangleq \frac{\omega_l - \omega_{\text{ref}}}{\omega_{\text{ref}}} \times 10^6. \quad (2.43)$$

Normally,  $\omega_{\text{ref}}$  is taken to be that of tetramethylsilane -  $\text{Si}(\text{CH}_3)_4$ . According to convention, NMR spectra are usually displayed with the chemical shift (ppm) axis increasing from right to left (smaller chemical shifts imply greater shielding).

### 2.4.3 Spin-Spin Coupling

In addition to the chemical shift, another important feature is observed in high resolution NMR spectra that amounts to a secondary splitting of the spectral peaks into multiplets. This phenomenon arises from the fact that the investigated nucleus will be influenced not only by the local magnetic environment due to the surrounding electrons, but also by the magnetic dipoles of adjacent nuclei within the same molecule. This interaction is referred to as “spin-spin coupling” or simply, “J-coupling.” Though a thorough treatise is beyond the scope of this text, the underlying mechanisms can be elucidated by considering the Hamiltonian operator for a simple two spin system:

$$\hat{H} = -\gamma B_0(1 - \sigma_1)\hat{S}_{z,1} - \gamma B_0(1 - \sigma_2)\hat{S}_{z,2} + \frac{2\pi J_{12}}{\hbar}\hat{\mathbf{S}}_1 \cdot \hat{\mathbf{S}}_2, \quad (2.44)$$

where the subscripting indexes the particular nucleus, and  $J_{12}$  is the “spin-spin coupling constant.” When considering the composite wave functions:

$$\begin{aligned} \psi_1 &= \alpha(1)\alpha(2) \\ \psi_2 &= \beta(1)\alpha(2) \\ \psi_3 &= \alpha(1)\beta(2) \\ \psi_4 &= \beta(1)\beta(2), \end{aligned}$$

solving for the allowed energies yields:

$$E_1 = -\gamma\hbar B_0 \left(1 - \frac{\sigma_1 + \sigma_2}{2}\right) + \frac{\pi\hbar J_{12}}{2} \quad (2.45)$$

$$E_2 = -\frac{\hbar}{2} [(\gamma B_0)^2(\sigma_1 - \sigma_2)^2 + (2\pi J_{12})^2]^{1/2} - \frac{\pi\hbar J_{12}}{2} \quad (2.46)$$

$$E_3 = \frac{\hbar}{2} [(\gamma B_0)^2(\sigma_1 - \sigma_2)^2 + (2\pi J_{12})^2]^{1/2} - \frac{\pi\hbar J_{12}}{2} \quad (2.47)$$

$$E_4 = \gamma\hbar B_0 \left(1 - \frac{\sigma_1 + \sigma_2}{2}\right) + \frac{\pi\hbar J_{12}}{2}. \quad (2.48)$$

Because only one spin may transition between energy states at a given time,

the frequencies associated with allowable transitions are:

$$\omega_{1,2} = \frac{\omega_0}{2\pi} \left( 1 - \frac{\sigma_1 + \sigma_2}{2} \right) - \frac{J_{12}}{2} - \frac{1}{4\pi} [\omega_0^2(\sigma_1 - \sigma_2)^2 + (2\pi J_{12})^2]^{1/2} \quad (2.49)$$

$$\omega_{1,3} = \frac{\omega_0}{2\pi} \left( 1 - \frac{\sigma_1 + \sigma_2}{2} \right) - \frac{J_{12}}{2} + \frac{1}{4\pi} [\omega_0^2(\sigma_1 - \sigma_2)^2 + (2\pi J_{12})^2]^{1/2} \quad (2.50)$$

$$\omega_{2,4} = \frac{\omega_0}{2\pi} \left( 1 - \frac{\sigma_1 + \sigma_2}{2} \right) + \frac{J_{12}}{2} + \frac{1}{4\pi} [\omega_0^2(\sigma_1 - \sigma_2)^2 + (2\pi J_{12})^2]^{1/2} \quad (2.51)$$

$$\omega_{3,4} = \frac{\omega_0}{2\pi} \left( 1 - \frac{\sigma_1 + \sigma_2}{2} \right) + \frac{J_{12}}{2} - \frac{1}{4\pi} [\omega_0^2(\sigma_1 - \sigma_2)^2 + (2\pi J_{12})^2]^{1/2}, \quad (2.52)$$

where  $\omega_{i,j}$  denotes a transition from state  $i$  to state  $j$ . The above represents a so-called “second order spectrum” for the two-spin system for general choices of  $\sigma_1$ ,  $\sigma_2$ , and  $J_{12}$ . However, for  $\omega_0|\sigma_1 - \sigma_2| \gg 2\pi J_{12}$ , the  $J_{12}$  term inside the square root in (2.49) through (2.52) may be neglected, yielding a “first order spectrum.” In the example of the two spin system (designated as an “AX” system), the resulting first order spectrum would then appear as a pair of doublets, with centers separated by  $\omega_0|\sigma_1 - \sigma_2|/2\pi$  and an intra-doublet spacing of  $2\pi J_{12}$ . For the hydrogen nucleus, the splitting patterns for first order spectra can be predicted using the so-called “ $n + 1$  rule,” which states that if a proton is coupled to  $n$  equivalent nuclei, the multiplicity of the resulting peak is  $n + 1$ . Note that if all protons in a given molecule are equivalent, no splitting occurs.

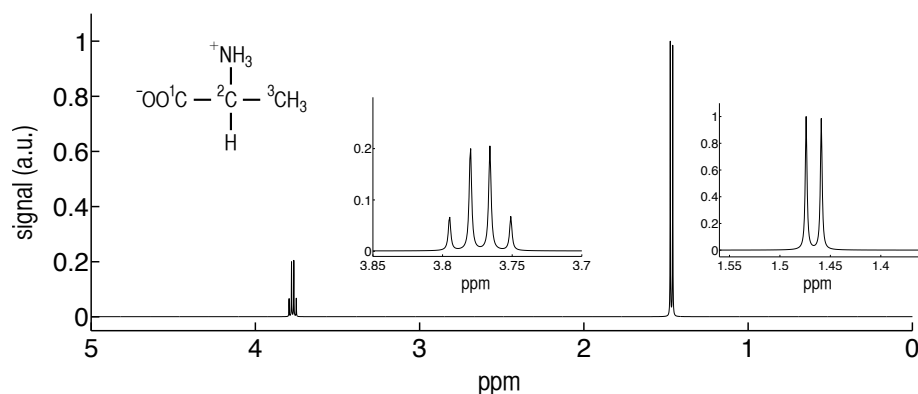


Figure 2.6: Simulated  $^1\text{H}$  NMR spectrum and chemical structure of Alanine, demonstrating the predicted peak splitting due to spin-spin coupling. This  $\text{AX}_3$  system is represented by a doublet centered at 1.47 ppm, and a quartet at 3.78 ppm, which are illustrated in the accompanying magnified subplots.

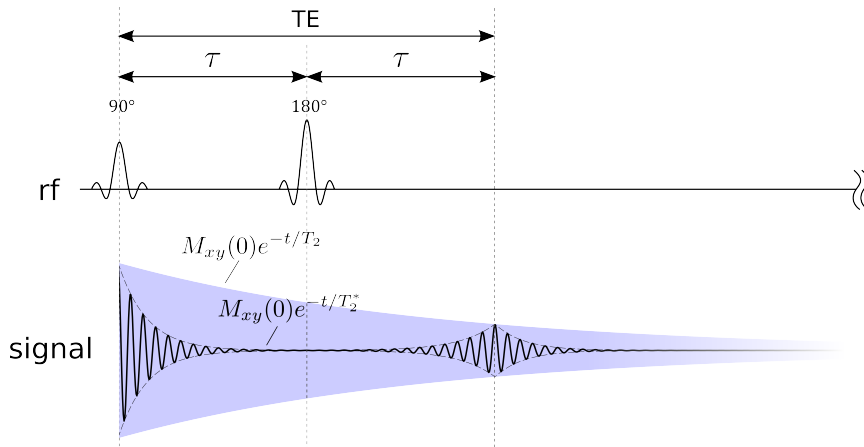


Figure 2.7: Schematic diagram representing the formation of a spin echo. Curved lines at the end of the diagram represent the completion of one TR.

#### 2.4.4 The Spin Echo

Section 2.3.3 introduced the concept of  $T_2^*$  weighting as a combination of the effects due to spin-spin interactions, and inhomogeneities present in the primary magnetic field. The magnetization due to the latter may be recovered by a technique known as the “spin echo” method. The success of the technique rests on the assumption that the field perturbations leading to  $T_2'$  effects are time-independent. Following the application of a  $90^\circ$  pulse, the spins will begin to lose phase coherence according to  $B_0(\mathbf{r})$ . After a time  $\tau$ , a second  $180^\circ$  pulse is applied, effectively inverting the phase of the spins. Because  $B_0$  is time-independent, the inverted phases will regain coherence, culminating in complete realignment at time  $TE \triangleq 2\tau$ , forming what is known as a “spin echo” (or “Hahn echo”). Time TE is known as the “echo time” of the experiment. Additional  $180^\circ$  pulses, applied at intervals of  $(2n - 1)\tau$  may be used to generate multiple echoes at times  $nTE$ , until the transverse magnetization is sufficiently diminished due to normal  $T_2$  processes. The entire pulse sequence may be repeated as needed, giving rise to a second time constant, TR, known as the “repetition time.”

## 2.5 Magnetic Resonance Imaging

In the decades following NMR’s inception, a number of works began to investigate potential *in vivo* applications. It wasn’t until 1971, however, when Raymond Damadian reported that typical relaxation times in malignant tumors differed significantly from those in normal tissue [49], that the diagnostic prospects of NMR began to emerge. Nonetheless, the NMR signal still

represented the bulk magnetization over the entire sample, and a suitable means of spatially-localizing NMR signals had yet to be discovered.

In the early 1970s, Peter Mansfield [50] and Paul Lauterbur [51], expanding upon the earlier work of Herman Carr [52], described how the addition of spatially-dependent magnetic field gradients could be used to form an image of the underlying spin distribution, with the first image of a living mouse being produced in 1974 [53]. The first MRI body scan of a human subject was conducted a number of years later by Damadian's group [54]. Since those early experiments, MRI has evolved into an exceptionally versatile and widespread imaging modality due to its noninvasiveness, and its ability to produce a myriad of different tissue contrasts emphasizing a variety of physiological phenomena.

Again assuming that all available magnetization has been transferred to the transverse plane,  $\omega_{\text{ref}} = \omega_0$ , and neglecting relaxation effects, (2.36) may once again be adapted as:

$$s(t) = \int_{\Omega \subset \mathbb{R}^3} \rho(\mathbf{r}) e^{j(\omega_0 t + \varphi(\mathbf{r}, t))} d\mathbf{r}, \quad (2.53)$$

where,

$$\rho(\mathbf{r}) = \omega_0 B_{xy}^{\text{rec}} C \rho_0(\mathbf{r}) (\gamma \hbar)^2 \frac{B_0}{4kT} \quad (2.54)$$

functions as an effective ‘‘spin density.’’ Here,  $\rho_0$  represents the number of spins per unit volume, and  $C$  is again a constant absorbing hardware-specific factors. Though  $\mathbf{B}^{\text{rec}}$  is assumed to be homogeneous, any spatial dependencies can be considered by allowing it to remain inside of the integral in (2.53). Note that  $\varphi$  in (2.53) now carries an explicit time-dependence, the purpose of which will be made clear in the following.

### 2.5.1 Spatial Encoding

Typically, MRI images are acquired using applied linear gradients, such that for an applied magnetic field,  $\mathbf{B}^G$ , the gradient vector is given by:

$$\begin{aligned} \mathbf{G}(t) &= \nabla B_z^G(\mathbf{r}) \\ &= G_x(t) \hat{\mathbf{i}} + G_y(t) \hat{\mathbf{j}} + G_z(t) \hat{\mathbf{k}}, \end{aligned} \quad (2.55)$$

where each  $G_x$ ,  $G_y$ , and  $G_z$  represents a linear gradient along the  $x$ ,  $y$ , and  $z$  Cartesian dimension, respectively. The  $z$ -component of the total effective field is then given by:

$$B_z(\mathbf{r}, t) = B_0 + \mathbf{r} \cdot \mathbf{G}(t), \quad (2.56)$$

leading to a position-dependent resonant frequency:

$$\omega(\mathbf{r}, t) = \omega_0 + \gamma \mathbf{r} \cdot \mathbf{G}(t). \quad (2.57)$$

The accumulated phase becomes:

$$\varphi_G(\mathbf{r}, t) = - \left( \omega_0 t + \gamma \mathbf{r} \cdot \int_0^t \mathbf{G}(\tau) d\tau \right). \quad (2.58)$$

Letting

$$\mathbf{k}(t) = \gamma \int_0^t \mathbf{G}(\tau) d\tau, \quad (2.59)$$

and substituting (2.58) into (2.53), the 1D spin density along  $\mathbf{G}$  is given by:

$$s(\mathbf{k}) = \int_{\Omega \subset \mathbb{R}^3} \rho(\mathbf{r}) e^{-2\pi j \mathbf{k} \cdot \mathbf{r}} d\mathbf{r}. \quad (2.60)$$

The measured signal is therefore revealed as the Fourier transform of the spin distribution. The values  $\mathbf{k}$  are commonly referred to as coordinates in “ $k$ -space” in the MR community, and represent “spatial frequencies” in units of [1/length]. Thus, a specific trajectory through  $k$ -space may be traversed through manipulation of  $\mathbf{G}(t)$ , either by modulating the gradient amplitude, or by varying the time during which the gradient remains in effect. In principle, the spin density may then be recovered by means of the inverse Fourier transform:

$$\rho(\mathbf{r}) = \mathcal{F}^{-1}\{s\}(\mathbf{r}) = \int_{-\infty}^{\infty} s(\mathbf{k}) e^{2\pi j \mathbf{k} \cdot \mathbf{r}} d\mathbf{k}. \quad (2.61)$$

### 2.5.2 Frequency Encoding and The Gradient Echo

Similar to the spin echo method described in section 2.4.4, the gradient echo method relies upon a manipulation of the transverse magnetization in order to coerce phase coherence. Following the  $90^\circ$  pulse, a constant gradient with negative polarity is applied at time  $t_1$ , leading to an accumulated phase given by:  $\varphi_G(\mathbf{r}, t) = \gamma \mathbf{r} \cdot \mathbf{G}(t - t_1)$ , indicating negative values of  $\mathbf{k}$ . This gradient is left on for duration  $\tau_-$ , upon which it is momentarily switched off, and then reapplied with the opposite (positive) polarity at time  $t_2$  for a duration of  $\tau_+$ . The accumulated phase then becomes:  $\varphi_G(\mathbf{r}, t) = \gamma \mathbf{r} \cdot \mathbf{G}(\tau_-) - \gamma \mathbf{r} \cdot \mathbf{G}(t - t_2)$ . It is therefore clear that at time  $\text{TE} = \tau_- + t_2$ , the accumulated phase will return to zero, effectively forming a “gradient echo.” The general condition

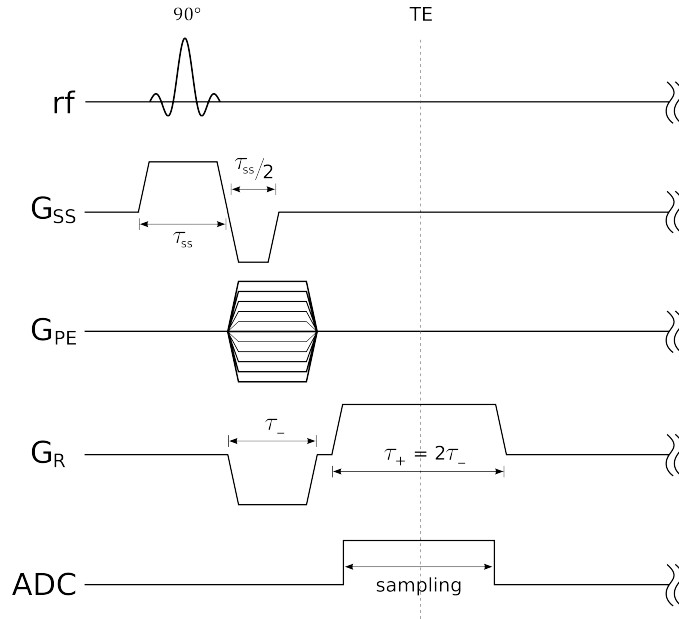


Figure 2.8: Schematic diagram for a typical 2D gradient echo sequence.  $G_{SS}$ : slice selection gradient;  $G_{PE}$ : phase encoding gradient;  $G_R$ : frequency encoding (readout) gradient; ADC: analog-to-digital conversion. For each TR, a different amplitude is used for  $G_{PE}$  in order to achieve proper phase encoding.

for the formation of a gradient echo is that the integrated area under the gradient waveform, i.e., its zeroth-order moment vanishes:

$$\int \mathbf{G}(t) dt = 0. \quad (2.62)$$

The times are often chosen so that the echo occurs at the center of the second gradient waveform, i.e., when  $\tau_+ = 2\tau_-$ . If data collection begins at  $t_2$ , this ensures that  $k$ -space is sampled symmetrically between  $\mathbf{k}_{\min} = -(\gamma/2\pi)\mathbf{G}(\tau_+/2)$  and  $\mathbf{k}_{\max} = (\gamma/2\pi)\mathbf{G}(\tau_+/2)$ , with the  $\mathbf{k} = \mathbf{0}$  point occurring at the center of the echo.

The above scheme demonstrates that with careful manipulation of the gradients, an entire “line” of  $k$ -space may be sampled within one TR, greatly improving the efficiency of a MRI experiment. Acquiring  $k$ -space data in this manner is referred to as “frequency encoding,” and the direction along which the gradient is applied the “read direction” (also “frequency encoding direction”).

### 2.5.3 Phase and Slice Encoding

In the most basic MRI acquisition scheme,  $k$ -space data are acquired along a Cartesian grid. Generally, frequency encoding is necessarily reserved for only one of the these dimensions, say the  $x$ -direction. Along each of the remaining two dimensions, short gradient pulses are applied in order to impart a position-dependent phase shift. This has the effect of moving to a particular value of  $k_y$  and  $k_z$ , upon which frequency encoding may be used to acquire all the  $k_x$  points corresponding to that location. This process is repeated until  $k_y$  and  $k_z$  have been sufficiently sampled. According to MR nomenclature, the  $y$ , and  $z$  dimensions are said to have been “phase encoded.”

It should be noted that while frequency encoding represents an efficient means for traversing  $k$ -space, phase encoding dictates that generally only one location per TR may be collected along the remaining Cartesian dimensions. The overall acquisition time for a 3D MR experiment is thus:

$$T_{\text{acq}} = N_y N_z \text{TR}, \quad (2.63)$$

according to the aforementioned convention, where  $N_y$  and  $N_z$  are the number of phase encoding steps in the  $y$  and  $z$  directions, respectively.

Often times, it is not necessary to acquire images of the full object, but only specific “slices” thereof. Slice selection can be accomplished using a combination of gradients and rf pulses in order to excite only those spins whose precessional frequencies lie within a certain range. Applying a linear, constant gradient,  $\mathbf{G}$ , the range of precessional frequencies is given by:

$$\omega(\mathbf{r}) = \omega_0 + \gamma \mathbf{r} \cdot \mathbf{G}. \quad (2.64)$$

In order to excite a slice with thickness  $\Delta \mathbf{r}$  centered at  $\mathbf{r}_0$ , the spectral profile of the rf pulse must range from  $\gamma \mathbf{G} \cdot (\mathbf{r}_0 - \Delta \mathbf{r}/2)$  to  $\gamma \mathbf{G} \cdot (\mathbf{r}_0 + \Delta \mathbf{r}/2)$ , which is accomplished by allowing the rf bandwidth,  $\text{BW}_{\text{rf}} = \gamma \mathbf{G} \cdot \Delta \mathbf{r}$ , or

$$\Delta \mathbf{r} = \frac{\text{BW}_{\text{rf}}}{\gamma \mathbf{G}}, \quad (2.65)$$

to make the dependence of the slice profile on rf bandwidth and the applied gradient more apparent.

### 2.5.4 Discretization and Sampling

Equation (2.61) implies that the MR signal is collected continuously, and that all values of  $\mathbf{k}$  are infinitely accessible. In common practice, the MR signal is sampled along the implemented  $k$ -space trajectory at regular intervals, leading to a finite set of discrete measurements. Considering the 1D case, the

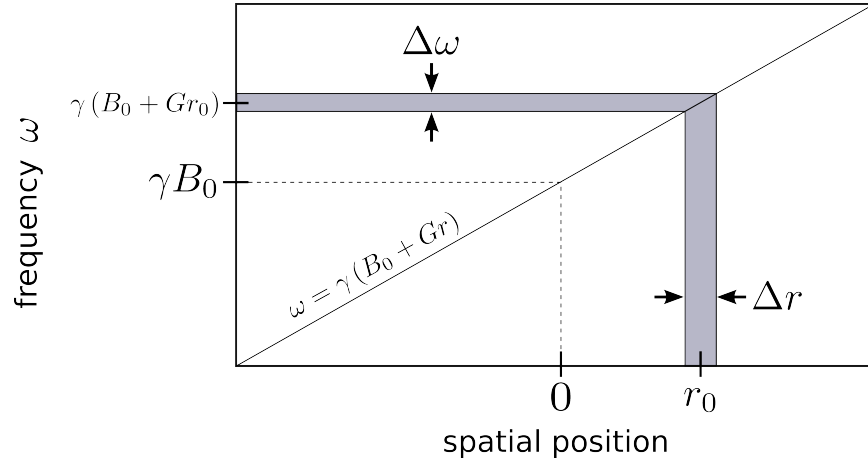


Figure 2.9: The relationship between rf bandwidth, gradient strength, and the slice selection profile for a given static magnetic field strength.

sampling interval,  $\Delta k$ , is determined via the gradient strength and duration as:

$$\Delta k = \gamma G \Delta t. \quad (2.66)$$

Modeling the sampling step as a multiplication with a Dirac comb distribution,  $\text{III}_p(x) \triangleq \sum_{n=-\infty}^{\infty} \delta(x - np)$ , the sampled signal can be expressed as:

$$\begin{aligned} s_{\text{III}}(k) &= s(k) \cdot \text{III}_{\Delta k}(k) \\ &= \sum_{n=-\infty}^{\infty} s(n\Delta k) \delta(k - n\Delta k). \end{aligned} \quad (2.67)$$

The inverse Fourier transform of this signal yields:

$$\begin{aligned} \hat{\rho}(x) = \mathcal{F}^{-1}\{s_{\text{III}}\}(x) &= \int_{-\infty}^{\infty} \left( \sum_{n=-\infty}^{\infty} s(n\Delta k) \delta(k - n\Delta k) \right) e^{2\pi j k x} dk \\ &= \sum_{n=-\infty}^{\infty} s(n\Delta k) e^{2\pi j n \Delta k x} \end{aligned} \quad (2.68)$$

for the reconstructed spin density. The convolution theorem for the Fourier transform, along with the fact that  $\mathcal{F}\{\text{III}_p\} = (1/p)\text{III}_{(1/p)}$  by the Poisson

summation formula, allows (2.68) to be re-expressed as:

$$\begin{aligned}
 \hat{\rho}(x) &= \left( \mathcal{F}^{-1}\{s\} * \mathcal{F}^{-1}\{\text{III}_{\Delta k}\} \right)(x) \\
 &= \rho(x) * \text{III}_{\left(\frac{1}{\Delta k}\right)}(x) \\
 &= \sum_{m=-\infty}^{\infty} \rho\left(x - \frac{m}{\Delta k}\right).
 \end{aligned} \tag{2.69}$$

The above implies that the inverse Fourier transform of the sampled signal yields an infinite series of copies of the spin distribution, spaced at intervals  $(1/\Delta k)$ . It is clear, therefore, that the sampling interval plays a fundamental role in the appearance of the reconstructed spin density. The quantity  $(1/\Delta k)$  is referred to as the ‘‘field of view’’ (FOV) in MR literature:

$$\frac{1}{\Delta k} \triangleq \text{FOV} = L. \tag{2.70}$$

Assuming that the spin distribution is compactly supported within  $\Omega$ , if  $L < \Omega$ , the copies will overlap - a phenomenon known as ‘‘aliasing.’’ Sampling intervals selected such that  $L > \Omega$  are said to be in compliance with the ‘‘Nyquist sampling criterion.’’

Of course, practical considerations mandate that only a finite number of  $k$ -space samples may be collected. This truncation can be modeled mathematically as a windowing of the sampled data by a rect function:

$$\text{rect}_p(x) = \begin{cases} 0 & |x| > \frac{p}{2} \\ \frac{1}{2} & |x| = \frac{p}{2} \\ 1 & |x| < \frac{p}{2} \end{cases} \tag{2.71}$$

such that,

$$\begin{aligned}
 s_{\text{III},W}(k) &= s(k) \cdot \text{III}_{\Delta k}(k) \cdot \text{rect}_W(k + (\Delta k/2)) \\
 &= \sum_{n=-N/2}^{N/2-1} s(n\Delta k) \delta(k - n\Delta k),
 \end{aligned} \tag{2.72}$$

where  $W \triangleq N\Delta k$  defines the width of the truncation window, and  $N$  equals the total number of  $k$ -space samples (generally taken to be even by conven-

tion). Again taking the inverse Fourier transform yields:

$$\hat{\rho}(x) = \mathcal{F}^{-1}\{s_{\text{III},W}\}(x) \quad (2.73)$$

$$\begin{aligned} &= \left( \mathcal{F}^{-1}\{s\} * \mathcal{F}^{-1}\{\text{III}_{\Delta k}\} * \mathcal{F}^{-1}\{\text{rect}_W(\cdot + \Delta k/2)\} \right)(x) \\ &= \sum_{m=-N/2}^{N/2} \rho\left(x - \frac{m}{\Delta k}\right) * W \text{sinc}(Wx) e^{-\pi j \Delta k x}, \end{aligned} \quad (2.74)$$

where  $\text{sinc}(x) \triangleq \sin(\pi x)/\pi x$ . Hence, the result of the truncation is a blurring of the infinitely sampled spin distribution by a sinc kernel. The amount of blurring is dependent upon  $W$ , increasing with narrowing window width.

The final connection between the sampled signal and the reconstructed spin density can be made by first discretizing the spin density:

$$\begin{aligned} \rho_{\text{III},L}(x) &= \hat{\rho}(x) \cdot \text{III}_{\Delta x}(x) \cdot \text{rect}_L(x + (\Delta x/2)) \\ &= \sum_{m=-M/2}^{M/2-1} \hat{\rho}(m\Delta x) \delta(x - m\Delta x), \end{aligned} \quad (2.75)$$

where  $L = M\Delta x$ . Taking the Fourier transform of (2.75):

$$\begin{aligned} \hat{s}(k) &= \mathcal{F}\{\rho_{\text{III},L}\}(k) \\ &= \sum_{m=-M/2}^{M/2-1} \hat{\rho}(m\Delta x) e^{-2\pi j m \Delta x}. \end{aligned} \quad (2.76)$$

Setting  $M = N$  and rewriting (2.74) as  $\hat{\rho}(x) = \sum_{n=-N/2}^{N/2} s(n\Delta k) e^{2\pi j n \Delta k x}$  and substituting into (2.76) leads to:

$$s\left(\frac{n}{L}\right) = \sum_{m=-N/2}^{N/2-1} \hat{\rho}\left(\frac{mL}{N}\right) e^{-2\pi j mn/N} \quad (2.77)$$

$$\hat{\rho}\left(\frac{mL}{N}\right) = \frac{1}{N} \sum_{n=-N/2}^{N/2-1} s\left(\frac{n}{L}\right) e^{2\pi j mn/N}, \quad (2.78)$$

thereby forming a discrete Fourier pair.

## 2.6 Localization Methods in Spectroscopy

In section 2.4, the measured signal was that produced by the bulk magnetization generated from the entire sample. While this may suffice for many

applications, in *in vivo* situations the ability to localize the NMR signal to a particular region of interest is often of paramount importance. This may stem from a need to either limit the spectral analysis to anatomical or functional regions shown to have specific diagnostic or prognostic value, or to exclude signals emanating from extraneous areas.

### 2.6.1 Single Voxel Spectroscopy

Single voxel spectroscopy (SVS) achieves the necessary localization by the same mechanisms described in section 2.5.3. In this case, a frequency-selective rf pulse in conjunction with slice selection gradients in all three Cartesian dimensions are employed in order to excite a 3D rectangular volume of interest (VOI). Two common SVS acquisition schemes for  $^1\text{H}$  applications include the stimulated acquisition mode (STEAM) [55–57] and point-resolved spectroscopy (PRESS) [58–61] sequences. STEAM employs three  $90^\circ$  pulses, generating three FIDs, four spin echoes, and one stimulated echo. The latter is usually considered the signal of interest, the others being nulled through the use of additional gradients. STEAM is generally preferred when short TE times are desired, minimizing  $T_2^*$  effects. However, only half of the signal is available when compared to traditional spin echo acquisitions, and remains more susceptible to diffusion effects. In PRESS, one  $90^\circ$  and two  $180^\circ$  pulses are applied along with two pairs of “crusher” (signal-nulling) gradients in order to generate two spin echoes, and to effectively null signal originating from outside the VOI.

### 2.6.2 Chemical Shift Imaging

Although single voxel spectroscopy is able to provide data within a specific VOI at high spectral resolution, its capacity for uncovering the spatial distribution of spectral content remains limited. Multivoxel spectroscopic techniques therefore aim to rectify this deficiency by adopting spatial localization techniques developed for MRI. The most basic MRSI acquisition scheme is known as chemical shift imaging (CSI) [62, 63], in which spatial localization is achieved by phase encoding along each Cartesian dimension (2D or 3D). The encoded signal is then allowed to evolve along an additional temporal dimension in the absence of gradients, using either FID or spin-echo methods. Denoting the spatio-spectral distribution of the imaged object as  $\rho(\mathbf{r}, f)$ , the measured signal can be expressed as:

$$s(\mathbf{k}, t) = \int_{-\infty}^{\infty} \int_{\Omega \subset \mathbb{R}^3} \rho(\mathbf{r}, f) e^{-2\pi j(\mathbf{k} \cdot \mathbf{r} + ft)} d\mathbf{r} df. \quad (2.79)$$

The measured data is collected by sampling along the temporal axis, and

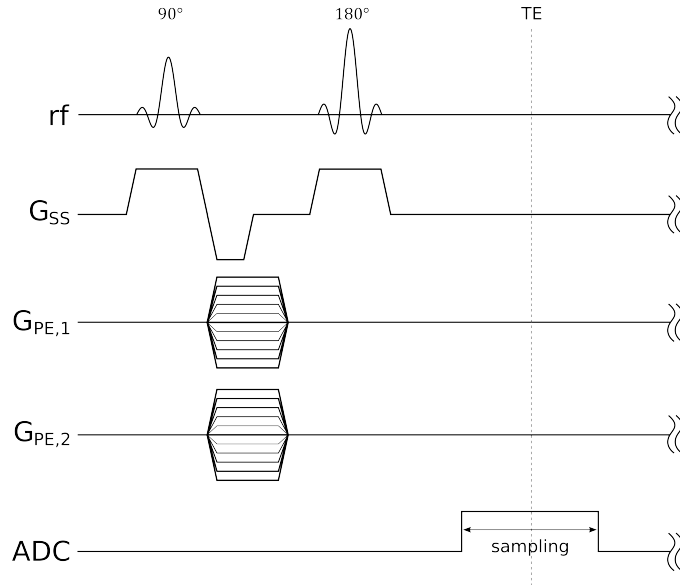


Figure 2.10: Schematic diagram of a typical spin-echo-based single-slice CSI sequence. At each TR, the desired slice is selectively excited, and subsequently phase encoded along the two remaining Cartesian dimensions. This type of acquisition scheme typically requires exceedingly long acquisition times, as only one point in  $k$ -space is collected for each repetition.

is then stored as a  $N_x \times N_y \times N_z \times T$  array, where  $N_x$ ,  $N_y$ , and  $N_z$  are the number of phase encodes in the  $x$ ,  $y$ , and  $z$  dimensions, respectively, and  $T$  is the number of acquired temporal samples. The resulting spatio-spectral distribution may then be recovered by applying the inverse Fourier transform along each array dimension. A common means of subsequent data visualization is achieved by integrating  $\rho(\mathbf{r}, f)$  along a particular range of frequencies,  $\Delta f$ , generating so-called “metabolic maps.”

Note that given the role of the temporal axis as the “read direction,” the efficient frequency encoding localization schemes introduced in section 2.5.2 can no longer be exploited, mandating that each location,  $\mathbf{k}$ , must be separately phase encoded (see figure 2.10). The total acquisition time for a CSI experiment therefore becomes:

$$T_{\text{acq}} = N_x N_y N_z \text{TR}. \quad (2.80)$$

As an example, consider that a CSI acquisition with  $N_x = 16$ ,  $N_y = 16$ ,  $N_z = 5$ , with  $\text{TR} = 1$  s would require a total acquisition time of twenty-one minutes – approaching the limit for clinically-acceptable human imaging studies.

### 2.6.3 Accelerated Acquisition Techniques

Given the long acquisition times associated with traditional CSI measurements, a considerable amount of effort has therefore been put towards the development of faster acquisition schemes. While many different approaches have been conceived, most have emerged as analogues to related MRI acquisition acceleration strategies such as spiral [64–66], steady-state free precession (SSFP) [67], echo-planar spectroscopic imaging (EPSI) [68–71], rosette [72], revolving spheres [73], and parallel imaging [74–76]. One of the most enduring and successful methods is the EPSI method, in which an oscillating gradient along one spatial dimension (for example, the  $x$ -direction) is utilized during data acquisition whereby one temporal sample is collected for each gradient lobe, effectively sampling an entire plane in the corresponding Fourier domains. The overall acquisition time is then reduced by a factor of  $N_x$ . Nonetheless, EPSI places a significant burden on the MR gradient system in order to achieve the slew rates necessary to achieve sufficient spectral bandwidth for typical MRSI studies. Furthermore, it has been shown [77] that the signal averaging necessary in order to achieve similar SNR values to traditional CSI measurements leads to comparable scan times. Lastly, as with EPI methods in traditional MRI, EPSI remains particularly susceptible to field inhomogeneity effects, possibly leading to additional artifacts and spectral lineshape distortions.



## Chapter 3

# MRSI Processing and Reconstruction

### 3.1 Limitations in MRSI

While the clinical prospects afforded by non-invasive *in vivo* investigation of metabolic concentrations and their spatial distributions are manifold, research in magnetic resonance spectroscopic imaging has remained hindered by a number of limitations. While many of the involved factors may be similarly implicated in structural MRI acquisitions, their increased severity for MRSI measurements mandates deliberate consideration. Though by no means a fully-exhaustive enumeration, the following represent the salient obstacles governing MRSI.

#### 3.1.1 Sensitivity

As was discussed in section 2.3.2, for a biological sample at room temperature, NMR remains a relatively insensitive technique. For standard proton imaging, this insensitivity is countervailed by the nearly 100% natural abundance of the  $^1\text{H}$  nucleus, and the large concentration of water (40-45 mol/liter) in biological tissue, thus enabling high SNR structural imaging. However, *in vivo* concentrations of other  $^1\text{H}$ -containing chemical compounds of interest tend to be orders of magnitude lower, thereby comprising a much smaller percentage of the overall spin density. Reliable detection of these compounds may therefore often be achievable only via repeated measurements and signal averaging, leading to further protracted measurement times. A number of MR-observable metabolites and their literature-derived concentrations in the human brain [78–80] are provided in table 3.1.

	Concentration (mmol/L)
Acetate	0.0-0.5
NAA	7.5-17.0
NAAG	0.5-2.5
ATP	2.0-4.0
Alanine	0.1-1.5
GABA	1.0-2.0
Ascorbic acid	0.5-1.5
Aspartate	1.0-2.0
Choline (total)	0.5-2.5
Creatine	4.5-10.5
Ethanolamine	0.0-1.5
Glucose	1.0-2.0
Glutamate	6.0-12.5
Glutamine	3.0-6.0
Glutathione	1.5-3.0
Glycerophosphorylcholine	0.5-1.5
Glycine	0.2-1.0
Glycogen	3.0-6.0
Homocarnosine	0.1-0.4
Myo-inositol	4.0-9.0
Scyllo-inositol	0.2-0.5
Lactate	0.2-1.0
Phosphocreatine	3.0-5.5
Phosphorylcholine	0.2-1.0
Phosphorylethanolamine	1.0-2.0
Pyruvate	0.0-0.5
Serine	0.2-2.0
Succinate	0.0-0.5
Taurine	2.0-6.0
Threonine	0.0-0.5

Table 3.1: Average concentrations of NMR-observable metabolites in the human brain. It is important to note that these values represent concentrations that are typically three to five orders of magnitude smaller than that of water.

### 3.1.2 Resolution and Pointspread Function

Within most clinical settings, practical restrictions on the total measurement time effectively limit the number of procurable phase encoding steps, and generally only the lowest spatial frequencies are acquired (i.e., those typically containing the highest signal energy). This curtailed measurement process engenders a number of consequences for reconstructed volumes produced by

the inverse discrete Fourier transform. For standard 3D CSI implementations utilizing sampling intervals in accordance with the Nyquist criterion, the corresponding voxel dimension are given by:

$$\Delta x = \frac{1}{N_x \Delta k_x}, \quad \Delta y = \frac{1}{N_y \Delta k_y}, \quad \Delta z = \frac{1}{N_z \Delta k_z}. \quad (3.1)$$

Timing considerations often yield choices for  $N_x$ ,  $N_y$ , and  $N_z$  that translate to nominal voxel dimensions on the order of 0.5 - 2.0 cm<sup>3</sup>, representing considerably coarser resolutions than seen in standard structural MRI. Moreover, in the absence of any additional spatial filtering, the (1D) pointspread function (PSF) is given by:

$$\text{PSF}(x) = \mathcal{F}^{-1}\{\text{rect}_W\}(x) = W \text{sinc}(Wx), \quad (3.2)$$

or when considering the sampling procedure by:

$$\begin{aligned} \text{PSF}(x) &= \left( \mathcal{F}^{-1}\{\text{rect}_W\} * \mathcal{F}^{-1}\{\text{III}_{\Delta k}\} \right)(x) \\ &= \sum_{n=-N/2}^{N/2} e^{2\pi j n \Delta k x} \\ &= D_N(x), \end{aligned} \quad (3.3)$$

where  $D_N$  is the Dirichlet kernel. A broadening of the PSF is therefore effectuated as a greater number of phase encodes are discarded, reducing the width of the sampling window. As this PSF is convolved with the spatial spin distribution, the actual voxel size is then taken to be the FWHM of the main lobe of the PSF – 21% larger than the nominal voxel size. Furthermore, as a result of residual phase dispersal, only 87% of the reconstructed voxel signal is contained within the nominal dimensions – the remainder being distributed along adjacent voxels [81]. This phenomenon is often referred to as signal or spectral “leakage,” though is also known by the more nefarious appellation of “voxel bleeding.” This spread is most conspicuous near regions characterized by large discrepancies in spin density, and is particularly problematic for <sup>1</sup>H MRSI of the brain, where cortical spectra are frequently contaminated by strong peripheral signals produced by the extra-cranial lipids. At the acquisition level, numerous efforts have been made in order to mitigate these PSF effects, either by utilizing the accelerated acquisition schemes described in section 2.6.3 to traverse more distal regions of  $k$ -space, employing higher-order magnetic field gradients [82], or applying density weighting [83].

### 3.1.3 Field Inhomogeneity

Although the external field may in general be considered as homogenous, the introduction of a sample may give rise to spatially-dependent inhomogeneity.

genities, largely due to variations in material susceptibility across the object. In this case, the acquired signal may be re-expressed as:

$$s(\mathbf{k}, t) = \int_{-\infty}^{\infty} \int_{\Omega \subset \mathbb{R}^3} \rho(\mathbf{r}, f) e^{-2\pi j(\mathbf{k} \cdot \mathbf{r} + (f + \gamma \Delta B_0(\mathbf{r}))t)} df. \quad (3.4)$$

Equation (3.4) implies that the measured spectrum at position  $\mathbf{r}$  will be shifted by an amount  $\Delta f(\mathbf{r}) = \gamma B_0(\mathbf{r})$  in the temporal frequency domain. Furthermore, a significantly varying  $B_0(\mathbf{r})$  across the voxel volume leads to an additional loss of phase coherence, shortening  $T_2^*$ . While these effects may be negligible for structural MRI, they are particularly disadvantageous when considering the large voxel dimensions normally encountered in MRSI, where attendant  $T_2^*$  reductions lead to significant spectral lineshape broadening and distortions. While most modern MR systems are equipped with active shimming systems, whereby additional gradients are utilized to compensate for sample-induced perturbations, corrections may generally be applied only up to first or second order. Strong residual inhomogeneity effects can therefore considerably reduce data quality, and remain pervasive in numerous aspects of the MRSI acquisition process.

## 3.2 Standard Acquisition and Pre-processing Pipeline

Given the aforementioned limitations, a number of important acquisition and data processing steps have become necessary in order to ensure adequate  $^1\text{H}$  MRSI data quality for subsequent processing and analysis. While by no means fully comprehensive, the following addresses the principle concerns.

### 3.2.1 Water Suppression

To reliably isolate and detect the metabolite signals of interest, the dominant water resonance must first be suppressed. This is normally accomplished during the MRSI acquisition with the aid of additional pulse modules that aim to either selectively excite the metabolite resonances while confining the water magnetization to the longitudinal axis, or by selective rephasing of the metabolites following wide-band excitation. Techniques belonging to the first category include the use of binomial pulse sequences [84–88], chemical shift selective (CHESS) excitation [89], and variable pulse powers and optimized relaxation delays (VAPOR) [90], while the latter includes MEGA [91] and water suppression by gradient-tailored excitation (WATERGATE) [92]. Additional methods that achieve suppression by exploiting the differences

in  $T_1$  relaxation between the metabolites and water include DEFT [93] and WET [94].

### 3.2.2 Volume Selection

As mentioned previously, the broad pointspread function often leads to severe contamination of the metabolite spectra by the extra-cranial lipid signals in *in vivo*  $^1\text{H}$  MRSI studies of the human brain. Though these artifacts are easily recognizable by a trained reviewer, they are problematic due to both their magnitude and overlapping chemical shifts with a number of metabolites of interest. The latter precludes the repurposing of the aforementioned techniques for removing the unwanted water resonance, and generally obfuscates reliable quantitation and processing. In most cases, lipid suppression is attempted during acquisition either by designating a VOI by means of selective excitation, or by actively nulling signals originating from lipid-containing regions. The former includes previously discussed methods such as STEAM or PRESS for selecting the VOI, yet care must be taken when determining the corresponding rf pulse shapes and durations due to so-called “chemical shift displacement” errors. These can be understood by recalling equations (2.64) and (2.65), and considering the frequency bandwidth between two separate compounds,  $i$  and  $j$ ,  $\omega_{i,j}$ . Forming the ratio of these two bandwidths yields:

$$\Delta x' = \frac{\omega_{i,j}}{\text{BW}_{\text{rf}}} \Delta x, \quad (3.5)$$

implying a relative displacement between the localized volumes. Considering the large voxel sizes in MRSI, and the addition of phase-encoding not present in single voxel methods, if  $\omega_{i,j}$  is large, considerable shifts may ensure which become spatially-resolved unless  $\text{BW}_{\text{rf}}$  is sufficient large, and may therefore lead to poorly localized or distorted spectra.

Improved localization can be achieved by employing methods that use adiabatic full passage (AFP) refocusing pulses [95], such as localized adiabatic spin-echo refocusing (LASER) [96]. In the basic LASER routine, the entire sample is excited with a single adiabatic pulse, after which 3D localization is achieved by three pairs of AFP pulses to selectively refocus three orthogonal slices. LASER is particularly advantageous due to its relative  $B_1$  insensitivity when compared to other localization methods. However, the increased sequence duration due to the large number of refocusing pulses makes it less suitable for short TE measurements. The semi-LASER [97] sequence addresses this limitation by replacing the initial AFP pulses with a normal excitation pulse, suppressing spurious FIDs or echoes with optimized crusher gradients.

An alternative strategy to selective excitation is through outer volume suppression (OVS) [98–102], where numerous slices positioned over the offending

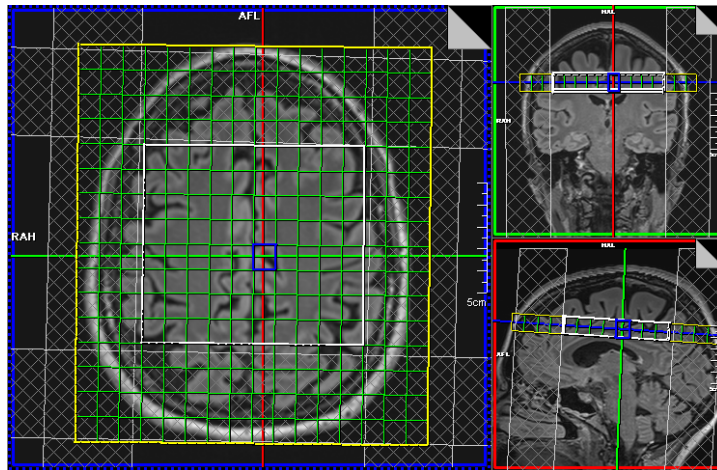


Figure 3.1: Sample single-slice CSI acquisition protocol of the human brain, including volume pre-selection (white box) and outer volume selection (crosshatched slabs).

regions are selectively excited and then dephased using crusher gradients, leaving the water and metabolite signals unperturbed for subsequent measurement. These modules can often be inserted into existing PRESS or STEAM sequences, though are often sensitive to  $B_1$  and  $T_1$  effects as with water suppression methods, and remain an active area of research in MRSI. An example of VOI selection and OVS slab placement during a typical scanning session is displayed in figure 3.1.

### 3.2.3 Pre-processing

In spite of the compensatory mechanisms employed in order to circumvent or abate the various detrimental factors affecting raw data quality, most MRSI measurements require a degree of additional pre-processing prior to analysis. This may be necessary due to the presence of static or dynamic field inhomogeneity effects, residual water or lipid signals, low SNR, or severe data truncation artifacts. A typical MRSI pre-processing pipeline (e.g. [103, 104]) may therefore include the following steps:

#### 1. Residual Water Removal

A number of the techniques outlined in section 3.2.1 have been shown to achieve excellent water suppression under favorable measurement conditions. However, many remain sensitive to  $T_1$ ,  $B_1$ , or  $B_0$  effects, which may result in either incomplete or failed water suppression, or unintentional suppression of the metabolites if the excitation bandwidth is not chosen carefully. To address the former, post-processing

tools have been developed that attempt to estimate and remove residual water or other nuisance components. Popular approaches include the use of low-pass finite impulse response (FIR) filters [105, 106], wavelets [107], and state-space methods. One prevalent method comprising the latter category is the Hankel singular value decomposition (HSVD) [108], a time-domain subspace approach that models an input signal as a sum of exponentially-damped sinusoids. The water signal is then approximated as a mixture of overlapping Lorentzian peaks, and subtracted from the input. This procedure has since inspired numerous variants such as HLSVD [109], HTLS [110], HTLS-PK [111], and KNOB-SVD [112], which exploit varying degrees of prior knowledge during the estimation procedure to fit spectroscopic data.

## 2. Temporal Apodization and Zero-Filling

Normally, the data acquisition duration for each phase encoding step is sufficiently long such that the acquired signal has decayed well below the noise level by the end of sampling. Given the incoherence between the temporal and spectral domains, the SNR in the latter may be improved by multiplying the time-domain signal by an appropriate choice of apodization function, which aims to preserve high SNR portions of the signal near the beginning of the FID (or echo) while attenuating the primarily noise-containing regions at the end. Two routinely used filters are based on Gaussian and exponential functions:

$$h_{\text{Gauss}}(t) = e^{-\frac{t^2}{\sigma^2}} \quad (3.6)$$

$$h_{\text{exp}}(t) = e^{-\Gamma t}. \quad (3.7)$$

Optimal sensitivity may be attained using the latter filter with  $\Gamma = 1/T_2^*$ , i.e., by matching the decay envelope of the signal. This sensitivity gain, however, is accomplished at the expense of a doubling of the spectral linewidth. Other values of  $\Gamma$  or  $\sigma$  may be selected to achieve different effects. For example, selecting a negative value of  $\Gamma$  in (3.7) will cause  $h_{\text{exp}}$  to assume the role of an inverse or deconvolution filter, reducing the overall spectral linewidth, but resulting in an additional loss of SNR. The effects of various temporal apodization filters on the reconstructed spectrum is illustrated in figure 3.2.

Zero filling the time-domain data, whereby a sequence of zeros is appended to the end of the sampled signal, may be used to improve the overall appearance of a spectrum, interpolating intermediate points between the spectral samples. This is often used in conjunction with (3.6) or (3.7) when working with truncated data in order to circumvent the associated spectral artifacts, or to improve digital resolution when visualizing narrow spectral peaks.

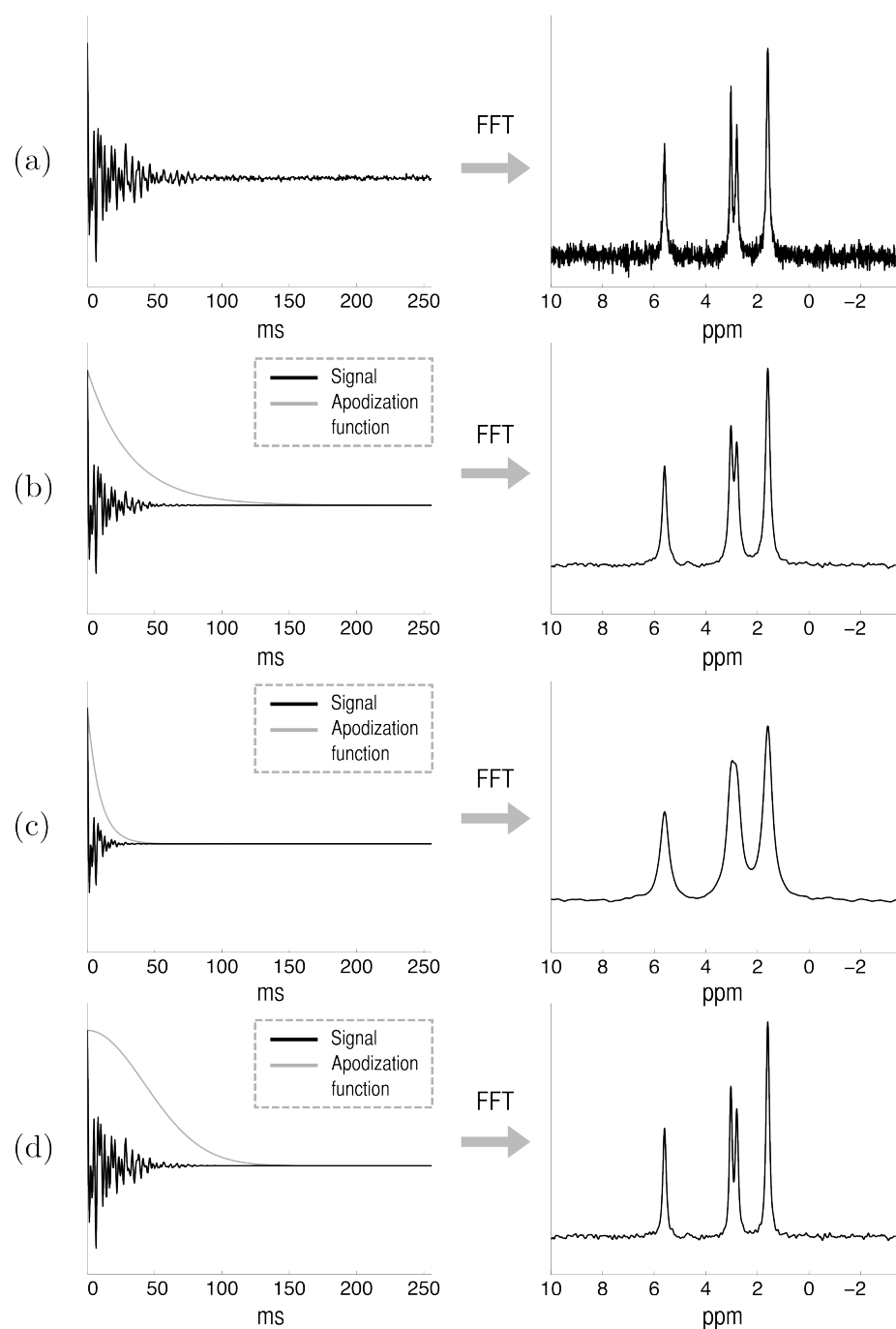


Figure 3.2: The effect of temporal apodization on a FID and its corresponding spectrum (black) using various filter functions (gray). (Row a) The original FID and its associated spectrum after Fourier transformation. (Row b) The effect of multiplying the FID with an exponential function matched to the decay envelope of the time-domain signal; the resultant spectrum illustrates an increase in SNR, accompanied by a doubling of the spectral linewidths. (Row c) Electing a filter that decays too rapidly leads to a significant increase in SNR at the expense of severely reduced spectral resolution. (Row d) Effect of temporal apodization using a Gaussian, rather than exponential, filter.

### 3. Phase Correction and Eddy Current Compensation

It is often the case that the first collected sample point does not correspond to zero phase points in the acquired echo or FID, which will lead to a reconstructed spectrum in which the real-valued component (typically used for quantitation) does not correspond to a pure Lorentzian absorption or dispersion lineshape. To correct for these deviations, the complex time-domain data must be multiplied by an additional complex phase factor,  $e^{j\vartheta}$ , where

$$\vartheta = \vartheta_0 + \vartheta_1(\omega - \omega_c). \quad (3.8)$$

Here  $\vartheta_0$  represents a “zeroth order” phase correction, and is frequency-independent. The  $\vartheta_1$  term denotes a “first order” correction, which applies a linearly-varying phase shift centered at a reference frequency,  $\omega_c$ . For single voxel spectra, zero and first order phase correction is often performed interactively, which becomes less feasible for MRSI datasets due to the large number of spectra. A number of automated phase correction algorithms have therefore been developed, for example by employing the Hilbert transform [113], optimizing the baseline [114], estimating phase distortions from prominent spectral peaks [115], exploiting lineshape symmetries [116], and adopting maximum likelihood (ML) approaches [117].

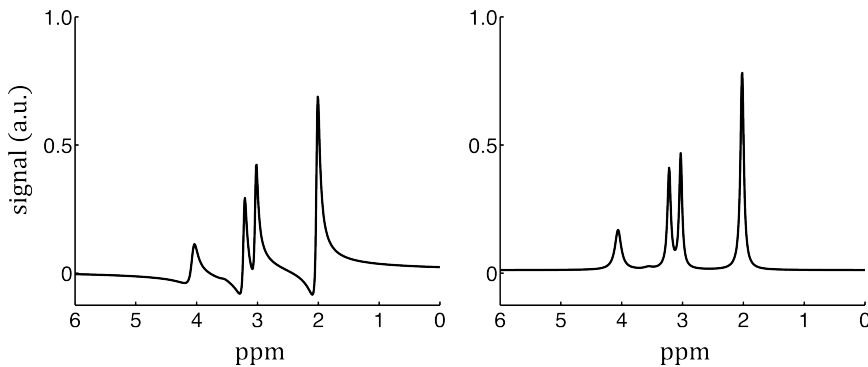


Figure 3.3: Example of a poorly phased (left), and correctly phased (right) MR spectrum.

A further source of lineshape distortions are residual eddy currents produced in conducting media during gradient switching, which produce time and position-dependent phase shifts throughout the acquisition. These currents may be counterbalanced at the hardware level through active shielding and gradient pre-emphasis, yet residual effects are common, often necessitating additional post-processing of the acquired spectra. One of the earliest proposed techniques for automatic

eddy current compensation is that of [118], where the phase of the acquired spectrum is corrected point-wise with the aid of a reference signal – often an unsuppressed water signal collected contemporaneously with the MRSI data. Other methods include the QUALITY routine [119], whereby a reference signal is used to estimate and correct for deviations from Lorentzian lineshapes, and techniques based on the continuous wavelet transform (CWT) [120].

#### 4. Spatial Filtering

Although precautions are taken during acquisition so as to suppress undesirable signals such as those due to peripheral lipids in  $^1\text{H}$  MRSI, these measures may yield imperfect outcomes. Coupled with the broad PSF, these residual signals still hold the potential to contaminate more remote regions of the VOI, further frustrating clinical interpretation and quantitative analysis. To mitigate these truncation artifacts, the  $k$ -space data is multiplied by a smooth apodizing function, which mitigates the influence of the PSF side lobes by further sacrificing spatial resolution. These functions are normally chosen to be symmetric, paralleling common  $k$ -space acquisition schemes. Some popular choices include the Cosine, Hanning, Hamming, Gaussian, and Kaiser-Bessel windows:

$$\cos\left(\frac{\pi k}{2k_{\max}}\right) \quad (\text{Cosine}) \quad (3.9)$$

$$0.54 + 0.46 \cos\left(\frac{\pi k}{k_{\max}}\right) \quad (\text{Hamming}) \quad (3.10)$$

$$\cos^2\left(\frac{\pi k}{2k_{\max}}\right) \quad (\text{Hanning}) \quad (3.11)$$

$$e^{-\frac{(2k)^2}{k_{\max}^2}} \quad (\text{Gaussian}) \quad (3.12)$$

$$f_{k_{\max}}(k) \frac{I_0(b f_{k_{\max}}(k))}{I_0(b)} \quad (\text{Kaiser-Bessel}), \quad (3.13)$$

where  $I_0$  is a modified Bessel function of the first kind,  $k_{\max}$  is the largest acquired spatial frequency, and

$$f_{k_{\max}}(k) \triangleq \begin{cases} \left(1 - \left(\frac{k}{k_{\max}}\right)^2\right)^{1/2}, & |k| < k_{\max} \\ 0, & \text{otherwise.} \end{cases} \quad (3.14)$$

Figure 3.4 displays the effects of various windowing methods on a simulated object designed to mimic the extra-cranial lipids in the human brain, illustrating both the profound effects of the PSF as well as the accompanying losses in spatial resolution incurred when employing additional  $k$ -space filtering.

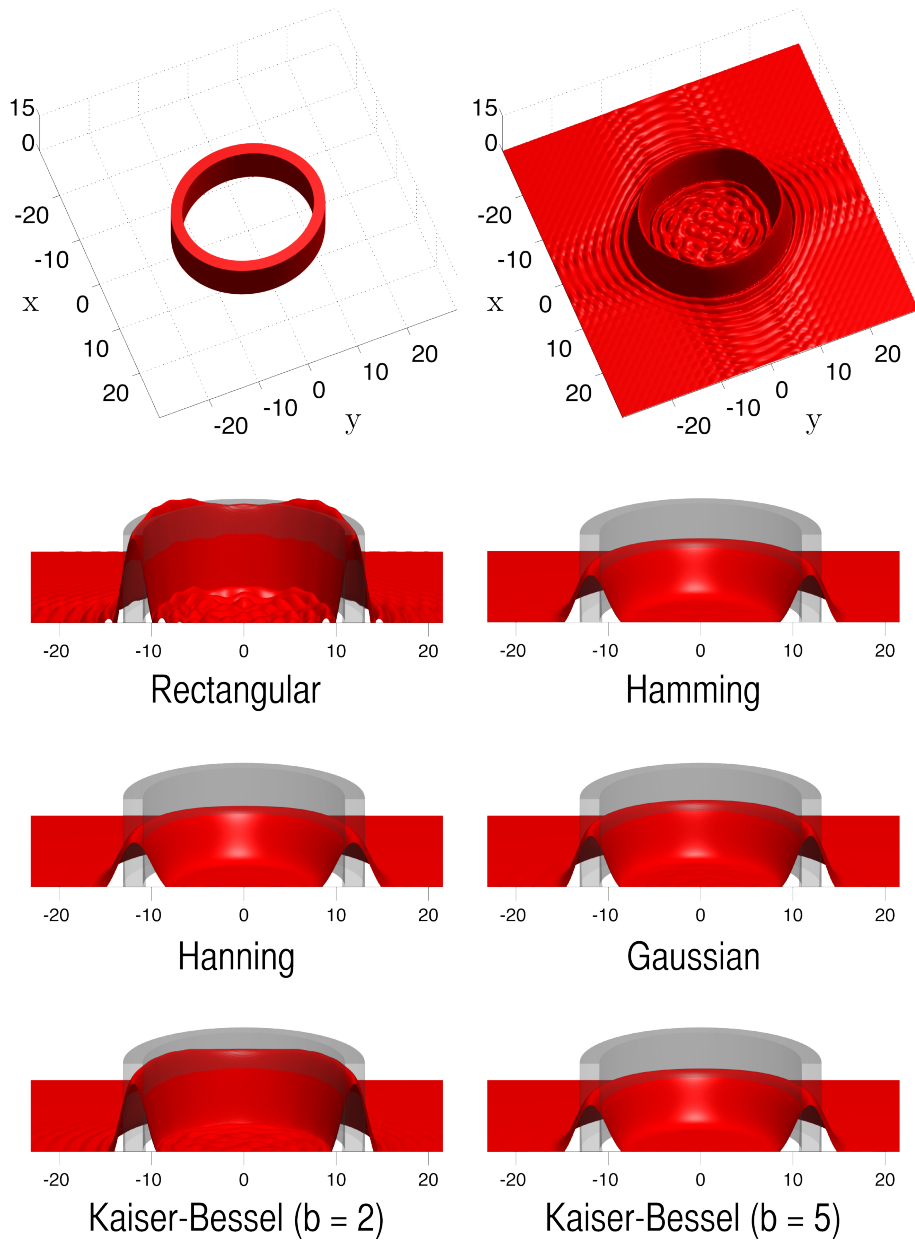


Figure 3.4: The effect of various symmetric  $k$ -space apodization windows on the spatial signal. (Top row, left) The original object, representing a simplification of the extra-cranial lipids in the human brain. (Top row, right) The original object following apodization of the  $k$ -space data with a rectangular window function, whereby all but the central  $32 \times 32$  phase encodes are discarded. The remaining rows depict an enhanced cross-section of the object following the application of various window functions, illustrating the tradeoff between spatial resolution and signal contamination. The original object is superimposed (gray) as a reference.

### 3.3 Non-Fourier Reconstruction

While the Fourier transform has been often lauded as a technique that remains impartial to the acquisition method employed to produce the observed data, it implicitly assumes that the underlying object is band-limited to the extent of the acquired spatial frequencies. The monumental success of structural MRI can be partially ascribed to its capability to sufficiently satisfy this requirement, providing the necessary sensitivity to traverse remote regions in  $k$ -space. Unfortunately, the protracted acquisition times required for MRSI, as well as the low inherent sensitivity as described in section 3.1, create circumstances under which violations of the band-limited assumption are progressively exacerbated as fewer spatial frequencies are collected. Aside from the complications surrounding inhomogeneity effects, the resulting coarse voxels have a reduced capacity for representing fine anatomical structures, thereby limiting clinical utility. Moreover, the need to marginalize extra-cranial lipid signals in  $^1\text{H}$  applications in the brain due to concomitant truncation artifacts often entails the usage of rectangular VOIs, which ineluctably exclude the lateral cortices from subsequent analyses. These considerations challenge the appositeness of the direct use of the inverse Fourier transform in MRSI reconstruction, and an area of research entirely dedicated to the investigation of alternative reconstruction strategies has therefore developed in parallel to the measurement acceleration endeavors described in section 2.6.3.

#### 3.3.1 Model-Based Reconstruction

Fundamentally, the MRSI measurement process can be described as a linear system, whereby the input function,  $f$ , is encoded by the acquisition system, represented as a linear mapping,  $\mathcal{A}$ , and then corrupted by additive noise,  $\eta$ :

$$\begin{aligned}\tilde{s} &= \mathcal{A}\{f\} + \eta \\ &= s + \eta.\end{aligned}\tag{3.15}$$

Here,  $s$  denotes the expected system output, and  $\tilde{s}$  the noisy observed output. The principle aim of the reconstruction is therefore to produce a faithful estimate of the original function,  $\hat{f}$ , which yields expected measurements that are maximally-consistent with  $\tilde{s}$ . One common means of satisfying this criterion is through a variational framework, minimizing the squared residual error between the acquired and theoretically-predicted measurements, also known as the “least squares” (LS) method:

$$\hat{f} = \arg \min_f \|\tilde{s} - \mathcal{A}\{f\}\|_{L^2}^2.\tag{3.16}$$

The LS formulation can also be considered from a statistical perspective as maximizing the probability of the observed data given the acquisition model:

$$\hat{f} = \arg \max_f \mathbb{p}(\mathcal{A}\{f\} + \eta | \tilde{s}) = \arg \max_f \mathbb{p}(\eta). \quad (3.17)$$

The predominant sources of noise in an MR experiment are primarily attributable to random thermal fluctuations produced by the coil electronics and the sample, and are generally considered to be zero-mean additive white Gaussian (AWGN), i.e.,  $\eta \sim \mathcal{N}(0, \sigma^2)$ , where  $\sigma^2$  is the noise variance. Hence, expression (3.17) can be expanded as:

$$\begin{aligned} \hat{f} &= \arg \max_f \left( \frac{1}{2\pi\sigma^2} \right)^{1/2} e^{-\frac{\|\tilde{s} - \mathcal{A}\{f\}\|_{L^2}^2}{2\sigma^2}} \\ &= \arg \max_f \log \left( \left( \frac{1}{2\pi\sigma^2} \right)^{1/2} e^{-\frac{\|\tilde{s} - \mathcal{A}\{f\}\|_{L^2}^2}{2\sigma^2}} \right) \\ &= \arg \max_f \left( -\frac{\|\tilde{s} - \mathcal{A}\{f\}\|_{L^2}^2}{2\sigma^2} \right) + C \\ &= \arg \min_f \|\tilde{s} - \mathcal{A}\{f\}\|_{L^2}^2, \end{aligned} \quad (3.18)$$

$$(3.19)$$

where (3.18) follows from the fact that the logarithm of a function attains its maximum at the same point as the function itself, and  $C$  is a constant.

Although the system input usually represents continuous real-world objects or phenomena, the collected data are most often acquired through sampling, and are both digitally stored and processed. In this case, letting  $\mathcal{X}$  denote the set of acquired sampling locations, the discrete measurements can be expressed as:

$$\tilde{s}|_{\mathcal{X}} = \mathcal{A}\{f\}|_{\mathcal{X}} + \eta|_{\mathcal{X}}, \quad (3.20)$$

or,

$$\tilde{\mathbf{s}} = \mathbf{s} + \mathbf{n}, \quad (3.21)$$

in vector notation, where  $\tilde{\mathbf{s}}, \mathbf{s}, \mathbf{n} \in \mathbb{C}^M$ , with  $M = |\mathcal{X}|$ . Viewed in this light, expression (3.20) necessarily engenders a continuous-discrete LS problem of the form:

$$\arg \min_f \|\tilde{\mathbf{s}} - \mathcal{A}\{f\}|_{\mathcal{X}}\|_{\ell_2}^2. \quad (3.22)$$

In practice, (3.22) cannot be investigated directly, as analytical continuous-domain expressions for  $s$  (and likewise,  $f$ ) are typically unavailable. Rather, a discrete approximation of the mapping  $\mathcal{A}\{f\}$  is sought, thereby leading to the fully discretized signal model:

$$\begin{aligned} \tilde{\mathbf{s}} &= \mathbf{A}\mathbf{x} + \mathbf{n} \\ &= \hat{\mathbf{s}} + \mathbf{n}, \end{aligned} \quad (3.23)$$

where  $\mathbf{x} \in \mathbb{C}^N$ ,  $\hat{\mathbf{s}} \in \mathbb{C}^M$  and  $\mathbf{A} \in \mathbb{C}^{M \times N}$ . Though the ramifications of this approximation may be far from trivial, we shall defer a more thorough exposition to later chapters, dropping the  $\hat{\cdot}$  and assuming implicit discretization in the interim. The resultant LS problem is then given by:

$$\hat{\mathbf{x}} = \arg \min_{\mathbf{x}} \|\hat{\mathbf{s}} - \mathbf{A}\mathbf{x}\|_{\ell_2}^2, \quad (3.24)$$

which admits a closed-form solution:

$$\hat{\mathbf{x}} = (\mathbf{A}^H \mathbf{A})^{-1} \mathbf{A}^H \hat{\mathbf{s}} = \mathbf{A}^+ \hat{\mathbf{s}}, \quad (3.25)$$

where  $\mathbf{A}^+$  denotes the Moore-Penrose pseudoinverse.

In the case of MRSI, given a set  $\mathcal{X} = \{\mathcal{K}, \mathcal{T}\}$ , where  $\mathcal{K} = \{\mathbf{k}_m\}_{m=1}^M$ ,  $\mathcal{T} = \{t_i\}_{i=1}^T$  denote the set of acquired samples in the spatial Fourier ( $k$ -space) and temporal domains, respectively, the discrete measurements are given by:

$$\begin{aligned} \tilde{s}|_{\mathcal{X}} = \tilde{s}[\mathbf{k}_m, t_i] &= \int_{-\infty}^{\infty} \int_{\Omega \in \mathbb{R}^3} \rho(\mathbf{r}, f) e^{-2\pi j(\mathbf{k}_m \cdot \mathbf{r} + ft_i)} d\mathbf{r} df + \eta[\mathbf{k}_m, t_i], \\ & m = 1, \dots, M, i = 1, \dots, T. \end{aligned} \quad (3.26)$$

In typical reconstruction settings, the spatial integral in equation (3.26) is generally discretized such that:

$$\tilde{s}[\mathbf{k}_m, t_i] = \sum_{n=1}^N F_n[\mathbf{k}_m] c_n[t_i] + \eta[\mathbf{k}_m, t_i], \quad (3.27)$$

or in matrix/vector notation:

$$\tilde{\mathbf{s}}[t_i] = \mathbf{F}\mathbf{c}[t_i] + \mathbf{n}[t_i], \quad (3.28)$$

with

$$\tilde{\mathbf{s}}[t_i] = \begin{pmatrix} \tilde{s}[\mathbf{k}_1, t_i] \\ \tilde{s}[\mathbf{k}_2, t_i] \\ \vdots \\ \tilde{s}[\mathbf{k}_M, t_i] \end{pmatrix}, \quad \mathbf{n}[t_i] = \begin{pmatrix} \eta[\mathbf{k}_1, t_i] \\ \eta[\mathbf{k}_2, t_i] \\ \vdots \\ \eta[\mathbf{k}_M, t_i] \end{pmatrix}, \quad (3.29)$$

Under this formulation, the encoding scheme,  $\mathbf{F}$ , contains the Fourier exponentials:

$$\mathbf{F} = \begin{pmatrix} e^{-2\pi j\mathbf{k}_1 \cdot \mathbf{r}_1} & e^{-2\pi j\mathbf{k}_1 \cdot \mathbf{r}_2} & \dots & e^{-2\pi j\mathbf{k}_1 \cdot \mathbf{r}_N} \\ e^{-2\pi j\mathbf{k}_2 \cdot \mathbf{r}_1} & e^{-2\pi j\mathbf{k}_2 \cdot \mathbf{r}_2} & \dots & e^{-2\pi j\mathbf{k}_2 \cdot \mathbf{r}_N} \\ \vdots & \vdots & \ddots & \vdots \\ e^{-2\pi j\mathbf{k}_M \cdot \mathbf{r}_1} & e^{-2\pi j\mathbf{k}_M \cdot \mathbf{r}_2} & \dots & e^{-2\pi j\mathbf{k}_M \cdot \mathbf{r}_N} \end{pmatrix}, \quad (3.30)$$

while

$$\mathbf{c}[t_i] = \begin{pmatrix} c_1[t_i] \\ c_2[t_i] \\ \vdots \\ c_N[t_i] \end{pmatrix}, \quad (3.31)$$

are the corresponding amplitude coefficients at each time sample,  $t_i$ . Moreover, if  $\mathbf{F}$  is assumed to be square ( $N = M$ ), the LS solution is given by:

$$\hat{\mathbf{c}}[t_i] = (\mathbf{F}^H \mathbf{F})^{-1} \mathbf{F}^H \tilde{\mathbf{s}}[t_i] \quad (3.32)$$

$$= \mathbf{F}^H \tilde{\mathbf{s}}[t_i], \quad (3.33)$$

since  $\mathbf{F}$  is unitary, yielding the familiar standard inverse discrete Fourier transform (DFT) as covered in section 2.5.4.

Although the above exposition has simply established congruence with earlier descriptions, an interesting observation follows when considering (3.33) in the absence of noise, and substituting into (3.28) such that,

$$\tilde{\mathbf{s}}[t_i] = \mathbf{F} (\mathbf{F}^H \mathbf{s}[t_i]) + \mathbf{n}[t_i]. \quad (3.34)$$

When viewed in this context, the term within the parentheses in (3.34) prescribes a parametric form for the underlying spatio-spectral distribution, which for the above standard reconstruction scheme is simply its Fourier representation. It is therefore natural to contemplate whether alternative parametrizations could yield improved reconstruction performance, and mitigate the seemingly ineluctable artifacts associated with inverse DFT reconstructions. Hence, a renewed interpretation within the linear system framework has unearthed a plenitude of new possibilities.

### 3.3.2 Use of Explicit Prior Knowledge

MRSI measurements are commonly performed as part of a scanning regime that routinely includes high-resolution structural imaging among other MR modalities. A question therefore arose regarding the extent to which such supplemental information could be exploited to compensate for the dearth of high-frequency content, and to influence the MRSI reconstruction process.

One of the earliest such methods to explore this possibility, standing in the vanguard of so-called ‘‘constrained reconstruction’’ approaches for MR [121–123], was the spectral localization by imaging (SLIM) technique [124], positing that the spatial distribution of chemical species of interest tends to parallel that of water in biological samples. Therefore, knowledge of anatomical features derived from structural  $^1\text{H}$  MRI could be used as *a priori* information in the reconstruction of spectroscopic images. In a typical SLIM

experiment, high-resolution structural images are partitioned into a set of  $K$  anatomically-defined compartments that are considered to be spectrally homogeneous. In this case, the spatio-spectral distribution of the object can be decomposed as:

$$\rho_{\text{SLIM}}(\mathbf{r}, f) = \sum_{\kappa=1}^K \mathbb{1}_{\kappa}(\mathbf{r}) q_{\kappa}(f), \quad (3.35)$$

where  $q_{\kappa}$  is the unknown spectrum associated with compartment  $\kappa$ , and  $\mathbb{1}_{\kappa}$  are binary spatial basis functions such that

$$\mathbb{1}_{\kappa}(\mathbf{r}) \triangleq \begin{cases} 1 & \mathbf{r} \in \text{compartment } \kappa \\ 0 & \text{otherwise.} \end{cases} \quad (3.36)$$

Substituting (3.35) for  $\rho(\mathbf{r}, f)$  in (2.79):

$$\begin{aligned} s(\mathbf{k}, t) &= \int_{-\infty}^{\infty} \int_{\Omega \subset \mathbb{R}^3} \sum_{\kappa=1}^K \mathbb{1}_{\kappa}(\mathbf{r}) q_{\kappa}(f) e^{-2\pi j(\mathbf{k} \cdot \mathbf{r} + ft)} d\mathbf{r} df \\ &= \sum_{\kappa=1}^K \underbrace{\int_{\Omega \subset \mathbb{R}^3} \mathbb{1}_{\kappa}(\mathbf{r}) e^{-2\pi j \mathbf{k} \cdot \mathbf{r}} d\mathbf{r}}_{X_{\kappa}(\mathbf{k})} \cdot \underbrace{\int_{-\infty}^{\infty} q_{\kappa}(f) e^{-2\pi j ft} df}_{c_{\kappa}(t)} \end{aligned} \quad (3.37)$$

$$= \sum_{\kappa=1}^K X_{\kappa}(\mathbf{k}) c_{\kappa}(t). \quad (3.38)$$

Echoing the discussion in section 3.3.1, the spatial integral defining the forward encoding scheme in (3.37) generally requires discretization, as neither the basis functions nor their Fourier transform tend to concede readily accessible analytical descriptions. The expected discretized signal model is therefore given by:

$$s[\mathbf{k}_m, t_i] = \sum_{\kappa=1}^K X_{\kappa}[\mathbf{k}_m] c_{\kappa}[t_i], \quad (3.39)$$

or in matrix/vector notation:

$$\mathbf{s}[t_i] = \mathbf{X} \mathbf{c}[t_i], \quad (3.40)$$

where

$$\mathbf{X} = \begin{pmatrix} X_1[\mathbf{k}_1] & X_2[\mathbf{k}_1] & \cdots & X_K[\mathbf{k}_1] \\ X_1[\mathbf{k}_2] & X_2[\mathbf{k}_2] & \cdots & X_K[\mathbf{k}_2] \\ \vdots & \vdots & \ddots & \vdots \\ X_1[\mathbf{k}_M] & X_2[\mathbf{k}_M] & \cdots & X_K[\mathbf{k}_M] \end{pmatrix}, \quad (3.41)$$

$$\mathbf{c}[t_i] = \begin{pmatrix} c_1[t_i] \\ c_2[t_i] \\ \vdots \\ c_K[t_i] \end{pmatrix}. \quad (3.42)$$

It is clear that (3.39) represents an over-determined linear system of equations as long as the number of acquired phase encodes,  $M$ , exceeds the number of compartments,  $K$ . The compartmental spectra,  $c_\kappa[t_i]$  may then be estimated on a point-by-point basis via the LS criterion:

$$\hat{\mathbf{c}}[t_i] = \arg \min_{\mathbf{c}[t_i]} \|\tilde{\mathbf{s}} - \mathbf{X}\mathbf{c}[t_i]\|_{\ell_2}^2, \quad (3.43)$$

or in closed form,

$$\hat{\mathbf{c}}[t_i] = (\mathbf{X}^H \mathbf{X})^{-1} \mathbf{X}^H \tilde{\mathbf{s}}[t_i] = \mathbf{X}^+ \tilde{\mathbf{s}}[t_i]. \quad (3.44)$$

Part of the allure of the SLIM method lies in the prospects of recovering compartmentally-localized spectra with as few as  $K$  phase encodes, provided  $\mathcal{K}$  is chosen non-trivially. Such reduced sampling requirements could translate to drastically-reduced acquisition times so long as the compartmental model befits the specific application. Furthermore, the interpretation of the compartments as “generalized voxels”, which may assume arbitrary geometries, effectively circumvents the rectangular voxel restrictions imposed by traditional inverse Fourier reconstructions. Secondary analyses of the SLIM technique [122, 125, 126] demonstrated that the noise sensitivity is inversely proportional to compartmental volume, and that inter-compartmental signal leakage is completely annulled so long as the homogeneity assumption remains valid. This requirement, however, is rarely satisfied in practice, resulting in spectral contamination dictated by the frequency content of the inhomogeneities, the measured  $k$ -space data, and the compartment geometries. It should be mentioned, however, that estimated SLIM spectra converge to the true average compartmental spectra as  $M \rightarrow \infty$ .

A number of extensions have since been proposed to the SLIM method, either as attempts to improve reconstruction performance by enriching the underlying signal model, or to better exploit the various advantages afforded by the framework. Soon after the publication of the original SLIM technique, the spectral localization with optimal point spread function (SLOOP) method [127] suggested a means for optimizing sensitivity and minimizing the potential for signal contamination in a SLIM experiment. This was achieved by establishing a criterion for selecting  $\mathcal{K}$  so as to tailor the spatial response function (SRF) to the shape of each compartment, where:

$$\text{SRF}_\kappa(\mathbf{r}) = \sum_{m=1}^M X_\kappa^+[\mathbf{k}_m] e^{-2\pi j \mathbf{k}_m \cdot \mathbf{r}}, \quad (3.45)$$

where the spatial variable has been expressed in the continuous domain in order to emphasize resolution independence. The SRF can be considered to represent the spatial origin of all elements contributing to the estimated signal associated with a particular basis element (i.e., the individual compartment in the SLIM framework). In general, for a designated linear acquisition scheme,  $\mathbf{A} \in \mathbb{C}^{M \times N}$ , under which a set of  $N$  basis functions are encoded using  $\{\mathbf{k}_m\}_{m=1}^M$  spatial frequencies, the SRF corresponding to the  $n^{\text{th}}$  basis function can be expressed as:

$$\text{SRF}_n(\mathbf{r}) = \sum_{m=1}^M A_n^+[\mathbf{k}_m] e^{-2\pi j \mathbf{k}_m \cdot \mathbf{r}}. \quad (3.46)$$

A generalized series model approach labeled GSLIM [128] was also proposed as a compromise between SLIM and traditional Fourier constructions, profiting from both the high-resolution information imparted by the former while capturing unanticipated spatial variations through the use of Fourier-type spatial harmonics. In GSLIM, the spatio-spectral distribution is given by:

$$\rho_{\text{GSLIM}}(\mathbf{r}, f) = \sum_{l=1}^L \underbrace{\sum_{\kappa=1}^K \mathbf{1}_{\kappa}(\mathbf{r}) q_{\kappa}(f)}_{\rho_{\text{SLIM}}(\mathbf{r}, f)} a_l(f) e^{2\pi j \mathbf{k}_l \cdot \mathbf{r}}, \quad (3.47)$$

such that the measured signal becomes:

$$s(\mathbf{k}, t) = \sum_{l=1}^L \sum_{\kappa=1}^K \int_{\Omega \subset \mathbb{R}^3} \mathbf{1}_{\kappa}(\mathbf{r}) e^{-2\pi j(\mathbf{k}-\mathbf{k}_l) \cdot \mathbf{r}} d\mathbf{r} \cdot \int_{-\infty}^{\infty} a_l(f) q_{\kappa}(f) e^{-2\pi j f t} df. \quad (3.48)$$

As  $q_{\kappa}$  and  $\mathbf{1}_{\kappa}$  are pre-determined using the original SLIM framework, the GSLIM coefficients,  $a_l$  can be computed by expressing (3.48) in the temporal Fourier domain:

$$\mathcal{F}_t\{s\}(\mathbf{k}, f) = \sum_{l=1}^L a_l(f) \underbrace{\sum_{\kappa=1}^K q_{\kappa}(f) \int_{\Omega \subset \mathbb{R}^3} \mathbf{1}_{\kappa}(\mathbf{r}) e^{-2\pi j(\mathbf{k}-\mathbf{k}_l) \cdot \mathbf{r}} d\mathbf{r}}_{G(\mathbf{k}-\mathbf{k}_l, f)}, \quad (3.49)$$

and solving the resulting linear system of equations.

One of the primary transgressors undermining the compartmental inhomogeneity assumption is the presence of local field inhomogeneities, which if omitted from the signal model may lead to shifted spectral peaks appearing as spurious resonances in the reconstructed SLIM spectra. These field inhomogeneities are accounted for explicitly in the natural linewidth chemical

shift imaging (NL-CSI) [129] and BSLIM methods [130], where an additional measured static field map is acquired and incorporated into the reconstruction process. The former defines compartments to match the Fourier pixel size in traditional CSI reconstructions, such that  $K \approx M$ . The BSLIM technique adheres more closely to the original conception of anatomically-defined compartments, defining the spatio-spectral distribution as:

$$\rho_{\text{BSLIM}}(\mathbf{r}, f) = \sum_{\kappa=1}^K \mathbb{1}_{\kappa}(\mathbf{r}) q_{\kappa}(f - \Delta f(\mathbf{r})), \quad (3.50)$$

thereby leading to a measured signal:

$$\begin{aligned} s(\mathbf{k}, t) &= \int_{-\infty}^{\infty} \int_{\Omega \subset \mathbb{R}^3} \sum_{\kappa=1}^K \mathbb{1}_{\kappa}(\mathbf{r}) q_{\kappa}(f - \Delta f(\mathbf{r})) e^{-2\pi j(\mathbf{k} \cdot \mathbf{r} + ft)} d\mathbf{r} df \\ &= \sum_{\kappa=1}^K \underbrace{\int_{\Omega \subset \mathbb{R}^3} \mathbb{1}_{\kappa}(\mathbf{r}) e^{-2\pi j(\mathbf{k} \cdot \mathbf{r} + \Delta f(\mathbf{r}))} d\mathbf{r}}_{H_{\kappa}(\mathbf{k}, t)} \cdot \underbrace{\int_{-\infty}^{\infty} q_{\kappa}(f) e^{-2\pi jft} df}_{c_{\kappa}(t)} \\ &= \sum_{\kappa=1}^K H_{\kappa}(\mathbf{k}, t) c_{\kappa}(t). \end{aligned} \quad (3.51)$$

Contrasting (3.51) with (3.37), it is apparent that the difference lies in the newfound time-dependence of  $H_{\kappa}$ , which absorbs the position-dependent phase shifts specified by the field inhomogeneity map,  $\Delta f(\mathbf{r})$ . Many of the same algorithmic considerations for SLIM equally apply to the BSLIM method, indicating that spectral contamination artifacts are minimized as long as the measured field map accurately represents the underlying effective field, and that the spectral homogeneity assumption holds once these effects have been accounted for.

An additional virtue of the SLIM framework is that it remains independent of the elected MRSI acquisition strategy, assuring its congruence with a variety of additional acceleration techniques. For example, in [131], SLIM was combined with sensitivity encoding (SENSE) [132] to assess the spectral contents of small lesions in stroke patients. SLIM and/or its variants have also been utilized for  $^1\text{H}$  applications using pre-clinical models of stroke [133], post-acquisition suppression of extramyocellular lipids in the human calf [134], as well as for  $^{31}\text{P}$  MRSI studies of the human myocardium [135–137].

### 3.3.3 Regularization

While methods such as SLIM may be adequate for applications where average or compartmental spectra are sufficient, they are ultimately circumscribed

by the spectral homogeneity requirement, which greatly limits their clinical admissibility. This constraint is further confounded by the non-trivial segmentation problem, as well as by the lack of established criteria for selecting the number of compartments. Moreover, the very supposition equating structural anatomy and the spatio-spectral distribution of non-water resonances may be overly presumptuous or application-dependent, in which case a universal means for determining *a priori* compartment geometries becomes elusive. The avail of such methods utilizing explicit prior knowledge is therefore brought into contention, thus establishing the need for more flexible procedures that are better able to assimilate prior information and data heterogeneity.

Mathematically, additional assumptions or prior knowledge can also be integrated into the reconstruction through regularization, which assumes the form of an additional penalty term in conjunction with the data consistency criterion in the variational formulation,

$$\arg \min_f \underbrace{\|\tilde{\mathbf{s}} - \mathcal{A}\{f\}\|_{L^2}^2}_{\text{data consistency}} + \underbrace{\mathcal{R}(f)}_{\text{regularization}}, \quad (3.52)$$

where  $\mathcal{R}$  represents additional criteria used to enforce the designated constraints. Regularization is often indispensable for obtaining unique solutions when considering ill-posed inverse problems, where a significant nullspace exists for the forward operator,  $\mathcal{A} : X \rightarrow Y$ , i.e.,

$$\ker \mathcal{A} \triangleq \{f \in X : \mathcal{A}\{f\} = 0\} \neq \{0\}, \quad (3.53)$$

which is akin to a system matrix  $\mathbf{A} \in \mathbb{C}^{M \times N}$  where  $M < N$  in the finite-dimensional case. One prevailing regularizer for these scenarios is  $\mathcal{R} = \lambda \|\Gamma\{f\}\|_{L^2}^2$ , in which (3.52) is termed ‘‘Tikhonov regularization,’’ where  $\Gamma$  is a continuous linear operator that extracts desirable information from an input (e.g., weightings, derivatives, etc.), and  $\lambda \in \mathbb{R}$  is a parameter controlling the relative weighting between the data consistency and regularization penalties. When  $\Gamma = \iota$ , where  $\iota$  is the identity operator, Tikhonov regularization tends to favor smooth solutions possessing low total signal energy (small  $L^2$  norm). Quadratic norms have remained popular as regularizers as they admit closed form solutions, thereby providing unfettered access to the SRF (3.46). Indeed, considering the discrete problem ( $\Gamma = \mathbf{I}$ ):

$$\arg \min_{\mathbf{x}} \|\tilde{\mathbf{s}} - \mathbf{A}\mathbf{x}\|_{\ell_2}^2 + \lambda \|\mathbf{x}\|_{\ell_2}^2, \quad (3.54)$$

the solution can be expressed as:

$$\hat{\mathbf{x}} = (\mathbf{A}^H \mathbf{A} + \lambda \mathbf{I})^{-1} \mathbf{A}^H \tilde{\mathbf{s}}. \quad (3.55)$$

Another important concept that often plays a role in discretized regularization problems is the notion of sparsity, whereby a signal can be considered as “sparse” if it primarily consists of a minimal number of non-zero elements. Depending on the application, an input signal may often be assumed to be itself inherently sparse, or admit a sparse representation when expressed in a particular basis. Within the framework of (3.52), the most straightforward sparsity-promoting selection for  $\mathcal{R}$  is the  $\ell_0$  pseudo-norm, which returns the number of non-zero coefficients for an input vector, leading to problems of the form:

$$\arg \min_{\mathbf{x}} \|\tilde{\mathbf{s}} - \mathbf{A}\mathbf{x}\|_{\ell_2}^2 + \lambda \|\mathbf{x}\|_{\ell_0}. \quad (3.56)$$

Unfortunately, the  $\ell_0$  penalty is non-convex, and solutions to (3.56) can only be obtained through computationally-demanding combinatorial search methods or heuristic approaches [138, 139]. Therefore, the  $\ell_0$  penalty is often supplanted by the family of convex  $\ell_p$ -norms ( $p \geq 1$ ) to yield a relaxation of the original sparse recovery problem, thereby providing access to a wealth of efficient algorithms that exist for convex optimization. In many instances, the topology induced by the  $\ell_1$  norm has been shown to favor sparse solutions, leading to a class of problems of the form:

$$\arg \min_{\mathbf{x}} \|\tilde{\mathbf{s}} - \mathbf{A}\mathbf{x}\|_{\ell_2}^2 + \lambda \|\mathbf{x}\|_{\ell_1}, \quad (3.57)$$

collectively referred to as basis pursuit (BP) [140] or least absolute shrinkage and selection operator (LASSO) [141, 142] problems. Though widely used in a variety of scientific disciplines,  $\ell_1$ -penalized reconstruction methods have been pivotal to the success of compressed sensing (CS) [143, 144] and its applications to MR (e.g., see [145–148]).

Another espoused and auspicious regularizer is the total variation (TV) seminorm, which was introduced in [149] as a means of measuring first degree information content in an input signal:

**Definition 1** (Total Variation). *The total variation of a continuous-domain function  $f$  on interval  $[a, b] \subset \mathbb{R}$ , is defined as the supremum of absolute differences over the set of partitions,  $\mathcal{P} = \{P = \{x_0, x_1, \dots, x_P\} : P \text{ is a partition of } [a, b]\}$  on its domain:*

$$\text{TV}_a^b(f) \triangleq \sup_P \sum_n |f(x_n) - f(x_{n-1})|. \quad (3.58)$$

If  $\Omega$  is an open subset of  $\mathbb{R}^n$ , for a function  $f \in L^1(\Omega)$ , the total variation is defined as:

$$\text{TV}_\Omega(f) \triangleq \sup \left\{ \int_\Omega f(\mathbf{r}) \text{div } v(\mathbf{r}) d\mathbf{r} : v \in C_c^1(\Omega, \mathbb{R}^n), \|v\|_{L^\infty} \leq 1 \right\}, \quad (3.59)$$

where  $C_c^1(\Omega, \mathbb{R}^n)$  is the set of continuously-differentiable vector-valued functions compactly supported in  $\Omega$ .

Moreover, if  $f \in C_c^1(\Omega, \mathbb{R})$ , then the total variation can be equivalently expressed as [150]:

$$\text{TV}_\Omega(f) = \int_\Omega |\nabla f(\mathbf{r})| d\mathbf{r}. \quad (3.60)$$

In discrete settings, for a multidimensional signal subscripted by  $d$  indices,  $\mathbf{x} \in \mathbb{R}^{N_1 \times \dots \times N_d}$ , TV is typically expressed as one of either:

$$\text{TV}_\Omega^{\text{iso}}(\mathbf{x}) = \sum_{i_1, i_2, \dots, i_d \in \Omega} \left| \left( \sum_{l=1}^d |D_l\{\mathbf{x}\}|^2 \right)^{1/2} \right| \quad (\text{isotropic TV}), \quad (3.61)$$

or,

$$\text{TV}_\Omega^{\text{ani}}(\mathbf{x}) = \sum_{i_1, i_2, \dots, i_d \in \Omega} \left| \sum_{l=1}^d |D_l\{\mathbf{x}\}| \right| \quad (\text{anisotropic TV}). \quad (3.62)$$

Here,  $D_l$  represents a discrete difference operator along the  $l^{\text{th}}$  dimension, such that:

$$[D_l\{\mathbf{x}\}]_{i_1, i_2, \dots, i_d} = [\mathbf{x}]_{i_1, i_2, \dots, i_l, \dots, i_d} - [\mathbf{x}]_{i_1, i_2, \dots, i_l-1, \dots, i_d}. \quad (3.63)$$

Much of the allure of TV rests in its proclivity for removing noise-like artifacts while preserving discerning features in an input signal, and has gained notoriety within the MR community due to its versatility in addressing a wide array of problems such as denoising [151–153], suppression of truncation artifacts / deblurring [154, 155], and inpainting for sensitivity maps [156].

While the GSLIM method was conceived in order to address the potential shortcomings of SLIM, practical implementations have typically been able to accommodate only low frequency intra-compartmental variations. Abandoning the compartmental formulation altogether, [157] devised a modification of the well-established Papoulis-Gerchberg (PG) algorithm [158, 159] by considering only the expected support region of the imaged object. The reconstruction was posed as a Tikhonov regularization problem, whereby the spatio-spectral distribution was estimated at high-resolution by minimizing the energy of the extrapolated high spatial frequencies:

$$\mathbf{c}[f_l] = \arg \min_{\mathbf{c}[f_l]} \|\tilde{\mathbf{s}}[f_l] - \mathbf{F}\mathbf{c}[f_l]\|_{\ell_2}^2 + \lambda (\mathbf{c}[f_l]^H \mathbf{T}\mathbf{c}[f_l]), \quad (3.64)$$

where  $\{f_l\}_{l=1}^L$  is the set of discretized measurements in the temporal frequency domain, and  $\mathbf{T}$  is a binary diagonal matrix specifying the support

region. Improvements in the resulting PSF were reported throughout the entire reconstructed volume when compared to zero-filled inverse DFT, but were primarily localized to the periphery of the support region.

Alternatively, an early contribution towards the next generation of anatomically-driven MRSI reconstruction algorithms was proposed in [160], which aimed to exploit the versatility afforded by regularization-based reconstruction while retaining salient object features furnished by high-resolution structural MRI. To accomplish this, the basic GSLIM model was supplemented by local B-spline basis functions in order to capture local intensity variations such as those due to lesions or model mis-match errors, which would normally mandate significant Fourier expansions:

$$\rho_{\text{IMBR}}(\mathbf{r}, f) = \underbrace{\sum_{l=1}^L \sum_{\kappa=1}^K \mathbf{1}_{\kappa}(\mathbf{r}) c_{\kappa,l}(f) e^{2\pi j \mathbf{k}_l \cdot \mathbf{r}}}_{\text{compartmental basis functions}} + \underbrace{\sum_{p=1}^{P^2} d_p(f) \beta^3(\mathbf{r} - \mathbf{r}_p)}_{\text{local basis functions}}, \quad (3.65)$$

where  $\beta^3$  is a cubic B-spline function. The attendant iterative reconstruction procedure was then given by the following optimization problem:

$$\hat{\mathbf{c}}[f_l], \hat{\mathbf{d}}[f_l] = \arg \min_{\mathbf{c}[f_l], \mathbf{d}[f_l]} \|\hat{\mathbf{s}}[f_l] - \mathbf{s}[f_l]\|_{\ell_2}^2 + \lambda (\|\mathbf{c}[f_l]\|_{\ell_1} + \|\mathbf{d}[f_l]\|_{\ell_1}), \quad (3.66)$$

with,

$$s(\mathbf{k}, f) = \int_{\Omega \in \mathbb{R}^3} \rho_{\text{IMBR}}(\mathbf{A}\mathbf{r} + \mathbf{b}, f) e^{-2\pi j(\mathbf{k} \cdot \mathbf{r} + (f + \Delta f(\mathbf{r}))t)} d\mathbf{r} df, \quad (3.67)$$

where  $\mathbf{A}$  and  $\mathbf{b}$  represent affine transformation parameters that are re-estimated at each iteration in order to minimize mis-registration errors between the acquired structural and MRSI datasets.

Although the method proposed in [160] affords greater flexibility to capture unpredictable spatial variations, it maintains an appreciable reliance upon explicit boundary information, predisposing it to artifacts arising from model mis-match errors. Recognizing the demonstrated utility of high-resolution prior anatomical information, while simultaneously seeking greater data autonomy, the MRSI reconstruction community began to explore alternative mechanisms by which these constraints could be implicitly effectuated. In [161], the underlying data model was considered as a linear combination of box-shaped voxel functions,  $\phi$ :

$$\rho_{\text{HHSL}}(\mathbf{r}, f) = \sum_{n=1}^N u[\mathbf{r}_n, f] \phi(\mathbf{r} - \mathbf{r}_n), \quad (3.68)$$

where  $\{\mathbf{r}_n\}_{n=1}^N$  denotes the discrete set of voxels comprising a high-resolution anatomical reference. The expected signal can therefore be expressed as:

$$s(\mathbf{k}, f) = \sum_{n=1}^N \int_{\Omega \in \mathbb{R}^3} u[\mathbf{r}_n, f] \phi(\mathbf{r} - \mathbf{r}_n) e^{-2\pi j \mathbf{k} \cdot \mathbf{r}} d\mathbf{r} \quad (3.69)$$

$$= \sum_{n=1}^N u[\mathbf{r}_n, f] \Phi(\mathbf{k}) e^{-2\pi j \mathbf{k} \cdot \mathbf{r}_n}, \quad (3.70)$$

where  $\Phi$  is the Fourier transform of  $\phi$ , and is analogous to  $X_\kappa$  in (3.37). Once the raw data was corrected for  $B_0$ -induced spectral shifts, the reconstruction consisted of estimating the weighting coefficients,  $u$ , at each frequency position,  $f_l$ :

$$\hat{\mathbf{u}}[f_l] = \arg \min_{\mathbf{u}[f_l]} \|\tilde{\mathbf{s}}[f_l] - \mathbf{s}[f_l]\|_{\ell_2}^2 + \lambda \|\mathbf{L}\mathbf{u}[f_l]\|_{\ell_2}^2. \quad (3.71)$$

In this case, the regularization term consists of a spatial smoothing operator,  $\mathbf{L}$ , which penalizes local intensity variations between neighboring voxels that are suspected of belonging to the same tissue class:

$$\|\mathbf{L}\mathbf{u}\|_{\ell_2}^2 = \sum_{i=1}^N \sum_{\substack{i < j \\ j \in \Omega_i}} w_{i,j} |u[\mathbf{r}_i] - u[\mathbf{r}_j]|^2, \quad (3.72)$$

where the time-dependence has been dropped for ease of notation. In (3.72),  $\Omega_i$  denotes the set of voxels that are spatially adjacent to  $\mathbf{r}_i$ . The weights,  $w_{i,j}$ , were pre-computed with the aid of anatomical navigator scans, and could be adjusted to reflect perceived confidences in the ascertained boundary information. Posing the reconstruction in this manner essentially facilitates a compromise between data consistency and anatomical prior information, which may be modulated by the choice of  $\lambda$ . Moreover, inconsistencies between structural and spectral content will tend to manifest as degraded or biased denoising performance, rather than as additional artifacts. Interestingly, a similar selective smoothing approach was proposed in [162], but was implemented via an ad-hoc iterative scheme similar to the PG procedure.

Until this point, constraints imposed by the above described methods have been applied strictly in the spatial domain, allowing the estimated spectra to remain maximally consistent with the observed measurements, given the appointed data model. As has been discussed, this may result in unexpected spectral behavior when discordancies exist between the model and the acquired data. A number of methods have therefore sought to further improve the problem conditioning by prescribing models for both the spatial and spectral components of the MRSI signal. In [163], the underlying data

model was given by:

$$\rho_{\text{EJM}}(\mathbf{r}, f) = \sum_{n=1}^N \sum_{l=1}^L v[\mathbf{r}_n, f_l] \phi(\mathbf{r} - \mathbf{r}_n) \psi(f - f_l), \quad (3.73)$$

where  $\phi$ , and  $\psi$  are box-shaped voxel functions in the spatial and temporal frequency domains, respectively. The measured signal model was expressed as:

$$s(\mathbf{k}, t) = \Phi(\mathbf{k}) \Psi(t) \sum_{n=1}^N \sum_{l=1}^L v[\mathbf{r}_n, f_l] e^{-\alpha[\mathbf{r}_n]t} e^{-2\pi j(\mathbf{k} \cdot \mathbf{r}_n + f_l t)} \quad (3.74)$$

where

$$\alpha[\mathbf{r}_n] = \frac{1}{T_2^*[\mathbf{r}_n]} + 2\pi j \bar{\beta}[\mathbf{r}_n], \quad (3.75)$$

with  $\bar{\beta}$  the mean frequency shift in voxel  $\mathbf{r}_n$ . The quantity  $\alpha[\mathbf{r}_n]$  was estimated from separately acquired high-resolution magnitude and phase images prior to the reconstruction. Analogous with  $\Phi$ ,  $\Psi$  represents the Fourier transform of the frequency domain voxel function,  $\psi$ , and is analogous to  $c_\kappa$  in (3.37). Given the anticipated MR spectral profile as a combination of Lorentzian lineshapes with the potential for smoothly-varying baseline components (e.g., residual water, lipids, short  $T_2$  macromolecules, etc.), the spectrum in each voxel was modeled as:

$$v[\mathbf{r}_n, f_l] = \sum_{p=1}^L w[\mathbf{r}_n, p] \delta[f_l - p] + \sum_{p=1}^S w[\mathbf{r}_n, L + p] \mathcal{T}_p[\mathbf{r}_n], \quad (3.76)$$

where  $\delta$  is the Dirac delta function, and  $\mathcal{T}_p$  are Chebyshev polynomials. As the reconstruction was ultimately performed on the high-resolution grid specified by  $\{\mathbf{r}_n\}$ , spatial prior knowledge was necessary in order to improve the inverse problem conditioning. The high-resolution reference image was therefore partitioned into  $K$  pairwise disjoint anatomically-defined regions,  $\Omega_\kappa$ , such that  $\Omega = \bigcup_{\kappa} \Omega_\kappa$ . However, similar to [161], the compartments themselves were not treated as separate basis functions, but were used to prescribe a set of boundaries within which the spectral profiles were assumed to be smoothly-varying. This latter assumption was incorporated into the reconstruction procedure through the use of a modified (isotropic) TV penalty:  $\text{TV}_\Omega = \sum_{\kappa=1}^{K-1} \text{TV}_{\Omega_\kappa}$ . The final reconstruction was therefore given as:

$$\hat{\mathbf{w}}[f_l] = \arg \min_{\mathbf{w}[f_l]} \|\tilde{\mathbf{s}}[f_l] - \mathbf{s}[f_l]\|_{\ell_2}^2 + \lambda_1 \text{TV}_\Omega(\mathbf{w}[f_l]) + \lambda_2 \|\mathbf{w}[f_l]\|_{\ell_1}. \quad (3.77)$$

Incidentally, the K-Bayes method for MRSI reconstruction [164] was proposed nearly concurrently, stipulating a similar voxel-based signal model to

(3.67). However, rather than a regularized sparse optimization problem, the reconstruction was formulated within a Bayesian framework. In this case, the acquisition model was considered as a likelihood function, with pre-computed estimates of relaxation and field inhomogeneity parameters, while expected spatial characteristics of spectral content within anatomically-defined tissue boundaries were assimilated into a prior distribution through Markov Random Field (MRF) models. The reconstruction then consisted of maximizing the posterior distribution, achieved via an expectation-maximization (EM) approach.

Although the majority of the methods recounted above were devised and validated for traditional Cartesian MRSI acquisitions, a number of studies have sought to capitalize on the advancing accelerated imaging techniques described in section 2.6.3 in conjunction with the powerful variational reconstruction framework posited by (3.52). Many notable examples have emerged within parallel imaging employing sensitivity encoding (SENSE), where multichannel coil sensitivity information is exploited in order to correct for the systematic aliasing artifacts incurred through undersampling. In this case, the basic acquisition scheme can be expressed as:

$$\tilde{s}_c(\mathbf{k}, t) = \int_{-\infty}^{\infty} \int_{\Omega \in \mathbb{R}^3} \varsigma_c(\mathbf{r}) \rho(\mathbf{r}, f) e^{-2\pi j(\mathbf{k} \cdot \mathbf{r} + ft)} d\mathbf{r} df + \eta_c(\mathbf{k}, t), \quad (3.78)$$

where  $\varsigma_c$  denotes the spatial sensitivity profile, and  $\eta_c$  the noise associated with the  $c^{\text{th}}$  coil. Expression (3.78) is commonly discretized as:

$$\tilde{\mathbf{s}}[t_i] = \mathbf{E}\mathbf{c}[t_i] + \mathbf{n}[t_i], \quad (3.79)$$

where the terms pertaining to the individual coil elements are concatenated along the rows of  $\tilde{\mathbf{s}}$ ,  $\mathbf{E}$ , and  $\mathbf{n}$ . In the original weak SENSE formulation [132], compensation for aliasing artifacts is performed at the center of each reconstructed voxel. While this may be adequate for typical structural MRI resolutions, variations in the sensitivity profiles over typical MRSI voxel sizes may preclude proper unfolding, thereby occasioning additional artifacts. This potential limitation was addressed in [165] by over-discretizing the encoding operator, and then solving the conventional LS problem (3.24), which furnishes an implicit interpolation model and enables usage of the complete high-resolution sensitivity information. Alternatively, in [166], PEPSI [70] data was collected from central  $k$ -space regions at the Nyquist rate, along with high-resolution coil sensitivity maps. The reconstruction was then posed as a Tikhonov regularization problem:

$$\hat{\mathbf{c}}[t_i] = \arg \min_{\mathbf{c}[t_i]} \|\tilde{\mathbf{s}}[t_i] - \mathbf{E}\mathbf{c}[t_i]\|_{\ell_2}^2 + \lambda \|\mathbf{c}[t_i]\|_{\ell_2}^2, \quad (3.80)$$

where  $\hat{\mathbf{c}}[t_i]$  was estimated on the same spatial grid as the sensitivity maps.

Rather than formulating the reconstruction procedure as a separate recovery problem for each temporal/spectral frame, [167] attempted to exploit the full  $k$ - $f$  volumetric information by optimizing along the spatial and temporal frequency dimensions simultaneously. An efficient variable density spiral acquisition scheme was employed to generate both the MRSI data, and a high-resolution water reference dataset. The latter was used to derive estimates of the field inhomogeneity profile and coil sensitivity maps (both incorporated into the spatial encoding scheme,  $\mathbf{E}$ ), as well as spatio-spectral support regions delineating the metabolites and extra-cranial lipids. The full reconstruction problem was then given as:

$$\hat{\mathbf{C}} = \arg \min_{\mathbf{C}} \|\tilde{\mathbf{S}} - \mathbf{E}\mathbf{C}\|_F^2 + \lambda_1 \left\| \sum_{l=1}^d |\mathbf{D}_l \mathbf{C}|^2 \right\|_S + \lambda_2 \|\mathbf{C}\|_S, \quad (3.81)$$

where the regularizing functions were restricted to the metabolite support region. Here,  $\mathbf{D}_l$  denotes the matrix representation of the discrete differences operator given by (3.63),  $\tilde{\mathbf{S}} = (\tilde{\mathbf{s}}[f_1], \tilde{\mathbf{s}}[f_2], \dots, \tilde{\mathbf{s}}[f_L])$ ,  $\mathbf{C} = (\mathbf{c}[f_1], \mathbf{c}[f_2], \dots, \mathbf{c}[f_L])$ , and  $\|\cdot\|_S$  is the absolute sum norm, here defined as:  $\|\mathbf{A}\|_S \triangleq \sum_{i,j} |A_{i,j}|$ .

While the above methods address the limited unfolding capacity or resolution constraints, they do not directly confront the lingering truncation artifacts that may potentially countervail the merits of sensitivity encoded spectroscopic imaging. Attempting to integrate the over-discretization approach in [165] with concepts proposed in [168], the method of [169] ventured to directly control the SRF by minimizing deviations from a voxel-specific target function,  $\mathbf{T}$ . In this case, the penalized LS criterion was employed to optimize the reverse encoding scheme itself, such that:

$$\hat{\mathbf{F}} = \arg \min_{\mathbf{F}} \|\mathbf{F}\mathbf{E} - \mathbf{T}\|_F^2 + \lambda (\mathbf{F}\mathbf{\Psi}\mathbf{F}^H), \quad (3.82)$$

where  $\mathbf{\Psi}$  is the coil noise covariance matrix of the system. Under this formulation, the regularization parameter,  $\lambda$ , regulates the tradeoff between conformity with the designated target function and SNR performance. Tested target SRFs included well-localized functions such as Gaussian and Dirac distributions in order to minimize the spectral leakage artifacts normally attributable to appreciable PSF side lobes. The final reconstruction was then performed by applying the estimated inverse encoding to the measurements:

$$\hat{\mathbf{c}}[t_i] = \hat{\mathbf{F}}\tilde{\mathbf{s}}[t_i]. \quad (3.83)$$

### 3.3.4 General Decomposition Models

When viewed against the original SLIM concept, it is evident that MRSI reconstruction methodology has experienced a gradual disinclination towards

explicit data models, where the use of stringent anatomical or spectral constraints severely limited the admissible solution space. These techniques were therefore largely supplanted by those favoring the variational framework along with regularization, which facilitated a more suitable compromise between the observed data and the expected signal behavior. Nonetheless, it may be contended that the panoply of explicit prior knowledge that can be profitably integrated into a given MRSI reconstruction routine has been only partially explored. For example, [170] and [171] made use of the fact that chemical concentrations must be non-negative, and in principle lead to non-negative spectral lineshapes and amplitudes. The underlying data model can then be expressed as:

$$\rho_{\text{NN}}(\mathbf{r}, f) = \sum_{\kappa=1}^K a_{\kappa}(\mathbf{r})q_{\kappa}(f), \quad a_{\kappa} : \mathbb{R}^d \rightarrow \mathbb{R}_+, \quad q_{\kappa} : \mathbb{R} \rightarrow \mathbb{R}_+, \quad (3.84)$$

where  $a_{\kappa}$  are general spatial basis functions and  $q_{\kappa}$  are the associated spectra. The reconstruction can therefore be regarded as a classical blind source separation (BSS) or dictionary learning (DL) problem, given that neither  $a_{\kappa}$  nor  $q_{\kappa}$  are known *a priori*:

$$\hat{\mathbf{A}}, \hat{\mathbf{Q}} = \arg \min_{\mathbf{A}, \mathbf{Q}} \|\tilde{\mathbf{P}} - \mathbf{A}\mathbf{Q}\|_F^2, \quad \text{such that } \mathbf{A} \in \mathbb{R}_+^{M \times K}, \quad \mathbf{Q} \in \mathbb{R}_+^{K \times L}, \quad (3.85)$$

where  $\tilde{\mathbf{P}}$  is the inverse Fourier transform of the observed measurements,  $\mathbf{Q}$  contains the  $K$  spectral components, and  $\mathbf{A}$  their corresponding contributions. In [170], the BSS problem was addressed via a Bayesian framework, whereby the likelihood was given by (3.85), and the non-negativity constraints were reflected in the priors,  $p(\mathbf{A})$  and  $p(\mathbf{Q})$ . Alternatively, [171] attempted to solve (3.85) directly via a non-negative matrix factorization approach [172, 173].

It is important to note that the joint estimation of  $\mathbf{A}$  and  $\mathbf{Q}$  in (3.85) is a fundamentally non-convex problem. Nonetheless, generalized bilinear formulations in the form:

$$\rho_{\text{BILIN}}(\mathbf{r}, f) = \sum_{\kappa=1}^K u_{\kappa}(\mathbf{r})v_{\kappa}(f), \quad (3.86)$$

as well as the attendant LS reconstruction framework proffer a number of sizable advantages. First and foremost, when optimizing over an entire dataset, such decompositions allow for the exploitation of latent spatio-temporal correlations while simultaneously decoupling the individual domains. Ancillary constraints may then be separately imposed on the temporal and spatial components, rather than on the data when considered as a whole. Secondly, the portrayal of the object as consisting of a finite linear combination of

unspecified components inspires a feature-based interpretation of the data, rather than the standard voxel-based analysis. This distinction reverberates one of the more compelling aspects of SLIM and its variants, namely, that while the number of observations comprising the data is often (comparatively) large, a low-dimensional representation can often be ascertained.

This concept of low dimensionality is often encapsulated through the rank of the matrix representation of  $\rho_{\text{BILIN}}$ , i.e., the number of linearly-independent columns. Given this notion, the dimensionality of a given dataset can be ascertained through so-called “rank-revealing” transforms, such as the singular value decomposition (SVD), or principle component analysis (PCA) [174], as manifested by a small number of non-trivial singular values. The MR community has recently witnessed an outburst of reconstruction methodologies seeking to capitalize on the surmised low-dimensional structure underlying seemingly complex objects and processes, most notably in the field of dynamic MRI [147, 175–184]. In the following chapter, a method that extends these concepts to MRSI, while simultaneously drawing upon the established merits of the aforementioned regularized techniques, will be presented and discussed.



## Chapter 4

# MRSI Reconstruction by Low-Rank Component Analysis

### 4.1 Introduction

In the previous chapter, a general bilinear data decomposition model was introduced as a means of segregating spatial and temporal signal behavior, while simultaneously divulging and preserving intrinsic spatio-temporal correlations through the minimum norm variational framework. The notion of dimensionality was also discussed as an instrumental property of the underlying data, which has motivated a profusion of novel reconstruction and acquisition strategies in other MR-related disciplines. In this chapter<sup>1</sup>, we first suggest, and provide justification for the translation of these concepts to MRSI applications. We subsequently propose a novel reconstruction method and corresponding algorithm, where the underlying spatio-spectral distribution is estimated on a high-resolution grid by incorporating both supplementary structural scans and sophisticated regularization techniques. Finally, experimental results are presented for reconstructions obtained both through simulated and authentic MRSI measurements, followed by a discussion of the recognized merits.

### 4.2 Bilinear Models for MRSI

We consider a general bilinear model (also referred to as the “partially-separable” model [175]) for the spatio-spectral distribution function as de-

---

<sup>1</sup>This chapter is partially based on the publication:

J. Kasten, F. Lazeyras, and D. Van De Ville, “Data-Driven MRSI Spectral Localization Via Low-Rank Component Analysis,” *IEEE Transactions on Medical Imaging*, vol. 32, no. 10, pp. 1853-1863, 2013 [185].

scribed in chapter 3:

$$\rho(\mathbf{r}, f) = \sum_{\kappa=1}^K u_{\kappa}(\mathbf{r})v_{\kappa}(f). \quad (4.1)$$

Provided  $u_{\kappa}$  and  $v_{\kappa}$  are  $L^2$  functions, (4.1) is always valid in the limiting case  $K \rightarrow \infty$  given the following theorem [186]:

**Theorem 1.** *Let  $X \times Y$  denote the Cartesian product of measure spaces  $X$  and  $Y$ . The set of functions  $\sum_m f_m(x)g_m(y)$  for  $f_m \in L^2(X)$  and  $g_m \in L^2(Y)$ , with  $m$  finite, forms a dense subset in  $L^2(X \times Y)$ .*

Due to the linearity of the spatial and temporal Fourier transforms, a similar decomposition should hold for the acquired measurements under ideal experimental conditions:

$$s(\mathbf{k}, t) = \int_{-\infty}^{\infty} \int_{\Omega \in \mathbb{R}^3} \sum_{\kappa=1}^K u_{\kappa}(\mathbf{r})v_{\kappa}(f)e^{-2\pi j(\mathbf{k} \cdot \mathbf{r} + ft)} d\mathbf{r}df \quad (4.2)$$

$$= \sum_{\kappa=1}^K \underbrace{\int_{\Omega \in \mathbb{R}^3} u_{\kappa}(\mathbf{r})e^{-2\pi j\mathbf{k} \cdot \mathbf{r}} d\mathbf{r}}_{\varrho_{\kappa}(\mathbf{k})} \cdot \underbrace{\int_{-\infty}^{\infty} v_{\kappa}(f)e^{-2\pi jft} df}_{\xi_{\kappa}(t)} \quad (4.3)$$

$$= \sum_{\kappa=1}^K \varrho_{\kappa}(\mathbf{k})\xi_{\kappa}(t). \quad (4.4)$$

Given the acquired measurements, obtained at  $k$ -space locations  $\{\mathbf{k}_m\}_{m=1}^M$  and temporally sampled at  $\{t_i\}_{i=1}^T$ , such that  $\tilde{\mathbf{S}} \in \mathbb{C}^{M \times T}$ , expression (4.4) remains valid as long as the rank,  $K \leq \min(M, T)$ . In practice, however, non-ideal experimental conditions (e.g., noise, inhomogeneity or off-resonance effects, etc.) generally preclude a straightforward estimation of  $K$  from the raw measurements. Therefore, alternative means of establishing the data dimensionality are needed, and will be discussed later in this chapter.

The use of the general bilinear model (4.1) for MRSI applications can be justified by the fact that in most *in vivo* settings, the number of detectable metabolites in a given spectrum is small (e.g., see table 3.1). In this case,  $K$  can be regarded as the total number of observable resonances, with  $v_{\kappa}$  the characteristic spectral profile of the  $\kappa^{\text{th}}$  resonance, and  $u_{\kappa}$  its corresponding spatial distribution. Alternatively,  $K$  can be interpreted as the number of pairwise disjoint, spectrally homogeneous compartments as with SLIM-type methods, in which case  $v_{\kappa}$  would represent the corresponding spectral profiles. These scenarios may be considered as prescribing effective upper and lower bounds for  $K$ , respectively, which in general are largely exceeded by

the number of phase encoding steps ( $\sim 256 - 1024$ ) or temporal samples ( $\sim 512 - 1024$ ) in typical MRSI acquisitions.

As mentioned in the previous chapter, a number of methods have emerged within the field of dynamic MR seeking to exploit the inherent low-dimensionality conjectured to underlie processes displaying a high degree of spatio-temporal correlation. For these applications, the proposed approaches generally fall into two categories: (i) the temporal basis functions are first determined from limited  $k$ -space data acquired at high temporal resolution (often through rank-revealing transformations such as the SVD), which are then used to guide the estimation of the attendant spatial basis functions from either a separate, or combined acquisition with greater  $k$ -space coverage but limited temporal sampling [175, 177, 187, 188]. (ii) The reconstruction is performed over the composite spatio-temporal dataset, whereby low-rank solutions are exacted explicitly, or through the use of additional regularizing penalties such as the Schatten  $p$ -norms [176, 178, 189–191].

Despite the reported success of these approaches, a number of crucial disparities confound straightforward translation to MRSI settings. Firstly, MRSI temporal signals are characterized by a decaying exponential behavior, which in concert with low metabolite SNR renders matrix recovery approaches particularly susceptible to noise-generated artifacts and biases. Secondly, estimated temporal basis functions are typically corrupted by field inhomogeneity and off-resonance effects, which may significantly bias recovery of the corresponding spatial components. Nonetheless, approach (ii) has been explored as part of a general denoising scheme for CSI acquisitions [192], whereas (i) quite recently served as the motivation for a hybrid CSI/EPSI sequence, for which reconstructions employed additional spatial regularization to recover high-resolution spatio-spectral volumes [193]. Thus, the extension of minimum rank principles to MRSI reconstruction, though still inchoate, has manifested clear potential.

### 4.3 Proposed Method: Preliminaries

Ideally, we aspire to recover spatio-spectral volumes at resolutions comparable to those afforded by structural MRI, given only a limited set of  $k$ -space measurements. The often severe ill-posedness of this problem therefore mandates the utilization of prior information in order to improve its conditioning. As was discussed during the previous chapter, while the integration of supplementary MR scans may be of potential value in guiding MRSI reconstructions, overly-assertive assimilation carries a significant risk of introducing additional model mis-match errors. In order to circumvent these imperilments, we seek to delimit the solution space through a set of comparatively general assumptions:

1. The inherent MRSI signal resides within a low dimensional subspace. Furthermore, within this subspace, the bilinear model posited in (4.1) remains valid.
2. The predominant sources of signal distortion are attributable to local susceptibility effects, which tend to disallow the presumed spatio-temporal separability.
3. The underlying spatial components,  $u_\kappa$ , belong to a class of real-valued, non-negative piecewise smooth functions that may contain a finite number of sharp edges.

The first assumption was discussed earlier in section 4.2; the two remaining postulates and their respective implementations will be discussed in the following sections.

### 4.3.1 Inhomogeneity Compensation

Revisiting expression (3.51) in chapter 3, it is evident that the presence of local field inhomogeneities tends to subvert the separability of the basic bilinear model. Although separable solutions could be found given a suitable decomposition of the acquired data, for example using the SVD, they would inevitably reflect any inhomogeneity-induced perturbations. To compensate, an additional measurement of the field inhomogeneity,  $\Delta f(\mathbf{r})$ , is therefore necessary, primarily reflecting any sample-specific magnetic susceptibilities. One central aspect is that the spatial resolution of this map can be arbitrarily chosen (within measurement system limitations), and may be used to define the spatial grid over which the reconstruction is performed. In order to isolate these effects, we encapsulate them within the form of an operator,  $\mathcal{B}_{\Delta f}$ , acting in the designated high-resolution space, whose action is to effectively shift a spatio-spectral volume along the temporal frequency axis in accordance with  $\Delta f(\mathbf{r})$ :

**Definition 2.** *Given a spatial inhomogeneity profile,  $\Delta f(\mathbf{r})$ , the spectral deformation operator,  $\mathcal{B}_{\Delta f}$ , acting upon a spatio-spectral volume,  $\rho$ , is given by:*

$$\mathcal{B}_{\Delta f}\{\rho\}(\mathbf{r}, f) \triangleq \rho(\mathbf{r}, f + \Delta f(\mathbf{r})), \quad (4.5)$$

*when applied in the temporal frequency domain, or by:*

$$\mathcal{B}_{\Delta f}\{\mathcal{F}_t^{-1}\{\rho\}\}(\mathbf{r}, t) \triangleq e^{-2\pi j\Delta f(\mathbf{r})t}\mathcal{F}_t^{-1}\{\rho\}(\mathbf{r}, t), \quad (4.6)$$

*in the temporal domain, where  $\mathcal{F}_t$  denotes the temporal Fourier transform.*

The effect of the  $\mathcal{B}_{\Delta f}$  on a slice of a generic spatio-spectral volume is illustrated in figure 4.1. In general, the latter form of definition 2 is preferable,

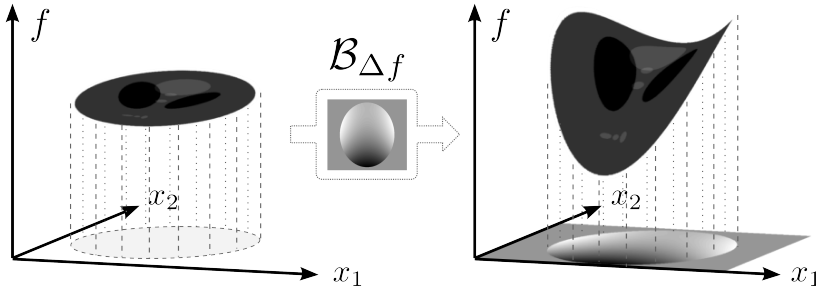


Figure 4.1: Effect of the spectral deformation operator,  $\mathcal{B}_{\Delta f}$ , on a slice of a generic spatio-spectral volume.

as it eliminates the need for explicit interpolation models in the attendant discrete reconstructions. It is therefore beneficial to focus on decompositions of the form:  $\rho(\mathbf{r}, t) = \sum_{\kappa} u_{\kappa}(\mathbf{r})\xi_{\kappa}(t)$ . Letting  $\mathcal{F}_{\mathbf{r}}$  denote the spatial Fourier transform, the conjectured measurement process can then be represented by the following system:

$$\tilde{s}(\mathbf{k}, t) = \mathcal{F}_{\mathbf{r}}\{\mathcal{B}_{\Delta f}\{\rho\}\}(\mathbf{k}, t) + \eta(\mathbf{k}, t) \quad (4.7)$$

$$= \mathcal{F}_{\mathbf{r}}\left\{\mathcal{B}_{\Delta f}\left\{\sum_{\kappa} u_{\kappa}\xi_{\kappa}\right\}\right\}(\mathbf{k}, t) + \eta(\mathbf{k}, t). \quad (4.8)$$

### 4.3.2 Total Variation-Based Spatial Regularization

In the previous chapter, the total variation (TV) semi-norm was introduced as a prevalent and compelling regularizer for feature-preserving signal denoising. Nonetheless, it has been shown that the use of TV often results in so-called “staircasing” artifacts, which are visually displeasing or physically implausible in the case of MRI [194, 195]. This is due to the fact that the standard TV penalty ( $L^1$  norm of the gradient) promotes images with sparse gradients, i.e., it favors piecewise constant solutions. Numerous techniques have since been proposed which explicitly address this issue, for example by utilizing higher-order functionals [196–201]. For our purposes, we adopt the “total generalized variation” (TGV) method of [151, 202, 203], which has been shown to be robust when compared to other methods exploiting higher-order signal information [204, 205]. Formally, the TGV of a function is defined as [202]:

**Definition 3.** Let  $\Omega \subset \mathbb{R}^d$  be a domain,  $k \geq 1$  and  $\alpha_0, \dots, \alpha_{k-1} > 0$ . The total generalized variation of order  $k$  with weight  $\alpha$  for  $f \in L^1_{\text{loc}}(\Omega)$  is defined

as the value of the functional:

$$\text{TGV}_\alpha^k(f) \triangleq \sup \left\{ \int_\Omega f(\mathbf{r}) \operatorname{div}^k p(\mathbf{r}) d\mathbf{r} : p \in C_c^k(\Omega, \operatorname{Sym}^k(\mathbb{R}^d)), \right. \\ \left. \|\operatorname{div}^l p\|_{L^\infty} \leq \alpha_l, l = 0, \dots, k-1 \right\}. \quad (4.9)$$

In the above definition,

$$\operatorname{Sym}^k(\mathbb{R}^d) = \left\{ \zeta : \mathbb{R}^d \times \dots \times \mathbb{R}^d \rightarrow \mathbb{R} : \zeta \text{ } k\text{-linear and symmetric} \right\}, \quad (4.10)$$

denotes the space of symmetric tensors of order  $k$ ,  $L_{\text{loc}}^1$  the space of locally-integrable functions (i.e., functions that are integrable on any compact subset of their domains), and  $\alpha_l$  are positive constants. For completeness, a tensor  $\zeta \in \operatorname{Sym}^k(\mathbb{R}^d)$  is considered to be symmetric if  $\zeta(a_1, \dots, a_k) = \zeta(\pi(a_1), \dots, \pi(a_k))$  for all permutations  $\pi$ . In general, we restrict ourselves to the case  $k = 2$ , in which case the space  $\operatorname{Sym}^2(\mathbb{R}^d)$  can be represented as the space of symmetric  $d \times d$  matrices, for which

$$(\operatorname{div} \zeta)_i = \sum_{j=1}^d \frac{\partial \zeta_{i,j}}{\partial x_j}, \quad \operatorname{div}^2 \zeta = \sum_{i=1}^d \frac{\partial^2 \zeta_{i,i}}{\partial x_i^2} + \sum_{i < j} 2 \frac{\partial^2 \zeta_{i,j}}{\partial x_i \partial x_j}. \quad (4.11)$$

Expression (4.9) for  $k = 2$  can also be linked via Fenchel duality theory [206] to the equivalent formulation:

$$\text{TGV}_\alpha^2(f) = \inf_p \alpha_1 \int_\Omega |\nabla f(\mathbf{r}) - p(\mathbf{r})| d\mathbf{r} + \alpha_0 \int_\Omega |\mathcal{E}p(\mathbf{r})| d\mathbf{r}, \quad (4.12)$$

where  $\mathcal{E}p = \frac{1}{2}(\nabla p + \nabla p^T)$  denotes the distributional symmetrized derivative of  $p$ . Under this formulation, TGV can be interpreted as an optimal weighting between first and second derivatives, and, like other second order penalties, will tend to favor piecewise linear solutions, thereby mitigating staircasing artifacts. In discrete settings, for a general input signal subscripted by  $d$  indices,  $\mathbf{x} \in \mathbb{R}^{N_1 \times \dots \times N_d}$ , the analog of (4.12) can be expressed as:

$$\text{TGV}_\alpha^2(\mathbf{x}) = \arg \min_{\mathbf{p}=(\mathbf{p}_1, \mathbf{p}_2, \dots, \mathbf{p}_d)} \alpha_1 \sum_{i_1, i_2, \dots, i_d \in \Omega} \left| \sum_{l=1}^d |D_l \{\mathbf{x}\} - \mathbf{p}_l| \right| + \\ \alpha_0 \sum_{i_1, i_2, \dots, i_d \in \Omega} \left| \sum_{l=1}^d |D_l \{\mathbf{p}_l\}| + \frac{1}{2} \sum_{m \neq l} |D_m \{\mathbf{p}_l\}| \right|, \quad (4.13)$$

where  $\mathbf{p}_l \in \mathbb{R}^{N_1 \times \dots \times N_d}$ , and  $D_l$  is a discrete differences operator as introduced in section 3.3.3.

## 4.4 Proposed Method: Reconstruction Framework

In accordance with our proposed criteria, we would like to apply the TGV framework only to the estimated spatial components,  $u_\kappa$ , which must therefore be isolated during the reconstruction process. These components are further assumed to be real-valued and non-negative in order to confer physical significance, and to better condition the accompanying reconstruction problem. It is clear from (4.8), however, that efforts to extricate spatial and spectral behavior may be stymied by  $\mathcal{B}_{\Delta f}$ , which mandates that  $u_\kappa$  and  $v_\kappa$  be jointly coupled in order to fall within its domain of definition. This complication can be avoided through a reinterpretation of  $u_\kappa$  as a spatio-spectral volume, but with no explicit time dependence, so that  $u_\kappa(\mathbf{r}, t) = u_\kappa(\mathbf{r}, t_0)$  for all  $t$ . This can be further illuminated by considering the discretized reconstruction setting, where the aim is to recover spatio-temporal distributions of the form:

$$\begin{aligned} \rho[\mathbf{r}_n, t_i] &= \sum_{\kappa=1}^K u_\kappa[\mathbf{r}_n] \xi_\kappa[t_i], \quad u_\kappa : \mathbb{R}^d \rightarrow \mathbb{R}_+, \xi_\kappa : \mathbb{R} \rightarrow \mathbb{C}, \\ n &= 1, \dots, N, \quad i = 1, \dots, T, \end{aligned} \quad (4.14)$$

or,

$$\mathbf{P} = \mathbf{U}\mathbf{\Xi}, \quad \mathbf{U} \in \mathbb{R}_+^{N \times K}, \quad \mathbf{\Xi} \in \mathbb{C}^{K \times T} \quad (4.15)$$

in matrix notation, with  $\{\mathbf{r}_n\}_{n=1}^N$  corresponding to the spatial grid of the acquired field inhomogeneity map. Expression (4.15) can also be regarded in vectorized form, whereupon the implicit temporal aspects of  $u_\kappa$  are exposed:

$$\text{vec}(\mathbf{P}) = \left( \mathbf{I}^{(T \times T)} \otimes \mathbf{U} \right) \text{vec}(\mathbf{\Xi}) \quad (4.16)$$

$$= \left( \mathbf{\Xi}^T \otimes \mathbf{I}^{(N \times N)} \right) \text{vec}(\mathbf{U}), \quad (4.17)$$

where  $\otimes$  denotes the Kronecker product, and the  $\text{vec}(\cdot)$  operation is such that for a  $d$ -dimensional input,  $\mathbf{A} \in \mathbb{C}^{N_1 \times \dots \times N_d}$ ,  $\text{vec}(\mathbf{A}) \in \mathbb{C}^{N_1 \dots N_d}$ . When  $d = 2$ , the  $\text{vec}(\cdot)$  operation amounts to forming a vector by stacking the columns of an input matrix. For ease of notation, we will henceforth denote vectorized counterparts of matrices and multi-dimensional arrays by their corresponding lowercase boldface letters and a  $(\vec{\cdot})$ , such that  $\text{vec}(\mathbf{A}) = \vec{\mathbf{a}}$ .

Hence, (4.16) and (4.17) can be expressed as:

$$\begin{aligned} \vec{\rho} &= \begin{pmatrix} \mathbf{U}[t_1] & \mathbf{0}^{(N \times K)} & \dots & \mathbf{0}^{(N \times K)} \\ \mathbf{0}^{(N \times K)} & \mathbf{U}[t_2] & \dots & \mathbf{0}^{(N \times K)} \\ \vdots & \vdots & \ddots & \vdots \\ \mathbf{0}^{(N \times K)} & \mathbf{0}^{(N \times K)} & \dots & \mathbf{U}[t_T] \end{pmatrix} \vec{\xi} = \mathbf{U}_{\otimes} \vec{\xi} \quad (4.18) \\ &= \left( \mathbf{\Xi}^T \otimes \mathbf{I}^{(N \times N)} \right) \vec{\mathbf{u}} = \mathbf{\Xi}_{\otimes} \vec{\mathbf{u}}, \quad (4.19) \end{aligned}$$

where  $\mathbf{U}[t_i] = (\mathbf{u}_1[t_i], \mathbf{u}_2[t_i], \dots, \mathbf{u}_K[t_i])$ . From the above, it is clear that  $\mathcal{B}_{\Delta f}$  is free to act solely upon  $u_{\kappa}$ , thereby allowing an investigation of the unperturbed temporal bases,  $\xi_{\kappa}$ . This notion of time-independence can be considered as an essential condition for the separability of (4.1), and is equivalent to the requirement that  $u_{\kappa}$  remain constrained to the  $f = 0$  plane in the temporal frequency domain.

Considering the temporal behavior of  $u_{\kappa}$  explicitly, the general form of the reconstruction procedure can be given in the discrete setting as:

$$\begin{aligned} \hat{\mathbf{U}}, \hat{\mathbf{\Xi}} &= \arg \min_{\mathbf{U}, \mathbf{\Xi}} \|\tilde{\mathbf{S}} - \mathbf{A}\mathbf{U}\mathbf{\Xi}\|_F^2 + \mu \text{TGV}_{\alpha}^2(\mathbf{U}), \\ \text{such that } \mathbf{U} &= \mathbf{U}[t_p] = \mathbf{U}[t_q] \in \mathbb{R}_+^{N \times K}, \text{ for all } t_p, t_q \in \{t_i\}_{i=1}^T, \quad (4.20) \end{aligned}$$

where  $\mu$  is a regularization parameter and  $\mathbf{A}$  represents the combined Fourier encoding and spectral deformation operators. The stipulation that spatial components be real-valued can be accounted for directly by supplanting  $\mathbf{U}$  in (4.20) with  $\mathbf{U}_{\mathfrak{R}} = \frac{1}{2}(\mathbf{U} + \mathbf{U}^*)$ , whereas the time-independence and non-negativity can be encompassed by a constraint set,  $\mathcal{C}_u$ . Furthermore, although no explicit assumptions were made with regards to the expected behavior of  $q_{\kappa}$ , for example the sparsity level or anticipated lineshape profiles, we prescribe the additional condition that  $\|\mathbf{\Xi}\|_F \leq 1$ , henceforth denoted as the constraint set  $\mathcal{C}_{\xi}$ , which has been shown to mitigate scaling ambiguities during the reconstruction procedure [179, 207, 208]. Reverting to the vectorized notation of (4.18) and (4.19), thereby allowing the establishment of  $\mathbf{F}$  and  $\mathbf{B}$  as the matrix analogs of  $\mathcal{F}_{\mathbf{r}}$  and  $\mathcal{B}_{\Delta f}$ , respectively, the reconstruction is then given by:

$$\begin{aligned} \hat{\vec{\mathbf{u}}}_{\mathfrak{R}}, \hat{\vec{\xi}} &= \arg \min_{\vec{\mathbf{u}}_{\mathfrak{R}}, \vec{\xi}} \|\vec{\tilde{\mathbf{s}}} - \mathbf{F}\mathbf{B}\mathbf{\Xi}_{\otimes} \vec{\mathbf{u}}_{\mathfrak{R}}\|_{\ell_2}^2 + \mu \text{TGV}_{\alpha}^2(\vec{\mathbf{u}}_{\mathfrak{R}}), \\ \text{such that } \vec{\mathbf{u}}_{\mathfrak{R}} &\in \mathcal{C}_u, \vec{\xi} \in \mathcal{C}_{\xi}. \quad (4.21) \end{aligned}$$

#### 4.4.1 Algorithm Description

In order to solve (4.21), we adopt an augmented Lagrangian (AL) approach, also known as the method of multipliers (e.g., [209, 210]), in which minimization is performed in an alternating fashion over a set of surrogate variables.

Under the AL formulation, the reconstruction is posed as:

$$\begin{aligned} \text{minimize } \mathcal{L} = & \|\vec{\mathbf{s}} - \mathbf{FB}\Xi_{\otimes} \vec{\mathbf{u}}_{\mathfrak{R}}\|_{\ell_2}^2 + \mu \text{TGV}_{\alpha}^2(\vec{\mathbf{y}}) + \beta \|\vec{\mathbf{u}}_{\mathfrak{R}} - \vec{\mathbf{y}}\|_{\ell_2}^2 + \\ & \langle \vec{\boldsymbol{\lambda}}, \vec{\mathbf{u}}_{\mathfrak{R}} - \vec{\mathbf{y}} \rangle, \text{ such that } \vec{\mathbf{u}}_{\mathfrak{R}} \in \mathcal{C}_u, \vec{\boldsymbol{\xi}} \in \mathcal{C}_{\xi}, \end{aligned} \quad (4.22)$$

where  $\vec{\boldsymbol{\lambda}}$  is an auxiliary variable whose role is that of a Lagrange multiplier, and  $\beta \in \mathbb{R}_+$  is a penalty parameter that effectively controls how closely (4.22) approximates (4.21). The complete reconstruction procedure is given by algorithm 1.

---

**Algorithm 1** Component-based MRSI Reconstruction

---

- 1: **Input:**  $\mu \geq 0, \beta > 0, \tau > 1, \vec{\mathbf{s}}, \vec{\mathbf{u}}_{\mathfrak{R},0}, \vec{\boldsymbol{\xi}}_0, \vec{\mathbf{y}}_0, \vec{\boldsymbol{\lambda}}_0$
  - 2: **repeat**
  - 3:   **repeat**
  - 4:      $\vec{\mathbf{u}}_{\mathfrak{R}}^{(n+1)} = \arg \min_{\vec{\mathbf{u}}_{\mathfrak{R}} \in \mathcal{C}_u} \|\vec{\mathbf{s}} - \mathbf{FB}\Xi_{\otimes}^{(n)} \vec{\mathbf{u}}_{\mathfrak{R}}\|_{\ell_2}^2 + \beta \|\vec{\mathbf{u}}_{\mathfrak{R}} - (\vec{\mathbf{y}}^{(n)} - \frac{\vec{\boldsymbol{\lambda}}^{(n)}}{\beta})\|_{\ell_2}^2$
  - 5:      $\vec{\boldsymbol{\xi}}^{(n+1)} = \arg \min_{\vec{\boldsymbol{\xi}} \in \mathcal{C}_{\xi}} \|\vec{\mathbf{s}} - \mathbf{FB}\mathbf{U}_{\mathfrak{R}\otimes}^{(n+1)} \vec{\boldsymbol{\xi}}\|_{\ell_2}^2$
  - 6:      $\vec{\mathbf{y}}^{(n+1)} = \arg \min_{\vec{\mathbf{y}}} \|\vec{\mathbf{u}}_{\mathfrak{R}}^{(n+1)} - (\vec{\mathbf{y}} - \frac{\vec{\boldsymbol{\lambda}}^{(n)}}{\beta})\|_{\ell_2}^2 + \frac{\mu}{\beta} \text{TGV}_{\alpha}^2(\vec{\mathbf{y}})$
  - 7:      $\vec{\boldsymbol{\lambda}}^{(n+1)} = \vec{\boldsymbol{\lambda}}^{(n)} + \beta(\vec{\mathbf{u}}_{\mathfrak{R}}^{(n+1)} - \vec{\mathbf{y}}^{(n+1)})$
  - 8:   **until** convergence or maximum allowable inner iterations reached
  - 9:    $\beta = \tau\beta$
  - 10: **until** convergence or maximum allowable outer iterations reached
- 

The  $\vec{\mathbf{y}}$  subproblem (algorithm 1, line 6) is referred to as the total (generalized) variation denoising problem, whose solution can be efficiently obtained by the primal-dual method originally proposed in [151]. To solve the  $\vec{\mathbf{u}}_{\mathfrak{R}}$  subproblem (algorithm 1, line 4), we use a fast projected gradient approach [211, 212], whereby at each iteration,  $l$ ,  $\vec{\mathbf{u}}_{\mathfrak{R}}$  is updated as:

$$\vec{\mathbf{u}}_{\mathfrak{R}}^{l+1} = \mathcal{P}_{\mathcal{C}_u} \left( \vec{\mathbf{u}}_{\mathfrak{R}}^{(l)} - \frac{1}{L} \nabla \mathcal{L}(\vec{\mathbf{u}}_{\mathfrak{R}}^{(l)}) \right), \quad (4.23)$$

where  $L$  is an appropriate upper bound on the Lipschitz constant of the gradient, and  $\mathcal{P}_{\mathcal{C}_u}$  is the Euclidean projector onto the set  $\mathcal{C}_u$ , whose action for the current case will be discussed shortly. The gradient step,  $\nabla \mathcal{L}(\vec{\mathbf{u}}_{\mathfrak{R}}^{(l)})$ ,

in (4.23) is given by:

$$\nabla \mathcal{L}(\vec{\mathbf{u}}_{\mathfrak{R}}^{(l)}) = \frac{1}{2} \mathfrak{Re} \left\{ \left( \Xi_{\otimes}^{(l)H} \mathbf{B}^H \mathbf{F}^H \mathbf{F} \mathbf{B} \Xi_{\otimes}^{(l)} + \beta \mathbf{I} \right) \vec{\mathbf{u}}_{\mathfrak{R}}^{(l)} - \Xi_{\otimes}^{(l)H} \mathbf{B}^H \mathbf{F}^H \vec{\mathbf{s}} - \beta \left( \vec{\mathbf{y}}^{(l)} - \frac{\vec{\boldsymbol{\lambda}}^{(l)}}{\beta} \right) \right\}. \quad (4.24)$$

For completeness,  $\mathbf{F}^H$  can be characterized as the inverse Fourier transform of the low resolution spatial components,  $\varrho_{\kappa}[\mathbf{k}_m]$ , sinc interpolated to the high-resolution spatial grid. Likewise,  $\mathbf{B}^H$  is determined through an appeal to definition 2 with a flip of sign. From an implementation standpoint, it is not necessary to construct the full forward and adjoint matrices in practice, as the associated operations may be applied point-wise along the temporal axis. It is particularly noteworthy that (4.24) may not be time-independent, therefore highlighting the indispensability of the projection step. This projection can be decomposed into two actions. The first effectuates time-independent solutions by projecting  $(\vec{\mathbf{u}}_{\mathfrak{R}}^{(l)} - (1/L)\nabla \mathcal{L}(\vec{\mathbf{u}}_{\mathfrak{R}}^{(l)}))$  onto its mean timecourse, effectively restricting spectral behavior to the  $f = 0$  plane. The second involves a projection onto the non-negative orthant, whereby  $\mathcal{P}_{\mathbb{R}_+}(u_{\mathfrak{R}}[\mathbf{r}_n]) = \max(0, u_{\mathfrak{R}}[\mathbf{r}_n])$ . Solutions to the  $\vec{\boldsymbol{\xi}}$  subproblem (algorithm 1, line 5) can be found using similar projected gradient approaches, where the projection step is given by:

$$\mathcal{P}_{\mathcal{C}_{\xi}}(\vec{\boldsymbol{\xi}}) = \begin{cases} \frac{\vec{\boldsymbol{\xi}}}{\|\vec{\boldsymbol{\xi}}\|_{\ell_2}}, & \|\vec{\boldsymbol{\xi}}\|_{\ell_2} \geq 1 \\ \vec{\boldsymbol{\xi}}, & \text{otherwise.} \end{cases} \quad (4.25)$$

One advantage to using the AL framework is that unlike traditional penalty methods,  $\beta$  does not need to grow very large in order to establish equivalence between (4.22) and (4.21). Nonetheless, we employ a continuation strategy, steadily increasing  $\beta$  by factors of  $\tau$  in an outer loop once convergence has been reached over the alternating minimization routine, in order to hasten overall algorithm convergence.

#### 4.4.2 Model Order Determination

Prior to the reconstruction, an initial determination must be made for the expected model order of (4.1). Robust estimation of the underlying data dimensionality from a series of measurements corrupted by noise represents an ongoing challenge in statistics, information theory, and machine learning, and amounts to the successful identification and segregation of the signal and noise subspaces. Several criteria have been proposed to achieve this task, including the minimum description length (MDL) [213], Akaike information criterion (AIC) [214], Scree test on residual percent variance [215],

cross-validation approaches [216–218], and the Bayesian information criterion (BIC) [219, 220]. With regards to the latter, a series of probabilistic PCA methods have been proposed (e.g., [221–224]), whereby the observed data,  $D$ , is considered to consist of a collection of high-dimensional random vectors:

$$\mathbf{x}_i = \mathbf{H}\mathbf{w} + \mathbf{m} + \boldsymbol{\eta}, \quad \mathbf{x}_i, \mathbf{m}, \boldsymbol{\eta} \in \mathbb{C}^N, \quad \mathbf{H} \in \mathbb{C}^{N \times K}, \quad \mathbf{w} \in \mathbb{C}^K, \quad (4.26)$$

where  $K < N$ . Here,  $\mathbf{H}$  are the unknown basis vectors,  $\mathbf{m}$  is the mean of the  $\mathbf{x}_i$ , and  $\boldsymbol{\eta}$  is AWGN noise distributed as  $\boldsymbol{\eta} \sim \mathcal{N}(\mathbf{0}, \sigma^2 \mathbf{I}^{(N \times N)})$ . It is also typically assumed that the weights  $\mathbf{w} \sim \mathcal{N}(\mathbf{0}, \mathbf{I}^{(K \times K)})$ . The probability of the data then becomes:

$$p(D|\mathbf{H}, \mathbf{m}, \sigma^2) = \prod_i p(\mathbf{x}_i|\mathbf{H}, \mathbf{m}, \sigma^2), \quad (4.27)$$

which is maximized at [222]:

$$\hat{\mathbf{H}} = \mathbf{U} \left( \boldsymbol{\Lambda} - \sigma^2 \mathbf{I}^{(K \times K)} \right)^{1/2} \mathbf{R}, \quad (4.28)$$

where  $\boldsymbol{\Lambda}$  is a diagonal matrix containing the  $K$  largest eigenvalues of the data covariance matrix,  $\mathbf{U}$  are the corresponding eigenvectors, and  $\mathbf{R}$  is an arbitrary orthogonal matrix. The objective is then to maximize the probability of the data, given a particular model order by integrating over the various parameters comprising the data model:

$$\text{maximize } p(D|\mathbf{H}, \mathbf{m}, \sigma^2) = \int_{\mathbf{H}, \mathbf{m}, \sigma^2} p(D|\mathbf{H}, \mathbf{m}, \sigma^2) p(\mathbf{H}, \mathbf{m}, \sigma^2) d\mathbf{H} d\mathbf{m} d\sigma^2. \quad (4.29)$$

For the proposed MRSI reconstruction method, we adopt the method of [223], which decomposes  $\mathbf{H}$  in a similar fashion to (4.28):

$$\mathbf{H} = \mathbf{U} \left( \mathbf{L} - \sigma^2 \mathbf{I}^{(K \times K)} \right)^{1/2} \mathbf{R}, \quad (4.30)$$

$$\text{such that } \mathbf{U}^H \mathbf{U} = \mathbf{I}^{(K \times K)}, \quad \mathbf{R}^H \mathbf{R} = \mathbf{I}^{(K \times K)}, \quad (4.31)$$

where  $\mathbf{L}$  is a general diagonal matrix. Priors are then introduced on each of the model parameters, and estimates are obtained by approximating the integral in (4.29) via Laplace's method [220, 225].

Due to the fact that the acquired measurements are typically corrupted by inhomogeneity and off-resonance effects, dimensionality estimates,  $K_{\text{est}}$ , obtained from the raw MRSI data will tend to overestimate the model order. The resulting values can therefore be considered as upper bounds, which for  $K_{\text{est}} \geq K$  should in principle result in greater noise contamination rather than model mis-match effects.

### 4.4.3 Selection of the Regularization Penalty

In the proposed framework, the choice of the regularization parameter,  $\mu$ , ultimately regulates the desired smoothness of the reconstructed volumes. Values that are too large will engender a loss of discriminating spatial features, whereas values that are too small tend to result in spurious signal contributions, either due to noise or discontinuities. The consequence of this judgement has provoked a considerable body of research dedicated towards the establishment of robust criteria for selecting optimal parameters that minimize the expected reconstruction error while limiting the regularization bias. Established approaches include the discrepancy principle [226, 227], generalized cross validation [228], and the L-curve [229, 230] (more detailed discussions can be found in [231, 232]). Generally, an appropriate choice of regularization parameter follows from a careful consideration of the data noise variance, and the (eigen) spectral properties of the employed operators, neither of which may be known *a priori*. Most of these methods, however, were developed under the linear, Tikhonov regularization framework, and their suitability in non-linear reconstruction settings is uncertain. A number of more recent studies have explored alternative frameworks for selecting regularization parameters for TV-based reconstructions, either adapting established linear methods [233], or by reformulating the reconstruction process within a probabilistic framework, whereby the regularization parameter is adaptively estimated [234, 235].

For our experiments, the regularization parameter was first determined empirically to minimize the peak signal-to-noise ratio (PSNR) for reconstructions based on numerically simulated ground truth measurements under varying noise levels. This allowed us to identify a series of  $\epsilon$  such that:

$$\|\vec{\mathbf{s}} - \mathbf{FB}\Xi_{\otimes} \vec{\mathbf{u}}_{\mathfrak{R}}\|_{\ell_2}^2 \leq \epsilon \|\vec{\mathbf{s}}\|_{\ell_2}^2. \quad (4.32)$$

These values were then used to inform discrepancy principle-based estimates of  $\mu$  for subsequent experiments using real MRSI data.

## 4.5 Validation in Phantom Data

In order to validate the proposed method, we scrutinize reconstructions furnished by both numerically simulated and haptic phantoms, i.e., objects of known geometry and/or composition that serve to reduce the number of experimental confounds. In the following, we provide detailed descriptions for each of the investigated datasets, as well as enumerate the various acquisition and pre-processing modules used to generate the raw input data. We then assess reconstruction performance for each scenario, and offer a discussion of the established results.

### 4.5.1 Simulated Data

For experiments based on simulated data, a numerical phantom was utilized consisting of three spectrally-homogeneous compartments, using a square FOV  $([-0.5, \dots, 0.5] \times [-0.5, \dots, 0.5])$  and a  $128 \times 128$  Cartesian sampling grid, as depicted in figure 4.2. A local static field inhomogeneity map was also simulated at the same resolution using a fourth-degree polynomial model along each planar Cartesian dimension, which was then thresholded by the combined support of the compartments. To emulate the effects due to changes in material susceptibility at the compartment interfaces, additional Laplacian-of-Gaussian filtered images (Gaussian kernel FWHM = three pixel units) for each compartment were added to the final map. To each compartment, a unique spectrum with fixed temporal resolution ( $T = 1024$  points) was associated. The final synthetic dataset was obtained by constructing BSLIM kernels for each compartment,  $H_\kappa[\mathbf{k}_m, t_i]$  (see (3.51)), using the high-resolution field map, and multiplying by the corresponding FID. The measurement process was then simulated by selecting the central phase encodes of the resulting dataset, taken to be a  $32 \times 32$  Cartesian  $k$ -space sampling grid, and adding zero-mean Gaussian white noise to the simulated MRSI data. To examine the robustness of the reconstruction to various noise conditions, five realizations for each of three noise scenarios were generated, corresponding to mean SNR values of 13.98, 10.02, and 7.03 dB, to which we further refer as Case 1, Case 2, and Case 3, respectively. Using the criterion in (4.32), values for  $\epsilon$  were estimated for each of the three cases, such that  $\epsilon_1 = 0.067$ ,  $\epsilon_2 = 0.163$ , and  $\epsilon_3 = 0.314$ . The initial dimensionality for all reconstructions was set at  $K_0 = 25$  via [223], based upon the raw Case 2 dataset. All computations were carried out in MATLAB 8 (The Mathworks Inc., Natick, MA, USA) on an Intel Xeon 3.33 GHz six-core processor under Mac OSX 10.8.2 with 32 GB RAM.

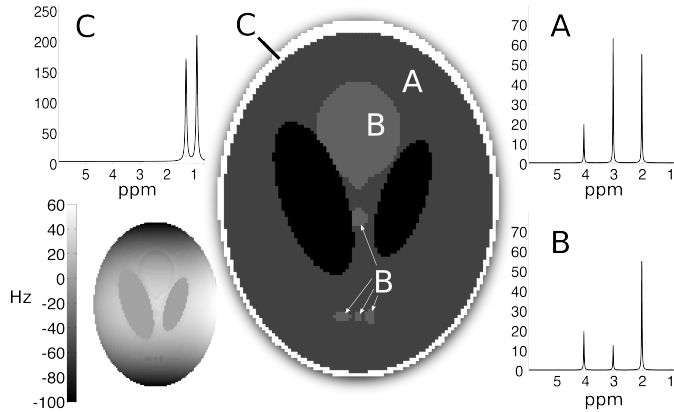


Figure 4.2: Numerical phantom composition and simulated static field inhomogeneity map (lower left).

To assess performance, four different reconstruction strategies were contrasted: (I) standard inverse DFT, (II) the adjoint solution, whereby  $\mathbf{F}^H$  and  $\mathbf{B}^H$  were applied directly to the raw measurements, (III) the proposed method in the absence of total generalized variation spatial regularization, and (IV) the full proposed method. Reconstructed images (Case 1), generated by integrating along the temporal frequency axis, as well as representative spectra for each method are collected in figure 4.3. For quantitative evaluation, each of the given spectra, as well as the reconstructed spatio-spectral volume as a whole, was compared against the ground truth data. The resulting mean PSNR values across realizations for each SNR scenario are collected in table 4.1. Following reconstructions, the SVD was computed for representative datasets in each case; the resulting singular value spectra are provided in figure 4.4 (a-c).

The limitations associated with MRSI reconstructions by low-resolution inverse DFT are clearly visible in figure 4.3 [I]. The spectral leakage artifacts, while expectedly severe near the compartment interface (4.3 [I(d)]), propagate even through the FOV center (4.3 [I(b)]), demonstrating the profound effects of the PSF. Concomitant lineshape distortions and spectral shifts are also apparent throughout the reconstructed data. Similarly, though the adjoint reconstruction (4.3 [II]) effectively compensates for the inhomogeneity-induced spectral shifts, it is unable to exploit the full high-resolution information from the field map, and to mitigate the PSF effects. In contrast, reconstructions using the proposed method (4.3 [III, IV]) best approximate the ground truth spatio-spectral distribution, offering vastly improved spatial localization and spectral lineshapes. Though the merits of the TGV penalty can be clearly recognized via improved spectral quality in 4.3 [IV(a), IV(b)], and markedly reduced spectral leakage from the outer-most compartment (4.3 [IV(c), IV(d)]), it can introduce slight partial-volume effects, which are most pronounced around areas containing differing spectral signatures that are small in comparison to the nominal CSI voxel size (4.3 [IV(c)] vs. 4.3 [III(c)]). Nonetheless, table 4.1 shows that by and large, the TGV regularization provides the best reconstruction quality by abating the most degrading influences.

Given the phantom conception, the desired result in the synthetic MRSI dataset would be such that the final reconstructed dataset lie completely within a three-dimensional subspace corresponding to the three ground truth compartments. In other words, an attendant spectral decomposition would yield only three non-trivial singular values. Although such idealized outcomes are generally precluded by the ill-posedness of the reconstruction, the proposed method does yield solutions in which the energy is primarily captured by just a few singular values, thereby suggesting ultimately low-dimensional representations (figure 4.4). This is easily contrasted to the inverse DFT and adjoint solutions, which are unable to adequately identify

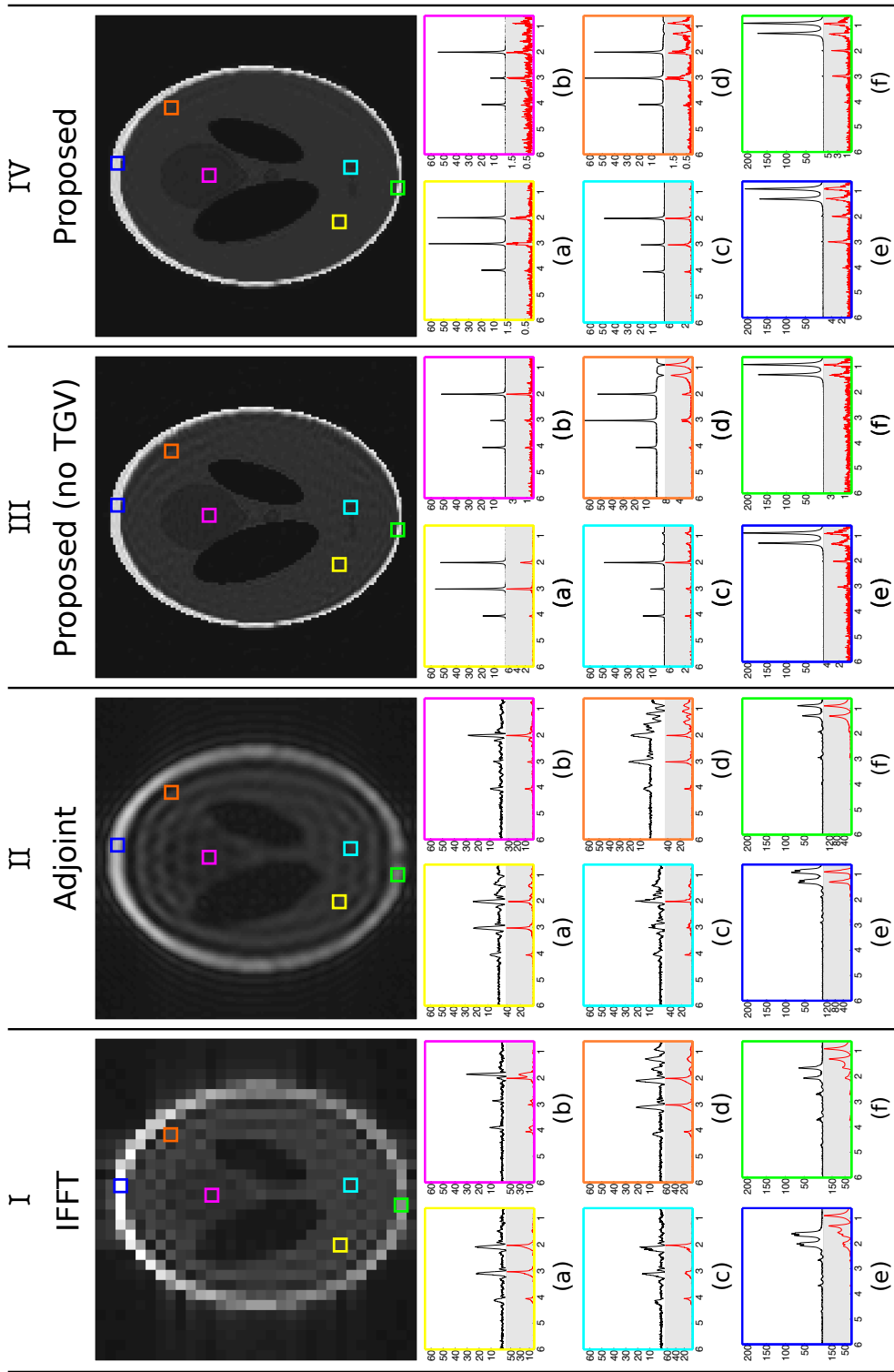


Figure 4.3: Reconstructed images for synthetic MRSI data (Case 1) along with representative spectra (real part shown) for each of the described methods: (I) standard inverse Fourier transform, (II) direct application of the adjoint operators, (III) proposed method with  $\mu = 0$ , (IV) proposed method with TGV regularization. The absolute error between each spectrum and the ground truth is plotted in red (note the changes in vertical axis scaling). Magnitude images were generated by integrating along the temporal frequency axis. Horizontal axis units for spectra are ppm.

RECONSTRUCTION METHOD			
IFFT			
SPECTRUM			
	<i>Case 1</i>	<i>Case 2</i>	<i>Case 3</i>
(a)	17.55 ± 0.02	17.33 ± 0.04	17.04 ± 0.05
(b)	15.01 ± 0.03	14.71 ± 0.05	14.25 ± 0.04
(c)	17.61 ± 0.04	17.30 ± 0.07	16.89 ± 0.07
(d)	18.30 ± 0.04	18.14 ± 0.04	17.86 ± 0.04
(e)	18.32 ± 0.00	18.31 ± 0.01	18.30 ± 0.01
(f)	19.50 ± 0.00	19.49 ± 0.01	19.47 ± 0.01
FULL	-	-	-
ADJOINT			
SPECTRUM			
	<i>Case 1</i>	<i>Case 2</i>	<i>Case 3</i>
(a)	21.60 ± 0.03	21.04 ± 0.08	20.34 ± 0.06
(b)	21.12 ± 0.07	20.17 ± 0.09	18.72 ± 0.04
(c)	21.22 ± 0.04	20.52 ± 0.05	19.75 ± 0.06
(d)	20.82 ± 0.03	20.54 ± 0.04	20.04 ± 0.05
(e)	24.64 ± 0.01	24.62 ± 0.03	24.56 ± 0.01
(f)	23.39 ± 0.01	23.37 ± 0.01	23.33 ± 0.03
FULL	20.61 ± 0.00	18.26 ± 0.00	16.41 ± 0.00
PROPOSED (NO TGV)			
SPECTRUM			
	<i>Case 1</i>	<i>Case 2</i>	<i>Case 3</i>
(a)	38.21 ± 3.28	31.42 ± 4.84	26.56 ± 1.22
(b)	35.31 ± 1.80	29.27 ± 0.71	24.89 ± 0.67
(c)	36.53 ± 2.02	27.97 ± 1.87	27.07 ± 1.50
(d)	38.13 ± 1.57	33.84 ± 2.09	30.10 ± 1.72
(e)	48.27 ± 2.01	41.69 ± 2.75	38.55 ± 2.42
(f)	51.67 ± 1.20	45.57 ± 0.68	40.47 ± 1.73
FULL	44.88 ± 4.85	31.77 ± 0.27	27.21 ± 0.26
PROPOSED			
SPECTRUM			
	<i>Case 1</i>	<i>Case 2</i>	<i>Case 3</i>
(a)	41.99 ± 3.23	37.85 ± 1.93	35.68 ± 1.68
(b)	36.62 ± 1.10	32.91 ± 0.39	30.41 ± 0.19
(c)	36.30 ± 2.59	32.29 ± 1.81	30.51 ± 1.39
(d)	40.98 ± 3.16	39.04 ± 2.44	36.62 ± 1.51
(e)	48.29 ± 4.11	46.31 ± 0.82	44.45 ± 1.19
(f)	48.79 ± 1.83	47.92 ± 0.63	43.99 ± 1.91
FULL	48.99 ± 1.04	43.81 ± 1.29	38.35 ± 4.21

Table 4.1: Numerical phantom dataset mean PSNR values plus standard deviations for the selected spectra and full reconstructed volumes (dB). The row initiated with the heading “FULL” reflects mean values over all voxels across realizations for the designated reconstruction method.

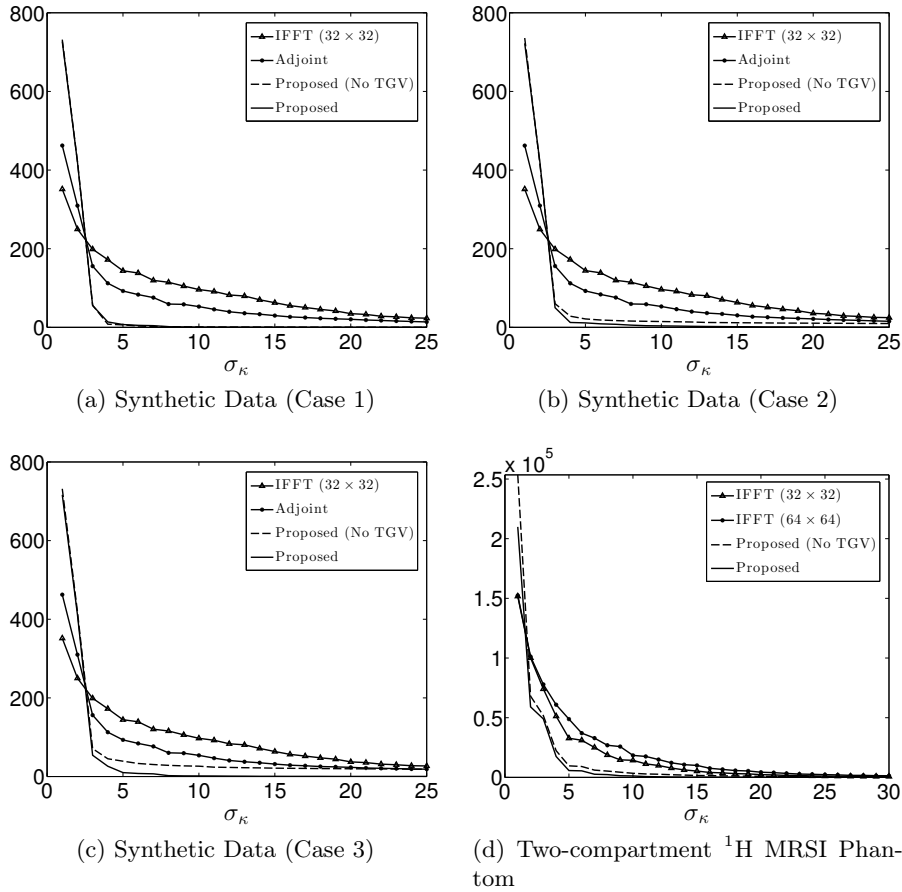


Figure 4.4: Singular value spectra for the reconstructed phantom datasets.

and expunge the field inhomogeneity and noise components, and therefore require higher dimensional subspaces to represent the observed data. The efficacy of the TGV regularization can also be discerned as the input SNR decreases, effectively attenuating the contribution of the accompanying noise subspaces.

#### 4.5.2 MRSI Phantom Data

To evaluate the performance of the algorithm using real-world data, we acquired two  $^1\text{H}$  CSI datasets on a 3.0 Tesla Siemens Trio MR scanner (Siemens Healthcare, Erlangen, Germany), using a two compartment test phantom, which is depicted in figure 4.5. The inner compartment (4.5 (A)) consisted of a sphere (diameter = 8.7 cm), containing 50 mmol/L N-acetyl-aspartic acid (NAA) and 50 mmol/L creatine (Cr) in standard buffer solutions. The

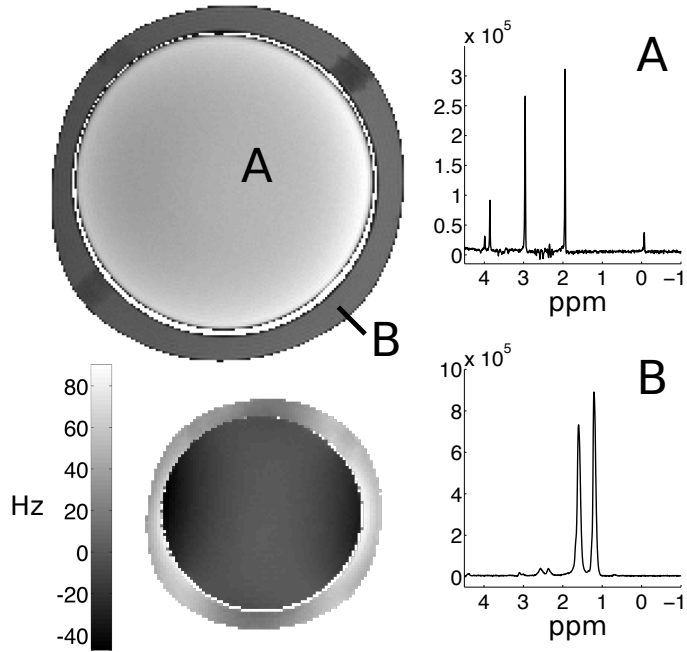


Figure 4.5:  $^1\text{H}$  Phantom composition and acquired static field inhomogeneity map (lower left).

outer cylindrical compartment (4.5 (B)) (height = 13.5 cm, diameter = 10.5 cm) was filled with corn oil. Single-voxel spectra were acquired for each compartment using a PRESS sequence (voxel size =  $15 \times 15 \times 15$  mm, TR = 1700 ms, TE = 288 ms, temporal bandwidth = 2 kHz, number of FID sampling points = 2048). Utilizing a semi-LASER sequence, water-suppressed CSI data was then acquired from a 10 mm slice thickness positioned at the center of the inner compartment (in-plane FOV =  $160 \times 160$  mm, TR = 1700 ms, TE = 288 ms, temporal bandwidth = 1.5 kHz, number of FID sampling points = 1024) using both  $32 \times 32$  and  $64 \times 64$  sampling grids. During the same scanning session, a local field map was estimated using two spoiled gradient echo sequences corresponding to the FOV of the CSI (nominal voxel size =  $1.56 \times 1.56 \times 10$  mm), with echo times selected so as to ensure the water and lipid resonances were in phase. Though two different CSI grid sizes were acquired, reconstructions were performed only using the lower resolution ( $32 \times 32$ ) data in order to better emulate typical clinical acquisition protocols. The underlying data dimensionality was estimated as  $K_0 = 35$ . As with the simulated data, resulting images and representative spectra for the different reconstruction strategies are collected in figure 4.6. In this case, however, the adjoint reconstruction has been replaced by the  $64 \times 64$  reference CSI data.

From an examination of figure 4.6, it is clear that inverse DFT reconstruc-

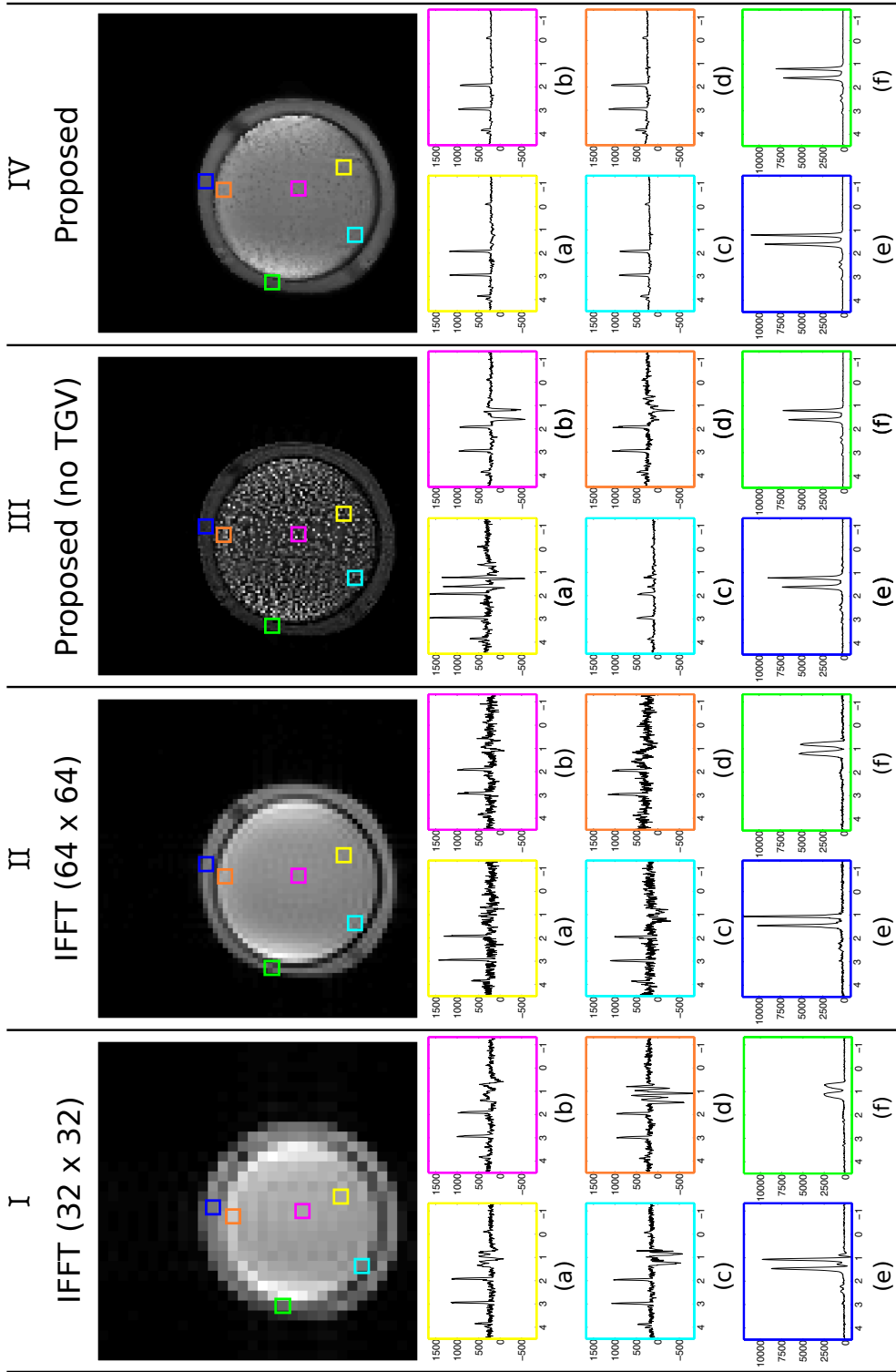


Figure 4.6: Reconstructed images for  $^1\text{H}$  MRSI data along with representative spectra (real part shown) for each of the described methods: (I) standard inverse Fourier transform ( $32 \times 32$ ), (II) standard inverse Fourier transform ( $64 \times 64$ ), (III) proposed method with  $\mu = 0$ , (IV) proposed method with TGV regularization. Magnitude images were generated by integrating along the temporal frequency axis. Horizontal axis units for spectra are ppm.

tions (4.6 [I]) are afflicted by similar artifacts as were prevalent in the synthetic case, namely, those due to spectral leakage, especially near the compartment interface. Spectral shifts and lineshape distortions due to the field inhomogeneity (depicted in figure 4.5) are also readily seen. For comparison, corresponding spectra taken from the  $64 \times 64$  inverse DFT reconstructions are illustrated in 4.6 [II], where improved spatial localization and reduced spectral leakage can be observed at the expense of SNR. Unlike the synthetic case, where the same model was used to both simulate and reconstruct the MRSI data, reconstructions based on real-world MR data underscore the indispensability and effectiveness of the TGV penalty. While the proposed method in the absence of TGV regularization (4.6 [III]) is able to recover the general phantom geometry, the lack of additional spatial constraints render the method incapable of recovering uncontaminated spectra, and hence little is gained by way of spectral quality over the standard DFT reconstructions. Though null-space contributions are presupposed given the ill-posedness of the unregularized reconstructions, a possibly incomplete measurement model, as discussed in greater detail later in this chapter, may explain the observed and seemingly exacerbated phase perturbations, as well as the incapability of the synthetic data to anticipate such artifacts. Alternatively, visual comparison between 4.6 [II] and 4.6 [IV] encourages the notion that the TGV penalty provides the necessary conditioning to recover the true underlying spatio-spectral distribution. Indeed, though some influence from the outer compartment can be discerned in 4.6 [IV(a)-IV(b)], the severity is greatly attenuated over reconstructions illustrated in 4.6 [I, III].

Although the underlying data presumably lies within a two-dimensional subspace corresponding to the inner and outer phantom compartments, subsequent spectral decompositions of the various reconstructions, collected in figure 4.4 (d), reflect the added complexities and increased difficulties encountered when working with real data. While reconstructions obtained through the proposed method lead to lower-dimensional representations when compared to their DFT counterparts, it is evident that unanticipated experimental confounds exist that incur further departures from the ideal. These may arise from the necessary discretization or mis-representation of the concerned continuous operators, and/or inaccuracies in the *a priori* information. For example, estimations of the local field inhomogeneities may be prone to errors stemming from an inappropriate choice of echo time or insufficient SNR. Moreover, although single-slice MRSI acquisitions are often regarded as purely two-dimensional datasets, significant variations in both the object geometry and the local susceptibility profile may exist throughout the slice thickness. While such heterogeneities were intentionally minimized or eliminated in the described phantom experiments so as to underscore in-plane reconstruction performance, their influence requires careful consideration in *in vivo* applications.

## 4.6 Adapting the Framework for *In Vivo* Settings

In order to achieve adequate SNR in typical clinical settings, the elected MRSI slice thicknesses are often designated as comparable to, or greater than nominal in-plane voxel dimensions ( $\sim 0.5\text{--}2.5$  cm). Given the resultant coarse voxel volumes, a re-examination of the theoretically predicted signal may be revealing. Taking into account static field inhomogeneities, and assuming without loss of generality that slice selection occurs along the  $z$ -direction, the measurements can be expressed as:

$$s(k_x, k_y, t) = \int_{-\infty}^{\infty} \int_{\Omega_{xy} \in \mathbb{R}^2} \left( \int_{z_0 - \frac{\Delta z}{2}}^{z_0 + \frac{\Delta z}{2}} \rho(\mathbf{r}, f) e^{-2\pi j \Delta f(\mathbf{r})t} dz \right) e^{-2\pi j(k_x x + k_y y + ft)} dx dy df, \quad (4.33)$$

where  $z_0$  corresponds to the slice center,  $\Delta z$  is the slice thickness, and  $\Omega_{xy}$  represents the in-plane FOV. It is clear from (4.33) that any spatial variations in  $\rho$  along the  $z$ -direction will be projected onto the slice plane, and will be imprinted with the full volumetric behavior of  $\Delta f(\mathbf{r})$ . Depending on the investigated anatomy, these variations may be substantial, which may in turn undermine the clinical utility of the resultant aggregate spatio-spectral information content.

With regards to the proposed reconstruction framework, this through-plane behavior carries a number of important consequences. The first pertains to so-called ‘‘partial volume’’ effects, whereby differing spatial (or likewise, spectral) characteristics will be amalgamated along the slice-select direction. In this case, the preeminence of total variation-based regularization becomes contentious, as any sharp object features displaying significant through-plane curvature will be diffused throughout the composite volume. Secondly, static local field maps estimated from images acquired using the same FOV as the MRSI measurements will represent conglomerated phase information, and will therefore remain limited in their capacity for abrogating volumetric lineshape distortions. In light of these arguments, it is therefore prudent to adapt the proposed method to explicitly take such volumetric aspects into account.

### 4.6.1 Incorporation of 3D Information

As was mentioned in section 4.3.1, though practical considerations severely limit achievable MRSI voxel volumes, far greater latitudes can be taken when selecting both the in-plane and through-plane resolutions of the ancillary field maps. These maps provide not only explicit phase information, but

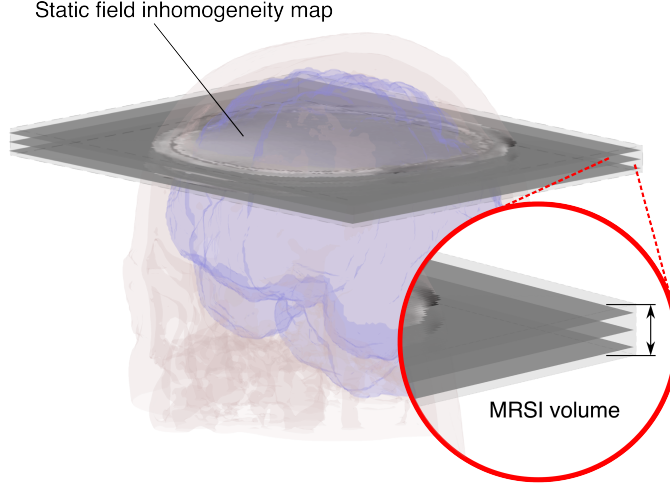


Figure 4.7: Schematic representation of the 3D reconstruction scheme. The MRSI slice is partitioned into subvolumes defined by the acquired static field map.

also contain a wealth of implicit high-frequency content, which conceivably may be used to recover the divested volumetric signal. We therefore extend the proposed method such that multiple field map slices are acquired in order to split the nominal MRSI slice thickness into a number of non-overlapping partitions, which are then jointly estimated during the reconstruction process. This procedure can be demonstrated pictorially by means of figure 4.7.

Unfortunately, the added recovery of volumetric information from a single MRSI slice exacerbates the ill-posedness of the reconstruction, mandating further mechanisms in order to constrain the solution space. The principal concern is that the recovered signal energy may be disproportionately apportioned to a small subset of the estimated slices. Though these outcomes may be obviated by strongly penalizing disparities in signal intensity along the slice-select direction, such measures would inevitably undermine the primary motivation by discouraging spatial variations. We therefore attempt to circumvent this apparent paradox by introducing an additional penalty into the reconstruction framework that penalizes through-plane deviations of the mean in-plane intensity of the spatial components. The modified reconstruction problem can then be expressed as:

$$\begin{aligned}
 \text{minimize } \mathcal{L} = & \|\vec{\mathbf{s}} - \mathbf{FB}\Xi_{\otimes} \vec{\mathbf{u}}_{\mathfrak{R}}\|_{\ell_2}^2 + \mu_1 \text{TGV}_{\alpha}^2(\vec{\mathbf{y}}) + \mu_2 \|\mathbf{D}_{ss} \mathbf{M}_{\perp} \vec{\mathbf{u}}_{\mathfrak{R}}\|_{\ell_2}^2 + \\
 & \beta \|\vec{\mathbf{u}}_{\mathfrak{R}} - \vec{\mathbf{y}}\|_{\ell_2}^2 + \langle \vec{\boldsymbol{\lambda}}, \vec{\mathbf{u}}_{\mathfrak{R}} - \vec{\mathbf{y}} \rangle, \\
 \text{such that } & \vec{\mathbf{u}}_{\mathfrak{R}} \in \mathcal{C}_u, \vec{\boldsymbol{\xi}} \in \mathcal{C}_{\xi},
 \end{aligned} \tag{4.34}$$

where  $\mathbf{M}_{\perp}$  computes the mean along the in-plane dimensions, and  $\mathbf{D}_{ss}$  repre-

sents a first-order forward discrete differences operation along the slice-select dimension. The  $\vec{\mathbf{u}}_{\mathfrak{R}}$  subproblem in algorithm 1 is then modified as:

$$\vec{\mathbf{u}}_{\mathfrak{R}}^{(n+1)} = \arg \min_{\vec{\mathbf{u}}_{\mathfrak{R}} \in \mathcal{C}_u} \left\| \vec{\mathbf{s}} - \mathbf{FB}\Xi_{\otimes}^{(n)} \vec{\mathbf{u}}_{\mathfrak{R}} \right\|_{\ell_2}^2 + \beta \left\| \vec{\mathbf{u}}_{\mathfrak{R}} - \left( \vec{\mathbf{y}}^{(n)} - \frac{\vec{\boldsymbol{\lambda}}^{(n)}}{\beta} \right) \right\|_{\ell_2}^2 + \mu_2 \left\| \mathbf{D}_{ss} \mathbf{M}_{\perp} \vec{\mathbf{u}}_{\mathfrak{R}} \right\|_{\ell_2}^2. \quad (4.35)$$

The attendant gradient step, (4.24), can similarly be adapted as:

$$\nabla \mathcal{L}(\vec{\mathbf{u}}_{\mathfrak{R}}^{(l)}) = \frac{1}{2} \mathfrak{Re} \left\{ \left( \Xi_{\otimes}^{(l)H} \mathbf{B}^H \mathbf{F}^H \mathbf{FB} \Xi_{\otimes}^{(l)} + \mu_2 \mathbf{M}_{\perp}^H \mathbf{D}_{ss}^H \mathbf{D}_{ss} \mathbf{M}_{\perp} + \beta \mathbf{I} \right) \vec{\mathbf{u}}_{\mathfrak{R}}^{(l)} - \Xi_{\otimes}^{(l)H} \mathbf{B}^H \mathbf{F}^H \vec{\mathbf{s}} - \beta \left( \vec{\mathbf{y}}^{(l)} - \frac{\vec{\boldsymbol{\lambda}}^{(l)}}{\beta} \right) \right\}. \quad (4.36)$$

### 4.6.2 *In Vivo* Experiments

To test the modified algorithm, a  $^1\text{H}$  CSI dataset was acquired in the brain from a healthy volunteer using the same protocol as described in section 4.5.2, but with an enlarged in-plane FOV of  $200 \times 200$  mm. In this case, however, three slices of a local field inhomogeneity map were obtained such that their combined volumes corresponded to that of the CSI slice (nominal voxel size =  $1.56 \times 1.56 \times 3.0$  mm, inter-slice spacing = 3.3 mm). Pre-processing prior to the reconstruction consisted of residual water signal filtering using the HSVD algorithm, and 10 Hz Gaussian line broadening (section 3.2.3). As no outer volume suppression was applied during the acquisition, additional pre-processing steps were necessary in order to attenuate signal contributions from the extra-cranial lipids. To accomplish this, a variant of [134] was utilized, whereby high-resolution reference scans were used to define metabolite and lipid-containing support regions. Lipid signal contributions were then estimated, and subsequently subtracted from the raw measurements by means of the BSLIM framework introduced in section 3.3.2. The model order was determined from the un-processed raw CSI data, and was estimated as  $K_0 = 30$ . The reconstruction results are collected in figure 4.8, where spatial metabolite maps are displayed for NAA, Cr, and choline (Cho) resonances for each of the slice partitions. Sample spectra produced by both the proposed method and DFT reconstructions are additionally contrasted in figure 4.9.

Upon inspection, variations along the slice-select direction for each of the metabolite maps can be discerned in figure 4.8, while the signal energy appears to be distributed evenly among the slices. Nonetheless, figures 4.8 and 4.9 highlight some of the difficulties encountered during *in vivo* scenarios, namely, the vast reduction in SNR when compared to the previously-described phantom experiments, and the pertinacity of the residual lipid

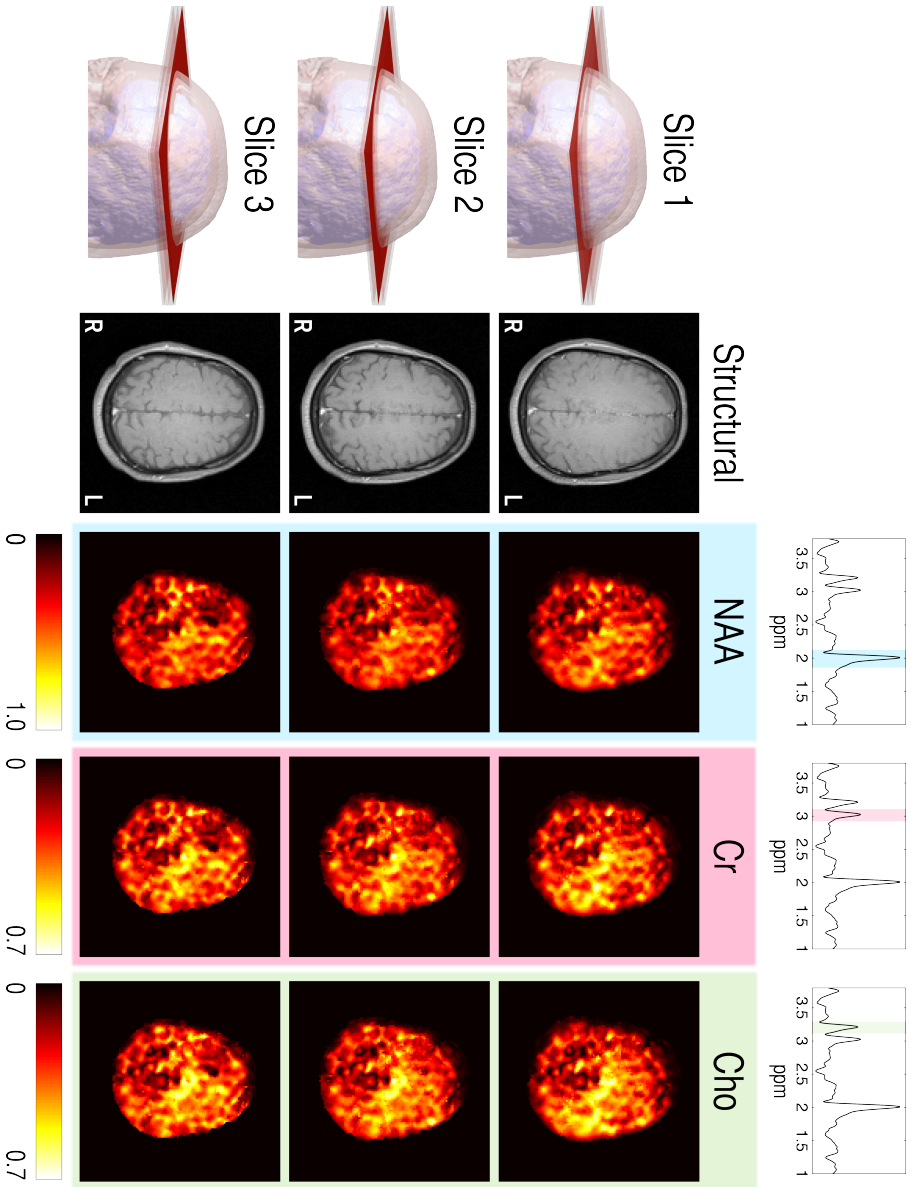


Figure 4.8: Reconstructed metabolite maps for NAA, Cr, and Cho, produced by the proposed method. The maps were produced by integrating the reconstructed spatio-spectral volumes under each of the resonances of interest (top), and then masking by the metabolite support region estimated during data pre-processing. Spatial variations along the slice profile can be observed, though the low input SNR and the lack of suitable ground-truth data disallows a straightforward interpretation of the results.

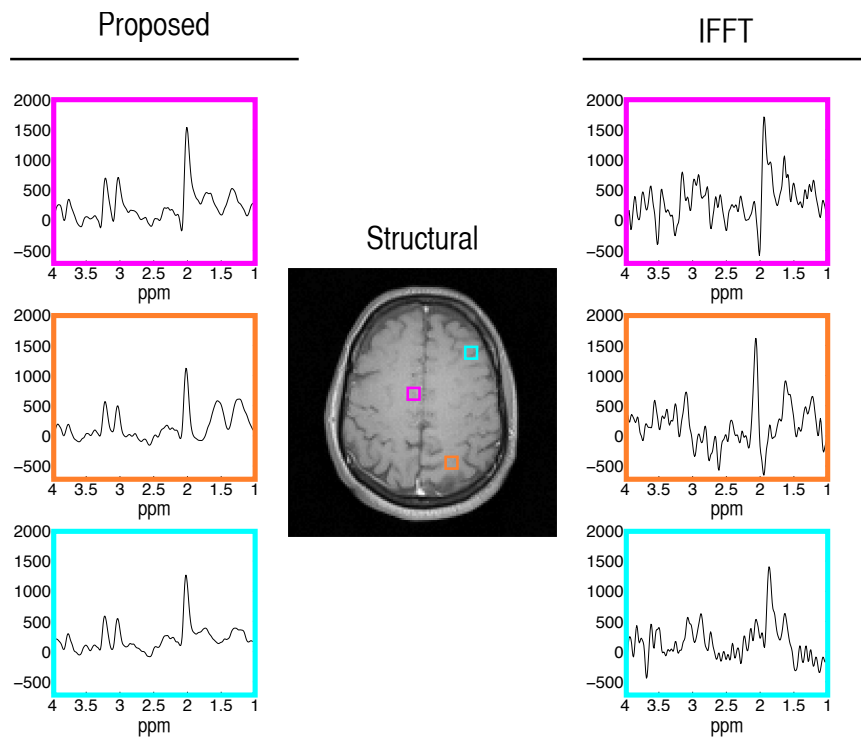


Figure 4.9: (Left) Sample spectra taken from the center slice of the reconstructed data generated by the proposed method. Improvements in both the SNR, and the phase behavior can be observed when compared to corresponding spectra produced by inverse DFT (right). In both cases, signal contamination from the extra-cranial lipids remain prevalent throughout the FOV.

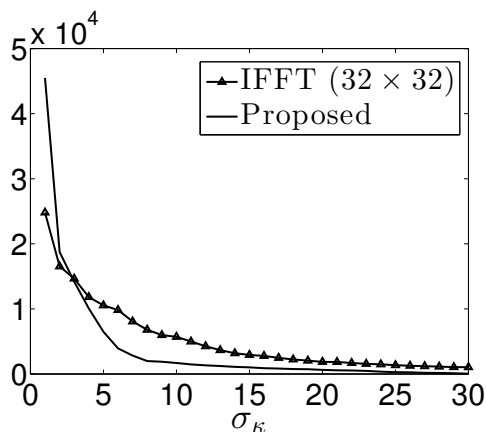


Figure 4.10: Singular value spectrum for the reconstructed  $^1\text{H}$  *in vivo* MRSI dataset.

signals. The former obfuscates attempts to separate the signal and noise subspaces, and thus, the resulting variational reconstruction framework will generally suffer greater noise bias. This relative diminution of the signal subspace can also be seen by regarding the resultant singular value spectrum, which is displayed alongside that of the inverse DFT reconstruction in figure 4.10.

## 4.7 Summary

In essence, the proposed scheme seeks a compromise between two broad generalizations concerning the problem geometry. The first, as was discussed in section 4.2, adheres to the validity of a bilinearly-representable functional form for the spatio-spectral distribution, whose dimensionality is presumed to be lower than that of the acquired measurements. We constrain solutions to meet this criterion by effectively placing an upper bound on the expected data dimensionality, and restricting the reconstruction process to the circumscribed subspace. The second, enforced by the total generalized variation-based spatial regularization, prescribes an implicit geometrical framework for the high-resolution model, stipulating that the spatial components represent a class a piecewise linear functions (piecewise constant with classical TV). Moreover, the non-linearity of total variation penalties facilitates the recovery of objects exhibiting strong edge behavior, resonating with common medical imaging applications where definitive borders exist between differing tissue types. Nonetheless, it is the synergy between the spatial regularization and the implicit high-resolution information carried by the field map that furnishes the necessary problem conditioning for high-resolution MRSI reconstruction. As section 4.6 demonstrated, the latter is an indis-

pensable ingredient when attempting to extricate volumetric information, and affords a liberal choice of reconstruction resolution. Nevertheless, these maps are still unable to account for dynamic phase perturbations, such as residual eddy currents, which are often problematic for MRSI. In general, spatial variations in  $\mathbf{B}_1$ , off-resonance effects, motion-induced artifacts, and flow phenomena reflect a number of common additional challenges in *in vivo* settings that are currently unaccounted for in the measurement model.

It should be noted that while the *in vivo* reconstruction results represent a significant improvement over standard inverse DFT, the lack of reliable ground truth data greatly confounds the robust assessment of reconstruction performance, especially with regards to the recovered volumetric information. A number of studies have attempted to investigate regional metabolite distributions in the human brain at enhanced spatial resolutions, such as [236, 237], which reported increased Cr and Cho concentrations along the inter-hemispheric fissure. While our results do not seem to corroborate these observations, it is important to bear in mind that individual outcomes do not necessarily communicate group-wide trends, and that additional experiments are needed before attempting further conjecture. Nonetheless, *in vivo* MRSI ultimately represents a unique, albeit limited, modality that cannot be easily validated. Though simplistic real-world phantom studies such as the one presented in section 4.5.2 serve as important first steps in characterizing a reconstruction method so as to identify potential biases, they remain limited in their capacity for elucidating reconstruction behavior when working with complex biological systems. More sophisticated ground truth models are therefore needed in order to provide further insights into expected *in vivo* performance.



## Chapter 5

# Haptic Phantoms for MRSI Testing and Validation

### 5.1 Introduction

The *in vivo* results presented in the previous chapter revealed a need to envision more robust means of both characterizing and validating new and original reconstruction methods, given the unavailability of high-resolution ground truth data for comparison. Though numerical or physical phantoms may be of use with regards to this task, their current incarnations represent overly naive approximations of the complex object geometries and acquisition conditions encountered in common biological applications. We therefore begin this chapter<sup>1</sup> by expounding upon the nature of these limitations, postulating the potential advantages obtained through the synergetic assimilation of the two phantom approaches. We accordingly propose a general framework for MR phantom generation that capitalizes on current trends in additive manufacturing technology, which affords greater flexibility in rapidly designing and manufacturing objects with highly customized geometries. We then describe the fabrication of a novel phantom for MRSI, and contrast the resulting simulated and experimental data. Finally, we demonstrate reconstructions using the method described in chapter 4, and conclude with a short discussion.

---

<sup>1</sup>This chapter is partially based on the publication:  
J. Kasten, T. Vetterli, F. Lazeyras, and D. Van De Ville, “3D-Printed Shepp-Logan Phantom as a Real-World Benchmark for MRI,” *Magnetic Resonance in Medicine*, [Accepted for publication December 4, 2014].

## 5.2 Limitations in Current Phantom-Based Testing

### 5.2.1 Haptic Phantoms

Although a number of geometrically complex physical phantoms currently exist on the market, they have been designed primarily with structural MR assessments in mind, and generally remain devoid of spectral diversity. For example, apart from the standard test phantoms supplied by the major scanner vendors, specialized phantoms, such as the ACR [238] and ADNI [239] phantoms, have been created for testing SNR, contrast-to-noise ratio (CNR), geometrical uniformity, slice thickness accuracy, etc., in order to synchronize and/or normalize scan parameters across vendors and institutions in large multi-site studies. Likewise, a 3D grid phantom was constructed in [240] in order to measure and compensate for image distortions due to gradient non-linearities. The MRSI community itself, however, has traditionally appropriated phantoms designed primarily for single voxel assessments, where structural heterogeneity is typically devalued in order to underscore spectral behavior. These phantoms are consequently limited in their capacity for evaluating the spatial characteristics of a given MRSI reconstruction strategy, and therefore maintain minimal predictive value when attempting to extrapolate performance to clinical settings. In contrast, in [241], a phantom consisting of an array of cone-shaped vials filled with various metabolites was fabricated, whereby the solution volume in a given MRSI slice could be modulated by changing the slice position. Nonetheless, such in-house exploits often represent substantial endeavors that cannot easily be transmitted among institutions. While it has been possible to commercially commission or develop customized phantoms in accordance with specific requirements, the invested time for prototyping and fabrication, as well as the associated costs, may also remain limiting factors.

### 5.2.2 Numerical Phantoms

Numerical phantoms remain popular among the image processing and reconstruction communities, as they facilitate quantitative comparisons between different algorithms. Moreover, they enable optimization over a wide variety of applicable object classes, which is particularly convenient when access to a scanner is limited or cost-prohibitive. Nevertheless, care must be taken to ensure that numerical studies faithfully represent the acquisition process. Perhaps the most often overlooked consideration in this regard is the proper distinction between the various discretization procedures. As discussed in section 3.3.1, the acquired measurements are obtained by sampling the observed MR signal, which in turn arises from purely continuous phenomena, namely, the object itself and the encoding scheme. By comparison, in typi-

cal reconstruction settings, the paucity of closed-form Fourier expressions for the vast majority of investigated objects impels a discrete approximation of the entire encoding process. Utilizing this approximation for both raw data simulation and the attendant reconstruction, however, defines a so-called “inverse crime” situation, in which the general disregard for the underlying continuous problem leads to artificially providential algorithm performance. A greatly preferable scenario for phantom testing is therefore one where the continuous-domain Fourier transform of the object can be expressed analytically, thereby adhering to the true measurement model, and allowing simulations that are resolution-independent.

Though closed-form Fourier expressions for arbitrary geometries may be difficult or even impossible to obtain, a number of works have presented analytical solutions for certain object classes. One of the initial works pertains to the inception of the now ubiquitous Shepp-Logan phantom [242], originally conceived for tomographic reconstruction evaluation, proposing a closed-form Fourier transform for an object comprised of 2D ellipses, which was later extended to the 3D case [243]. These object classes have been supplemented by the inclusion of Gaussian functions [244], linearly-varying functions with polygonal support [245], and 3D polyhedra [246, 247]. Recently, [248] extended these polygonal regions to those defined by 2D spline or Bézier contours, and even allowed for the modulation by sinusoidal or polynomial functions to mimic sensitivity maps for parallel MRI.

Ultimately, the discretization step represents just one of the multifarious elements introduced throughout the preceding chapters that define the acquisition process. Though a wide array of system behaviors may be accurately characterized and accommodated into the measurement model, the various system imperfections and nonlinearities that underlie acquired MR measurements can never be fully encapsulated through numerical simulation.

### 5.3 3D Printing: A Flexible Framework for MR Phantom Generation

From the discussions in section 5.2, it can be surmised that an ideal test bed for MRSI reconstruction would be such that a geometrically sophisticated haptic phantom, admitting a closed-form Fourier transform, were available, thereby allowing access to the benefits of both physical and numerical testing platforms. The former would enable the assessment of reconstruction performance under authentic experimental conditions, whereas the latter could be used to furnish a set of ideal reference measurements for comparison. Other desirable phantom properties would include a short overall production time, whereby prototypes could be rapidly fabricated under exigent circumstances,

and ease of accessibility in order to facilitate data comparison and exchange among scanners and institutions. Though a wealth of differing manufacturing technologies exists, one possible avenue for satisfying the above prerequisites is through the use of additive manufacturing, better known by the modern appellation of “3D printing.”

### 5.3.1 The 3D Printing Platform

Under the additive manufacturing platform, computer assisted design (CAD) software is used to generate models represented by faceted meshes, which are then exported to a printing device that gradually produces a solid object by successively layering material. Though 3D printing encompasses a variety of techniques, such as selective laser sintering (SLS), stereolithography (SLA), and multijet modeling (MJM), the recent rise in accessibility of consumer-level printers under the fused deposition modeling (FDM) platform, which utilizes extruded thermoplastics to form each layer, has led to an explosion in popularity. Furthermore, most interfacing software for 3D printers requires only a stereolithography (STL) file, promoting the open-source exchange of designs that has culminated in numerous online repositories. 3D printing is therefore an attractive prospect for MR applications due to the decreasing costs, routine use of MR-compatible materials such as acrylonitrile butadiene styrene (ABS), cross-institution accessibility, and as will be demonstrated in the following subsection, congruence of feasible designs with a class of analytical Fourier transforms.

### 5.3.2 Analytical Fourier Computations

Although closed-form Fourier expressions are available for a diverse assortment of object classes as presented in section 5.2.2, extending these results to account for the partial voluming associated with finite slice thicknesses may not be straightforward. Moreover, even when working within these geometrical confines, translating a given design to a physically realizable model may still prove to be a formidable process. As such, 3D printing offers a compelling resolution by proffering a set of CAD-driven faceted models, where analytical Fourier transforms are available for representing both the full 3D object and its 2D projections. To demonstrate the former, we first consider a solid polyhedral region,  $P$ , whose spatial support is denoted by  $\mathbf{1}_P(\mathbf{r})$ . The Fourier transform is then given by:

$$\mathcal{F}\{\mathbf{1}_P\}(\mathbf{k}) = \int_{\Omega \subset \mathbb{R}^3} \mathbf{1}_P(\mathbf{r}) e^{-2\pi j \mathbf{k} \cdot \mathbf{r}} d\mathbf{r} = \int_P e^{-2\pi j \mathbf{k} \cdot \mathbf{r}} d\mathbf{r}. \quad (5.1)$$

The right-hand side of expression (5.1) can be evaluated analytically, leading

to the following proposition:

**Proposition 1.** *Suppose  $P$  is a solid polyhedral region comprised of simple polygonal facets whose vertices are enumerated in a counter-clockwise fashion. The Fourier transform of  $\mathbf{1}_P$  is then given by:*

$$\mathcal{F}\{\mathbf{1}_P\}(\mathbf{k}) = \begin{cases} -\frac{1}{\|2\pi\mathbf{k}\|_{\ell_2}^2} \sum_{i=1}^{|\mathcal{F}|} \frac{\mathbf{k} \cdot \hat{\mathbf{n}}^{(i)}}{\|\mathbf{k}\|_{\ell_2}^2 - |\mathbf{k} \cdot \hat{\mathbf{n}}^{(i)}|^2} \sum_{n=1}^{|\mathcal{E}^{(i)}|} (\mathbf{k} \cdot \mathbf{l}_n^{(i)}) \\ j_0\left(\pi\mathbf{k} \cdot (\mathbf{v}_{n+1}^{(i)} - \mathbf{v}_n^{(i)})\right) e^{-2\pi j\mathbf{k} \cdot \mathbf{c}_n^{(i)}}, & \mathbf{k} \neq \mathbf{0} \\ m(P), & \mathbf{k} = \mathbf{0}, \end{cases} \quad (5.2)$$

where  $j_0$  is a zero-order spherical Bessel function, and  $m(P)$  denotes the Lebesgue measure (volume) of  $P$ . Similarly,  $\mathcal{F}$  is the family of polygonal facets comprising  $P$ , each with outward unit normal vector,  $\hat{\mathbf{n}}^{(i)}$ , and  $\mathcal{E}^{(i)}$  denotes the set of edges delimiting the  $i^{\text{th}}$  facet, with vertices,  $\{\mathbf{v}_n^{(i)}\}_{n=1}^{|\mathcal{E}^{(i)}|}$ , such that  $\mathbf{v}_{|\mathcal{E}^{(i)}|+n}^{(i)} = \mathbf{v}_n^{(i)}$ . Lastly,  $\mathbf{c}_n^{(i)} = (\mathbf{v}_{n+1}^{(i)} + \mathbf{v}_n^{(i)})/2$  represents the center of, and  $\mathbf{l}_n^{(i)} = (\mathbf{v}_{n+1}^{(i)} - \mathbf{v}_n^{(i)}) \times \mathbf{n}^{(i)}$  an in-plane vector normal to the  $n^{\text{th}}$  edge of the  $i^{\text{th}}$  facet.

A proof of proposition 1 is given both in [246] and in the appendix. Given the above, an analytical formulation of the expected MRSI measurements is straightforward so long as the spatial and temporal spaces remain separable, which may be presumed in the absence of spatially-dependent temporal phase perturbations. Discounting  $\mathbf{B}_1$  and relaxation effects, and letting  $\mathcal{P}$  denote the family of polyhedral regions comprising the phantom, the theoretical signal is given by:

$$s(\mathbf{k}, t) = \sum_{p=1}^{|\mathcal{P}|} w^{(p)} \left( \mathcal{F}\{\mathbf{1}^{(p)}\}(\mathbf{k}) \right) \left( \sum_{l=1}^L \int_{-\infty}^{\infty} \nu_l^{(p)}(f) e^{-2\pi jft} df \right), \quad (5.3)$$

where  $w^{(p)}$  are non-negative weights. Here,  $\nu_l$  represents a general spectral lineshape function with known analytical Fourier transform. Two appropriate choices for MR are Lorentzian and Gaussian functions:

$$\nu_l^{\text{Lorentz}}(f) = \frac{1}{\pi} \frac{(\Gamma_l/2)}{(f - f_l)^2 + (\Gamma_l/2)^2} \stackrel{\mathcal{F}_t}{\iff} e^{-2\pi jf_l t} e^{-\pi\Gamma_l|t|}, \quad (5.4)$$

$$\nu_l^{\text{Gauss}}(f) = e^{-\frac{(f-f_l)^2}{2\sigma_l^2}} \stackrel{\mathcal{F}_t}{\iff} (2\pi\sigma_l^2)^{1/2} e^{-2\pi jf_l t} e^{-2(\pi\sigma_l t)^2}. \quad (5.5)$$

For single-slice acquisitions, we again consider a single polyhedral region  $P \in \mathcal{P}$ , and a rectangular slice profile  $S$ , centered at a point  $\boldsymbol{\delta}$ . We also

introduce the transformation  $\mathcal{T} : X \rightarrow Y$ , from the laboratory frame to the frame oriented along the slice profile such that:

$$\begin{aligned}\mathcal{T}\{\mathbf{r}\} &= \mathbf{R}^{-1}(\mathbf{r} - \boldsymbol{\delta}) \\ &= \mathbf{p} = p_u \hat{\mathbf{e}}_u + p_v \hat{\mathbf{e}}_v + p_w \hat{\mathbf{e}}_w,\end{aligned}\quad (5.6)$$

where  $\hat{\mathbf{e}}_u$ ,  $\hat{\mathbf{e}}_v$ , and  $\hat{\mathbf{e}}_w$  are orthogonal unit vectors with  $\hat{\mathbf{e}}_w$  pointing along the slice-select direction, and  $\mathbf{R}$  is a pure rotation matrix. We further denote the restriction of  $\mathbb{1}_P$  to  $S$  as

$$\mathbb{1}_P|_S = \mathbb{1}_{P \cap S} = \mathbb{1}_R. \quad (5.7)$$

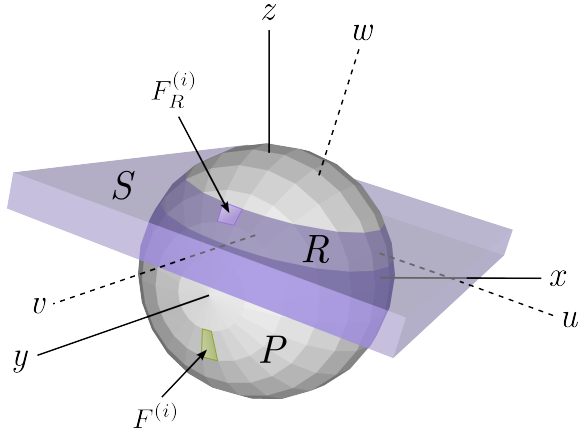


Figure 5.1: Graphical overview of the various geometrical entities and reference frames used for establishing the analytical single-slice MRSI signal produced from a planar-faceted object model.

A graphical overview of the described geometrical entities and reference frames is provided in figure 5.1. When expressed in the new coordinate frame, the Fourier transform of the projected object onto the slice profile is then given by:

$$\mathcal{F}\{\mathbb{1}_R\}(\kappa_u, \kappa_v) = \iint_{\Omega'_{uv} \in \mathbb{R}^2} \left( \int_{\Omega'_w \in \mathbb{R}} \mathbb{1}_R(\mathbf{R}\mathbf{p} + \boldsymbol{\delta}) dw \right) e^{-2\pi j(\kappa_u u + \kappa_v v)} dudv, \quad (5.8)$$

where  $\Omega'_{uv}$  and  $\Omega'_w$  denote the in-plane and through-plane FOV, respectively. Because  $P$  (and hence,  $R$ ) consists of planar facets, the integration along  $w$  in (5.8) simply outputs the unsigned area under each face, such that:

$$\mathcal{F}\{\mathbb{1}_R\}(\kappa_u, \kappa_v) = \sum_{i=1}^{|\mathcal{F}_R|} \iint_{F_{R,uv}^{(i)}} \mathbf{a}^{(i)} \cdot (\mathbf{p}_{uv} - \mathbf{p}_0^{(i)}) e^{-2\pi j(\kappa_u u + \kappa_v v)} dudv, \quad (5.9)$$

where  $\mathcal{F}_R$  denotes the set of faces comprising  $R$ , and  $F_{R,uv}^{(i)}$  the orthogonal projection of  $F_R^{(i)} \in \mathcal{F}_R$  onto the  $uv$ -plane. Additionally,  $\mathbf{p}_{uv}$  represents a general point in the  $uv$ -plane, and  $\mathbf{p}_0^{(i)}$  an arbitrary point on the  $i^{\text{th}}$  facet. The vector  $\mathbf{a}^{(i)}$  can be calculated from the unit outer normal vector of  $F_R^{(i)}$  in the slice frame,  $\hat{\mathbf{t}}^{(i)} = \mathcal{T}\{\hat{\mathbf{n}}^{(i)}\}$  as:

$$\mathbf{a}^{(i)} = - \left( \frac{t_u^{(i)}}{t_w^{(i)}} \hat{\mathbf{e}}_u + \frac{t_v^{(i)}}{t_w^{(i)}} \hat{\mathbf{e}}_v + \hat{\mathbf{e}}_w \right). \quad (5.10)$$

Expression (5.9) can also be determined analytically to give the following result:

**Proposition 2.** *Suppose  $P$  is a solid polyhedral region comprised of simple polygonal facets whose vertices are enumerated in a counter-clockwise fashion, and  $S$  is a rectangular MR slice profile. The Fourier transform of the 2D projection of  $\mathbf{1}_P|_S = \mathbf{1}_R$ , onto the slice profile is then given by:*

$$\mathcal{F}\{\mathbf{1}_R\}(\boldsymbol{\kappa}) = \begin{cases} -\frac{1}{\|2\pi\boldsymbol{\kappa}\|^2} \sum_{i=1}^{|\mathcal{F}_R|} \mathbf{a}^{(i)} \cdot \sum_{n=1}^{|\mathcal{E}^{(i)}|} e^{-2\pi j \boldsymbol{\kappa} \cdot \mathbf{d}_n^{(i)}} \left[ \left( \mathbf{m}_n^{(i)} - \left( \frac{2\boldsymbol{\kappa}}{\|\boldsymbol{\kappa}\|_{\ell_2}^2} + 2\pi j \left( \mathbf{d}_n^{(i)} - \mathbf{p}_{i,0} \right) \right) \cdot \left( \boldsymbol{\kappa} \cdot \mathbf{m}_n^{(i)} \right) \right) j_0 \left( \pi \boldsymbol{\kappa} \cdot \left( \mathbf{q}_{n+1}^{(i)} - \mathbf{q}_n^{(i)} \right) \right) - \pi \left( \boldsymbol{\kappa} \cdot \mathbf{m}_n^{(i)} \right) \left( \mathbf{q}_{n+1}^{(i)} - \mathbf{q}_n^{(i)} \right) j_1 \left( \pi \boldsymbol{\kappa} \cdot \left( \mathbf{q}_{n+1}^{(i)} - \mathbf{q}_n^{(i)} \right) \right) \right], & \boldsymbol{\kappa} \neq \mathbf{0} \\ \frac{1}{2} \sum_{i=1}^{|\mathcal{F}_R|} \mathbf{a}^{(i)} \cdot \left( \bar{\mathbf{p}}_{uv}^{(i)} - \mathbf{p}_0^{(i)} \right) \sum_{n=1}^{|\mathcal{E}^{(i)}|} \left( \hat{\mathbf{e}}_w \cdot \left( \mathbf{q}_n^{(i)} \times \mathbf{q}_{n+1}^{(i)} \right) \right), & \boldsymbol{\kappa} = \mathbf{0}, \end{cases} \quad (5.11)$$

where  $\boldsymbol{\kappa} = \kappa_u \hat{\mathbf{e}}_u + \kappa_v \hat{\mathbf{e}}_v + 0 \hat{\mathbf{e}}_w$ . Similarly,  $\{\mathbf{q}_n^{(i)}\}_{n=1}^{|\mathcal{E}^{(i)}|}$  denotes the set of comprising vertices, and  $\bar{\mathbf{p}}_{uv}^{(i)}$  the barycenter of the  $i^{\text{th}}$  facet, orthogonally projected onto the slice ( $uv$ ) plane. Finally,  $\mathbf{m}_n^{(i)} = (\mathbf{q}_{n+1}^{(i)} - \mathbf{q}_n^{(i)}) \times \hat{\mathbf{e}}_w$  represents an outer normal vector to the  $n^{\text{th}}$  edge of the  $i^{\text{th}}$  projected facet, and  $\mathbf{d}_n^{(i)} = (\mathbf{q}_{n+1}^{(i)} + \mathbf{q}_n^{(i)})/2$ .

A proof of proposition 2 is provided in the appendix. The expected MR signal for the projected slice can then be expressed as:

$$s(\boldsymbol{\kappa}, t) = \sum_{p=1}^{|\mathcal{P}|} w^{(p)} \left( \mathcal{F}\{\mathbf{1}^{(p)}|_S\}(\boldsymbol{\kappa}) \right) \left( \sum_{l=1}^L \int_{-\infty}^{\infty} \nu_l^{(p)}(f) e^{-2\pi j f t} df \right). \quad (5.12)$$

## 5.4 A 3D Printed Shepp-Logan Phantom for MRSI

### 5.4.1 Conception and Design

As proof of concept, we decided to begin our investigations by designing a 3D variant of the Shepp-Logan phantom, prescribing for each compartment a solution of known spectral content. The Shepp-Logan design was selected as a reference due to its simplicity, yet appositeness in representing prominent anatomical features of the human head, as well as its omnipresence among the image processing community. Certain adaptations, however, were necessary in order for the design to remain compatible with both the 3D printing process, and the study motivation. These mandated a tapering of the ellipsoids to ensure adequate structural support at each stage of the print, as well as a means for later filling. The smallest ellipsoids (corresponding to regions  $h$ ,  $i$ , and  $j$  in the original Shepp-Logan manuscript) were also restricted to remain spherical, and were scaled such that the diameter of each was comparable to the nominal voxel sizes in common MRSI settings. A schematic drawing of the finalized design is provided in figure 5.2. The material thickness of each of the interior compartments was chosen to be 2 mm, whereas the outer concentric shells were given a 3 mm thickness. The base plate thickness was set at 5 mm, with a 9 mm wall height. These values were shown to represent a suitable compromise between the required structural integrity, material usage, and the risk of component permeability. All designs were conceived using Sketchup Make 8 (Trimble Navigation Limited, Sunnyvale, California, USA).

### 5.4.2 Fabrication Process

Once the design stage was complete, a model was exported as a STL file, and printed with a Statasys Fortus 250mc (Stratasys Ltd., Eden Prairie, Minnesota, USA/Rehovot, Israel) FDM printer using ABS, for which select material properties are provided in table 5.1. ABS is an attractive choice for MR applications due to its low magnetic susceptibility, effectively rendering the resultant structures as “MR invisible.” The minimum achievable layer thickness for the printer (used in this study) was 0.178 mm, with a nominal in-plane accuracy of  $\pm 0.241$  mm (manufacturer specifications). During the fabrication process, the model geometry dictated that each of the components be printed separately. This was due to the fact that the printer can only achieve a reliable layering when there is adequate support underneath. Practically, most systems mandate that the angle formed between the surface normals and the printing plane,  $\theta \in [-45^\circ, 225^\circ]$ . When  $\theta$  falls outside of this range, an ancillary water-soluble material is printed to provide tempo-

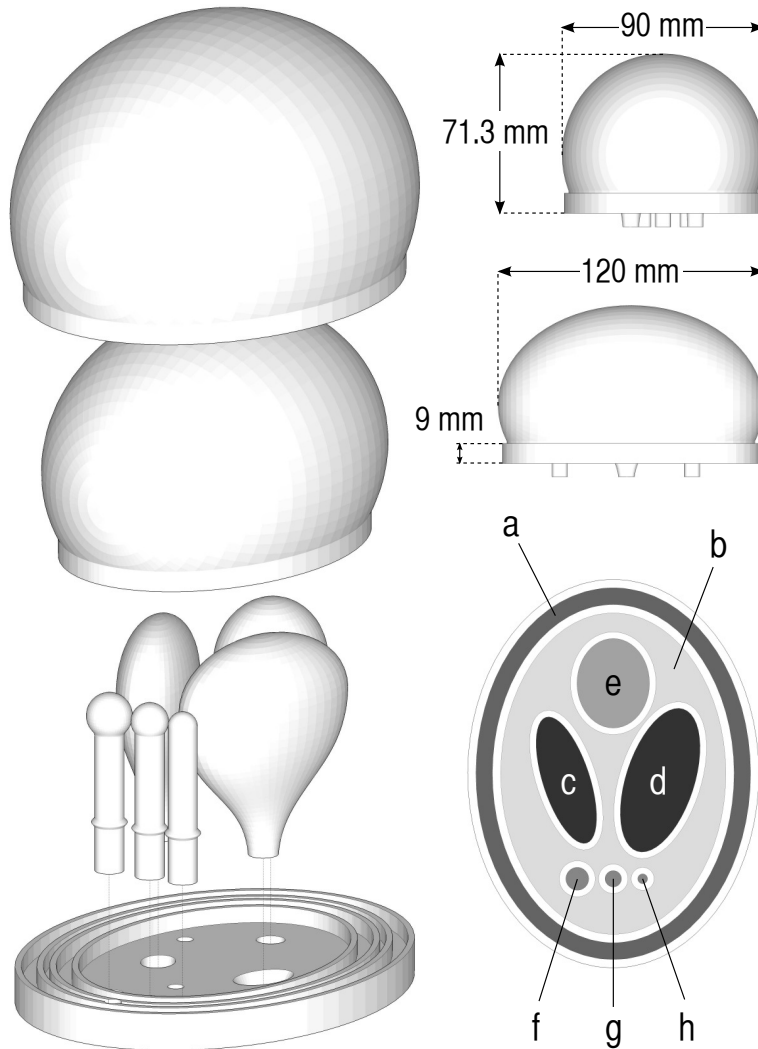


Figure 5.2: Schematic diagram of the 3D-printed Shepp-Logan phantom. (Left) Perspective view of the individual components comprising the phantom. (Top/Right) Profile views of the assembled phantom. (Bottom/Right) Axial section portraying the various phantom regions. Grayscale intensities serve as an aid to distinguish between spectrally-homogeneous compartments.

rary support, which is removed after printing. The entire phantom required approximately 10 hours of fabrication time, leading to a total manufacturing cost of around 300 USD. Once printed, the fidelity of the phantom to the original design was verified using a set of digital calipers.

Material Property	Value
Tensile Strength (Type 1, 0.125",0.2"/min)	37 MPa
Tensile Modulus (Type 1, 0.125",0.2"/min)	2,320 MPa
Flexural Strength (Method 1, 0.05"/min)	52 MPa
Heat Deflection (HDT) @ 66 psi	96° C
Dielectric Constant	2.9 - 2.6
Dielectric Strength	320 - 100 V/mm
Dissipation Factor	.0053 - .0046

Table 5.1: Selected Material Properties for ABS*plus*-P430 (manufacturer specifications).

Though the completed parts should ideally represent “solid” objects, a number of factors may preclude complete impermeability, such as incomplete layer adhesion, or compromises in the extruder trajectory. This can obviously present a problem if contamination between compartment-specific solutions is to be avoided. We therefore coated the exterior (and when possible, interior) surface of each printed component with a two part waterproof epoxy resin (*Prestolith special epoxy resin*, MOTIP DUBPLI GmbH, Haßmersheim, Germany), which has a nominal mixed viscosity of 950 mPa.s (manufacturer specifications). The same epoxy was used to join the separate components and to attach Luer connectors to the filling inlets into compartments *a* and *b*, which culminated in a robust object once assembled. The various stages of the phantom construction are documented in figure 5.3. It is important to note that given the asymmetry of the protruding inlets, the phantom can be unambiguously oriented within the MR scanner.

Upon assembly, interior phantom compartments *b*, *e*, *f*, *g*, and *h* were filled with solutions containing various concentrations of common brain metabolites, namely, NAA, Cho, Cr, and sodium L-lactate (Lac), prepared in phosphate buffered saline (PBS) containing 0.02% sodium azide to preclude microbial contamination. The pH of each solution was adjusted to 7.2 to mimic *in vivo* conditions. Compartments *c* and *d* consisted of just the buffer solution. The outer compartment (*a*) was filled with corn oil (Lip) in order to simulate the extra-cranial lipids. Specific concentrations and calculated volumes for all compartments are provided in Table 5.2. No additional T1-shortening agents were used. We emphasize that the utilized concentrations were chosen as significantly higher than those normally encountered *in vivo* in order to achieve a SNR better suited for testing and validation. When filling each of the compartments, special care was taken to inhibit air bubble



Figure 5.3: (Top/Left) The printed phantom components. (Top/Right) The completed phantom. (Bottom) The partially-assembled phantom following application of the epoxy coating.

formation, which can engender severe susceptibility effects in the acquired images. For the main compartment (*b*), the two filling inlet connections were used to mount a series of Luer valves, allowing a closed fluid current loop to be formed and any large air bubbles to be isolated and subsequently evacuated. For the remaining compartments, extra long syringe needles were used to ensure solution filling began at the base of each compartment. Once filled, compartments *a* and *b* were sealed using threaded stoppers compatible with the Luer connectors; the remaining compartments were sealed using paraffin.

## 5.5 Phantom Validation

In order to evaluate the design and fabrication process, the completed phantom was scanned on a Siemens 3.0 Tesla Trio MR scanner. The phantom was first positioned in the center of a 32-channel phased array head coil, with the major semi-axis oriented along the scanner bore (*z*-direction). Three coronal slices, positioned such that the top slice roughly corresponded to the center of regions *f*, *g*, and *h*, were acquired using a GRE sequence (FOV =  $160 \times 160 \times 10$  mm, TR = 400 ms, TE<sub>1</sub> = 2.46 ms, TE<sub>2</sub> = 4.92 ms, FA = 60°, BW = 1447 Hz/pixel, nominal voxel size =  $1.25 \times 1.25 \times 3.0$ , inter-slice spacing = 3.3 mm), and were used to generate a local field inhomogeneity map. The same spatial positioning and FOV was used to define a single MRSI slice, obtained using the same CSI protocol as described in section 4.5.2 (temporal sampling rate = 1.2 kHz). A transverse, high-resolution 3D MP-RAGE sequence (FOV =  $74.38 \times 140 \times 144$  mm, TR = 1750 ms, TE = 2.5 ms, TI = 900 ms, FA = 9°, BW = 210 Hz/pixel, nominal voxel size =  $0.547 \times 0.547 \times 0.9$  mm) was also acquired as a reference for translating the GRE / MRSI slice positioning onto the phantom model. Following phantom scanning, SVS spectra were acquired for each of the prepared solutions using a PRESS sequence (TR = 1700 ms, TE = 288 ms, temporal sampling rate = 2.0 kHz, number of temporal samples = 2048, nominal voxel size =  $15 \times 15 \times 15$  mm).

### 5.5.1 Structural Imaging

Once suitable position parameters were identified, three slices corresponding to the GRE sequence measurements were generated from the original phantom model, and their analytical Fourier transforms computed in accordance with (5.11), with a FOV and nominal spatial resolution chosen to match that of the measured data. The weights,  $w^{(p)}$ , were selected based on the Bloch equations for the GRE sequence, with literature-derived values of  $T_1$  and  $T_2$  for the buffer solution and corn oil. All calculations were performed in Matlab 8 on an Intel i7 2.66 GHz processor under Mac OSX 10.8.5 with

Region	Volume (mL)	N-Acetyl-L-aspartic acid [A5625]	Creatine [C0780]	Choline chloride [C7527]	Sodium L-lactate [L7022]	Corn Oil [C8267]
<b>a</b>	90.543	-	-	-	-	0.9 g/mL at 25°C
<b>b</b>	165.233	50 mmol	25 mmol	-	-	-
<b>c</b>	11.372	-	-	-	-	-
<b>d</b>	19.547	-	-	-	-	-
<b>e</b>	9.175	-	-	50 mmol	50 mmol	-
<b>f</b>	0.432	50 mmol	50 mmol	10 mmol	-	-
<b>g</b>	0.321	50 mmol	50 mmol	10 mmol	-	-
<b>h</b>	0.278	50 mmol	50 mmol	10 mmol	-	-

Table 5.2: Volumes, solution contents, and concentrations for each of the phantom compartments. Catalogue numbers for each reagent (Sigma-Aldrich, St. Louis, Missouri, USA) are provided in square brackets. All solutions were prepared in PBS (#10010, Thermo Fisher Scientific, Waltham, Massachusetts, USA) containing 0.02% sodium azide.

8 GB RAM. For comparison, rasterized counterparts for each of the slices were calculated based on Matlab's native `inpolygon` function, from which  $k$ -space data was generated via the DFT.

Resulting images for each of the rasterized, analytical, and measured datasets are collected in figure 5.4; all reconstructions were performed by inverse DFT of the simulated and acquired  $k$ -space samples. For the measured data, local static field inhomogeneity maps are also displayed for each slice. Maximum normalized cross correlation coefficients between the measured data and both the rasterized and analytical simulations are also provided for each reconstructed slice. Figure 5.4 serves as an edifying illustration of the various assumptions imposed when modeling the acquisition process. The utilization of rasterized images (figure 5.4, first row) reflects a discretization of the spatial integral in (5.8), whose DFT samples are considered as the measured data. The analytical case (figure 5.4, second row) clearly represents a more accurate portrayal of the Fourier transform and downsampling operations, simultaneously communicating the ramifications of additional confounds during the acquisition process, as evidenced by a visual comparison with the experimental data (figure 5.4, third row). Perhaps the most prominent examples are the reduced partial voluming around region  $e$  in the rasterized and analytical images in slice 1, where an ideal slice-select profile was assumed, and the lack of variation in the rf profile when compared to the measured data. The latter is made especially apparent through the normalized line profile plots for each of the reconstructions in figure 5.5. When viewing the static inhomogeneity profiles (figure 5.4, fourth row), some susceptibility effects can be recognized, predominantly around the lipid compartment and in the bottom slice around compartments  $f$ ,  $g$ , and  $h$ , paralleling the classical field response of a cylinder positioned perpendicular to the primary magnetic field [249].

### 5.5.2 Spectroscopic Imaging

For CSI simulations, spectral parameters for each of the prepared solutions were estimated from the SVS measurements using the HSVD algorithm. A CSI slice was then generated from the phantom model as with the GRE data, and analytical  $k$ -space measurements computed in accordance with (5.12). To facilitate visualization and interpretation, the analytical CSI data was then scaled using the Cho peak from compartment  $e$  in the acquired data as a reference, which was selected based on the relatively homogeneous local static inhomogeneity profile.

A few representative spectra are displayed in figure 5.6, where measured spectra are shown superimposed on their simulated counterparts. Here, the usual data truncation artifacts are observed, manifested primarily as spectral

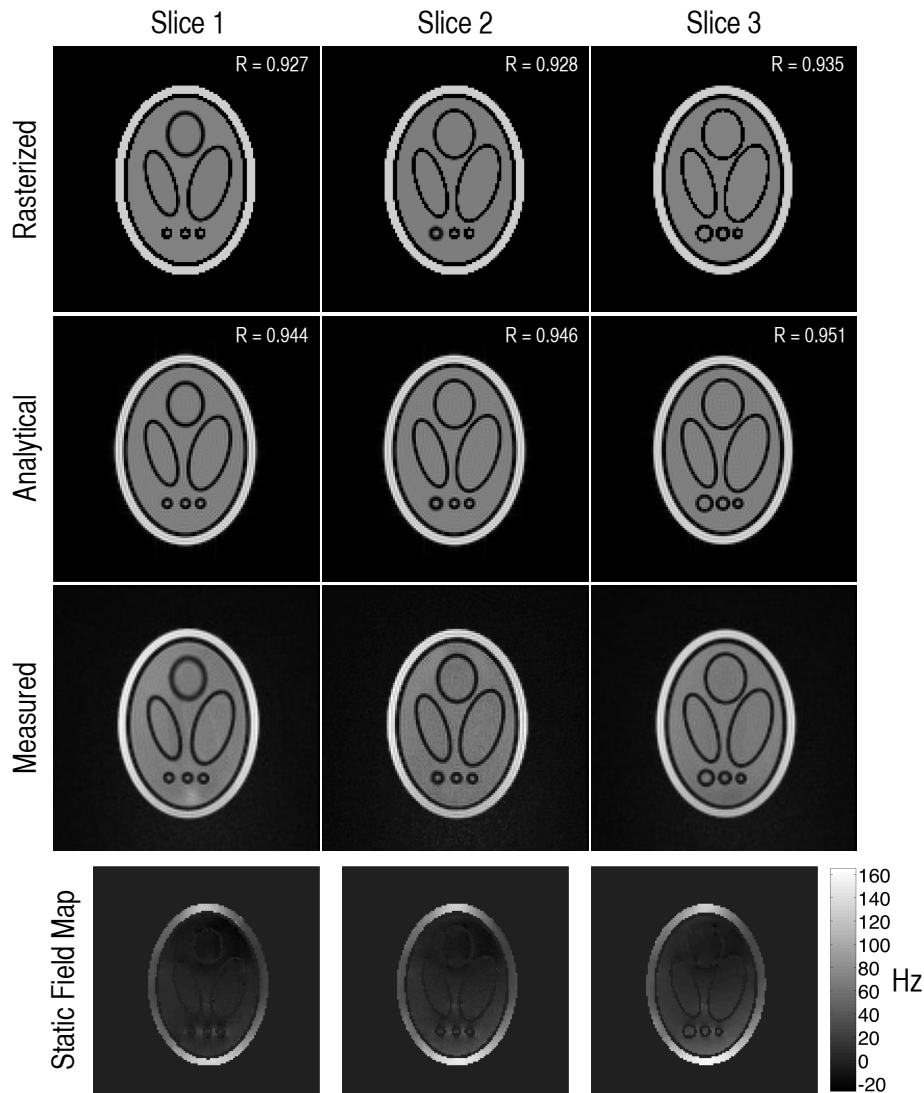


Figure 5.4: Reconstructed simulated and acquired images corresponding to each of the GRE slices. (Top row) Rasterized and simulated images. (Second row) Analytical simulated images. (Third row) Measured data. The small hyperintensity in slice 1 can be attributed to a slight mis-calibration in the coil combining algorithm. (Bottom row) static field inhomogeneity profiles for each of the GRE slices. The maximum value of the normalized cross correlation ( $R$ ) between the measured data and both the rasterized and analytical simulations is displayed for each slice, and substantiate an increased fidelity of the analytical simulations to the acquired measurements.

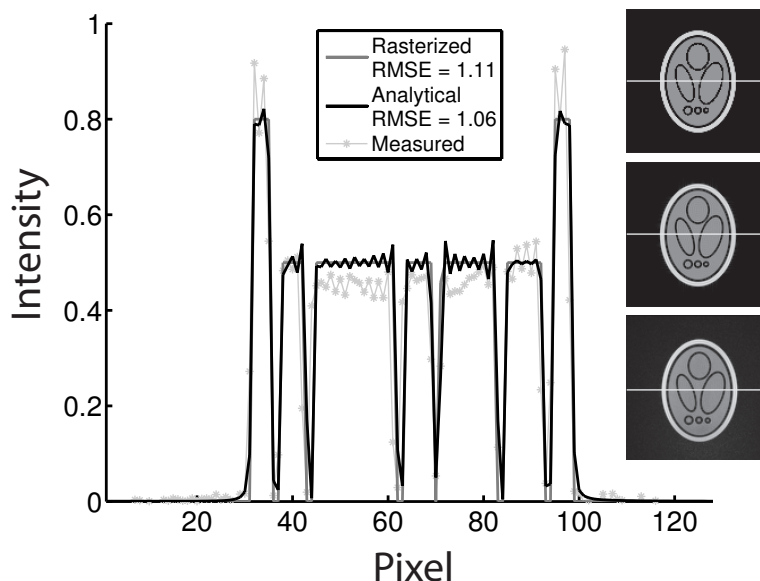


Figure 5.5: Sample line profile plots for the slice portrayed in the rightmost column of figure 5.4. RMSE values are given for both the rasterized and analytical reconstructions in reference to the measured data. The deviations of the measured data when compared against the simulated data reconstructions also indicate the presence of an inhomogeneous  $\mathbf{B}_1$  field, which is not accounted for during the simulation process.

leakage of the lipid signals into the interior compartments (figure 5.6 (i-iii)), as well as that of the large Cho peak in region  $e$  into region  $b$  (figure 5.6 (ii)). Spectral shifts and concomitant line broadening effects in the measured data due to the static inhomogeneity profile can also be discerned.

## 5.6 Component-Based Reconstructions

The geometrical sophistication of the haptic Shepp-Logan design when compared against the simple two-compartment phantom presented in section 4.5.2 provides a more exigent environment for MRSI reconstruction assessment, offering potentially greater insights into *in vivo* performance. We therefore sought to exploit this new platform by applying the (3D) reconstruction framework developed in chapter 4. The acquired MRSI data was first subjected to a number of pre-processing steps, which included residual water removal using the HSVD algorithm, as well as 5 Hz Gaussian line broadening along the temporal dimension. An initial determination of the data dimensionality was then made using the method described in section 4.4.2, estimated at  $K_0 = 40$ . The target reconstruction resolution was chosen

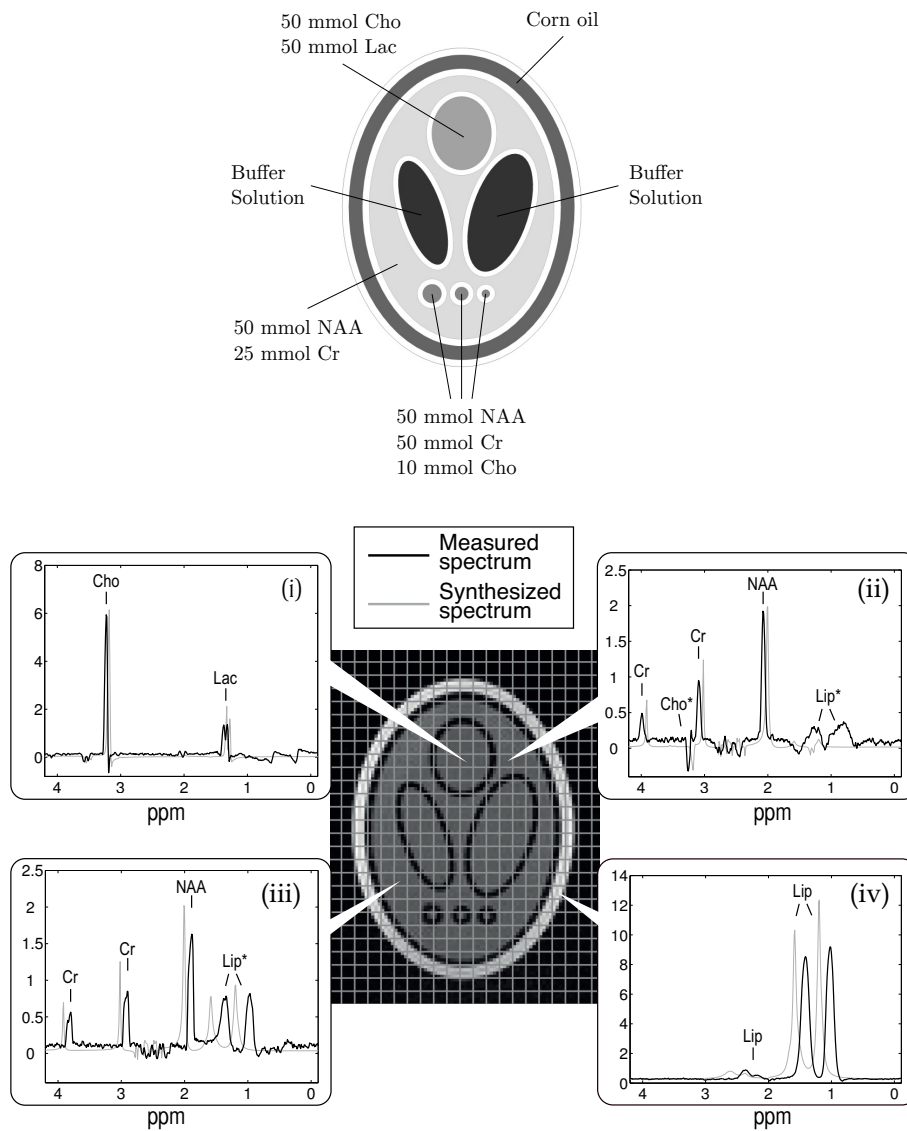


Figure 5.6: (Top) Reference schematic showing ground truth metabolite concentrations for each of the phantom compartments. (Bottom) CSI grid overlaid on a GRE structural image along with sample measured spectra (black), and their analytically-simulated counterparts (gray). The latter illuminate the various spectral shifts and line broadening effects due to the local static inhomogeneities present during the acquisition. Suspected truncation artifacts are denoted by an asterisk (\*) next to the offending resonance. Vertical axis scaling for all spectral plots is in arbitrary units (a.u.).

to be that of the three GRE images described in section 5.5, which were also used to define high-resolution support regions for the metabolite and lipid compartments. Following the reconstruction procedure, spatial maps of the NAA, Cr, and Cho resonances were generated through HSVD-based spectral fitting of the reconstructed data over the metabolite support region and the corresponding temporal frequency ranges. Resulting images for each of the three slices are collected in figure 5.7. Sample spectra from both inverse DFT reconstructions and those furnished via the proposed method are also displayed in figure 5.8.

It is clear from figure 5.7 that not only is the proposed method able to recover a number of prominent through-plane geometrical features, but also the small circular structures corresponding to compartments  $f$ ,  $g$ , and  $h$ , which are not resolvable when using standard DFT reconstructions. Nonetheless, the reconstruction is not able to fully extricate all through-plane variations, evidenced for example by the overestimation of NAA and Cr into compartment  $e$  in slice 3. Furthermore, a number of issues occur both in the posterior regions of slice 1 (adjacent to the small spherical compartments), and near the interface between the metabolite and lipid compartments, which manifest primarily as small areas of localized signal loss. However, the proposed method does altogether offer markedly superior spatial localization performance when compared against standard reconstruction schemes. This improved localization is also carried over to the spectral domain, where both abated contamination from the peripheral lipids and reduced lineshape distortions can be discerned. The mitigated PSF effects characterizing the former are easily observed when comparing figure 5.8(iii) to 5.8(vii), where the leakage artifacts stemming from both the Lip and Cho resonances in the DFT reconstructions have been largely suppressed using the proposed method. The improved lineshape profiles are particularly apparent when contrasting the spectra corresponding to compartment  $g$  (5.8(iv,viii)), where the presence of the Cho peak has been effectively disclosed.

## 5.7 Summary and Discussion

In this chapter, we have demonstrated the efficacy of 3D printing as a means of actualizing a class of phantom models for which analytical Fourier transforms are available for both the full 3D object and its projection onto a finite slice thickness. As proof of concept, we developed a novel Shepp-Logan-type phantom, envisioned as an early prototype for a new generation of phantoms designed specifically for characterizing and validating prospective MRSI reconstruction approaches. Such phantoms proffer a more unified testing framework, circumventing the various limitations confronted while exclusively considering numeric or haptic types. For example, reconstruc-

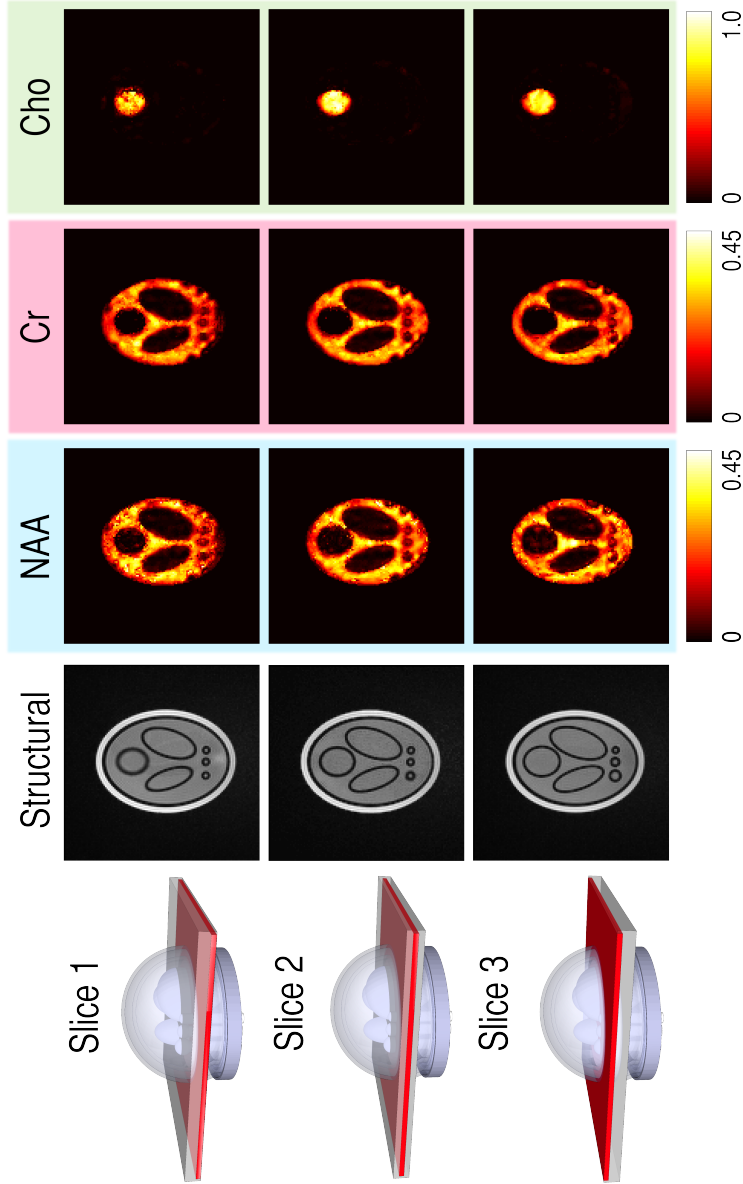


Figure 5.7: Metabolite maps corresponding to NAA, Cr, and Cho generated from the 3D Shepp-Logan phantom MRSI measurements using the proposed reconstruction method. The high-resolution maps were produced by HSVD-based spectral fitting of the indicated resonances over the predefined metabolite support region. Though the reconstructed metabolite profiles nicely correspond to their ground truth distributions, the recovery of through-plane geometry is only partially complete, as evidenced by the overestimation of NAA and Cr into compartment  $e$ . Areas of concentrated signal loss are also apparent towards the posterior regions of slice 1, and along the interface between the metabolite and lipid compartments, possibly reflecting localized phase perturbations that are not accounted for by the acquired static field inhomogeneity map.

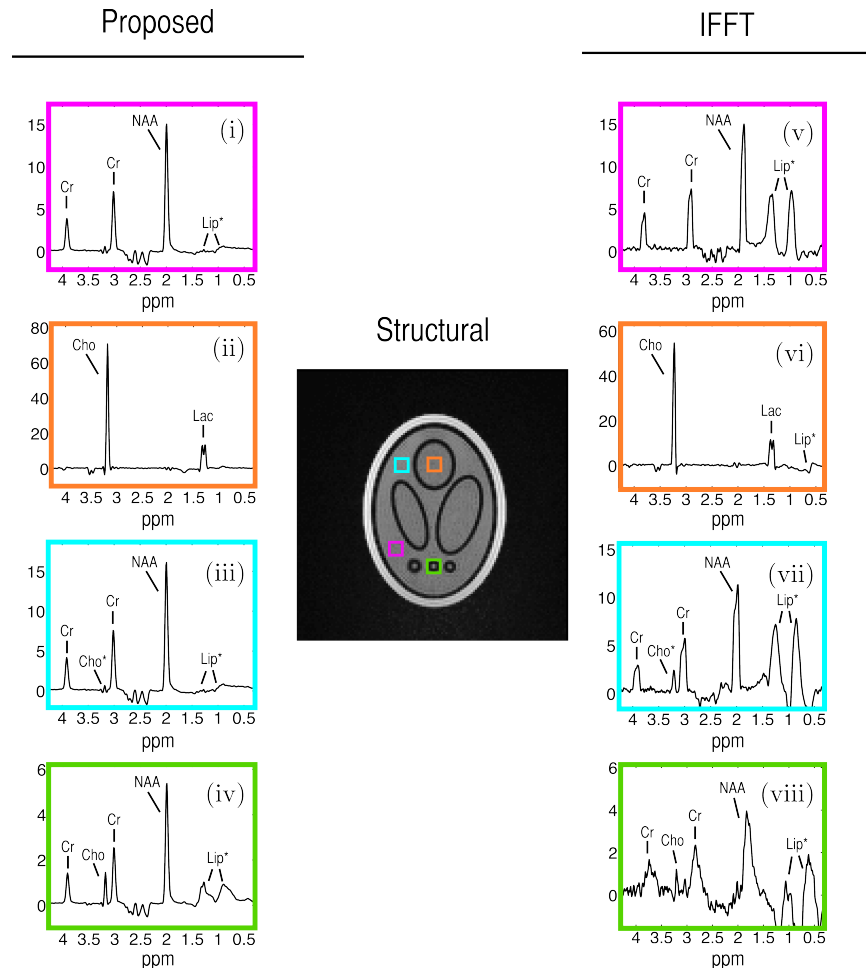


Figure 5.8: (Left) Sample spectra taken from the center slice of the 3D Shepp-Logan MRSI data reconstructed by the proposed method. A significant reduction in the spectral contamination artifacts (denoted by an asterisk next to the offending resonance) from both the peripheral lipids in compartment  $a$ , and the Cho in compartment  $e$  can be observed when compared against spectra reconstructed via standard inverse DFT (Right). Improvements in the spectral lineshape profiles are also manifest, and are particularly evident when contrasting the spectral signatures from compartment  $g$ , in which the Cho resonance – barely perceptible above the noise level in (viii) – has been effectively recovered in (iv). Vertical axis scaling for all spectral plots is in arbitrary units (a.u.).

tion techniques that are optimized based solely on numerical simulations may ultimately fail or introduce systematic bias when presented with real scanner data if important acquisition or object features are discounted or overlooked. Though a comprehensive account of all MR parameters and apertures within a reconstruction framework is by no means trivial, the use of a haptic phantom counterpart may facilitate identification of the most salient factors. In many cases, such elements may even be incorporated into the analytical signal model, allowing more complex and sophisticated simulations. This is certainly feasible for phenomena that are described as having a multiplicative effect on the signal, such as coil sensitivities or  $\mathbf{B}_1$  effects. On the other hand, attempts to incorporate experimental factors such as arbitrary phase perturbations (static or dynamic) regrettably lead to mathematically intractable situations, and therefore cannot be easily subsumed. Conversely, scanner hardware imperfections or patient-induced perturbations may be difficult to identify or characterize without knowledge of the ideal or unperturbed signal. Clearly, the more synergistic approach occasioned by 3D printing would serve as a preferred benchmark for MR reconstruction validation.

From an experimental standpoint, the strong correspondence between the acquired MR measurements and the analytically determined signal, as well as the paucity of any deleterious object-induced artifacts, effectively substantiates the 3D printing framework for MR phantom generation. Furthermore, the CSI measurements do not indicate any sign of solution contamination between the various compartments, corroborating the efficacy of the fabrication process, though thorough analysis requires additional longitudinal testing. Although the acquired static field maps revealed the presence of small susceptibility effects, these may remain inconsequential for a number of applications. Nonetheless, for situations where the elimination of such effects is paramount, the use of FDM, which may carry a risk of air becoming trapped between the individual material layers, may be dismissed in favor of alternative rapid prototyping technologies.

With regards to the performance of the reconstruction procedure presented in chapter 4, though vast improvements in the resulting spatio-spectral profiles were observed, a number of issues require further investigation. These pertain primarily to the localized losses in signal intensity both around the interface between the metabolite and lipid compartments, and the posterior region of the inferior slices. The former may result from phase perturbations that are not accounted for by the acquired field inhomogeneity map, and may be mitigated by considering either additional lipid suppression and/or more robust phase correction techniques during the pre-processing stages. The latter may be attributable to an irrecoverable loss of spectral signal due to dephasing caused by local susceptibilities, therefore highlighting the need for better shimming procedures. Additional studies are also needed in or-

der to fully characterize and influence the recovery of through-plane spatial variations, which is essential before progressing to *in vivo* scenarios. Though the inclusion of additional high-resolution information may aid in this task by further improving the problem conditioning, it is important to achieve an appropriate balance between the measured data and *a priori* assumptions, and to refrain from rendering the reconstruction method dependent upon a level of prior signal knowledge that is typically unavailable or unrealistic in common clinical settings.

We conclude this chapter by noting that the medical field has already embraced 3D printing as a promising tool, with applications in surgical planning, prosthetics, and tissue engineering, often relying upon imaging data for modeling patient-specific anatomical features (for reviews, see [250, 251]). Alternatively, we here introduce the converse, using 3D printing for validating and characterizing new imaging approaches. While the requirement for a haptic counterpart to a numerical design would somewhat undermine the flexibility afforded by strictly numerical testing – necessitating an archetypal phantom corresponding to the investigated anatomy or geometrical object type – this limitation may be counterbalanced by the steadily decreasing costs, reduced printing times, and the open-source prospects occasioned by rapid prototyping.

## Chapter 6

# Discussion and Outlook

Over the course of this PhD work, we have proposed a number of valuable tools for the advancement of magnetic resonance spectroscopic imaging. First and foremost, we developed a novel component-based high-resolution reconstruction method, which aims to surmount the inherent limitations in MRSI by prescribing an intrinsic spatio-spectral framework for the investigated object. Secondly, in order to better characterize and validate performance of the ensuing reconstructions, we introduced a flexible phantom-based testing platform, which capitalizes on recent advances in additive manufacturing. In the following sections, we recapitulate our primary contributions, identify possible extensions or potential avenues for improvement, and discuss future research directions.

### 6.1 Summary

#### **MRSI Reconstruction via Low-Rank Component Analysis**

In chapter 4, we developed a high-resolution MRSI reconstruction method, exploiting the investigated object's surmised low-dimensional inherent signal structure. This was accomplished by stipulating a bilinear form for the underlying spatio-spectral distribution, thereby enabling spatial and temporal/spectral behavior to be effectively de-coupled. Although such bilinear models have been previously proposed, our method can be characterized by a number of key differences. First, unlike existing methods, in which the model parameters in one domain (i.e., spatial or spectral) are pre-determined with the aid of additional reference scans, we jointly estimate both the spatial and spectral components, thereby circumventing the mismatch artifacts frequently afflicting reconstructions that are overly-reliant upon explicit prior knowledge. Second, despite the spatio-spectral coupling fomented by local

field inhomogeneities, signal separability is strictly enforced throughout the reconstruction procedure. The assured bilinear structure enables additional assumptions or *a priori* knowledge to be individually applied in each of the segregated domains, thereby providing justification for a wealth of sophisticated image and signal processing techniques. In the current scheme, an implicit geometrical framework is prescribed for the spatial components, stipulating that estimated spatial maps belong to a class of piecewise linear, real-valued, and non-negative functions. The former is achieved through the use of a total (generalized) variation regularization penalty, whereas the latter are compelled by various projection steps during the reconstruction process.

Though the acquired MRSI measurements are afflicted by a number of onerous experimental confounds, the proposed method implicates local static field inhomogeneities as the primary sources of signal corruption, which are consequently estimated and assimilated into the reconstruction through ancillary acquisitions. These estimated field maps play an integral role in the reconstruction procedure, both capacitating the compensation of the induced line broadening effects and spectral shifts, and serving as additional sources of explicit high-resolution information by which the problem conditioning may be improved. This latter amenity was further exploited in both chapters 4 and 5, whereby multiple field maps were acquired along the MRSI slice thickness to effectively guide the recovery of otherwise irretrievable through-plane variations. These promising results may therefore serve to extenuate the presupposed compromise underlying typical MRSI acquisition strategies, namely, that of dictating adequate spatial resolution while maintaining sufficient available signal.

### **Haptic Phantoms for MRSI**

Unlike many structural imaging modalities, where suitable gold standard measurements are available for validating new acquisition or reconstruction strategies, MRSI offers a fundamentally unique set of information that lacks a referential counterpart. This distinctiveness portends a number of challenges when considering techniques that allege to transcend prevailing methodologies, especially given the stringency required for medical applications. One prominent avenue for evaluating such methods is through the use of phantoms, whereby reconstruction results obtained from objects of known geometry serve as a proxy for *in vivo* performance. MR phantoms typically fall into one of two categories: haptic (physical) or numeric, each characterized by a number of advantages and limitations.

As physical entities, haptic phantoms generally provide more valuable insights into reconstruction performance under typical experimental condi-

tions. Nonetheless, though a multitude of haptic phantoms have been developed for assessing structural or spectral characteristics exclusively, there remains a general paucity of designs tailored for MRSI reconstruction validation, where an appreciable degree of heterogeneity is required in the two domains. Alternatively, numeric phantoms afford a greater degree of flexibility, enabling the optimization of a particular reconstruction strategy over an assortment of object classes without the various financial or material investments required for actual scanning.

In chapter 5, we endeavored to exploit the advantages afforded by both phantom types, proposing a more unified testing platform based on 3D printing. On the numerical side, the closed-form Fourier expressions made available through the use of the versatile faceted geometrical models utilized by 3D printing better represent the continuous MR encoding process, thereby leading to more realistic simulation data for both volumetric and single-slice MRSI acquisition strategies. Similarly, the reduced fabrication times and minimal costs associated with rapid prototyping facilitate phantom development for custom and/or transient applications. The resulting designs may then be readily disseminated, facilitating testing among multiple institutions and promoting reproducible research. As an archetypal proof of concept, we developed a variant of the prevalent Shepp-Logan phantom for MRSI, whereby each of the comprising compartments was filled with a solution of known spectral content. This phantom was successfully tested at 3 Tesla, and demonstrated excellent correspondence with the theoretically-predicted signal afforded through the associated numerical simulation data. These results thus underscore the most salient feature of the 3D printed phantom framework, namely, that it establishes a direct link between the numerically-obtained, and experimentally acquired MRSI measurements, which may serve to identify the most precarious elements beleaguering reconstruction quality.

## MRSI Reconstruction Results

Throughout the course of the dissertation, results obtained via the proposed reconstruction method have been presented for various experimental settings. For the 2D numerical Shepp Logan phantom and the simple two-compartment haptic phantom described in chapter 4, the estimated spatio-spectral distributions displayed superior spatial and spectral localization properties, as well as reduced noise contamination, when compared to those obtained using standard inverse DFT reconstructions. The compensatory mechanisms occasioned by the acquired static field inhomogeneity maps were also made manifest through improved lineshape profiles and abrogated spectral shifts. Furthermore, though a modest reduction in truncation artifacts were observed for the numeric data, the physical phantom recon-

structions underscored the efficacy of the total (generalized) variation regularization penalty in producing smooth solutions. In both cases, subsequent spectral analyses indicated that the proposed method promoted solutions admitting low-dimensional representations when compared against the initial estimation of the signal subspace, thereby substantiating one of the principal tenets of the reconstruction framework.

Although the results described above show promise, both experiments were performed using objects that were geometrically and spectrally homogeneous along the MRSI slice thickness. Such scenarios are typically unrealistic in clinical settings, thereby prompting the extension of the proposed method to account for through-plane variations. The preliminary *in vivo* results presented at the end of chapter 4 demonstrated that such variations may be recoverable by incorporating volumetric field map information and additional regularization along the slice direction. However, the general deficit of high-resolution reference data necessarily impedes straightforward interpretation. The behavior of the extended method was partially elucidated when considering the 3D-printed Shepp-Logan phantom reconstructions presented in chapter 5, where a number of prominent through-plane features were successfully recovered. Nevertheless, this discrimination was in some cases incomplete, and the estimated metabolite maps were partially marred by the presence of additional artifacts likely arising from localized phase perturbations or signal loss. Further investigations are therefore necessary in order to incontrovertibly identify both the sources of any such artifacts, as well as the conditions under which volumetric signal information can be reliably extricated.

## 6.2 Outlook

The methods and tools summarized above offer promising avenues for the advancement of magnetic resonance spectroscopic imaging. However, as with any burgeoning methodology, further development and experimentation is required in order to achieve any longstanding clinical impact. In this section, we highlight a number of additional considerations and possible extensions with regards to the presented work, and discuss potential future research directions.

### Model Enrichment

Ultimately, the development of non-Fourier techniques for MRSI can be classified into two primary endeavors. The first concerns the investigated object, and may be regarded as the pursuit of a suitable means for both translating prior assumptions based on qualitative observations or physical constraints

into a viable mathematical framework, and incorporating such presuppositions into the reconstruction process in an optimal and unbiased manner. In this respect, the profusion of additional high-resolution information afforded by alternative MR modalities has been far from exhausted. For example, although the proposed method intentionally refrained from exploiting explicit tissue boundary information in the preliminary *in vivo* reconstructions, there is evidence to suggest that regional concentrations of NAA, Cr, and Cho indeed vary across tissue type [236, 252, 253]. Such findings may therefore advocate the implicit integration of such tissue distributions into the reconstruction procedure via localized smoothing procedures as in [161, 254–256]. These may be further combined with prior knowledge of the spatial signal support in water-suppressed CSI, or even with the expected distribution of individual resonances in select applications where such distinctions are feasible. Nevertheless, care should be taken when introducing additional regularization penalties into the reconstruction framework, as the need to optimize over an increasing set of parameters typically diminishes clinical appeal.

The second aim concerns a robust formulation of the acquisition process itself. As with any model-based approach, reconstruction accuracy is typically circumscribed by the degree to which the measurement process is accurately represented. In its current incarnation, the proposed method has shown promise by explicitly accounting for the spatial encoding process, as well as the effects due to local static field inhomogeneities. These, however, represent only a subset of the variegated phenomena underlying real-world measurements. For example, although the use of adiabatic pulse sequences serves to minimize spatial  $\mathbf{B}_1$  variations, further improvements in reconstruction quality may be garnered through additional mapping of the rf field, for which a number of techniques have been previously developed [257–261]. Moreover, residual eddy currents due to gradient switching may give rise to additional dynamic phase perturbations that cannot be accommodated by static field mapping. Though a number of methods designed for eddy current compensation were discussed in section 3.2.3, many of these techniques rely upon external reference data – in most cases an unsuppressed water signal. While such ancillary measurements entail a negligible time commitment when considering single voxel measurements, the requirement for an unsuppressed signal corresponding to each acquired MRSI voxel significantly prolongs already lengthy acquisition durations, and are altogether impracticable for high-resolution reconstruction settings. Recourse, however, may be found through the use of field monitoring techniques [262–264], whereby the signal phase evolution is estimated by fitting a set of solid spherical harmonic basis functions to the phase time courses of an array of NMR probes [265] positioned around the sample.

## Reproducibility

One concern surrounding the proposed reconstruction method is that the joint estimation of the spatial and spectral components is a fundamentally non-convex problem. This pronouncement implies that the obtained solutions may in fact represent local minima, or that minor changes in the input conditions may have an appreciable impact on the estimated spatio-spectral distributions. Notwithstanding, the standard deviations resulting from quantitative comparisons as provided in table 4.1 support the stability of the proposed method in different noise scenarios. However, additional testing under varying experimental conditions is necessary in order to grant further assurances.

## Short Echo Time Acquisitions

For the  $^1\text{H}$  MRSI experiments presented throughout this dissertation, it should be noted that a relatively long echo time of 288 ms was chosen, generally restricting subsequent analyses to the large singlet resonances characterizing prominent metabolites. Alternatively, short TE measurements are warranted in certain applications for which spectral information from shorter  $T_2$  species is desired, which occasion additional encumbrances such as a less efficient water suppression, an increased lipid/metabolite ratio, and a more complex background spectral profile. Accordingly, commensurate compensatory mechanisms, for example, additional outer volume suppression modules, more robust water suppression techniques, or even explicit modeling of nuisance components, may be required in order to ensure accurate reconstruction quality.

## Combination with Advanced Acquisition Strategies

Although the focus of this dissertation remained on the development of advanced reconstruction methodologies, further progress in MRSI may be promoted by considering such techniques in concert with the progressive medley of innovative acquisition strategies. Indeed, current trends advocate the notion of designing novel acquisition schemes that best serve a particular reconstruction method. As an example, the virtues of the method proposed in chapter 4 were recently acknowledged in both [193] and [266], in which the presumed low intrinsic signal dimensionality served as motivation for a dual acquisition strategy. In the first step, a typical CSI sequence was employed, maintaining limited  $k$ -space coverage but high temporal resolution. The resulting measurements were then used to estimate a set of temporal basis functions by means of the SVD. A separate sequence was then used to produce a second set of measurements, this time with extended  $k$ -space

coverage but reduced temporal sampling, from which the remaining spatial bases were estimated using the LS framework along with varying degrees of regularization.

### Post-Acquisition Suppression of Nuisance Signals

In  $^1\text{H}$  applications, the metabolite signal of interest is typically overwhelmed by the dominant water and lipid resonances. While these nuisance components may be attenuated by the tailored sequence modules described in sections 3.2.1 and 3.2.2, the resulting MRSI datasets are often beleaguered by residual signals due to incomplete suppression. Moreover, while post-acquisition filtering techniques such as the HSVD have proven to be effective in removing residual water, they are less suitable for eradicating the lingering lipids, which exhibit a strong degree of spectral overlap with the desired metabolite signal. Some consolation, however, can be found in the fact that the spatial origin of the offending lipid resonances can often be directly ascertained from high resolution reference scans. A number of methods have therefore sought to exploit this knowledge, either through  $k$ -space extrapolation procedures [267], or SLIM-type methods [134, 268]. However, with most of these techniques, such knowledge is typically implemented as zero order information, i.e., simply the (binary) spatial support of the lipid-containing regions. Though perhaps sufficient in certain scenarios, such spatial homogeneity assumptions are generally inadequate for *in vivo* applications in the brain, and undermine the vast body of literature specifically devoted to the high-resolution dissociation of the water and fat resonances (e.g., [269–272]). Therefore, the development of methods seeking to exploit higher order information, for example by cultivating adaptable harmonic expansions or other efficient representations of the spatial lipid distribution, may be of considerable interest.

### The Specific Role of Field Inhomogeneities

It is clear from the presented experimental results that the acquired static field inhomogeneity maps are integral to the success of the proposed high-resolution reconstruction framework. Such observations may, however, appear as counterintuitive, as one of the generally acknowledged conditions for ensuring sufficient MRSI data quality is the adequate nullification of these very inhomogeneities through shimming. These dichotomous viewpoints pose an interesting dilemma for the proposed reconstruction framework. Looking to either extreme, it is evident that while perfect shimming (i.e.,  $\Delta f(\mathbf{x}) = 0$ ) would lead to improved spectral lineshapes and SNR, the attendant loss of discriminating spatial information content would have a detrimental impact on the spatial localization performance of the reconstruc-

tion. On the other hand, the additional reduction in phase coherence due to extremely poor shimming may precipitate inordinate signal loss. Further studies are therefore needed in order to identify an appropriate compromise, and to determine in general whether certain inhomogeneity profiles are ideally suited for the proposed reconstruction method.

# Appendix A

**Proposition 1.** *Suppose  $P$  is a solid polyhedral region comprised of simple polygonal facets whose vertices are enumerated in a counter-clockwise fashion. The Fourier transform of  $\mathbb{1}_P$  is then given by:*

$$\mathcal{F}\{\mathbb{1}_P\}(\mathbf{k}) = \begin{cases} -\frac{1}{\|2\pi\mathbf{k}\|_{\ell_2}^2} \sum_{i=1}^{|\mathcal{F}|} \frac{\mathbf{k} \cdot \hat{\mathbf{n}}^{(i)}}{\|\mathbf{k}\|_{\ell_2}^2 - |\mathbf{k} \cdot \hat{\mathbf{n}}^{(i)}|^2} \sum_{n=1}^{|\mathcal{E}^{(i)}|} (\mathbf{k} \cdot \mathbf{l}_n^{(i)}) \\ j_0\left(\pi\mathbf{k} \cdot (\mathbf{v}_{n+1}^{(i)} - \mathbf{v}_n^{(i)})\right) e^{-2\pi j\mathbf{k} \cdot \mathbf{c}_n^{(i)}}, & \mathbf{k} \neq \mathbf{0} \\ m(P), & \mathbf{k} = \mathbf{0}, \end{cases} \quad (\text{A.1})$$

where  $j_0$  is a zero-order spherical Bessel function, and  $m(P)$  denotes the Lebesgue measure (volume) of  $P$ . Similarly,  $\mathcal{F}$  is the family of polygonal facets comprising  $P$ , each with outward unit normal vector,  $\hat{\mathbf{n}}^{(i)}$ , and  $\mathcal{E}^{(i)}$  denotes the set of edges delimiting the  $i^{\text{th}}$  facet, with vertices,  $\{\mathbf{v}_n^{(i)}\}_{n=1}^{|\mathcal{E}^{(i)}|}$ , such that  $\mathbf{v}_{|\mathcal{E}^{(i)}|+n}^{(i)} = \mathbf{v}_n^{(i)}$ . Lastly,  $\mathbf{c}_n^{(i)} = (\mathbf{v}_{n+1}^{(i)} + \mathbf{v}_n^{(i)})/2$  represents the center of, and  $\mathbf{l}_n^{(i)} = (\mathbf{v}_{n+1}^{(i)} - \mathbf{v}_n^{(i)}) \times \mathbf{n}^{(i)}$  an in-plane vector normal to the  $n^{\text{th}}$  edge of the  $i^{\text{th}}$  facet.

*Proof.* We proceed by direct proof. We begin by first establishing the analytical Fourier transform of a 2D simple polygonal planar facet,  $F$ , such that,

$$\begin{aligned} \mathcal{F}\{\mathbb{1}_F\}(\mathbf{k}) &= \zeta(\mathbf{k}) = \int_{\Omega \in \mathbb{R}^2} \mathbb{1}_F(\mathbf{r}) e^{-2\pi j\mathbf{k} \cdot \mathbf{r}} d\mathbf{r} \\ &= \int_F e^{-2\pi j\mathbf{k} \cdot \mathbf{r}} d\mathbf{r}, \end{aligned} \quad (\text{A.2})$$

where  $\mathbf{k} = k_x \hat{\mathbf{i}} + k_y \hat{\mathbf{j}} + 0 \hat{\mathbf{k}}$  and  $\mathbf{r} = x \hat{\mathbf{i}} + y \hat{\mathbf{j}} + 0 \hat{\mathbf{k}}$ . Because  $F$  consists of a closed, piecewise smooth boundary,  $\partial F$ , we may make an appeal to the

divergence theorem, stating that:

$$\int_F \nabla \cdot \mathbf{F}(\mathbf{r}) \, d\mathbf{r} = \int_{\partial F} \mathbf{F}(\mathbf{r}) \cdot \hat{\mathbf{n}} \, dS, \quad (\text{A.3})$$

where  $\nabla \cdot \mathbf{F}(\mathbf{r}) = \frac{\partial F_x}{\partial x} + \frac{\partial F_y}{\partial y} + \frac{\partial F_z}{\partial z}$ , and  $\hat{\mathbf{n}}$  is the outward unit normal vector along the boundary  $\partial F$ . In this case, choosing the vector-valued function:

$$\mathbf{F}(\mathbf{r}) = \frac{j\mathbf{k}}{2\pi\|\mathbf{k}\|_{\ell_2}^2} e^{-2\pi j\mathbf{k}\cdot\mathbf{r}}, \quad \mathbf{k} \neq \mathbf{0}, \quad (\text{A.4})$$

such that,

$$\nabla \cdot \mathbf{F}(\mathbf{r}) = e^{-2\pi j\mathbf{k}\cdot\mathbf{r}} \left( \frac{k_x^2 + k_y^2}{\|\mathbf{k}\|_{\ell_2}^2} \right) = e^{-2\pi j\mathbf{k}\cdot\mathbf{r}}, \quad (\text{A.5})$$

expression (A.2) can be equivalently formulated as:

$$\begin{aligned} \zeta(\mathbf{k}) &= \int_F e^{-2\pi j\mathbf{k}\cdot\mathbf{r}} \, d\mathbf{r} \\ &= \int_F \nabla \cdot \mathbf{F}(\mathbf{r}) \, d\mathbf{r} \\ &= \frac{j}{2\pi\|\mathbf{k}\|_{\ell_2}^2} \int_{\partial F} e^{-2\pi j\mathbf{k}\cdot\mathbf{r}} (\mathbf{k} \cdot \hat{\mathbf{n}}) \, dS. \end{aligned} \quad (\text{A.6})$$

For the case  $\mathbf{k} = \mathbf{0}$ ,  $e^{-2\pi j\mathbf{0}\cdot\mathbf{r}} = 1$ , and (A.2) reduces to the well-known formula for the area of a polygon:

$$\zeta(\mathbf{0}) = m(F) = \text{Area}(F) = \frac{1}{2} \sum_{n=1}^{|\mathcal{E}|} \hat{\mathbf{n}}_F \cdot (\mathbf{v}_n \times \mathbf{v}_{n+1}), \quad (\text{A.7})$$

where  $m(F)$  denotes the Lebesgue measure of  $F$ . Similarly,  $\mathcal{E}$  denotes the set of vertices,  $\{\mathbf{v}_n\}_{n=1}^{|\mathcal{E}|}$  comprising  $F$ , enumerated in a counter-clockwise fashion such that  $\mathbf{v}_{|\mathcal{E}|+n} = \mathbf{v}_n$ , and  $\hat{\mathbf{n}}_F$  is the outward unit normal vector of the plane defined by  $F$ . When  $\mathbf{k} \neq \mathbf{0}$ , we note that  $\partial F$  consists of a series of line segments,  $E_n$ , each with unit tangent vector,  $\hat{\boldsymbol{\tau}}_n = (\mathbf{v}_{n+1} - \mathbf{v}_n)/d_n$ , where  $d_n = \|\mathbf{v}_{n+1} - \mathbf{v}_n\|_{\ell_2}$ . Then from (A.6), and noting that  $\hat{\mathbf{n}}$  is constant

along each facet:

$$\begin{aligned}
\zeta(\mathbf{k}) &= \frac{j}{2\pi\|\mathbf{k}\|_{\ell_2}^2} \sum_{n=1}^{|\mathcal{E}|} (\mathbf{k} \cdot \hat{\mathbf{n}}_n) \int_{E_n} e^{-2\pi j \mathbf{k} \cdot \mathbf{r}} dS \\
&= \frac{j}{2\pi\|\mathbf{k}\|_{\ell_2}^2} \sum_{n=1}^{|\mathcal{E}|} \left( \mathbf{k} \cdot (\hat{\boldsymbol{\tau}}_n \times \hat{\mathbf{n}}_F) \right) \int_{-d_n/2}^{d_n/2} e^{-2\pi j \mathbf{k} \cdot (\mathbf{c}_n + u \hat{\boldsymbol{\tau}}_n)} du \\
&= \frac{j}{2\pi\|\mathbf{k}\|_{\ell_2}^2} \sum_{n=1}^{|\mathcal{E}|} \left( \mathbf{k} \cdot (\hat{\boldsymbol{\tau}}_n \times \hat{\mathbf{n}}_F) \right) \frac{\sin(\pi d_n \mathbf{k} \cdot \hat{\boldsymbol{\tau}}_n)}{\pi \mathbf{k} \cdot \hat{\boldsymbol{\tau}}_n} e^{-2\pi j \mathbf{k} \cdot \mathbf{c}_n} \\
&= \frac{j}{2\pi\|\mathbf{k}\|_{\ell_2}^2} \sum_{n=1}^{|\mathcal{E}|} (\mathbf{k} \cdot \mathbf{l}_n) j_0(\pi \mathbf{k} \cdot (\mathbf{v}_{n+1} - \mathbf{v}_n)) e^{-2\pi j \mathbf{k} \cdot \mathbf{c}_n}, \quad (\text{A.8})
\end{aligned}$$

where  $j_0$  is a zero-order spherical Bessel function, and  $\mathbf{l}_n = (\mathbf{v}_{n+1} - \mathbf{v}_n) \times \hat{\mathbf{n}}_F$  and  $\mathbf{c}_n = (\mathbf{v}_{n+1} + \mathbf{v}_n)/2$  are the outer normal vector and the center of the  $n^{\text{th}}$  edge, respectively.

Now consider a simple 3D polyhedron,  $P$ , comprised of simple polygonal facets. The Fourier transform is similarly given by:

$$\begin{aligned}
\mathcal{F}\{\mathbf{1}_P\}(\mathbf{k}) &= \int_P e^{-2\pi j \mathbf{k} \cdot \mathbf{r}} d\mathbf{r} \\
&= \frac{j}{2\pi\|\mathbf{k}\|_{\ell_2}^2} \int_{\partial P} e^{-2\pi j \mathbf{k} \cdot \mathbf{r}} (\mathbf{k} \cdot \hat{\mathbf{n}}) dS, \quad (\text{A.9})
\end{aligned}$$

for  $\mathbf{k} = k_x \hat{\mathbf{i}} + k_y \hat{\mathbf{j}} + k_z \hat{\mathbf{k}}$ . For the  $\mathbf{k} = \mathbf{0}$  case,  $\mathcal{F}\{\mathbf{1}_P\}(\mathbf{0}) = m(P)$ , which is simply the volume of  $P$ . For the  $\mathbf{k} \neq \mathbf{0}$  case, we note that the boundary,  $\partial P$ , can be described by a finite union of the comprising polygonal facets, and hence (A.6) can be applied recursively using the relation given by (A.8). Letting  $\mathbf{k} - (\mathbf{k} \cdot \hat{\mathbf{n}}_F^{(i)}) \hat{\mathbf{n}}_F^{(i)}$  denote the projection of  $\mathbf{k}$  onto the plane defined by the  $i^{\text{th}}$  facet with origin  $\boldsymbol{\delta}^{(i)}$ , (A.9) can be expressed as:

$$\mathcal{F}\{\mathbf{1}_P\}(\mathbf{k}) = \frac{j}{2\pi\|\mathbf{k}\|_{\ell_2}^2} \sum_{i=1}^{|\mathcal{F}|} \left( \mathbf{k} \cdot \hat{\mathbf{n}}_F^{(i)} \right) e^{-2\pi j \mathbf{k} \cdot \boldsymbol{\delta}^{(i)}} \zeta\left(\mathbf{k} - (\mathbf{k} \cdot \hat{\mathbf{n}}_F^{(i)}) \hat{\mathbf{n}}_F^{(i)}\right), \quad (\text{A.10})$$

which is equivalent to (A.1) once expanded.  $\square$

**Proposition 2.** *Suppose  $P$  is a solid polyhedral region comprised of simple polygonal facets whose vertices are enumerated in a counter-clockwise fashion, and  $S$  is a rectangular MR slice profile. The Fourier transform of the*

2D projection of  $\mathbf{1}_P|_S = \mathbf{1}_R$ , onto the slice profile is then given by:

$$\mathcal{F}\{\mathbf{1}_R\}(\boldsymbol{\kappa}) = \begin{cases} -\frac{1}{\|2\pi\boldsymbol{\kappa}\|^2} \sum_{i=1}^{|\mathcal{F}_R|} \mathbf{a}^{(i)} \cdot \sum_{n=1}^{|\mathcal{E}^{(i)}|} e^{-2\pi j \boldsymbol{\kappa} \cdot \mathbf{d}_n^{(i)}} \left[ \left( \mathbf{m}_n^{(i)} - \left( \frac{2\boldsymbol{\kappa}}{\|\boldsymbol{\kappa}\|_{\ell_2}^2} + 2\pi j \left( \mathbf{d}_n^{(i)} - \mathbf{p}_{i,0} \right) \right) \left( \boldsymbol{\kappa} \cdot \mathbf{m}_n^{(i)} \right) \right) j_0 \left( \pi \boldsymbol{\kappa} \cdot \left( \mathbf{q}_{n+1}^{(i)} - \mathbf{q}_n^{(i)} \right) \right) - \pi \left( \boldsymbol{\kappa} \cdot \mathbf{m}_n^{(i)} \right) \left( \mathbf{q}_{n+1}^{(i)} - \mathbf{q}_n^{(i)} \right) j_1 \left( \pi \boldsymbol{\kappa} \cdot \left( \mathbf{q}_{n+1}^{(i)} - \mathbf{q}_n^{(i)} \right) \right) \right], & \boldsymbol{\kappa} \neq \mathbf{0} \\ \frac{1}{2} \sum_{i=1}^{|\mathcal{F}_R|} \mathbf{a}^{(i)} \cdot \left( \bar{\mathbf{p}}_{uv}^{(i)} - \mathbf{p}_0^{(i)} \right) \sum_{n=1}^{|\mathcal{E}^{(i)}|} \left( \hat{\mathbf{e}}_w \cdot \left( \mathbf{q}_n^{(i)} \times \mathbf{q}_{n+1}^{(i)} \right) \right), & \boldsymbol{\kappa} = \mathbf{0}, \end{cases} \quad (\text{A.11})$$

where  $\boldsymbol{\kappa} = \kappa_u \hat{\mathbf{e}}_u + \kappa_v \hat{\mathbf{e}}_v + 0 \hat{\mathbf{e}}_w$ . Similarly,  $\{\mathbf{q}_n^{(i)}\}_{n=1}^{|\mathcal{E}^{(i)}|}$  denotes the set of comprising vertices, and  $\bar{\mathbf{p}}_{uv}^{(i)}$  the barycenter of the  $i^{\text{th}}$  facet, orthogonally projected onto the slice ( $uv$ ) plane. Finally,  $\mathbf{m}_n^{(i)} = (\mathbf{q}_{n+1}^{(i)} - \mathbf{q}_n^{(i)}) \times \hat{\mathbf{e}}_w$  represents an outer normal vector to the  $n^{\text{th}}$  edge of the  $i^{\text{th}}$  projected facet, and  $\mathbf{d}_n^{(i)} = (\mathbf{q}_{n+1}^{(i)} + \mathbf{q}_n^{(i)})/2$ .

*Proof.* We begin by examining vector-valued expressions of the form:

$$\boldsymbol{\Lambda}(\mathbf{k}) = \int_{\Omega \in \mathbb{R}^2} (\mathbf{r} - \mathbf{r}_0) \mathbf{1}_F(\mathbf{r}) e^{-2\pi j \mathbf{k} \cdot \mathbf{r}} d\mathbf{r} = \int_F (\mathbf{r} - \mathbf{r}_0) e^{-2\pi j \mathbf{k} \cdot \mathbf{r}} d\mathbf{r}, \quad (\text{A.12})$$

where  $F$  is a simple polygonal region as described above,  $\mathbf{k} = k_x \hat{\mathbf{i}} + k_y \hat{\mathbf{j}} + 0 \hat{\mathbf{k}}$ , and  $\mathbf{r}_0$  is an arbitrary point in the plane defined by  $F$ . For the case  $\mathbf{k} = \mathbf{0}$ ,

$$\boldsymbol{\Lambda}(\mathbf{0}) = \int_F \mathbf{r} d\mathbf{r} - \mathbf{r}_0 \int_F d\mathbf{r}. \quad (\text{A.13})$$

The first integral expression in (A.13) is simply  $m(F)\bar{\mathbf{r}}$ , where  $\bar{\mathbf{r}}$  is the barycenter of  $F$ ; the second is  $m(F)\mathbf{r}_0$ . Thus,

$$\begin{aligned} \boldsymbol{\Lambda}(\mathbf{0}) &= (\bar{\mathbf{r}} - \mathbf{r}_0) m(F) \\ &= \frac{1}{2} (\bar{\mathbf{r}} - \mathbf{r}_0) \sum_{n=1}^{|\mathcal{E}|} \hat{\mathbf{n}}_F \cdot (\mathbf{v}_n \times \mathbf{v}_{n+1}). \end{aligned} \quad (\text{A.14})$$

When considering the case  $\mathbf{k} \neq \mathbf{0}$ , we note that (A.12) can also be expressed as:

$$\boldsymbol{\Lambda}(\mathbf{k}) = \frac{j}{2\pi} \nabla_{\mathbf{k}} \zeta(\mathbf{k}) - \mathbf{r}_0 \zeta(\mathbf{k}), \quad (\text{A.15})$$

where  $\zeta(\mathbf{k})$  is given by (A.8) and,

$$\nabla_{\mathbf{k}} \triangleq \frac{\partial}{\partial k_x} \hat{\mathbf{i}} + \frac{\partial}{\partial k_y} \hat{\mathbf{j}} + \frac{\partial}{\partial k_z} \hat{\mathbf{k}}. \quad (\text{A.16})$$

Here,

$$\begin{aligned} \nabla_{\mathbf{k}} \zeta(\mathbf{k}) &= \frac{j}{2\pi} \sum_{n=1}^{|\mathcal{E}|} \nabla_{\mathbf{k}} \left[ \frac{(\mathbf{k} \cdot \mathbf{l}_n)}{\|\mathbf{k}\|_{\ell_2}^2} j_0 \left( \pi \mathbf{k} \cdot (\mathbf{v}_{n+1} - \mathbf{v}_n) \right) e^{-2\pi j \mathbf{k} \cdot \mathbf{c}_n} \right] \\ &= \frac{j}{2\pi} \sum_{n=1}^{|\mathcal{E}|} \left[ \left( \frac{\mathbf{l}_n}{\|\mathbf{k}\|_{\ell_2}^2} - \frac{2(\mathbf{k} \cdot \mathbf{l}_n)}{\|\mathbf{k}\|_{\ell_2}^4} - 2\pi j \frac{\mathbf{c}_n (\mathbf{k} \cdot \mathbf{l}_n)}{\|\mathbf{k}\|_{\ell_2}^2} \right) \right. \\ &\quad \cdot j_0 \left( \pi \mathbf{k} \cdot (\mathbf{v}_{n+1} - \mathbf{v}_n) \right) e^{-2\pi j \mathbf{k} \cdot \mathbf{c}_n} \\ &\quad \left. - \frac{\pi (\mathbf{k} \cdot \mathbf{l}_n)}{\|\mathbf{k}\|_{\ell_2}^2} (\mathbf{v}_{n+1} - \mathbf{v}_n) j_1 \left( \pi \mathbf{k} \cdot (\mathbf{v}_{n+1} - \mathbf{v}_n) \right) e^{-2\pi j \mathbf{k} \cdot \mathbf{c}_n} \right] \\ &= \frac{j}{2\pi \|\mathbf{k}\|_{\ell_2}^2} \sum_{n=1}^{|\mathcal{E}|} e^{-2\pi j \mathbf{k} \cdot \mathbf{c}_n} \left[ \left( \mathbf{l}_n - \left( \frac{2\mathbf{k}}{\|\mathbf{k}\|_{\ell_2}^2} + 2\pi j \mathbf{c}_n \right) (\mathbf{k} \cdot \mathbf{l}_n) \right) \right. \\ &\quad \cdot j_0 \left( \pi \mathbf{k} \cdot (\mathbf{v}_{n+1} - \mathbf{v}_n) \right) \\ &\quad \left. - \pi (\mathbf{k} \cdot \mathbf{l}_n) (\mathbf{v}_{n+1} - \mathbf{v}_n) j_1 \left( \pi \mathbf{k} \cdot (\mathbf{v}_{n+1} - \mathbf{v}_n) \right) \right]. \quad (\text{A.17}) \end{aligned}$$

Expression (A.15) can therefore be expanded as:

$$\begin{aligned} \mathbf{\Lambda}(\mathbf{k}) &= -\frac{1}{\|2\pi \mathbf{k}\|_{\ell_2}^2} \sum_{n=1}^{|\mathcal{E}|} e^{-2\pi j \mathbf{k} \cdot \mathbf{c}_n} \left[ \left( \mathbf{l}_n - \left( \frac{2\mathbf{k}}{\|\mathbf{k}\|_{\ell_2}^2} + 2\pi j (\mathbf{c}_n - \mathbf{r}_0) \right) (\mathbf{k} \cdot \mathbf{l}_n) \right) \right. \\ &\quad \cdot j_0 \left( \pi \mathbf{k} \cdot (\mathbf{v}_{n+1} - \mathbf{v}_n) \right) \\ &\quad \left. - \pi (\mathbf{k} \cdot \mathbf{l}_n) (\mathbf{v}_{n+1} - \mathbf{v}_n) j_1 \left( \pi \mathbf{k} \cdot (\mathbf{v}_{n+1} - \mathbf{v}_n) \right) \right]. \quad (\text{A.18}) \end{aligned}$$

To establish a link with (A.11), we note that the Fourier transform of a linearly-varying scalar-valued function,  $g(\mathbf{r}) = \mathbf{a} \cdot (\mathbf{r} - \mathbf{r}_0) \mathbf{1}_F(\mathbf{r})$  is given by:

$$\begin{aligned} \mathcal{F}\{g\}(\mathbf{k}) &= \mathbf{a} \cdot \int_F (\mathbf{r} - \mathbf{r}_0) e^{-2\pi j \mathbf{k} \cdot \mathbf{r}} d\mathbf{r} \\ &= \mathbf{a} \cdot \mathbf{\Lambda}(\mathbf{k}). \quad (\text{A.19}) \end{aligned}$$

For the case of a polyhedral region  $P$  and MRSI slice profile  $S$ , the projection of  $P \cap S$  onto the slice profile can be expressed as a sum of such functions,

$f(\mathbf{r}) = \sum_{i=1}^{|\mathcal{F}|} g^{(i)}(\mathbf{r}) = \sum_{i=1}^{|\mathcal{F}|} \mathbf{a}^{(i)} \cdot (\mathbf{r} - \mathbf{r}_0^{(i)}) \mathbb{1}_{F^{(i)}}(\mathbf{r})$ , each with support  $F^{(i)} \in \mathcal{F}$ , with  $F^{(i)} \cap F^{(j)} = \emptyset$  for all  $i, j$ . Thus,

$$\begin{aligned}
 \mathcal{F}\{f\}(\mathbf{k}) &= \sum_{i=1}^{|\mathcal{F}|} \int_{\Omega \in \mathbb{R}^2} g^{(i)} e^{-2\pi j \mathbf{k} \cdot \mathbf{r}} d\mathbf{r} \\
 &= \sum_{i=1}^{|\mathcal{F}|} \int_{F^{(i)} \in \mathcal{F}} \mathbf{a}^{(i)} \cdot (\mathbf{r} - \mathbf{r}_0^{(i)}) e^{-2\pi j \mathbf{k} \cdot \mathbf{r}} d\mathbf{r} \\
 &= \sum_{i=1}^{|\mathcal{F}|} \mathbf{a}^{(i)} \cdot \Lambda^{(i)}(\mathbf{k}).
 \end{aligned} \tag{A.20}$$

□

# Bibliography

- [1] S. J. Nelson, “Multivoxel Magnetic Resonance Spectroscopy of Brain Tumors,” *Mol. Cancer Ther.*, vol. 2, no. 5, pp. 497–507, May 2003.
- [2] A. Horská and P. B. Barker, “Imaging of Brain Tumors: MR Spectroscopy and Metabolic Imaging,” *Neuroimaging Clin. N. Am.*, vol. 20, no. 3, pp. 293–310, Aug 2010.
- [3] A. M. Omuro, C. C. Leite, K. Mokhtari, and J.-Y. Delattre, “Pitfalls in the Diagnosis of Brain Tumours,” *The Lancet Neurology*, vol. 5, no. 11, pp. 937–948, 2006.
- [4] R. Hourani, L. J. Brant, T. Rizk, J. D. Weingart, P. B. Barker, and A. Horska, “Can Proton MR Spectroscopic and Perfusion Imaging Differentiate Between Neoplastic and Nonneoplastic Brain Lesions in Adults?” *AJNR Am J Neuroradiol*, vol. 29, no. 2, pp. 366–372, Feb 2008.
- [5] G. S. Payne and M. O. Leach, “Applications of Magnetic Resonance Spectroscopy in Radiotherapy Treatment Planning,” *Br J Radiol*, vol. 79 Spec No 1, pp. 16–26, Sep 2006.
- [6] F. Earnest, P. J. Kelly, B. W. Scheithauer, B. A. Kall, T. L. Cascino, R. L. Ehman, G. S. Forbes, and P. L. Axley, “Cerebral Astrocytomas: Histopathologic Correlation of MR and CT Contrast Enhancement with Stereotactic Biopsy,” *Radiology*, vol. 166, no. 3, pp. 823–827, Mar 1988.
- [7] D. Kondziolka, L. D. Lunsford, and A. J. Martinez, “Unreliability of Contemporary Neurodiagnostic Imaging in Evaluating Suspected Adult Supratentorial (Low-Grade) Astrocytomas,” *J. Neurosurg.*, vol. 79, no. 4, pp. 533–536, Oct 1993.
- [8] A. J. Martin, H. Liu, W. A. Hall, and C. L. Truwit, “Preliminary Assessment of Turbo Spectroscopic Imaging for Targeting in Brain Biopsy,” *AJNR Am J Neuroradiol*, vol. 22, no. 5, pp. 959–968, May 2001.

- [9] A. Stadlbauer, S. Gruber, C. Nimsy, R. Fahlbusch, T. Hammen, R. Buslei, B. Tomandl, E. Moser, and O. Ganslandt, "Preoperative Grading of Gliomas by Using Metabolite Quantification with High-Spatial-Resolution Proton MR Spectroscopic Imaging," *Radiology*, vol. 238, no. 3, pp. 958–969, Mar 2006.
- [10] M. C. Preul, Z. Caramanos, D. L. Collins, J. G. Villemure, R. Leblanc, A. Olivier, R. Pokrupa, and D. L. Arnold, "Accurate, Noninvasive Diagnosis of Human Brain Tumors by Using Proton Magnetic Resonance Spectroscopy," *Nat. Med.*, vol. 2, no. 3, pp. 323–325, Mar 1996.
- [11] A. R. Tate, C. Majós, A. Moreno, F. A. Howe, J. R. Griffiths, and C. Arús, "Automated Classification of Short Echo Time in In Vivo  $^1\text{H}$  Brain Tumor Spectra: A Multicenter Study," *Magnetic Resonance in Medicine*, vol. 49, no. 1, pp. 29–36, 2003.
- [12] A. Di Costanzo *et al.*, "Multiparametric 3T MR Approach to the Assessment of Cerebral Gliomas: Tumor Extent and Malignancy," *Neuroradiology*, vol. 48, no. 9, pp. 622–631, Sep 2006.
- [13] A. Stadlbauer, E. Moser, S. Gruber, R. Buslei, C. Nimsy, R. Fahlbusch, and O. Ganslandt, "Improved Delineation of Brain Tumors: an Automated Method for Segmentation Based on Pathologic Changes of  $^1\text{H}$ -MRSI Metabolites in Gliomas," *NeuroImage*, vol. 23, no. 2, pp. 454–461, 2004.
- [14] A. Pirzkall, T. R. McKnight, E. E. Graves, M. P. Carol, P. K. Sneed, W. W. Wara, S. J. Nelson, L. J. Verhey, and D. A. Larson, "MR-Spectroscopy Guided Target Delineation for High-grade Gliomas," *International Journal of Radiation Oncology\*Biophysics\*Physics*, vol. 50, no. 4, pp. 915–928, 2001.
- [15] O. Ganslandt, A. Stadlbauer, R. Fahlbusch, K. Kamada, R. Buslei, I. Blumcke, E. Moser, and C. Nimsy, "Proton Magnetic Resonance Spectroscopic Imaging Integrated into Image-Guided Surgery: Correlation to Standard Magnetic Resonance Imaging and Tumor Cell Density," *Neurosurgery*, vol. 56, no. 2 Suppl, pp. 291–298, Apr 2005.
- [16] T. R. McKnight, M. H. von dem Bussche, D. B. Vigneron, Y. Lu, M. S. Berger, M. W. McDermott, W. P. Dillon, E. E. Graves, A. Pirzkall, and S. J. Nelson, "Histopathological Validation of a Three-Dimensional Magnetic Resonance Spectroscopy Index as a Predictor of Tumor Presence," *J. Neurosurg.*, vol. 97, no. 4, pp. 794–802, Oct 2002.
- [17] A. A. Chan, A. Lau, A. Pirzkall, S. M. Chang, L. J. Verhey, D. Larson, M. W. McDermott, W. P. Dillon, and S. J. Nelson, "Proton Magnetic

- Resonance Spectroscopy Imaging in the Evaluation of Patients Undergoing Gamma Knife Surgery for Grade IV Gliomas,” *J. Neurosurg.*, vol. 101, no. 3, pp. 467–475, Sep 2004.
- [18] E. E. Graves *et al.*, “A Preliminary Study of the Prognostic Value of Proton Magnetic Resonance Spectroscopic Imaging in Gamma Knife Radiosurgery of Recurrent Malignant Gliomas,” *Neurosurgery*, vol. 46, no. 2, pp. 319–326, Feb 2000.
- [19] E. E. Graves, S. J. Nelson, D. B. Vigneron, L. Verhey, M. McDermott, D. Larson, S. Chang, M. D. Prados, and W. P. Dillon, “Serial Proton MR Spectroscopic Imaging of Recurrent Malignant Gliomas after Gamma Knife Radiosurgery,” *AJNR Am J Neuroradiol*, vol. 22, no. 4, pp. 613–624, Apr 2001.
- [20] M. A. Jacobs, P. B. Barker, P. A. Bottomley, Z. Bhujwala, and D. A. Bluemke, “Proton Magnetic Resonance Spectroscopic Imaging of Human Breast Cancer: A Preliminary Study,” *Journal of Magnetic Resonance Imaging*, vol. 19, no. 1, pp. 68–75, 2004.
- [21] J. Scheidler, H. Hricak, D. B. Vigneron, K. K. Yu, D. L. Sokolov, L. R. Huang, C. J. Zaloudek, S. J. Nelson, P. R. Carroll, and J. Kurhanewicz, “Prostate Cancer: Localization with Three-Dimensional Proton MR Spectroscopic Imaging—Clinicopathologic Study,” *Radiology*, vol. 213, no. 2, pp. 473–480, 1999.
- [22] J. Kurhanewicz, M. G. Swanson, S. J. Nelson, and D. B. Vigneron, “Combined Magnetic Resonance Imaging and Spectroscopic Imaging Approach to Molecular Imaging of Prostate Cancer,” *Journal of Magnetic Resonance Imaging*, vol. 16, no. 4, pp. 451–463, 2002.
- [23] J. J. Fütterer *et al.*, “Prostate Cancer Localization with Dynamic Contrast-enhanced MR Imaging and Proton MR Spectroscopic Imaging,” *Radiology*, vol. 241, no. 2, pp. 449–458, 2006.
- [24] M. J. Albers *et al.*, “Hyperpolarized  $^{13}\text{C}$  Lactate, Pyruvate, and Alanine: Noninvasive Biomarkers for Prostate Cancer Detection and Grading,” *Cancer Research*, vol. 68, no. 20, pp. 8607–8615, 2008.
- [25] T. Kobus, T. Hambrock, C. A. H. van de Kaa, A. J. Wright, J. O. Barentsz, A. Heerschap, and T. W. Scheenen, “In Vivo Assessment of Prostate Cancer Aggressiveness Using Magnetic Resonance Spectroscopic Imaging at 3 T with an Endorectal Coil,” *European Urology*, vol. 60, no. 5, pp. 1074–1080, 2011.
- [26] T. Fujimoto, T. Nakano, T. Takano, Y. Hokazono, T. Asakura, and T. Tsuji, “Study of Chronic Schizophrenics Using  $^{31}\text{P}$  Magnetic

- Resonance Chemical Shift Imaging,” *Acta Psychiatrica Scandinavica*, vol. 86, no. 6, pp. 455–462, 1992.
- [27] S. R. Dager, N. M. Corrigan, T. L. Richards, and S. Posse, “Research Applications of Magnetic Resonance Spectroscopy to Investigate Psychiatric Disorders,” *Top Magn Reson Imaging*, vol. 19, no. 2, pp. 81–96, Apr 2008.
- [28] E. Adalsteinsson, E. Sullivan, N. Kleinhans, D. Spielman, and A. Pfefferbaum, “Longitudinal Decline of the Neuronal Marker N-Acetyl Aspartate in Alzheimer’s Disease,” *The Lancet*, vol. 355, no. 9216, pp. 1696–1697, 2000.
- [29] R. Sharma, P. A. Narayana, and J. S. Wolinsky, “Grey Matter Abnormalities in Multiple Sclerosis: Proton Magnetic Resonance Spectroscopic Imaging,” *Multiple Sclerosis*, vol. 7, no. 4, pp. 221–226, 2001.
- [30] J. Suhy, R. G. Miller, R. Rule, N. Schuff, J. Licht, V. Dronsky, D. Gelinas, A. A. Maudsley, and M. W. Weiner, “Early Detection and Longitudinal Changes in Amyotrophic Lateral Sclerosis by  $^1\text{H}$  MRSI,” *Neurology*, vol. 58, no. 5, pp. 773–779, Mar 2002.
- [31] L. M. Li, F. Cendes, S. B. Antel, F. Andermann, W. Serles, F. Dubeau, A. Olivier, and D. L. Arnold, “Prognostic Value of Proton Magnetic Resonance Spectroscopic Imaging for Surgical Outcome in Patients with Intractable Temporal Lobe Epilepsy and Bilateral Hippocampal Atrophy,” *Annals of Neurology*, vol. 47, no. 2, pp. 195–200, 2000.
- [32] S. B. Antel, L. M. Li, F. Cendes, D. L. Collins, R. E. Kearney, R. Shinghal, and D. L. Arnold, “Predicting Surgical Outcome in Temporal Lobe Epilepsy Patients Using MRI and MRSI,” *Neurology*, vol. 58, no. 10, pp. 1505–1512, May 2002.
- [33] J. W. Pan, D. D. Spencer, R. Kuzniecky, R. B. Duckrow, H. Hetherington, and S. S. Spencer, “Metabolic Networks in Epilepsy by MR Spectroscopic Imaging,” *Acta Neurologica Scandinavica*, vol. 126, no. 6, pp. 411–420, 2012.
- [34] J. W. Pan *et al.*, “7T MR Spectroscopic Imaging in the Localization of Surgical Epilepsy,” *Epilepsia*, vol. 54, no. 9, pp. 1668–1678, 2013.
- [35] G. E. Uhlenbeck and S. Goudsmit, “Ersetzung der Hypothese vom unmechanischen Zwang durch eine Forderung bezüglich des inneren Verhaltens jedes einzelnen Elektrons,” *Die Naturwissenschaften*, vol. 13, no. 47, pp. 953–954, 1925.

- [36] W. Pauli, "Über den Zusammenhang des Abschlusses der Elektronengruppen im Atom mit der Komplexstruktur der Spektren," *Zeitschrift für Physik*, vol. 31, no. 1, pp. 765–783, 1925.
- [37] P. A. M. Dirac, "The Quantum Theory of the Electron," *Proceedings of the Royal Society of London. Series A*, vol. 117, no. 778, pp. 610–624, 1928.
- [38] W. Pauli, "The Connection Between Spin and Statistics," *Phys. Rev.*, vol. 58, pp. 716–722, 1940.
- [39] W. Gerlach and O. Stern, "Das magnetische Moment des Silberatoms," *Zeitschrift für Physik*, vol. 9, pp. 353–255, 1922.
- [40] I. I. Rabi, S. Millman, P. Kusch, and J. R. Zacharias, "The Molecular Beam Resonance Method for Measuring Nuclear Magnetic Moments The Magnetic Moments of  ${}^3\text{Li}^6$ ,  ${}^3\text{Li}^7$  and  ${}^9\text{F}^{19}$ ," *Physical Review*, vol. 55, pp. 526–535, Mar 1939.
- [41] F. Bloch, W. W. Hansen, and M. Packard, "Nuclear Induction," *Phys. Rev.*, vol. 69, p. 127, Feb 1946.
- [42] E. M. Purcell, H. C. Torrey, and R. V. Pound, "Resonance Absorption by Nuclear Magnetic Moments in a Solid," *Phys. Rev.*, vol. 69, pp. 37–38, Jan 1946.
- [43] M. Bernstein, K. King, and X. Zhou, *Handbook of MRI Pulse Sequences*, M. Bernstein, K. King, and X. Zhou, Eds. Elsevier Academic Press, 2004.
- [44] D. R. Lide, Ed., *CRC Handbook of Chemistry and Physics*, 78th ed. CRC Press, Jun 1997.
- [45] R. R. Ernst and W. A. Anderson, "Application of Fourier Transform Spectroscopy to Magnetic Resonance," *Review of Scientific Instruments*, vol. 37, no. 1, pp. 93–102, 1966.
- [46] F. Bloch, "Nuclear Induction," *Phys. Rev.*, vol. 70, pp. 460–474, Oct 1946.
- [47] W. G. Proctor and F. C. Yu, "The Dependence of a Nuclear Magnetic Resonance Frequency upon Chemical Compound," *Phys. Rev.*, vol. 77, pp. 717–717, Mar 1950.
- [48] W. C. Dickinson, "Dependence of the  $\text{F}^{19}$  Nuclear Resonance Position on Chemical Compound," *Phys. Rev.*, vol. 77, pp. 736–737, Mar 1950.
- [49] R. Damadian, "Tumor Detection by Nuclear Magnetic Resonance," *Science*, vol. 171, no. 3976, pp. 1151–1153, 1971.

- [50] P. Mansfield and P. K. Grannell, "NMR 'Diffraction' in Solids?" *Journal of Physics C: Solid State Physics*, vol. 6, no. 22, p. L422, 1973.
- [51] P. C. Lauterbur, "Image Formation by Induced Local Interactions: Examples Employing Nuclear Magnetic Resonance," *Nature*, vol. 242, no. 5394, pp. 190–191, Mar 1973.
- [52] H. Carr, "Free Precession Techniques in Nuclear Magnetic Resonance," Ph.D. dissertation, Harvard University, 1952.
- [53] P. Lauterbur, "Magnetic Resonance Zeugmatography," *Pure and Applied Chemistry*, vol. 40, no. 1-2, pp. 149–157, 1974.
- [54] R. Damadian, M. Goldsmith, and L. Minkoff, "NMR in Cancer: XVI. FONAR Image of the Live Human Body," *Physiol. Chem. Phys.*, vol. 9, no. 1, pp. 97–100, 1977.
- [55] J. Granot, "Selected Volume Excitation Using Stimulated Echoes (VEST). Applications to Spatially Localized Spectroscopy and Imaging," *Journal of Magnetic Resonance (1969)*, vol. 70, no. 3, pp. 488–492, 1986.
- [56] J. Frahm, K.-D. Merboldt, and W. HŁnicke, "Localized Proton Spectroscopy Using Stimulated Echoes," *Journal of Magnetic Resonance (1969)*, vol. 72, no. 3, pp. 502–508, 1987.
- [57] R. Kimmich and D. Hoepfel, "Volume-Selective Multipulse Spin-Echo Spectroscopy," *Journal of Magnetic Resonance (1969)*, vol. 72, no. 2, pp. 379–384, 1987.
- [58] P. A. Bottomley, "Selective Volume Method for Performing Localized NMR Spectroscopy," US Patent, October 1984. [Online]. Available: <http://www.freepatentsonline.com/4480228.html>
- [59] P. A. Bottomley, "Spatial Localization in NMR Spectroscopy in vivo," *Annals of the New York Academy of Sciences*, vol. 508, no. 1, pp. 333–348, 1987.
- [60] W.-I. Jung, "Localized Double Spin Echo Proton Spectroscopy Part I: Basic Concepts," *Concepts in Magnetic Resonance*, vol. 8, no. 1, pp. 1–15, 1996.
- [61] W.-I. Jung, "Localized Double Spin Echo Proton Spectroscopy Part II: Weakly Coupled Homonuclear Spin Systems," *Concepts in Magnetic Resonance*, vol. 8, no. 2, pp. 105–118, 1996.

- [62] T. R. Brown, B. M. Kincaid, and K. Ugurbil, "NMR Chemical Shift Imaging in Three Dimensions." *Proceedings of the National Academy of Sciences of the United States of America*, vol. 79, no. 11, pp. 3523–3526, 1982.
- [63] A. Maudsley, S. Hilal, W. Perman, and H. Simon, "Spatially Resolved High Resolution Spectroscopy by "Four-Dimensional" NMR," *Journal of Magnetic Resonance (1969)*, vol. 51, no. 1, pp. 147–152, 1983.
- [64] E. Adalsteinsson, P. Irarrazabal, S. Topp, C. Meyer, A. Macovski, and D. M. Spielman, "Volumetric Spectroscopic Imaging with Spiral-Based k-space Trajectories," *Magn Reson Med*, vol. 39, no. 6, pp. 889–898, Jun 1998.
- [65] S. Sarkar, K. Heberlein, and X. Hu, "Truncation Artifact Reduction in Spectroscopic Imaging Using a Dual-Density Spiral k-Space Trajectory," *Magnetic Resonance Imaging*, vol. 20, no. 10, pp. 743–757, 2002.
- [66] D.-H. Kim, R. Henry, and D. M. Spielman, "Fast Multivoxel Two-Dimensional Spectroscopic Imaging at 3 T," *Magnetic Resonance Imaging*, vol. 25, no. 8, pp. 1155–1161, 2007.
- [67] W. Dreher, C. Geppert, M. Althaus, and D. Leibfritz, "Fast Proton Spectroscopic Imaging Using Steady-State Free Precession Methods," *Magnetic Resonance in Medicine*, vol. 50, no. 3, pp. 453–460, 2003.
- [68] P. Mansfield, "Spatial Mapping of the Chemical Shift in NMR," *Magnetic Resonance in Medicine*, vol. 1, no. 3, pp. 370–386, 1984.
- [69] S. Posse, C. DeCarli, and D. Le Bihan, "Three-Dimensional Echo-Planar MR Spectroscopic Imaging at Short Echo Times in the Human Brain," *Radiology*, vol. 192, no. 3, pp. 733–738, Sep 1994.
- [70] S. Posse, G. Tedeschi, R. Risinger, R. Ogg, and D. Le Bihan, "High Speed 1H Spectroscopic Imaging in Human Brain by Echo Planar Spatial-Spectral Encoding," *Magn Reson Med*, vol. 33, no. 1, pp. 34–40, Jan 1995.
- [71] D. N. Guilfoyle, A. Blamire, B. Chapman, R. J. Ordine, and P. Mansfield, "PEEP - A Rapid Chemical-Shift Imaging Method," *Magnetic Resonance in Medicine*, vol. 10, no. 2, pp. 282–287, 1989.
- [72] C. V. Schirda, C. Tanase, and F. E. Boada, "Rosette Spectroscopic Imaging: Optimal Parameters for Alias-Free, High Sensitivity Spectroscopic Imaging," *Journal of Magnetic Resonance Imaging*, vol. 29, no. 6, pp. 1375–1385, 2009.

- [73] S. Uribe, A. Guesalaga, R. Mir, M. Guarini, and P. Irarrázaval, "A 3D Trajectory for Undersampling k-space in MRSI Applications," *Magnetic Resonance Imaging*, vol. 25, no. 3, pp. 350–358, 2007.
- [74] U. Dydak, M. Weiger, K. P. Pruessmann, D. Meier, and P. Boesiger, "Sensitivity-encoded spectroscopic imaging," *Magnetic Resonance in Medicine*, vol. 46, no. 4, pp. 713–722, 2001.
- [75] F.-H. Lin, S.-Y. Tsai, R. Otazo, A. Caprihan, L. L. Wald, J. W. Belliveau, and S. Posse, "Sensitivity-Encoded (SENSE) Proton Echo-Planar Spectroscopic Imaging (PEPSI) in the Human Brain," *Magnetic Resonance in Medicine*, vol. 57, no. 2, pp. 249–257, 2007.
- [76] R. Otazo, S.-Y. Tsai, F.-H. Lin, and S. Posse, "Accelerated Short-TE 3D Proton Echo-Planar Spectroscopic Imaging Using 2D-SENSE with a 32-Channel Array Coil," *Magnetic Resonance in Medicine*, vol. 58, no. 6, pp. 1107–1116, 2007.
- [77] R. Pohmann, M. von Kienlin, and A. Haase, "Theoretical Evaluation and Comparison of Fast Chemical Shift Imaging Methods," *Journal of Magnetic Resonance*, vol. 129, no. 2, pp. 145–160, 1997.
- [78] R. A. De Graaf, *In Vivo NMR Spectroscopy: Principles and Techniques*, 2nd ed. The Atrium, Southern Gate, Chichester, West Sussex P019 8SQ, England: John Wiley & Sons, 2007.
- [79] V. Govindaraju, K. Young, and A. A. Maudsley, "Proton NMR Chemical Shifts and Coupling Constants for Brain Metabolites," *NMR in Biomedicine*, vol. 13, no. 3, pp. 129–153, 2000.
- [80] T. L. Perry, K. Berry, S. Hansen, S. Diamond, and C. Mok, "Regional Distribution of Amino Acids in Human Brain Obtained at Autopsy," *Journal of Neurochemistry*, vol. 18, no. 3, pp. 513–519, 1971.
- [81] A. Maudsley, "Sensitivity in Fourier Imaging," *Journal of Magnetic Resonance (1969)*, vol. 68, no. 2, pp. 363–366, 1986.
- [82] R. Pohmann, E. Rommel, and M. von Kienlin, "Beyond k-Space: Spectral Localization Using Higher Order Gradients," *Journal of Magnetic Resonance*, vol. 141, no. 2, pp. 197–206, 1999.
- [83] A. Greiser and M. von Kienlin, "Efficient k-Space Sampling by Density-Weighted Phase-Encoding," *Magnetic Resonance in Medicine*, vol. 50, no. 6, pp. 1266–1275, 2003.
- [84] V. S. Sklenář and Z. Starčuk, "1-2-1 Pulse Train: A New Effective Method of Selective Excitation for Proton NMR in Water," *Journal of Magnetic Resonance (1969)*, vol. 50, no. 3, pp. 495–501, 1982.

- [85] P. Plateau and M. Gueron, "Exchangeable Proton NMR Without Base-Line Distorsion, Using New Strong-Pulse Sequences," *Journal of the American Chemical Society*, vol. 104, no. 25, pp. 7310–7311, 1982.
- [86] H. Bleich and J. Wilde, "Solvent Resonance Suppression Using a Sequence of Strong Pulses," *Journal of Magnetic Resonance (1969)*, vol. 56, no. 1, pp. 154–155, 1984.
- [87] Z. Starčuk and V. S. Sklenář, "New Hard Pulse Sequences for the Solvent Signal Suppression in Fourier-Transform NMR. I," *Journal of Magnetic Resonance (1969)*, vol. 61, no. 3, pp. 567–570, 1985.
- [88] Z. Starčuk and V. S. Sklenář, "New Hard Pulse Sequences for Solvent Signal Suppression in Fourier Transform NMR II," *Journal of Magnetic Resonance (1969)*, vol. 66, no. 2, pp. 391–397, 1986.
- [89] A. Haase, J. Frahm, W. Hanicke, and D. Matthaei, "1H NMR Chemical Shift Selective (CHESS) Imaging," *Physics in Medicine and Biology*, vol. 30, no. 4, p. 341, 1985.
- [90] I. Tkáč, Z. Starčuk, I.-Y. Choi, and R. Gruetter, "In vivo 1H NMR Spectroscopy of Rat Brain at 1 ms Echo Time," *Magnetic Resonance in Medicine*, vol. 41, no. 4, pp. 649–656, 1999.
- [91] M. Mescher, A. Tannus, M. Johnson, and M. Garwood, "Solvent Suppression Using Selective Echo Dephasing," *Journal of Magnetic Resonance, Series A*, vol. 123, no. 2, pp. 226–229, 1996.
- [92] M. Piotto, V. Saudek, and V. Sklenář, "Gradient-Tailored Excitation for Single-Quantum NMR Spectroscopy of Aqueous Solutions," *Journal of Biomolecular NMR*, vol. 2, no. 6, pp. 661–665, 1992.
- [93] E. D. Becker, J. A. Feretti, and T. C. Farrar, "Driven Equilibrium Fourier Transform Spectroscopy. A New Method for Nuclear Magnetic Resonance Signal Enhancement," *Journal of the American Chemical Society*, vol. 91, no. 27, pp. 7784–7785, 1969.
- [94] R. Ogg, R. Kingsley, and J. Taylor, "WET, a T1- and B1-Insensitive Water-Suppression Method for in Vivo Localized 1H NMR Spectroscopy," *Journal of Magnetic Resonance, Series B*, vol. 104, no. 1, pp. 1–10, 1994.
- [95] M. S. Silver, R. I. Joseph, and D. I. Hoult, "Selective Spin Inversion in Nuclear Magnetic Resonance and Coherent Optics Through an Exact Solution of the Bloch-Riccati Equation," *Phys. Rev. A*, vol. 31, pp. 2753–2755, Apr 1985.

- [96] M. Garwood and L. DelaBarre, "The Return of the Frequency Sweep: Designing Adiabatic Pulses for Contemporary NMR," *Journal of Magnetic Resonance*, vol. 153, no. 2, pp. 155–177, 2001.
- [97] T. W. J. Scheenen, D. W. J. Klomp, J. P. Wijnen, and A. Heerschap, "Short Echo Time 1H-MRSI of the Human Brain at 3T with Minimal Chemical Shift Displacement Errors Using Adiabatic Refocusing Pulses," *Magnetic Resonance in Medicine*, vol. 59, no. 1, pp. 1–6, 2008.
- [98] S. Singh, B. K. Rutt, and R. M. Henkelman, "Projection Presaturation: A Fast and Accurate Technique for Multidimensional Spatial Localization," *Journal of Magnetic Resonance (1969)*, vol. 87, no. 3, pp. 567–583, 1990.
- [99] S. Singh, B. K. Rutt, and S. Napel, "Projection Presaturation. II. Single-Shot Localization of Multiple Regions of Interest," *Journal of Magnetic Resonance (1969)*, vol. 90, no. 2, pp. 313–329, 1990.
- [100] S. Singh and W. Brody, "Projection Presaturation. III. Accurate Selective Excitation or Presaturation of the Regions of Tailored Shape in the Presence of Short-T1 Species," *Journal of Magnetic Resonance, Series B*, vol. 101, no. 1, pp. 52–62, 1993.
- [101] A. Chu, J. R. Alger, G. J. Moore, and S. Posse, "Proton Echo-Planar Spectroscopic Imaging with Highly Effective Outer Volume Suppression Using Combined Presaturation and Spatially Selective Echo Dephasing," *Magnetic Resonance in Medicine*, vol. 49, no. 5, pp. 817–821, 2003.
- [102] A. Henning, A. Fuchs, J. B. Murdoch, and P. Boesiger, "Slice-Selective FID Acquisition, Localized by Outer Volume Suppression (FIDLOVS) for 1H-MRSI of the Human Brain at 7 T with Minimal Signal Loss," *NMR in Biomedicine*, vol. 22, no. 7, pp. 683–696, 2009.
- [103] A. A. Maudsley *et al.*, "Comprehensive Processing, Display and Analysis for In Vivo MR Spectroscopic Imaging," *NMR in Biomedicine*, vol. 19, no. 4, pp. 492–503, 2006.
- [104] S. Posse, R. Otazo, S. R. Dager, and J. Alger, "MR Spectroscopic Imaging: Principles and Recent Advances," *Journal of Magnetic Resonance Imaging*, vol. 37, no. 6, pp. 1301–1325, 2013.
- [105] T. Sundin, L. Vanhamme, P. V. Hecke, I. Dologlou, and S. V. Huffel, "Accurate Quantification of 1H Spectra: From Finite Impulse Response Filter Design for Solvent Suppression to Parameter Estimation," *Journal of Magnetic Resonance*, vol. 139, no. 2, pp. 189–204, 1999.

- 
- [106] D. Marion, M. Ikura, and A. Bax, "Improved Solvent Suppression in One- and Two-Dimensional NMR Spectra by Convolution of Time-Domain Data," *Journal of Magnetic Resonance (1969)*, vol. 84, no. 2, pp. 425–430, 1989.
- [107] J.-P. Antoine, C. Chauvin, and A. Coron, "Wavelets and Related Time-Frequency Techniques in Magnetic Resonance Spectroscopy," *NMR in Biomedicine*, vol. 14, no. 4, pp. 265–270, 2001.
- [108] H. Barkhuijsen, R. de Beer, and D. van Ormondt, "Improved Algorithm for Noniterative Time-Domain Model Fitting to Exponentially Damped Magnetic Resonance Signals," *Journal of Magnetic Resonance (1969)*, vol. 73, no. 3, pp. 553–557, 1987.
- [109] W. Pijnappel, A. van den Boogaart, R. de Beer, and D. van Ormondt, "SVD-Based Quantification of Magnetic Resonance Signals," *Journal of Magnetic Resonance (1969)*, vol. 97, no. 1, pp. 122–134, 1992.
- [110] S. Vanhuffel, H. Chen, C. Decanniere, and P. Vanhecke, "Algorithm for Time-Domain NMR Data Fitting Based on Total Least Squares," *Journal of Magnetic Resonance, Series A*, vol. 110, no. 2, pp. 228–237, 1994.
- [111] H. Chen, S. V. Huffel, D. van Ormondt, and R. de Beer, "Parameter Estimation with Prior Knowledge of Known Signal Poles for the Quantification of NMR Spectroscopy Data in the Time Domain," *Journal of Magnetic Resonance, Series A*, vol. 119, no. 2, pp. 225–234, 1996.
- [112] P. Stoica, Y. Selen, N. Sandgren, and S. Van Huffel, "Using Prior Knowledge in SVD-Based Parameter Estimation for Magnetic Resonance Spectroscopy—the ATP Example," *Biomedical Engineering, IEEE Transactions on*, vol. 51, no. 9, pp. 1568–1578, Sep 2004.
- [113] R. R. Ernst, "Numerical Hilbert Transform and Automatic Phase Correction in Magnetic Resonance Spectroscopy," *Journal of Magnetic Resonance (1969)*, vol. 1, no. 1, pp. 7–26, 1969.
- [114] D. E. Brown, T. W. Campbell, and R. N. Moore, "Automated Phase Correction of FT NMR Spectra by Baseline Optimization," *Journal of Magnetic Resonance (1969)*, vol. 85, no. 1, pp. 15–23, 1989.
- [115] J. van Vaals and P. van Gerwen, "Novel Methods for Automatic Phase Correction of NMR Spectra," *Journal of Magnetic Resonance (1969)*, vol. 86, no. 1, pp. 127–147, 1990.

- [116] A. Heuer, "A New Algorithm for Automatic Phase Correction by Symmetrizing Lines," *Journal of Magnetic Resonance (1969)*, vol. 91, no. 2, pp. 241–253, 1991.
- [117] L. Chen, Z. Weng, L. Goh, and M. Garland, "An Efficient Algorithm for Automatic Phase Correction of NMR Spectra Based on Entropy Minimization," *Journal of Magnetic Resonance*, vol. 158, no. 1-2, pp. 164–168, 2002.
- [118] U. Klose, "In Vivo Proton Spectroscopy in the Presence of Eddy Currents," *Magn Reson Med*, vol. 14, no. 1, pp. 26–30, Apr 1990.
- [119] A. A. De Graaf, J. E. Van Dijk, and W. M. M. J. Bovée, "Quality: Quantification Improvement by Converting Lineshapes to the Lorentzian Type," *Magnetic Resonance in Medicine*, vol. 13, no. 3, pp. 343–357, 1990.
- [120] D. Barache, J.-P. Antoine, and J.-M. Dereppe, "The Continuous Wavelet Transform, an Analysis Tool for NMR Spectroscopy," *Journal of Magnetic Resonance*, vol. 128, no. 1, pp. 1–11, 1997.
- [121] E. M. Haacke, Z. P. Liang, and S. H. Izen, "Constrained Reconstruction: A Superresolution, Optimal Signal-to-Noise Alternative to the Fourier Transform in Magnetic Resonance Imaging," *Med Phys*, vol. 16, pp. 388–397, 1989.
- [122] Z.-P. Liang, F. Boada, R. Constable, E. M. Haacke, P. Lauterbur, and M. R. Smith, "Constrained Reconstruction Methods in MR Imaging," *Reviews of Magnetic Resonance in Medicine*, vol. 4, pp. 67–185, 1992.
- [123] Z.-P. Liang and P. Lauterbur, "Constrained Imaging: Overcoming the Limitations of the Fourier Series," *Engineering in Medicine and Biology Magazine, IEEE*, vol. 15, no. 5, pp. 126–132, Sep 1996.
- [124] X. Hu, D. N. Levin, P. C. Lauterbur, and T. Spraggins, "SLIM: Spectral Localization by Imaging," *Magn Reson Med*, vol. 8, no. 3, pp. 314–322, Nov 1988.
- [125] Z. Liang and P. Lauterbur, "A Theoretical Analysis of the SLIM Technique," *Journal of Magnetic Resonance, Series B*, vol. 102, no. 1, pp. 54–60, 1993.
- [126] X. Hu and Z. Wu, "SLIM Revisited," *IEEE Trans Med Imaging*, vol. 12, pp. 583–587, 1993.
- [127] M. von Kienlin and R. Mejia, "Spectral Localization with Optimal Pointspread Function," *Journal of Magnetic Resonance*, vol. 94, no. 2, pp. 268–287, 1991.

- [128] Z. P. Liang and P. C. Lauterbur, "A Generalized Series Approach to MR Spectroscopic Imaging." *IEEE Trans Med Imaging*, vol. 10, no. 2, pp. 132–137, 1991.
- [129] A. Bashir and D. A. Yablonskiy, "Natural Linewidth Chemical Shift Imaging (NL-CSI)." *Magn Reson Med*, vol. 56, no. 1, pp. 7–18, Jul 2006.
- [130] I. Khalidov, D. Van De Ville, M. Jacob, F. Lazeyras, and M. Unser, "BSLIM: Spectral Localization by Imaging with Explicit  $B_0$  Field Inhomogeneity Compensation," *IEEE Transactions on Medical Imaging*, vol. 26, no. 7, pp. 990–1000, 2007.
- [131] L. An, S. Warach, and J. Shen, "Spectral Localization by Imaging Using Multielement Receiver Coils," *Magn Reson Med*, vol. 66, pp. 1–10, Jul 2011.
- [132] K. P. Pruessmann, M. Weiger, M. B. Scheidegger, and P. Boesiger, "SENSE: Sensitivity Encoding for Fast MRI," *Magn Reson Med*, vol. 42, pp. 952–962, Nov 1999.
- [133] J. A. Kmiecik, C. D. Gregory, Z.-P. Liang, P. C. Lauterbur, and M. J. Dawson, "Lactate Quantitation in a Gerbil Brain Stroke Model by GSLIM of Multiple-Quantum-Filtered Signals," *Journal of Magnetic Resonance Imaging*, vol. 9, no. 4, pp. 539–543, 1999.
- [134] Z. Dong and J.-H. Hwang, "Lipid Signal Extraction by SLIM: Application to 1H MR Spectroscopic Imaging of Human Calf Muscles," *Magnetic Resonance in Medicine*, vol. 55, no. 6, pp. 1447–1453, 2006.
- [135] R. Löffler, R. Sauter, H. Kolem, A. Haase, and M. von Kienlin, "Localized Spectroscopy from Anatomically Matched Compartments: Improved Sensitivity and Localization for Cardiac 31P MRS in Humans," *Journal of Magnetic Resonance*, vol. 134, no. 2, pp. 287–299, 1998.
- [136] M. Meininger, W. Landschütz, M. Beer, T. Seyfarth, M. Horn, T. Pabst, A. Haase, D. Hahn, S. Neubauer, and M. von Kienlin, "Concentrations of Human Cardiac Phosphorus Metabolites Determined by SLOOP 31P NMR Spectroscopy," *Magnetic Resonance in Medicine*, vol. 41, no. 4, pp. 657–663, 1999.
- [137] M. Beer, T. Seyfarth, J. Sandstede, W. Landschütz, C. Lipke, H. Köstler, M. von Kienlin, K. Harre, D. Hahn, and S. Neubauer, "Absolute Concentrations of High-Energy Phosphate Metabolites in Normal, Hypertrophied, and Failing Human Myocardium Measured

- Noninvasively with 31P-SLOOP Magnetic Resonance Spectroscopy,” *Journal of the American College of Cardiology*, vol. 40, no. 7, pp. 1267–1274, 2002.
- [138] S. Mallat and Z. Zhang, “Matching Pursuits with Time-Frequency Dictionaries,” *Signal Processing, IEEE Transactions on*, vol. 41, no. 12, pp. 3397–3415, Dec 1993.
- [139] Y. Pati, R. Rezaifar, and P. Krishnaprasad, “Orthogonal Matching Pursuit: Recursive Function Approximation with Applications to Wavelet Decomposition,” in *Signals, Systems and Computers, 1993. 1993 Conference Record of The Twenty-Seventh Asilomar Conference on*, vol. 1, Nov 1993, pp. 40–44.
- [140] S. S. Chen, D. L. Donoho, Michael, and A. Saunders, “Atomic Decomposition by Basis Pursuit,” *SIAM Journal on Scientific Computing*, vol. 20, pp. 33–61, 1998.
- [141] R. Tibshirani, “Regression Shrinkage and Selection Via the Lasso,” *Journal of the Royal Statistical Society, Series B*, vol. 58, pp. 267–288, 1994.
- [142] T. Hastie, R. Tibshirani, and J. Friedman, *The Elements of Statistical Learning: Data Mining, Inference, and Prediction*, 2nd ed. Springer, 2009.
- [143] D. Donoho, “Compressed Sensing,” *Information Theory, IEEE Transactions on*, vol. 52, no. 4, pp. 1289–1306, Apr 2006.
- [144] E. Candes, J. Romberg, and T. Tao, “Robust Uncertainty Principles: Exact Signal Reconstruction from Highly Incomplete Frequency Information,” *Information Theory, IEEE Transactions on*, vol. 52, no. 2, pp. 489–509, Feb 2006.
- [145] M. Lustig, D. Donoho, and J. M. Pauly, “Sparse MRI: The Application of Compressed Sensing for Rapid MR Imaging,” *Magn Reson Med*, vol. 58, pp. 1182–1195, Dec 2007.
- [146] M. Lustig, D. Donoho, J. Santos, and J. Pauly, “Compressed Sensing MRI,” *Signal Processing Magazine, IEEE*, vol. 25, no. 2, pp. 72–82, Mar 2008.
- [147] M. Lustig, J. Santos, D. Donoho, and J. Pauly, “k-t SPARSE: High Frame Rate Dynamic MRI Exploiting Spatio-Temporal Sparsity,” in *Proceedings of the 14th Annual Meeting of ISMRM, Seattle, Washington, USA*, 2006, p. 2420.

- [148] S. Hu, M. Lustig, A. Balakrishnan, P. E. Larson, R. Bok, J. Kurhanewicz, S. J. Nelson, A. Goga, J. M. Pauly, and D. B. Vigneron, "3D Compressed Sensing for Highly Accelerated Hyperpolarized  $(^{13}\text{C})$  MRSI with In Vivo Applications to Transgenic Mouse Models of Cancer," *Magn Reson Med*, vol. 63, pp. 312–321, Feb 2010.
- [149] L. I. Rudin, S. Osher, and E. Fatemi, "Nonlinear Total Variation Based Noise Removal Algorithms," *Physica D: Nonlinear Phenomena*, vol. 60, pp. 259–268, 1992.
- [150] T. Chan, S. Osher, and J. Shen, "The Digital TV Filter and Nonlinear Denoising," *Image Processing, IEEE Transactions on*, vol. 10, no. 2, pp. 231–241, Feb 2001.
- [151] F. Knoll, K. Bredies, T. Pock, and R. Stollberger, "Second Order Total Generalized Variation (TGV) for MRI," *Magnetic Resonance in Medicine*, vol. 65, no. 2, pp. 480–491, 2011.
- [152] Y. Wang and H. Zhou, "Total Variation Wavelet-Based Medical Image Denoising," *International Journal of Biomedical Imaging*, p. 6, 2006.
- [153] Y. Kim, P. M. Thompson, and L. A. Vese, "HARDI Data Denoising Using Vectorial Total Variation and Logarithmic Barrier," *Inverse Problems and Imaging*, vol. 4, no. 2, pp. 273–310, May 2010.
- [154] K. T. Block, M. Uecker, and J. Frahm, "Suppression of MRI Truncation Artifacts Using Total Variation Constrained Data Extrapolation," *Int J Biomed Imaging*, vol. 2008, Aug 2008.
- [155] C. Gnahn, M. Bock, P. Bachert, W. Semmler, N. G. R. Behl, and A. M. Nagel, "Iterative 3D Projection Reconstruction of  $^{23}\text{Na}$  Data with  $^1\text{H}$  MRI Constraints," *Magnetic Resonance in Medicine*, vol. 71, no. 5, pp. 1720–1732, 2014.
- [156] F. Huang, Y. Chen, G. R. Duensing, J. Akao, A. Rubin, and C. Saylor, "Application of Partial Differential Equation-Based Inpainting on Sensitivity Maps," *Magnetic Resonance in Medicine*, vol. 53, no. 2, pp. 388–397, 2005.
- [157] S. Plevritis and A. Macovski, "Spectral Extrapolation of Spatially Bounded Images [MRI Application]," *Medical Imaging, IEEE Transactions on*, vol. 14, no. 3, pp. 487–497, Sep 1995.
- [158] R. Gerchberg, "Super-Resolution Through Error Energy Reduction," *Optica Acta: International Journal of Optics*, vol. 21, no. 9, pp. 709–720, 1974.

- 
- [159] A. Papoulis, "A New Algorithm in Spectral Analysis and Band-Limited Extrapolation," *Circuits and Systems, IEEE Transactions on*, vol. 22, no. 9, pp. 735–742, Sep 1975.
- [160] M. Jacob, X. Zhu, A. Ebel, N. Schuff, and Z.-P. Liang, "Improved Model-Based Magnetic Resonance Spectroscopic Imaging," *Medical Imaging, IEEE Transactions on*, vol. 26, no. 10, pp. 1305–1318, Oct 2007.
- [161] J. P. Haldar, D. Hernando, S.-K. Song, and Z.-P. Liang, "Anatomically Constrained Reconstruction from Noisy Data," *Magnetic Resonance in Medicine*, vol. 59, no. 4, pp. 810–818, 2008.
- [162] X. Hu and A. Stillman, "Technique for Reduction of Truncation Artifact in Chemical Shift Images," *Medical Imaging, IEEE Transactions on*, vol. 10, no. 3, pp. 290–294, Sep 1991.
- [163] R. Eslami and M. Jacob, "Robust Reconstruction of MRSI Data Using a Sparse Spectral Model and High Resolution MRI Priors," *Medical Imaging, IEEE Transactions on*, vol. 29, no. 6, pp. 1297–1309, Jun 2010.
- [164] J. Kornak, K. Young, B. Soher, and A. Maudsley, "Bayesian k-Space-Time Reconstruction of MR Spectroscopic Imaging for Enhanced Resolution," *Medical Imaging, IEEE Transactions on*, vol. 29, no. 7, pp. 1333–1350, Jul 2010.
- [165] J. Sánchez-González, J. Tsao, U. Dydak, M. Desco, P. Boesiger, and K. Paul Pruessmann, "Minimum-Norm Reconstruction for Sensitivity-Encoded Magnetic Resonance Spectroscopic Imaging," *Magnetic Resonance in Medicine*, vol. 55, no. 2, pp. 287–295, 2006.
- [166] R. Otazo, F.-H. Lin, G. Wiggins, R. Jordan, D. Sodickson, and S. Posse, "Superresolution Parallel Magnetic Resonance Imaging: Application to Functional and Spectroscopic Imaging," *NeuroImage*, vol. 47, no. 1, pp. 220–230, 2009.
- [167] S. Bhave, R. Eslami, and M. Jacob, "Sparse Spectral Deconvolution Algorithm for Noncartesian MR Spectroscopic Imaging," *Magnetic Resonance in Medicine*, vol. 71, no. 2, pp. 469–476, 2014.
- [168] K. Pruessmann and K. Tsao, "Magnetic Resonance Imaging Method," U.S. Patent 7,342,397, March 11, 2008.
- [169] T. Kirchner, A. Fillmer, J. Tsao, K. P. Pruessmann, and A. Henning, "Reduction of Voxel Bleeding in Highly Accelerated Parallel  $^1\text{H}$  MRSI by Direct Control of the Spatial Response Functions," *Magnetic Resonance in Medicine*, 2014.

- [170] M. Ochs, R. Stoyanova, F. Arias-Mendoza, and T. Brown, "A New Method for Spectral Decomposition Using a Bilinear Bayesian Approach," *Journal of Magnetic Resonance*, vol. 137, no. 1, pp. 161–176, 1999.
- [171] P. Sajda, S. Du, T. Brown, R. Stoyanova, D. Shungu, X. Mao, and L. Parra, "Nonnegative Matrix Factorization for Rapid Recovery of Constituent Spectra in Magnetic Resonance Chemical Shift Imaging of the Brain," *Medical Imaging, IEEE Transactions on*, vol. 23, no. 12, pp. 1453–1465, Dec 2004.
- [172] D. D. Lee and S. Seung, "Learning the Parts of Objects by Non-Negative Matrix Factorization," *Nature*, vol. 401, pp. 788–791, Oct 1999.
- [173] A. Cichocki, A. H. Phan, and R. Zdunek, *Nonnegative Matrix and Tensor Factorizations: Applications to Exploratory Multi-way Data Analysis and Blind Source Separation*. Chichester: Wiley, 2009.
- [174] K. Pearson, "On Lines and Planes of Closest Fit to Systems of Points in Space," *Philosophical Magazine*, vol. 2, no. 11, pp. 559–572, 1901.
- [175] Z.-P. Liang, "Spatiotemporal Imaging with Partially Separable Functions," in *Biomedical Imaging: From Nano to Macro, 2007. ISBI 2007. 4th IEEE International Symposium on*, Apr 2007, pp. 988–991.
- [176] J. Haldar and Z.-P. Liang, "Spatiotemporal Imaging with Partially Separable Functions: A Matrix Recovery Approach," in *Biomedical Imaging: From Nano to Macro, 2010 IEEE International Symposium on*, Apr 2010, pp. 716–719.
- [177] H. Pedersen, S. Kozerke, S. Ringgaard, K. Nehrke, and W. Y. Kim, "k-t PCA: Temporally Constrained k-t BLAST Reconstruction Using Principal Component Analysis," *Magn Reson Med*, vol. 62, pp. 706–716, Sep 2009.
- [178] S. Lingala, Y. Hu, E. DiBella, and M. Jacob, "Accelerated Dynamic MRI Exploiting Sparsity and Low-Rank Structure: k-t SLR," *Medical Imaging, IEEE Transactions on*, vol. 30, no. 5, pp. 1042–1054, May 2011.
- [179] S. Lingala and M. Jacob, "A Blind Compressive Sensing Frame Work for Accelerated Dynamic MRI," in *Biomedical Imaging (ISBI), 2012 9th IEEE International Symposium on*, May 2012, pp. 1060–1063.
- [180] M. Usman, C. Prieto, T. Schaeffter, and P. G. Batchelor, "k-t Group Sparse: A Method for Accelerating Dynamic MRI," *Magn Reson Med*, vol. 66, pp. 1163–1176, Oct 2011.

- 
- [181] B. Zhao, J. Haldar, A. Christodoulou, and Z.-P. Liang, "Image Reconstruction From Highly Undersampled (k,t)-Space Data with Joint Partial Separability and Sparsity Constraints," *Medical Imaging, IEEE Transactions on*, vol. 31, no. 9, pp. 1809–1820, Sep 2012.
- [182] J. Haldar, "Low-Rank Modeling of Local k-Space Neighborhoods (LO-RAKS) for Constrained MRI," *Medical Imaging, IEEE Transactions on*, vol. 33, no. 3, pp. 668–681, Mar 2014.
- [183] P. J. Shin, P. E. Z. Larson, M. A. Ohliger, M. Elad, J. M. Pauly, D. B. Vigneron, and M. Lustig, "Calibrationless Parallel Imaging Reconstruction Based on Structured Low-Rank Matrix Completion," *Magnetic Resonance in Medicine*, vol. 72, no. 4, pp. 959–970, 2014.
- [184] F. Lam, S. D. Babacan, J. P. Haldar, M. W. Weiner, N. Schuff, and Z.-P. Liang, "Denoising Diffusion-Weighted Magnitude MR Images Using Rank and Edge Constraints," *Magnetic Resonance in Medicine*, vol. 71, no. 3, pp. 1272–1284, 2014.
- [185] J. Kasten, F. Lazeyras, and D. Van De Ville, "Data-Driven MRSI Spectral Localization Via Low-Rank Component Analysis," *Medical Imaging, IEEE Transactions on*, vol. 32, no. 10, pp. 1853–1863, Oct 2013.
- [186] M. Reed and B. Simon, *Methods of Modern Mathematical Physics I: Functional Analysis*, 1st ed. Academic Press, Jan 1980.
- [187] H. Jung, K. Sung, K. S. Nayak, E. Y. Kim, and J. C. Ye, "k-t FOCUSS: A General Compressed Sensing Framework for High Resolution Dynamic MRI," *Magnetic Resonance in Medicine*, vol. 61, no. 1, pp. 103–116, 2009.
- [188] H. Jung, J. Park, J. Yoo, and J. C. Ye, "Radial k-t FOCUSS for High-Resolution Cardiac Cine MRI," *Magnetic Resonance in Medicine*, vol. 63, no. 1, pp. 68–78, 2010.
- [189] E. J. Candès and B. Recht, "Exact Matrix Completion via Convex Optimization," *Found. Comput. Math.*, vol. 9, no. 6, pp. 717–772, Dec 2009.
- [190] A. Majumdar and R. K. Ward, "An Algorithm for Sparse MRI Reconstruction by Schatten p-Norm Minimization," *Magnetic Resonance Imaging*, vol. 29, no. 3, pp. 408–417, 2011.
- [191] B. Recht, M. Fazel, and P. Parrilo, "Guaranteed Minimum-Rank Solutions of Linear Matrix Equations via Nuclear Norm Minimization," *SIAM Review*, vol. 52, no. 3, pp. 471–501, 2010.

- [192] H. Nguyen, X. Peng, M. Do, and Z.-P. Liang, “Denoising MR Spectroscopic Imaging Data with Low-Rank Approximations,” *Biomedical Engineering, IEEE Transactions on*, vol. 60, no. 1, pp. 78–89, Jan 2013.
- [193] F. Lam and Z.-P. Liang, “A Subspace Approach to High-Resolution Spectroscopic Imaging,” *Magnetic Resonance in Medicine*, vol. 71, no. 4, pp. 1349–1357, 2014.
- [194] A. Chambolle and T. Pock, “A First-Order Primal-Dual Algorithm for Convex Problems with Applications to Imaging,” *J. Math. Imaging Vis.*, vol. 40, pp. 120–145, May 2011.
- [195] T. Chan, S. Esedoglu, F. Park, and A. Yip, “Recent Developments in Total Variation Image Restoration,” in *Handbook of Mathematical Models in Computer Vision*, N. Paragios, Y. Chen, and O. D. Faugeras, Eds. Springer-Verlag, 2005.
- [196] T. Chan, A. Marquina, and P. Mulet, “High-Order Total Variation-Based Image Restoration,” *SIAM Journal on Scientific Computing*, vol. 22, no. 2, pp. 503–516, 2000.
- [197] S. Setzer and G. Steidl, “Variational Methods with Higher Order Derivatives in Image Processing,” in *Approximation XII*, M. Neamtu and L. Schumaker, Eds. Brentwood: Nashboro Press, 2008, pp. 360–386.
- [198] G. Maso, I. Fonseca, G. Leoni, and M. Morini, “A Higher Order Model for Image Restoration: The One-Dimensional Case,” *SIAM Journal on Mathematical Analysis*, vol. 40, no. 6, pp. 2351–2391, 2009.
- [199] Y. Hu and M. Jacob, “Higher degree total variation (HDTV) regularization for image recovery,” *Image Processing, IEEE Transactions on*, vol. PP, no. 99, p. 1, 2012.
- [200] Z. Dogan, S. Lefkimmiatis, A. Bourquard, and M. Unser, “A Second-Order Extension of TV Regularization for Image Deblurring,” in *Image Processing (ICIP), 2011 18th IEEE International Conference on*, sept. 2011, pp. 705–708.
- [201] S. Lefkimmiatis, J. Ward, and M. Unser, “Hessian Schatten-Norm Regularization for Linear Inverse Problems,” *Image Processing, IEEE Transactions on*, vol. 22, no. 5, pp. 1873–1888, May 2013.
- [202] K. Bredies, K. Kunisch, and T. Pock, “Total Generalized Variation,” *SIAM Journal on Imaging Sciences*, vol. 3, no. 3, pp. 492–526, 2010.

- 
- [203] K. Bredies and T. Valkonen, “Inverse Problems with Second-Order Total Generalized Variation Constraints,” in *Proceedings of SampTA 2011 – 9th International Conference on Sampling Theory and Applications, Singapore*, 2011.
- [204] Y. Hu, G. Ongie, S. Ramani, and M. Jacob, “Generalized Higher Degree Total Variation (HDTV) Regularization,” *Image Processing, IEEE Transactions on*, vol. 23, no. 6, pp. 2423–2435, Jun 2014.
- [205] K. Papafitsoros and C. Schönlieb, “A Combined First and Second Order Variational Approach for Image Reconstruction,” *Journal of Mathematical Imaging and Vision*, vol. 48, no. 2, pp. 308–338, 2014.
- [206] S. Boyd and L. Vandenberghe, *Convex Optimization*. Cambridge University Press, March 2004.
- [207] K. Kreutz-Delgado, J. F. Murray, B. D. Rao, K. Engan, T.-W. Lee, and T. J. Sejnowski, “Dictionary Learning Algorithms for Sparse Representation,” *Neural Comput.*, vol. 15, no. 2, pp. 349–396, Feb 2003.
- [208] M. Yaghoobi, T. Blumensath, and M. Davies, “Dictionary Learning for Sparse Approximations With the Majorization Method,” *Signal Processing, IEEE Transactions on*, vol. 57, no. 6, pp. 2178–2191, Jun 2009.
- [209] M. Afonso, J. Bioucas-Dias, and M. Figueiredo, “Fast Image Recovery Using Variable Splitting and Constrained Optimization,” *Image Processing, IEEE Transactions on*, vol. 19, no. 9, pp. 2345–2356, Sep 2010.
- [210] P. L. Combettes and J.-C. Pesquet, “Proximal Splitting Methods in Signal Processing,” in *Fixed-Point Algorithms for Inverse Problems in Science and Engineering*, ser. Springer Optimization and Its Applications, H. H. Bauschke, R. S. Burachik, P. L. Combettes, V. Elser, D. R. Luke, and H. Wolkowicz, Eds. Springer New York, 2011, pp. 185–212.
- [211] Y. Nesterov, “A Method for Solving the Convex Programming Problem with Convergence Rate  $\mathcal{O}(1/k^2)$ ,” *Dokl. Akad. Nauk SSSR*, vol. 269(3), pp. 543–547, 1983.
- [212] A. Beck and M. Teboulle, “A Fast Iterative Shrinkage-Thresholding Algorithm for Linear Inverse Problems,” *SIAM Journal on Imaging Sciences*, vol. 2, no. 1, pp. 183–202, 2009.
- [213] J. Rissanen, “Modeling by Shortest Data Description,” *Automatica*, vol. 14, no. 5, pp. 465–471, 1978.

- 
- [214] H. Akaike, "A New Look at the Statistical Model Identification," *Automatic Control, IEEE Transactions on*, vol. 19, no. 6, pp. 716–723, Dec 1974.
- [215] R. B. Cattell, "The Scree Test for the Number of Factors," *Multivariate Behavioral Research*, vol. 1, no. 2, pp. 245–276, 1966.
- [216] D. W. Osten, "Selection of Optimal Regression Models Via Cross-Validation," *Journal of Chemometrics*, vol. 2, no. 1, pp. 39–48, 1988.
- [217] S. Wold, "Cross-Validatory Estimation of the Number of Components in Factor and Principal Components Models," *Technometrics*, vol. 20, no. 4, pp. 397–405, 1978.
- [218] G. Diana and C. Tommasi, "Cross-Validation Methods in Principal Component Analysis: A Comparison," *Statistical Methods and Applications*, vol. 11, no. 1, pp. 71–82, 2002.
- [219] G. Schwarz, "Estimating the Dimension of a Model," *The Annals of Statistics*, vol. 6, no. 2, pp. 461–464, Mar 1978.
- [220] R. E. Kass and A. E. Raftery, "Bayes Factors and Model Uncertainty," Department of Statistics, University of Washington, Tech. Rep. 254, Mar 1993.
- [221] S. Roweis, "EM Algorithms for PCA and SPCA," in *Proceedings of the 1997 Conference on Advances in Neural Information Processing Systems 10*, ser. NIPS '97. Cambridge, MA, USA: MIT Press, 1998, pp. 626–632.
- [222] M. E. Tipping and C. M. Bishop, "Probabilistic Principal Component Analysis," *Journal of the Royal Statistical Society. Series B (Statistical Methodology)*, vol. 61, no. 3, pp. 611–622, 1999.
- [223] T. Minka, "Automatic Choice of Dimensionality for PCA," M.I.T., MIT Media Laboratory, Vision and Modeling Group 20 Ames Street, Cambridge, MA 02139, Tech. Rep. 514, Dec 2000.
- [224] D. C. Hoyle, "Automatic PCA Dimension Selection for High Dimensional Data and Small Sample Sizes," *Journal of Machine Learning Research*, vol. 9, pp. 2733–2759, Dec 2008.
- [225] L. Tierney and J. B. Kadane, "Accurate Approximations for Posterior Moments and Marginal Densities," *Journal of the American Statistical Association*, vol. 81, no. 393, pp. 82–86, 1986.
- [226] V. Morozov, *Methods for Solving Incorrectly Posed Problems*, 1st ed., Z. Nashed, Ed. Springer-Verlag, Dec 1984.

- [227] P. C. Hansen, *Rank-Deficient and Discrete Ill-Posed Problems: Numerical Aspects of Linear Inversion*. Philadelphia, PA, USA: Society for Industrial and Applied Mathematics, 1998.
- [228] G. H. Golub, M. T. Heath, and G. Wahba, "Generalized Cross-Validation as a Method for Choosing a Good Ridge Parameter," *Technometrics*, vol. 21, pp. 215–223, 1979.
- [229] P. C. Hansen, "Analysis of Discrete Ill-Posed Problems by Means of the L-Curve," *SIAM Review*, vol. 34, no. 4, pp. 561–580, 1992.
- [230] P. C. Hansen, "The L-Curve and its Use in the Numerical Treatment of Inverse Problems," in *Computational Inverse Problems in Electrocardiography*, ser. Advances in Computational Bioengineering, P. R. Johnston, Ed. Southampton: WIT Press, 2001, no. 5, pp. 119–142.
- [231] N. Galatsanos and A. Katsaggelos, "Methods for Choosing the Regularization Parameter and Estimating the Noise Variance in Image Restoration and Their Relation," *Image Processing, IEEE Transactions on*, vol. 1, no. 3, pp. 322–336, Jul 1992.
- [232] A. Thompson, J. Brown, J. Kay, and D. Titterington, "A Study of Methods of Choosing the Smoothing Parameter in Image Restoration by Regularization," *Pattern Analysis and Machine Intelligence, IEEE Transactions on*, vol. 13, no. 4, pp. 326–339, Apr 1991.
- [233] H. Liao, F. Li, and M. K. Ng, "Selection of Regularization Parameter in Total Variation Image Restoration," *J. Opt. Soc. Am. A*, vol. 26, no. 11, pp. 2311–2320, Nov 2009.
- [234] J. P. Oliveira, J. M. Bioucas-Dias, and M. A. Figueiredo, "Adaptive Total Variation Image Deblurring: A Majorization-Minimization Approach," *Signal Processing*, vol. 89, no. 9, pp. 1683–1693, 2009.
- [235] S. Babacan, R. Molina, and A. Katsaggelos, "Parameter Estimation in TV Image Restoration Using Variational Distribution Approximation," *Image Processing, IEEE Transactions on*, vol. 17, no. 3, pp. 326–339, March 2008.
- [236] A. Maudsley, C. Domenig, V. Govind, A. Darkazanli, C. Studholme, K. Arheart, and C. Bloomer, "Mapping of Brain Metabolite Distributions by Volumetric Proton MR Spectroscopic Imaging (MRSI)," *Magnetic Resonance in Medicine*, vol. 61, no. 3, pp. 548–559, 2009.
- [237] W. Bogner, S. Gruber, S. Trattnig, and M. Chmelik, "High-Resolution Mapping of Human Brain Metabolites by Free Induction Decay  $^1\text{H}$  MRSI at 7T," *NMR in Biomedicine*, vol. 25, no. 6, pp. 873–882, 2012.

- [238] Phantom Test Guidance for the ACR MRI Accreditation Program. Online. The American College of Radiology. 1891 Preston White Dr. Reston, VA 20191-4397. [Online]. Available: <http://www.acr.org/~/media/ACR/Documents/Accreditation/MRI/LargePhantomGuidance.pdf>
- [239] J. L. Gunter, M. A. Bernstein, B. J. Borowski, C. P. Ward, P. J. Britson, J. P. Felmlee, N. Schuff, M. Weiner, and C. R. Jack, "Measurement of MRI Scanner Performance with the ADNI Phantom," *Medical Physics*, vol. 36, no. 6, pp. 2193–2205, 2009.
- [240] D. Wang, D. M. Doddrell, and G. Cowin, "A Novel Phantom and Method for Comprehensive 3-Dimensional Measurement and Correction of Geometric Distortion in Magnetic Resonance Imaging," *Magnetic Resonance Imaging*, vol. 22, no. 4, pp. 529–542, 2004.
- [241] D.-C. Woo, B.-S. Kim, S.-L. Jung, H.-J. Park, H.-S. Rhim, G.-H. Jahng, and B.-Y. Choe, "Development of a Cone-Shape Phantom for Multi-Voxel MR Spectroscopy," *Journal of Neuroscience Methods*, vol. 162, pp. 101–107, 2007.
- [242] L. Shepp and B. Logan, "The Fourier Reconstruction of a Head Section," *Nuclear Science, IEEE Transactions on*, vol. 21, no. 3, pp. 21–43, Jun 1974.
- [243] C. G. Koay, J. E. Sarlls, and E. Özarıslan, "Three-Dimensional Analytical Magnetic Resonance Imaging Phantom in the Fourier Domain," *Magnetic Resonance in Medicine*, vol. 58, no. 2, pp. 430–436, 2007.
- [244] L. Greengard and C. Stucchio, "Spectral Edge Detection in Two Dimensions Using Wavefronts," *Applied and Computational Harmonic Analysis*, vol. 30, no. 1, pp. 69–95, 2011.
- [245] K. McInturff and P. Simon, "The Fourier Transform of Linearly Varying Functions with Polygonal Support," *Antennas and Propagation, IEEE Transactions on*, vol. 39, no. 9, pp. 1441–1443, Sep 1991.
- [246] J. Komrska, "Algebraic Expressions of Shape Amplitudes of Polygons and Polyhedra," *Optik*, vol. 80, no. 4, pp. 171–183, May 1988.
- [247] T. Ngo, G. Fung, B. Tsui, E. McVeigh, and D. Herzka, "Three Dimensional Digital Polyhedral Phantom Framework with Analytical Fourier Transform and Applications in Cardiac Imaging," in *Proceedings of the 19th Annual Meeting of the International Society for Magnetic Resonance in Medicine (ISMRM)*. International Society for Magnetic Resonance in Medicine, 2011, p. 1310.

- [248] M. Guerquin-Kern, L. Lejeune, K. Pruessmann, and M. Unser, "Realistic Analytical Phantoms for Parallel Magnetic Resonance Imaging," *Medical Imaging, IEEE Transactions on*, vol. 31, no. 3, pp. 626–636, Mar 2012.
- [249] M. E. Haacke, R. W. Brown, M. R. Thompson, and R. Venkatesan, *Magnetic Resonance Imaging: Physical Principles and Sequence Design*, 1st ed. Wiley-Liss, Jun 1999.
- [250] J. Giannatsis and V. Dedoussis, "Additive Fabrication Technologies Applied to Medicine and Health Care: A Review," *The International Journal of Advanced Manufacturing Technology*, vol. 40, no. 1-2, pp. 116–127, 2009.
- [251] F. Rengier, A. Mehndiratta, H. von Tengg-Kobligk, C. Zechmann, R. Unterhinninghofen, H.-U. Kauczor, and F. Giesel, "3D Printing Based on Imaging Data: Review of Medical Applications," *International Journal of Computer Assisted Radiology and Surgery*, vol. 5, no. 4, pp. 335–341, 2010.
- [252] Y. Wang and S.-J. Li, "Differentiation of Metabolic Concentrations Between Gray Matter and White Matter of Human Brain by in vivo  $^1\text{H}$  Magnetic Resonance Spectroscopy," *Magnetic Resonance in Medicine*, vol. 39, no. 1, pp. 28–33, 1998.
- [253] N. Schuff, F. Ezekiel, A. C. Gamst, D. L. Amend, A. A. Capizzano, A. A. Maudsley, and M. Weiner, "Region and Tissue Differences of Metabolites in Normally Aged Brain Using Multislice  $^1\text{H}$  Magnetic Resonance Spectroscopic Imaging," *Magnetic Resonance in Medicine*, vol. 45, no. 5, pp. 899–907, 2001.
- [254] D. M. Strong, P. Blomgren, and T. F. Chan, "Spatially Adaptive Local-Feature-Driven Total Variation Minimizing Image Restoration," in *Proceedings of the SPIE*, ser. Statistical and Stochastic Methods in Image Processing II, vol. 3167. San Diego: International Society for Optics and Photonics, Jul 1997, pp. 222–233.
- [255] A. E. Hamidi, M. Ménard, M. Lugiez, and C. Ghannam, "Weighted and Extended Total Variation for Image Restoration and Decomposition," *Pattern Recognition*, vol. 43, no. 4, pp. 1564–1576, 2010.
- [256] C. Gnahn, N. G. Behl, A. Biller, P. Bachert, and A. M. Nagel, "Anatomically Weighted 2nd Order Total Variation Reconstruction of  $^{23}\text{Na}$  Using  $^1\text{H}$  Prior Information," in *Proceedings of the 22nd Annual Meeting of the International Society for Magnetic Resonance in Medicine (ISMRM)*, Milano, Italy, May 2014, p. 1525.

- [257] J. P. Hornak, J. Szumowski, and R. G. Bryant, "Magnetic Field Mapping," *Magnetic Resonance in Medicine*, vol. 6, no. 2, pp. 158–163, 1988.
- [258] S. Akoka, F. Franconi, F. Seguin, and A. L. Pape, "Radiofrequency Map of an NMR Coil by Imaging," *Magnetic Resonance Imaging*, vol. 11, no. 3, pp. 437–441, 1993.
- [259] R. Stollberger and P. Wach, "Imaging of the Active  $b_1$  Field in Vivo," *Magnetic Resonance in Medicine*, vol. 35, no. 2, pp. 246–251, 1996.
- [260] C. H. Cunningham, J. M. Pauly, and K. S. Nayak, "Saturated Double-Angle Method for Rapid  $B_1+$  Mapping," *Magnetic Resonance in Medicine*, vol. 55, no. 6, pp. 1326–1333, 2006.
- [261] L. I. Sacolick, F. Wiesinger, I. Hancu, and M. W. Vogel, " $B_1$  Mapping by Bloch-Siegert Shift," *Magnetic Resonance in Medicine*, vol. 63, no. 5, pp. 1315–1322, 2010.
- [262] C. Barmet, N. D. Zanche, and K. P. Pruessmann, "Spatiotemporal Magnetic Field Monitoring for MR," *Magnetic Resonance in Medicine*, vol. 60, no. 1, pp. 187–197, 2008.
- [263] C. Barmet, B. Wilm, M. Pavan, and K. Pruessmann, "A Third-Order Field Camera with Microsecond Resolution for MR System Diagnostics," in *Proceedings ISMRM, 17th Scientific Meeting and Exhibition*, 2009.
- [264] B. J. Wilm, C. Barmet, M. Pavan, and K. P. Pruessmann, "Higher Order Reconstruction for MRI in the Presence of Spatiotemporal Field Perturbations," *Magnetic Resonance in Medicine*, vol. 65, no. 6, pp. 1690–1701, 2011.
- [265] N. De Zanche, C. Barmet, J. A. Nordmeyer-Massner, and K. P. Pruessmann, "NMR Probes for Measuring Magnetic Fields and Field Dynamics in MR Systems," *Magnetic Resonance in Medicine*, vol. 60, no. 1, pp. 176–186, 2008.
- [266] Z.-H. Wu, F. Lam, C. Ma, and Z.-P. Liang, "Improved Image Reconstruction for Subspace-Based Spectroscopic Imaging Using Non-Quadratic Regularization," in *Engineering in Medicine and Biology Society (EMBC), 2014 36th Annual International Conference of the IEEE*, Aug 2014, pp. 2432–2435.
- [267] C. I. Haupt, N. Schuff, M. W. Weiner, and A. A. Maudsley, "Removal of Lipid Artifacts in  $^1\text{H}$  Spectroscopic Imaging by Data Extrapolation," *Magnetic Resonance in Medicine*, vol. 35, no. 5, pp. 678–687, 1996.

- [268] C. Ma, F. Lam, R. Larsen, B. Sutton, and Z.-P. Liang, "Removal of Lipid Nuisance Signals in MRSI Using a Spatial-Spectral Lipid Model," in *Proceedings of the 21st Annual Meeting of the International Society for Magnetic Resonance in Medicine (ISMRM)*, Salt Lake City, Utah, Apr 2013, p. 2036.
- [269] S. B. Reeder, A. R. Pineda, Z. Wen, A. Shimakawa, H. Yu, J. H. Brittain, G. E. Gold, C. H. Beaulieu, and N. J. Pelc, "Iterative Decomposition of Water and Fat with Echo Asymmetry and Least-Squares Estimation (IDEAL): Application with Fast Spin-Echo Imaging," *Magnetic Resonance in Medicine*, vol. 54, no. 3, pp. 636–644, 2005.
- [270] H. Yu, C. A. McKenzie, A. Shimakawa, A. T. Vu, A. C. Brau, P. J. Beatty, A. R. Pineda, J. H. Brittain, and S. B. Reeder, "Multiecho Reconstruction for Simultaneous Water-Fat Decomposition and  $T_2^*$  Estimation," *Journal of Magnetic Resonance Imaging*, vol. 26, no. 4, pp. 1153–1161, 2007.
- [271] J. Ma, "Dixon Techniques for Water and Fat Imaging," *Journal of Magnetic Resonance Imaging*, vol. 28, no. 3, pp. 543–558, 2008.
- [272] D. Hernando, P. Kellman, J. P. Haldar, and Z.-P. Liang, "Robust Water/Fat Separation in the Presence of Large Field Inhomogeneities Using a Graph Cut Algorithm," *Magnetic Resonance in Medicine*, vol. 63, no. 1, pp. 79–90, 2010.

# Jeffrey Adam Kasten

---

## CONTACT INFORMATION:

École Polytechnique Fédérale Lausanne (EPFL)  
The Swiss Federal Institute of Technology, Lausanne  
BM 4.130 Bâtiment BM, Station 17  
CH-1015 Lausanne  
Tel: +41 (0) 21 693 1117  
Fax: +41 (0) 21 693 6990  
E-mail: Jeffrey.Kasten@epfl.ch

---

## EDUCATION:

---

- 2010-Present** **PhD Candidate** Institute of Bioengineering, École Polytechnique Fédérale de Lausanne, Switzerland. Expected completion in winter, 2014
- 2000-2004** **BA** in Physics, Department of Physics and Astronomy, Northwestern University, Evanston, Illinois, USA

## PROFESSIONAL SOCIETIES:

---

Institute of Electrical and Electronics Engineers (IEEE), USA  
International Society for Magnetic Resonance in Medicine (ISMRM), USA

## PROFESSIONAL and RESEARCH EXPERIENCE:

---

**2010-Present** *PhD Candidate, Medical Image Processing Lab, Institute of Bioengineering, EPFL*

*Thesis advisor: Dimitri Van De Ville, PhD*

*Thesis co-advisor: François Lazeyras, PhD*

Research: The aim of my research is to develop novel reconstruction methods for magnetic resonance spectroscopic imaging (MRSI), with  $^{31}\text{P}$  and  $^1\text{H}$  *in vivo* applications. Connected topics include the study of inverse problems, sparse methods in signal processing, and pulse sequence optimization.

**2005-2010** *Research Associate, Center for Imaging of Neurodegenerative Diseases, San Francisco Veterans Affairs Medical Center*

*Director: Michael Weiner, MD*

Management: Imaging project manager for studies in Sickle Cell Disease, Major Depressive Disorder, Primary HIV infection, and Normal Aging. Responsibilities included image processing (image registration, tissue segmentation, lobar parcellation, hippocampal voluming, quantitation and fitting of single voxel spectroscopic data, diffusion tensor analysis), as well as basic data

acquisition. Responsible for training all new staff in MR scanner operation and emergency procedures.

Research: Developed image processing pipeline tools for in-house Bayesian perfusion data reconstruction method (Kornak, J, Young, K, Schuff, N, Maudsley, AA, Weiner, MW (2009). K-Bayes Reconstruction for Perfusion MRI I: Concepts and Application. *Journal of Digital Imaging* 2010 Jun, 23(3), 277-86). Worked on the integration of zero-filled k-space perfusion data, multi-modal image registration, and tissue segmentation using the Python programming language in order to generate high-resolution perfusion maps for 4 Tesla MRI data.

**2003-2004** *Undergraduate Researcher, Mesoscopic Physics Group, Northwestern University, Evanston, Illinois*

*Mentors: Venkat Chandrasekhar, PhD, Paul Cadden-Zimansky, PhD*

Research: Fabrication of a close-approach mechanism for a low-temperature Atomic Force Microscope (AFM) using piezo-ceramic actuators and multi-channel voltage amplifiers. Production and testing of electrically connected tuning fork cantilever AFM tips.

## **TEACHING and MENTORING EXPERIENCE:**

---

**2011-present** Image Processing I & II, Master Program, EPFL, Teaching Assistant, Switzerland

**2011-present** Mentoring and supervising Master-level and undergraduate students completing semester projects in the Medical Image Processing Lab, EPFL, Switzerland

**2013** EPFL Summer Research Program (SRP) undergraduate student mentor, Switzerland

## **CONFERENCES and MEETINGS:**

---

**2014** International Society for Magnetic Resonance in Medicine (ISMRM) Annual Meeting, Milan, Italy

**2013** Signal Processing with Adaptive Sparse Structured Representations (SPARS), Lausanne, Switzerland

**2013** International Society for Magnetic Resonance in Medicine (ISMRM) Annual Meeting, Salt Lake City, UT, USA

**2013** International Symposium on Biomedical Imaging (ISBI), San Francisco, CA, USA

**2012** Swiss Society for Biomedical Engineering Annual Meeting, Lausanne, Switzerland

**2011** Center for Biomedical Imaging Research Day, Geneva, Switzerland

**2011** Lemanic Neuroscience Annual Meeting, Les Diablerets, Switzerland

**2011** National Competence Center for Biomedical Imaging Annual Meeting, Lausanne, Switzerland

**2011** Biomedical and Astronomical Signal Processing workshop, Villars-sur-Ollon, Switzerland

**2010** Workshop on Advanced Statistical Concepts for Multimodal MRI: Theory and Applications, San Francisco, CA

## ABSTRACTS:

---

1. *In vivo* MRSI Reconstruction by Low-Rank Component Analysis Using 3-D High-resolution Field Inhomogeneity Mapping. **Kasten, J**, Lazeyras, F, Van De Ville, V, *Proceedings of the 2014 Annual Meeting of the International Society for Magnetic Resonance in Medicine (ISMRM)*, Milan, Italy, 2014
2. Automatic Model Recovery for MRSI Reconstruction. **Kasten, J**, Lazeyras, F, Van De Ville, V, *Proceedings of the 2013 Annual Meeting of the International Society for Magnetic Resonance in Medicine (ISMRM)*, Salt Lake City, UT, USA, 2013
3. Magnetic Resonance Spectroscopic Imaging by Low-rank Component Analysis. **Kasten, J**, Lazeyras, F, Van De Ville, V, *Proceedings of the 2012 Annual Meeting of the Swiss Society for Biomedical Engineering*, Lausanne, Switzerland, 2012
4. A Randomized Trial of the Safety and Benefit of Transfusion Vs. Standard Care In the Prevention of Sickle Cell-Related Complications In Adults: a Preliminary Report From the Phase II NHLBI Comprehensive Sickle Cell Centers (CSCC) Study of Neuropsychological Dysfunction and Neuroimaging Abnormalities In Neurologically Intact Adult Patients with Sickle Cell Disease. Vichinsky, E, Neumayr, L, Gold, JI, Weiner, MW, **Kasten, J**, Truran, D, Snyder, C, Kesler, K, Hussein, AM, Harrington, TJ, McMahon, L, Gordeuk, VR, Kutlar, A, Orringer, EP, De Castro, LM, Field, J, Swerdlow, PS, Bessman, JD, Snyder, R, Strouse, JJ, Armstrong, D, *The 53<sup>rd</sup> ASH Annual Meeting and Exposition*, Orange County, USA, 2011

## PEER REVIEWED PUBLICATIONS:

---

1. **Kasten, J**, Vetterli, T, Lazeyras, F, Van De Ville, D (2014). 3D-Printed Shepp-Logan Phantom as a Real-World Benchmark for MRI, *Magnetic Resonance in Medicine* (Accepted, 4 December, 2014)
2. Buchs, JB, Buehler, L, Moll, S, Ruttimann, R, Nastasi, A, **Kasten, J**, Morel, P, Lazeyras, F (2014). DCD Pigs' Kidneys Analyzed by MRI to Assess *Ex Vivo* Their Viability, *Transplantation*, 2014 January, 97(2), 148-153
3. **Kasten, J**, Lazeyras, F, Van De Ville, D (2013). Data-Driven MRSI Spectral Localization via Low-Rank Component Analysis *IEEE Transactions on Medical Imaging*, 2013 June, 32(10), 1853-1863
4. **Kasten, J**, Lazeyras, F, Van De Ville, D (2013). Data-Driven MRSI Spectral Localization using Non-Cartesian Sampling Trajectories *Proceedings of the Ninth IEEE International Symposium on Biomedical Imaging: From Nano to Macro*, April 2013
5. Vichinsky, EP, Neumayr, LD, Gold, JI, Weiner, MW, Rule, RR, Truran, D, **Kasten, J**, *et al.* (2010). Neuropsychological Dysfunction and Neuroimaging Abnormalities in Neurologically Intact Adults with Sickle Cell Anemia *JAMA*, 2010 May, 303(18), 1823-31

## LANGUAGES:

---

English	(Mother tongue)
Russian	(Basic)
French	(Limited working proficiency)
Spanish	(Limited working proficiency)